学位論文

A Search for a keV Signature of Dark Matter with Suzaku Observations of the X-ray Diffuse Background

(「すざく」衛星による X 線背景放射の観測を用いた

keV 領域における暗黒物質からの信号の探索)

平成 26 年 12 月 博士 (理学) 申請

東京大学大学院理学系研究科
物理学専攻

関谷 典央

Abstract

Modern astrophysical and cosmological observations have shown the existence of "dark matter" in the Universe through the noticeable impact it has had on dynamic structure formation. The required mass density and spatial distribution of dark matter have been constrained both observationally and theoretically. As it is not "baryonic" mater, which forms a part of the Standard Model of particle physics, the nature of dark matter is an issue of fundamental importance in all of physics. Although several candidates such as "WIMPs" (weakly interacting massive particles), "super-WIMPs" and "sterile neutrinos" have been postulated, no conclusive evidence for these has been found from either direct or indirect dark matter searches. Searching for photon emission from the decay or annihilation of dark matter particles through astrophysical observations is a promising approach to the discovery of the nature of dark matter, and the X-ray region is one of the possible windows for the indirect detection of WIMPs, fermionic super-WIMPs and sterile neutrinos. In this thesis, we performed the deepest search for X-ray line emission from non-baryonic matter. In consideration of the current capabilities of X-ray observatories, we decided to aim our search at dark matter associated with the Milky Way galaxy in order to increase the signal-to-noise ratio. Further, we used the "XIS" instruments of "Suzaku" because of their stable and low Non-X-ray Background. We selected 187 data sets of blank sky regions from 2005 to 2013 out of the Suzaku archive and used careful screening to extract the pure X-ray Diffuse Background spectra covering the 0.5 – 7.0 keV energy range. The energy spectra were well described by X-ray emission due to charge exchange around the Solar System, hot plasma in and around the Milky Way, and a superposition of extra-galactic point sources. This is consistent with previous studies. We also curried out an accurate adjustment of the instrumental responses to X-ray signals by using multiple calibration data sets of the Crab Nebula. We also improved the technique of subtracting lines of instrumental origin. We next searched for narrow line emission in the region between 0.5 and 7.0 keV, and found possible signatures. Lastly, the confidence level of each detection was evaluated by considering that the dark matter line energy was not known *a priori* in the blind search ("look elsewhere effect"). After taking into account this effect, our results found no significant detection of line emission from dark matter. The possible dark matter line at 3.5 keV that has been reported in past studies was not detected in this analysis. We also obtained the tightest upper limit on dark matter line intensities in the 0.5 – 7.0 keV range, $\sim 5 \times 10^{-4}$ photons cm^{-2} s^{-1} sr^{-1} per $M_\odot$ pc^{-2}, and improved on the previous results ($\sim 1 \times 10^{-3}$ photons cm^{-2} s^{-1} sr^{-1} per $M_\odot$ pc^{-2} in the 1 – 7 keV). Assuming sterile neutrinos make up dark matter, we also tightened the constraints on their masses and mixing angles.

Contents

List of Tables

List of Figures

1　Introduction

The concept of "dark matter" was first introduced to explain the dynamics of galaxies in clusters in 1930s and has been established by both observational results and theoretical understanding of the Universe. The evidence for the existence of dark matter has also been provided by the rotation curve of spiral galaxies including the Milky Way galaxy with the H I observations (e.g. Corbelli et al., 2010; Chemin et al., 2009), the X-ray emission of hot ionized plasma in clusters (e.g. Sarazin, 1986; Evrard et al., 1996; Einasto & Einasto, 2000; Buote, 2004) and groups of galaxies and lensing of gravitational sources (e.g. Refregier, 2003). By the cosmological data such as results of cosmic microwave background observations, it is considered to constitute about a quarter of the total energy density in the present Universe while ordinary matter (luminous or baryonic matter) comprises less than 5 % of that (the rest is dark energy), and it occupies more than 80 % of the total mass density (e.g. Hinshaw et al., 2013). It also affects on dynamical structure of celestial objects, such as galaxies, clusters of galaxies and large scale structure of the Universe by gravitation. The current "standard cosmology", Λ-Cold Dark Matter (CDM) model, assumes that dark energy (or Λ term) and dark matter play prominent roles in gravitational effects in the structure formation in the Universe. Recently it is widely regarded as the important constituent member of the Universe.

Unlike baryonic matter, it does not interact with the electromagnetic force and the strong nuclear force but only with the gravitational force (and the weak nuclear force). As the nucleosynthesis model in the early Universe limits on the fraction of baryons (e.g. Dar, 1995), dark matter should not be baryonic matter, or particles within the "Standard Model" of particle physics. The candidates of dark matter can be exotic particles in extensions of the Standard Model as shown below. The nature of dark matter is still one of the great mysteries of science and a dark matter search is important for understanding the structure forming and evolution of the Universe in astrophysics and for understanding the electroweak symmetry breaking in particle physics.

Dark matter has to be stable or cosmologically long-lived, and be produced an adequate amount in the early Universe. It must also weakly interact with the particles in the Standard Model and be consistent with astrophysical and cosmological bounds. As possible candidates, for example, WIMPs (weakly interacting massive particles) including neutralinos, super-WIMPs (especially fermionic ones) including gravitinos, axion and sterile neutrinos with their masses ranging from micro-eV to TeV have been proposed (e.g. Feng, 2010). The WIMPs are the particles in the supersymmetric theories (SUSY) and the most popular CDM candidates. They are the hypothetical particles which interact with the Standard Model with

roughly electroweak strength. Their masses should be from GeV to TeV and heavy enough so that they become non-relativistic already at decoupling. Through the introduction of the WIMPs, we are able to explain the required dark matter density in the present Universe. The super-WIMPs are also the possible dark matter candidates which interact super-weakly (i.e. much weaker than the Fermi interaction strength) with the Standard Model particles. Abe et al. (2014) denied the possibility that bosonic super-WIMPs constitute all of dark matter by direct detection limits obtained with the XMASS (liquid xenon detector in the Kamioka Observatory). Fermionic ones are still dark matter candidates and include many kinds of the SUSY particles (e.g. gravitino; Buchmüller et al., 2007) with their masses ranging from micro-eV to keV. The axion is also the CDM candidate and resolve the strong CP problem in quantum chromodynamics (e.g. Holman et al., 1983). It is supposed to interact with a photon in magnetic fields. Right-handed neutrinos (e.g. sterile neutrinos; Dodelson & Widrow, 1994; Asaka et al., 2005) are the Warm Dark Matter (WDM) candidates and predicted to decay into Standard Model particles.

Several approaches have been tried by direct and indirect detection to find the nature of dark matter. For example, laboratory experiments have been conducted to directly detect the WIMPs by testing their interaction with laboratory nucleons (Saab, 2013). However, all of them are not successful at present, and more viable alternative approaches are needed. One of open windows for indirect detection is the X-ray (or gamma-ray) emission search for decaying or annihilating dark matter.

In this thesis, we searched for an X-ray signature from dark matter to provide valuable constraints on the parameter space of extensions to the Standard Model. We first reviewed the previous X-ray search approaches in Chapter 2, and set our observational strategy in Chapter 3. The XIS instruments of the Suzaku satellite we selected to use in this thesis were introduced in Chapter 4. Then, Data reduction and background emission modeling were shown in Chapter 5, and trials to search for X-ray emission from dark matter with improved sensitivity was performed in Chapter 6. Finally, discussion and conclusion of this thesis were summarized in Chapter 7 and 8, respectively.

All error ranges state corresponding to 90 % confidence levels, and vertical error bars in the figures indicate 1σ levels, through this thesis. Throughout this paper, we assumed the cosmological parameters: the energy density parameters $\Omega_{\rm m} = 0.27$, $\Omega_{\Lambda} = 0.73$ and the Hubble constant $h_0 = 0.7$.

2 Review of dark matter search with X-ray satellites

2.1 Dark matter line emission

It is theoretically assumed that some of dark matter candidates decay into multi-bodies or annihilate each other and emit a photon. For example, GeV-mass WIMPs possibly annihilate and emit GeV gamma-ray signals. The WIMPs, the fermionic super-WIMPs and the sterile neutrinos also possess two-body radiative decay channels: (dark matter) $\rightarrow \gamma + \gamma$ or (dark matter) $\rightarrow$ another particle $+ \gamma$. In the case of a decaying dark matter, a possible appearance energy of its signal is widely conceivable. A heavy dark matter can also produce a low energy photon by a radiative decay (e.g. Demidov & Gorbunov, 2014). Anyway, we have potential to detect such emission from dark matter. One of windows for the indirect detection of the decaying dark matter is open to the X-ray energy range (Abazajian et al., 2001b).

The decaying dark matter has a cosmologically long lifetime: much longer than the age of the Universe (e.g. Boyarsky & Ruchayskiy, 2008). Although it decays rarely, its signal from a dark-matter-rich object is detectable. In a typical galaxy, for example, the amount of dark matter particles with the 1 keV mass are estimated to be $10^{74} - 10^{77}$. If its lifetime is equal to the age of the Universe ($\sim 10^{18}$ sec), its decay rate in the galaxy is $10^{56} - 10^{59}$ per second, corresponding to $10^{44} - 10^{47}$ erg/s as contrasted with the total X-ray luminosity of the Andromeda galaxy (M31) in the 0.1 – 2.4 keV range $\sim 10^{39}$ erg/s (Supper et al., 1997). Inversely, if the decaying dark matter with the 1 keV mass exists, its lifetime should be at least 6 orders of magnitude longer than the age of the Universe. At any rate, we are possible to detect dark matter line emission in the X-ray range from gravitational sources.

2.2 Dark matter search by X-ray observatories

In this past year, a lot of dark matter searches were conducted with X-ray observations of gravitational sources by using X-ray satellites. We summarized the previous dark mater searches with X-ray observatories in Table 2.1. Boyarsky et al. (2007) searched dark matter in the Milky Way with data sets of blank sky regions, and gave the tight restriction on the dark matter line intensities. Horiuchi et al. (2014) also obtained the tightest constraint with M31 observational data. Several authors have claimed the possible detection, but no report was supported by independent analyses. Loewenstein & Kusenko (2010) found a spectral feature at 2.5 keV in the energy spectrum of the Willman I dwarf galaxy (one of the satellite galaxies of the Milky Way). After the careful analysis, however, this line feature was denied

as dark matter origin (Nieto & Mirabal, 2010). Although Prokhorov & Silk (2010) reported a signature at 8.7 keV observed with Suzaku in Koyama et al. (2007a) as excess in the Fe XXVI Lyman-γ line, the energy resolution of the current X-ray observatories did not allow to reach any conclusion. As a whole, no hard evidence for these possible lines was obtained so far.

Table 2.1   Previous searches for a keV signature of dark matter (examples).

Reference	Target	Instrument (Satellite)	Exposure [ksec]	Note
Boyarsky+ 2006b	MW[*]	XMM-Newton	1450	
Boyarsky+ 2006c	Coma, Virgo	XMM-Newton	20, 40	
Boyarsky+ 2006d	LMC[†]	XMM-Newton	20	
Riemer-Sørensen+ 2006	MW	Chandra	–	
Watson+ 2006	M31 center	XMM-Newton	35	
Riemer-Sørensen+ 2007	A520	Chandra	67	
Boyarsky+ 2007	MW, UMi[‡]	XMM-Newton	547, 7	
Abazajian+ 2007	MW	Chandra	1500	
Boyarsky+ 2008	Bullet Cluster	Chandra	450	
Boyarsky+ 2009	M31 center	XMM-Newton	130	
Loewenstein+ 2009	UMi[‡]	Suzaku	70	
Riemer-Sørensen+ 2009	Draco[§]	Chandra	32	
Loewenstein+ 2010	Willman 1[§]	Chandra	100	2.5 keV line (1.8σ).
Prokhonov+ 2010	MW center	Suzaku	370	8.7 keV line (3.0σ).
Boyarsky+ 2010	M31, Fornax, Sculptor	XMM-Newton, Chandra	400, 52, 162	No 2.5 keV line.
Nieto+ 2010	Willman 1[§]	Chandra	100	No 2.5 keV line.
Borriello+ 2012	M33	XMM-Newton	20 – 30	
Watson+ 2012	M31 off-center	Chandra	53	
Loewenstein+ 2012	Willman 1	XMM-Newton	60	
Kusenko+ 2013	UMi, Draco	Suzaku	200, 200	
Horiuchi+ 2014	M31	Chandra	404	
Bulbul+ 2014	Clusters	XMM-Newton	8855	3.5 keV line (4.3σ).
Boyarsky+ 2014a	M31, Perseus	XMM-Newton	2452, 745	3.5 keV line (4.4σ).
	MW	XMM-Newton	15700	No 3.5 keV line.
Boyarsky+ 2014b	MW center	XMM-Newton	2640	3.5 keV line (5.7σ).

Notes.

[*] The Milky Way galaxy.

[†] Large Magellanic Cloud.

[‡] UMi: Ursa Minor dwarf galaxy.

[§] Dwarf galaxies (satellite galaxies of the Milky Way)

2.3   Possible 3.5 keV line detection

In 2014, several researchers reported possible X-ray line emission around 3.5 keV (e.g. Bulbul et al., 2014; Boyarsky et al., 2014). The detection reports of the 3.5 keV line were summarized in Table 2.2. In Bulbul et al. (2014), the first report of this line, XMM-Newton observational spectra of 73 clusters of galaxies were used and stacked to search for an unidentified line with high statistics. The significance of this detection was up to 4.3σ (not taking into account the "look elsewhere effect" detailed in Chapter 6). On the other hand, Boyarsky et al. (2014) found this line in the outskirts of the Perseus cluster and in the center of the M31 with 4.4σ significance. This line have only been detected in XMM-Newton and Chandra observational spectra of clusters of galaxies and nearby galaxies; this is instrumental-limited and target-limited. In the XMM-Newton observations of blank sky fields with exposure time of 15.7 Msec (Boyarsky et al., 2014), this signature was not found. Although Urban et al. (2014) reported 3.5 keV line detection with Suzaku observational data of the Perseus cluster, Tamura et al. (2014) denied this line detection with the same instruments and the same target. In these detection reports, there are worries about some systematic uncertainties due to the instruments of XMM-Newton and Chandra, and stacking data of clusters with diverse redshift and characters. Tamura et al. (2014) and Carlson et al. (2015) also pointed out underestimation of the K XVIII line emissivity at 3.5 keV (e.g. Figure 3.2 in Chapter 3) in these reports. At present time, no conclusive evidence for the 3.5 keV line have been obtained yet.

Table 2.2 Detection reports of the possible 3.5 keV signature (Iakubovskyi, 2014).

Reference	Target	Instrument	Exposure [ksec]	Energy [keV]	Intensity $[10^{-6}\ \mathrm{cm}^{-2}\ \mathrm{s}^{-1}]$
Bulbul+ 2014	Full stacked clusters	MOS[†]	6784	3.57±0.02	4.0±0.8
	Full stacked clusters	PN[†]	2071	3.51±0.03	$3.9^{+0.6}_{-1.0}$
	Coma+Cen+Oph*	MOS	525	3.57(fix)	$15.9^{+3.4}_{-3.8}$
	Coma+Cen+Oph	PN	184	3.57(fix)	< 9.5(90%)
	Perseus*	MOS	317	3.57(fix)	$52.0^{+24.1}_{-15.2}$
	Perseus	PN	38	3.57(fix)	< 17.7(90%)
	Perseus	MOS	317	3.57(fix)	$21.4^{+7.0}_{-6.3}$
	Perseus	PN	38	3.57(fix)	< 16.1(90%)
	Clusters	MOS	5941	3.57(fix)	$2.1^{+0.4}_{-0.5}$
	Clusters	PN	1849	3.57(fix)	$2.0^{+0.3}_{-0.5}$
	Perseus	ACIS-S[‡]	0.9	3.56±0.02	$10.2^{+3.7}_{-3.5}$
	Perseus	ACIS-I[‡]	0.5	3.56(fix)	$18.6^{+7.8}_{-8.0}$
	Virgo*	ACIS-I	0.5	3.56(fix)	< 9.1(90%)
Boyarsky+ 2014a	M31	MOS	979	3.53±0.03	$4.9^{+1.6}_{-1.3}$
	M31	MOS	1473	3.50 − 3.56	< 1.8(2σ)
	Perseus	MOS	529	3.50±0.04	7.0±2.6
	Perseus	PN	216	3.46±0.04	9.2±3.1
	MW	MOS	15700	3.45 − 3.58	< 0.7(2σ)
Riemer-Sørensen+ 2014	MW center	ACIS-I	751	∼3.5	< 25(2σ)
Jeltema+ 2014	MW center	MOS	1375	∼3.5	< 41
	MW center	PN	487	∼3.5	< 32
	M31	MOS	979	3.53±0.07	2.1±1.5
Boyarsky+ 2014b	MW center	MOS	2640	3.539±0.011	29±5
Malyshev+ 2014	Combined dSphs	MOS+PN	822+233	3.55(fix)	< 0.254(90%)
Urban+ 2014	Perseus core	XIS[§]	740	$3.510^{+0.023}_{-0.008}$	$32.5^{+3.7}_{-4.3}$
	Perseus confined	XIS	740	$3.592^{+0.021}_{-0.024}$	$18.8^{+6.5}_{-5.5}$
	Coma*	XIS	164	∼3.45	∼30
	Ophiuchus*	XIS	83	∼3.45	∼40
	Virgo	XIS	90	3.55	< 6.5(2σ)

Notes.

∗ Clusters of galaxies.

† X-ray CCD instruments of XMM-Newton.

‡ X-ray CCD instruments of Chandra.

§ X-ray CCD instruments of Suzaku.

2.4   Sterile neutrinos as dark matter candidates

Recently, the sterile neutrinos as dark matter candidates attract a lot of attention. They are hypothetical particles beyond the Standard Model which have right-handed chirality while the ordinary neutrinos (electron-, mu- and tau-neutrino; hereafter active neutrinos) have left-handed chirality and interact only gravitationally and weakly with the active neutrinos. They could be sufficiently generated in the early Universe through given mechanisms (Dodelson & Widrow, 1994; Shi & Fuller, 1999; Kusenko, 2006; Shaposhnikov & Tkachev, 2006; Petraki & Kusenko, 2008). The relic sterile neutrino abundance from scattering-induced conversion of the active neutrinos was first analytically estimated by Dodelson & Widrow (1994) and able to account for all of dark matter. The model containing the sterile neutrinos (neutrino Minimal Standard Model; νMSM) is strongly motivated by the neutrino flavor oscillation (non-zero masses and mixing of the active neutrinos) which is supported by the atmospheric neutrino evidence of the Super-Kamiokande (Fukuda et al., 1998), the baryon asymmetry of the Universe and other curious things beyond the Standard Model (e.g. Asaka & Shaposhnikov, 2005; Asaka et al., 2005). Moreover, introducing the sterile neutrinos may also help to explain several observed phenomena: the pulsar kicks (Kusenko & Segrè, 1997; Fuller et al., 2003; Kusenko, 2004; Kusenko et al., 2008), the fast growth of black holes (Munyaneza & Biermann, 2005, 2006) and the enhanced molecular hydrogen production associated with the early star formation (Biermann & Kusenko, 2006; Stasielak et al., 2007). A keV-mass sterile neutrino is a WDM candidate (e.g. Abazajian et al., 2001a). It resolves several inconsistencies between the predictions of the CDM model and the observational results such as the shape and smoothness of dark matter halos (Goerdt et al., 2006; Gilmore et al., 2007; Wyse & Gilmore, 2008; Lovell et al., 2014).

The flavor oscillation between the sterile neutrino and the active neutrinos (or radiative decay) is predicted (Figure 2.1) although its mixing angle may be really small. On this occasion, a photon with the energy $E = m_\mathrm{s}/2$ is emitted (m_s is a sterile neutrino mass). Since the keV-mass sterile neutrino should decay and produce a keV X-ray photon, a search for this radiative decay line emission in the X-ray range is meaningful. The decay rate (Γ), the inverse of their lifetime, is written as

$$\begin{aligned}
\Gamma &= \frac{9\alpha G_\mathrm{F}{}^2}{1024\pi^2} m_\mathrm{s}{}^5 \sin^2 2\theta \\
&= 1.4 \times 10^{-32} \left(\frac{m_\mathrm{s}}{1\ \mathrm{keV}}\right)^5 \left(\frac{\sin^2 2\theta}{10^{-10}}\right)\ \mathrm{s}^{-1},
\end{aligned} \tag{2.1}$$

where α is the fine-structure constant, G_F is the Fermi constant and θ is a sterile neutrino mixing angle (Pal & Wolfenstein, 1982). Its line flux is proportional to Γ (detailed in Chapter 3). Thus, astrophysical X-ray observations give constraints on parameters of their masses and mixing angles. Figure 2.2 shows their constraints by previous works. Since the remaining parameter space is not so large, the search for radiative decay line emission of the sterile

neutrinos is one of the exciting frontiers both for astrophysics and for particle physics.
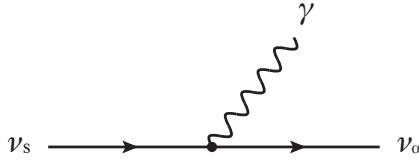
Figure 2.1   Feynman diagram of a sterile neutrino radiative decay. $\nu_{\rm s}$, ν_α and γ indicate a sterile neutrino, an active neutrino and a photon, respectively.
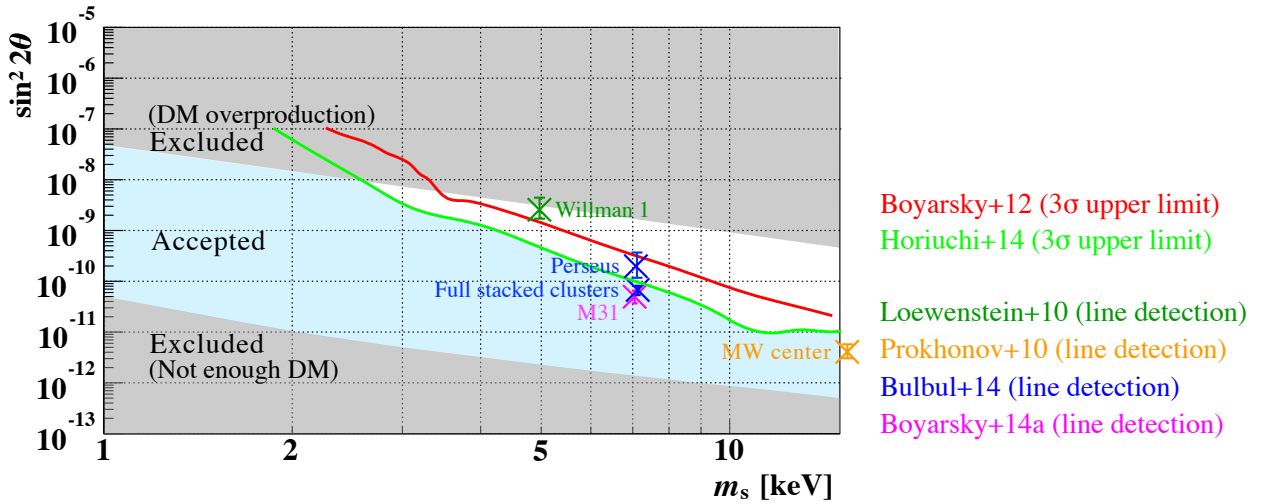
Figure 2.2   Constraints on (allowed region of) the sterile neutrino masses $m_{\rm s}$ and mixing angles $\sin^2 2\theta$. Their 3σ bounds by previous works are indicated (red and yellowish green solid lines; Boyarsky et al., 2012; Horiuchi et al., 2014). The regions above these solid lines had been excluded and the cyan shaded region had been accepted until this work was done. The cross marks indicate the parameters ($m_{\rm s}$ and $\sin^2 2\theta$) derived from the energies and intensities of the possible lines by previous works if they originate from the sterile neutrinos. The grey shaded regions are excluded by the non-resonant (upper region; no lepton asymmetry; Boyarsky et al., 2009a) and the resonant production with the maximal lepton asymmetry attainable in the νMSM (lower region; Shaposhnikov, 2008; Laine & Shaposhnikov, 2008). The region below 1 keV is ruled out by the Tremaine-Gunn phase-space density considerations (Boyarsky et al., 2009a) and on the Lyman-α analysis (Boyarsky et al., 2009b,c).

3 Dark matter detection strategy

3.1 Purpose for this thesis

In order to search for dark matter line emission, we must consider the following points:

1. Collecting an adequate amount of photon emission from dark matter.
   $\rightarrow$ Selecting target including an adequate amount of dark matter.
   $\rightarrow$ Observing target with large grasp (instrumental effective area $\times$ field of view) and long exposure time.

2. Avoiding photons from background plasma emission.
   $\rightarrow$ Selecting target whose background plasma emission is weak.

3. Selecting the most sensitive instrument for this search.

4. Accurately modeling background plasma emission.

5. Accurately reproducing instrumental response to signals.

Generally, Points 1. and 2. are incompatible. In this chapter, we considered these points of view, and looked for the best target, instrument and analysis method for this search.

3.2 Expected dark matter line intensity

First of all, we estimated the line intensity of dark matter line emission for a given dark matter column density of a target. In the case of radiative decay, especially a two-body decay case: (dark matter) $\rightarrow$ another particle $+ \gamma$, producing a photon with the monochromatic energy $E = m_{\mathrm{DM}}/2$ (e.g. sterile neutrinos; mainly dealt in this Chapter), its line flux F is

$$F = \frac{\Gamma}{m_{\mathrm{DM}}} \int_{\mathrm{FoVcone}} \frac{\rho_{\mathrm{DM}}(\boldsymbol{r})}{4\pi|\boldsymbol{D}_{\mathrm{L}} + \boldsymbol{r}|^2} d\boldsymbol{r}, \tag{3.1}$$

where Γ is a decay rate, the inverse of its lifetime, m_{DM} is a dark matter mass, $\boldsymbol{r}$ indicates three-dimensional coordinates with its origin at the target and $\boldsymbol{D}_{\mathrm{L}}$ is a luminosity distance to the target and the integration range is inside a cone produced by a field of view (FoV). In the case of the small FoV ($\Omega \ll 1$), F is rewritten as

$$F = \frac{\Gamma S_{\mathrm{DM}} \Omega}{4\pi m_{\mathrm{DM}}}, \tag{3.2}$$

where S_{DM} is a dark matter column density which is equal to a dark matter density ρ_{DM} integrated along a line of sight:

$$S_{\mathrm{DM}} = \int_{\mathrm{l.o.s.}} \rho_{\mathrm{DM}}(r) dr, \tag{3.3}$$

where r is a Earth-centered one-dimensional coordinate. Thus, the line intensity ($I = F/\Omega$) is proportional to S_{DM}:

$$I = \frac{\Gamma S_{\mathrm{DM}}}{4\pi m_{\mathrm{DM}}}. \tag{3.4}$$

In the annihilation case, the signal intensity is proportional to $\int_{\mathrm{l.o.s.}} \rho_{\mathrm{DM}}^{2} dr$. We are able to discuss the annihilation case in the same way of the decay case.

3.3   Expected line detection limit

In consideration of only statistic uncertainty, the significance (confidence level defined as Z in unit of σ here) of the dark matter line detection is simply equal to signal-to-noise ratio (SNR) expressed in

$$Z = \mathrm{SNR} = \frac{S}{\sqrt{S + 2B}}, \tag{3.5}$$

where B is a background photon count and S is a signal photon count in dark matter line emission determined by subtraction of $(S + B) - B$ (Bradt, 2004). In the case of the dark matter line intensity I_{S} and the background specific intensity I_{B}, S and B are

$$S = I_{\mathrm{S}} \times A \times \Omega \times T, \tag{3.6}$$

$$B = I_{\mathrm{B}} \times A \times \Omega \times T \times \Delta E, \tag{3.7}$$

where A is an effective area of an instrument, Ω is a FoV, T is an exposure time and ΔE is an energy resolution defined as 5.2σ: 2.2 times full width half maximum (FWHM): to collect 99 % of photons in the Gaussian line. From Eq.(3.5), (3.6) and (3.7), the $Z\sigma$ detection limit of the line intensity ($I_{\mathrm{S},Z\sigma}$) is

$$I_{\mathrm{S},Z\sigma} = \frac{Z^2 + \sqrt{Z^4 + 8 \cdot Z^2 \cdot I_{\mathrm{B}} \cdot A \cdot \Omega \cdot T \cdot \Delta E}}{2 \cdot A \cdot \Omega \cdot T}. \tag{3.8}$$

Especially, the 3σ line detection limit ($I_{\mathrm{S},3\sigma}$) is

$$I_{\mathrm{S},3\sigma} = \frac{3^2 + \sqrt{3^4 + 8 \cdot 3^2 \cdot I_{\mathrm{B}} \cdot A \cdot \Omega \cdot T \cdot \Delta E}}{2 \cdot A \cdot \Omega \cdot T}. \tag{3.9}$$

As shown in Eq.3.9, it is necessary for the sensitive dark matter line search to be low background, large grasp ($A \times \Omega$), long exposure time and high energy resolution.

3.4   Target selection

A suitable target for the dark matter search seems to be an object with high dark matter column density such as groups and clusters of galaxies. However, this kind of the target also has high temperature ($kT > 1$ keV) optically-thin plasma in large quantities and its X-ray emission washes out possibly weak dark matter line emission (shown as the red and blue lines in Figure 3.1). The plasma emission brightness is proportional to the square of its density.

Moreover, many of atomic lines from this plasma interrupt the line search (Figure 3.2), especially in the low or moderate instrumental energy resolution case (> 100 eV). On the other hand, a relatively X-ray-faint target such as dwarf and spiral galaxies has an advantage in background plasma emission although its possible dark matter emission is expected to be lower than that of the X-ray-bright target. The lowest plasma emission is the "X-ray Diffuse Background" (XDB) which consists of the Milky Way and unresolved extragalactic plasma emission distributed over the whole sky (shown as the black line in Figure 3.1). In the 'blank sky' regions which are dominated by the XDB, we are also possible to find dark matter associated with the Milky Way.
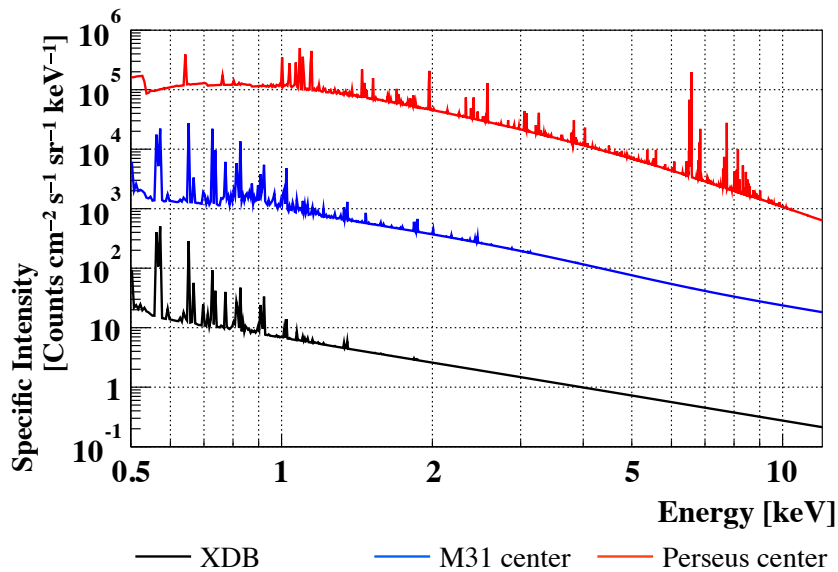
Figure 3.1 Specific intensities of the typical XDB (Yoshino et al., 2009), the center of the M31 and the Perseus cluster (Tamura et al., 2009) in the 0.5 – 12.0 keV range. Note that detector responses are not convolved.
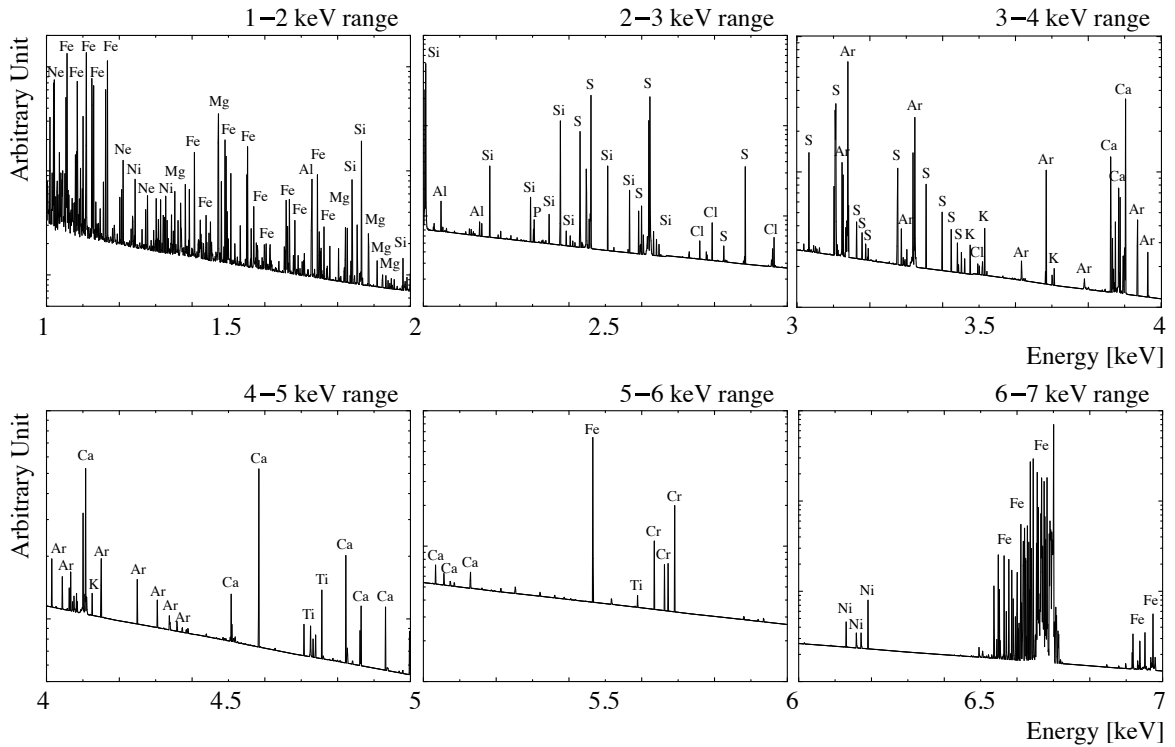
Figure 3.2   Specific intensity of the optically-thin thermal CIE plasma emission in the
$1.0 - 7.0$ keV range. The plasma temperature $kT = 2$ keV ($T \sim 2.3 \times 10^7$ K; a possible
temperature of clusters of galaxies) and the element abundances are set to the Solar-
neighbor values (Anders & Grevesse, 1989).

In order to select the best suitable target for the dark matter search, we must know the dark
matter column density which is proportional to its line intensity, and the plasma emission
brightness as background for various candidates. Figure 3.3 (from FIG.1 in Boyarsky et al.,
2010) shows the dark matter column densities (S_{DM}) of various objects: galaxies, groups
and clusters of galaxies. S_{DM} are roughly ranging from 50 to 10^3 $M_\odot$ pc^{-2} although large
scattering exists. In the center of the M31 and the Perseus cluster (hereafter simply Perseus),
for instance, $S_{\mathrm{DM}} \sim 600$ $M_\odot$ pc^{-2} Widrow & Dubinski (2005); Boyarsky et al. (2014) and
$S_{\mathrm{DM}} \sim 800$ $M_\odot$ pc^{-2} (Bulbul et al., 2014; Tamura et al., 2014), respectively[*3.1].

The dark matter mass distribution in the Milky Way was also estimated over the whole
sky by two methods. One was from the rotation curve obtained by the H I survey (Remmen,
2011; Sofue, 2012). The other was from the NFW profile which was expressed in

$$\rho_{\mathrm{DM,NFW}}(R) = \frac{\rho_0}{X(1+X)^2}, \tag{3.10}$$

where $X = R/h$, R is a distance from the Galactic center, h is the scale radius and ρ_0 is the
dark matter density at the Galactic center (introduced by Navarro et al., 1996). We assumed
$\rho_0 = 1.06 \times 10^{-2}$ $M_\odot$ pc^{-3} and $h = 12.53$ kpc as the parameters of the NFW model from

---

*3.1 $M_\odot$ is the Solar mass ($\sim 2.0 \times 10^{33}$ g).

Sofue (2012). The column density of dark matter in the Milky Way is expressed in

$$S_{\mathrm{DM}} = \int_0^\infty \rho_{\mathrm{DM}} \left(\sqrt{r_\odot{}^2 + z^2 - 2r_\odot z \cos\phi} \right) dz, \qquad (3.11)$$

where $r_\odot$ is the distance from the Galactic center to the Sun ($\sim$ 8 kpc), z is a vertical distance from the Galactic plane and ϕ is an angle from the Galactic center related to Galactic coordinates (l, b) via

$$\cos\phi = \cos l \cos b. \qquad (3.12)$$

S_{DM} distributions as functions of ϕ estimated from the two methods are shown in Figure 3.4. Typically, $S_{\mathrm{DM}} \sim 50\ M_\odot\ \mathrm{pc}^{-2}$ for the direction of the Galactic anti-center and $S_{\mathrm{DM}} > 100\ M_\odot\ \mathrm{pc}^{-2}$ for the Galactic center ($\phi < 60°$).
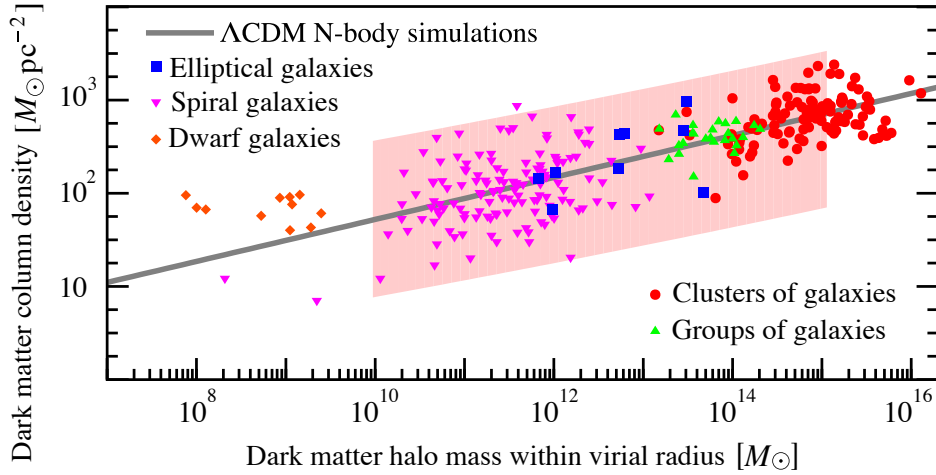
Figure 3.3   Dark matter column densities of various objects: galaxies, groups and clusters of galaxies as functions of dark matter halo masses within virial radii[*3.2] (FIG.1 in Boyarsky et al., 2010).

[*3.2] They are derived from the virial theorem $U = -2T$ where U and T are the gravitational potential energy and the total kinetic energy, respectively. The average dark matter density within the virial radius is $\sim$ 200 times higher than the critical density of the present Universe ($\sim 10^{-29}\ \mathrm{g\ cm}^{-3}$).
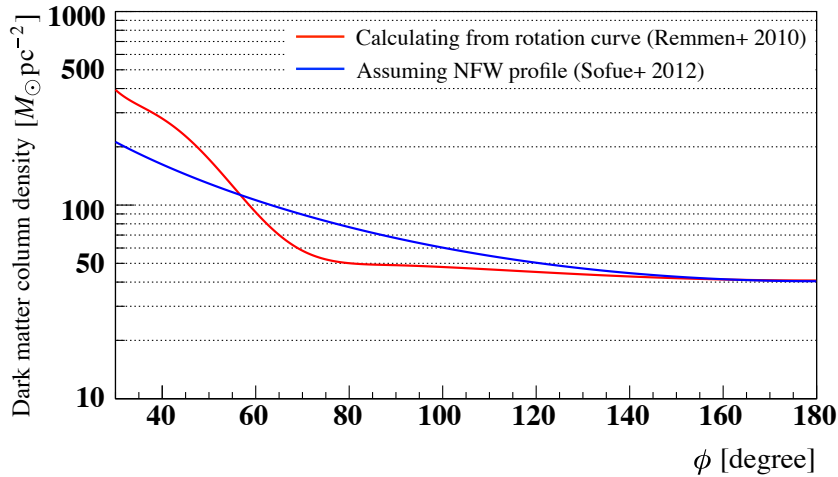
Figure 3.4   Comparison of two column density distributions as functions of ϕ: from the rotation curve and the NFW profile.

The plasma emission from galaxies, groups and clusters of galaxies and the XDB have been well investigated and modeled with X-ray satellites by previous works as shown in Figure 3.1. Because the Galactic center has much brighter background plasma emission including multiple atomic line emission than the typical XDB in the Galactic anti-center, we considered the two directions as different targets for the dark matter search.

Then, we compared the various targets and selected the best suited target for the dark matter search. Figure 3.5 shows the 3σ line detection limits for the various targets (the XDB, the M31 and the Perseus) with Eq.3.9. Hereafter in this thesis, the unit of all line intensities are defined as "LU", which is equal to photons cm^{-2} s^{-1} sr^{-1}. Since the background plasma emission of the M31 and the Perseus are $\sim 10^2$ and $\sim 10^4$ times higher than that of the XDB, their line detection limits are ~ 10 and $\sim 10^2$ times higher. On the other hand, the expected dark matter line intensities (column densities) of the M31 and the Perseus are ~ 12 and ~ 16 times higher than that of the XDB. In order to take account of both advantages of the background plasma emission and the dark matter line intensities, the 3σ line detection limits normalized with dark matter column densities of the XDB, the M31 and the Perseus were compared in Figure 3.6. We found that the XDB was the best target for the dark matter line search in the keV range under the same conditions of the observation (effective area, FoV, energy resolution and exposure time).
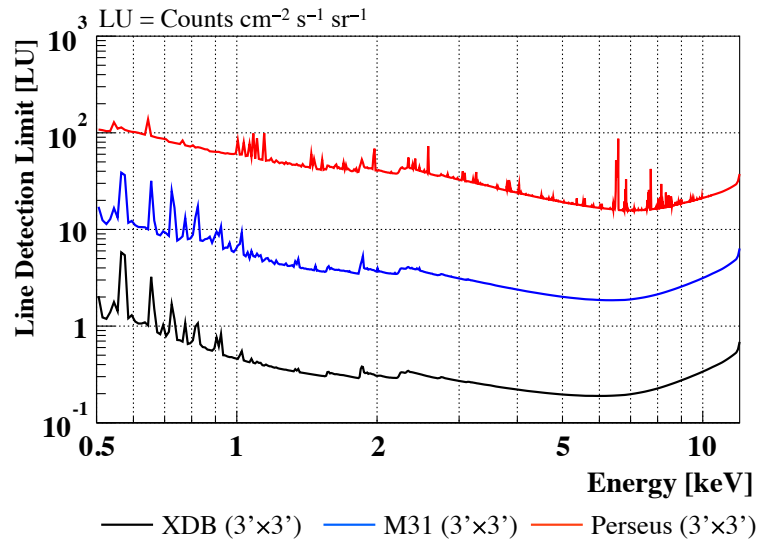
Figure 3.5 3σ line detection limits for various targets (the XDB, the M31 and the Perseus) with the Suzaku XIS, $3' \times 3'$ of FoV and 100 ksec of exposure time. LU (Line Unit) is equal to photons cm^{-2} s^{-1} sr^{-1}.
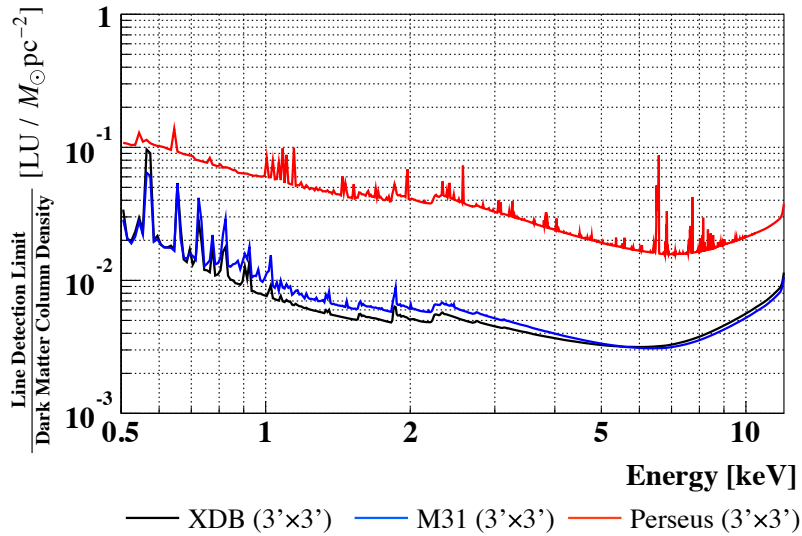
Figure 3.6 Same as Figure 3.5 but for 3σ line detection limits normalized by their column densities.

3.5 X-ray Diffuse Background

Since we are in the dark matter distribution of the Milky Way, we have potential to detect its signal over the whole sky. In searching for dark matter associating with the Milky Way, the XDB lies in this way as the background plasma emission. Fortunately, the XDB intensity is lower than that of any other background plasma emission from possible targets for the dark matter search. Furthermore, little atomic lines as obstacles for this search appear above

~ 1 keV in the XDB in contrast to the other targets such as clusters of galaxies.

The XDB have been investigated and modeled with the Suzaku XIS by previous works (e.g. Yoshino et al., 2009; Yoshitake et al., 2013). The XDB is considered to originate in the following components:

1. The Heliospheric Solar Wind Charge Exchange (H-SWCX; Cox, 1998; Cravens, 2000; Lallement, 2004)

2. The Local Hot Bubble (LHB; McCammon & Sanders, 1990)

3. Hot plasma of the Milky Way Halo (MWH; Yao et al., 2009; Hagihara et al., 2011; Sakai et al., 2014).

4. Unresolved extragalactic point sources called the Cosmic X-ray Background (CXB; Kushino et al., 2002; Smith et al., 2007)

5. High temperature ($kT \sim 1.0$ keV) plasma (High temperature component; Sekiya et al., 2014a)

The schematic XDB spectrum is shown in Figure 3.7.
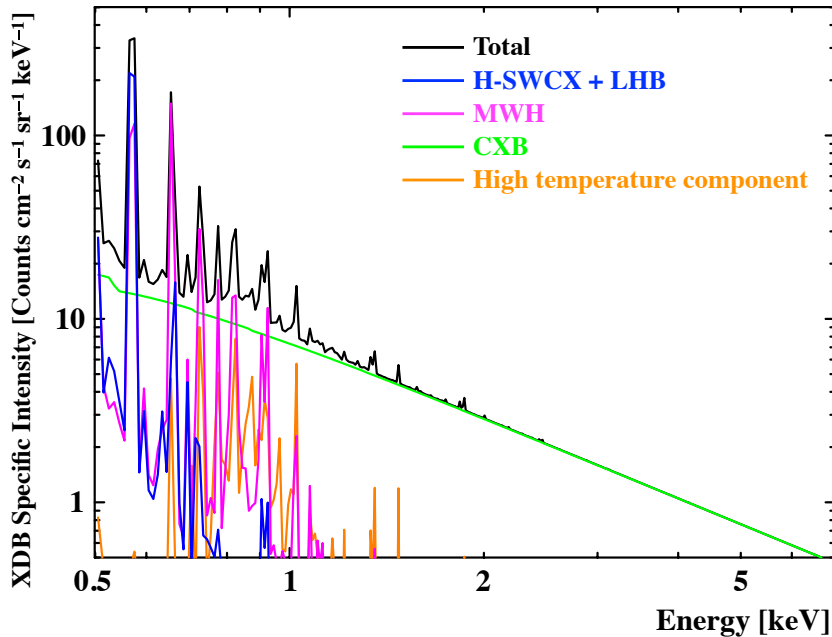
Figure 3.7   Schematic XDB spectrum. Note that a detector response is not convolved.

The SWCX was firstly discovered by the observation of the comet Hyakutake with ROSAT satellite (Lisse et al., 1996). When an ion X^{Q+} in the Solar wind interacts with a neutral atom Y (mainly hydrogen and helium), electrons bound in the neutral atom transfer to the excited state of the ion $X^{*(Q-1)+}$, and then move to ground state with the X-ray photon emission corresponding to the de-excitation energy. This process of charge exchange is expressed by the following equation:

$$X^{Q+} + Y \; \rightarrow \; X^{*(Q-1)+} + Y^{+} \; \rightarrow \; X^{(Q-1)+} + Y^{+} + h\nu \; . \tag{3.13}$$
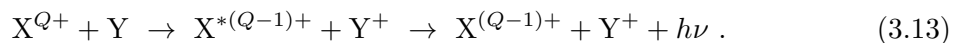
The two kinds of SWCX appear in the XDB energy spectra: one is the Geocoronal SWCX (G-SWCX) which is due to interaction between the Solar wind and the Earth's exosphere, the other is Heliospheric SWCX (H-SWCX) which is due to interaction between the Solar wind and neutral atoms in the interplanetary space. The former was firmly discovered by Fujimoto et al. (2007). The G-SWCX is sensitive to the short-term change of the Solar wind condition and shows correlation with the Solar wind ion flux. The latter was pointed out by Cox (1998) and simulated by Koutroumpa et al. (2006). Yoshitake et al. (2013) showed the long-term variability of the H-SWCX induced O VII line intensities due to the 11-year Solar activity.

The LHB is widely believed to exist as the result of one or more supernova explosions (Cox & Anderson, 1982). It is considered that the hot and optically-thin plasma with the temperature of $kT \sim 0.1$ keV ($T \sim 10^6$ K) and the density of $n_{\rm H} \sim 0.005$ cm^{-3} is embedded in a ~ 100 pc cavity of the cold interstellar medium in which the Solar System resides (McCammon & Sanders, 1990).

The MWH is the hotter plasma bound in the Milky Way with the temperature of $kT = 0.2$ – 0.4 keV possibly originating from the stellar wind, the supernova outflow from the Galactic disk and the infall of the intergalactic medium (Yao et al., 2009; Hagihara et al., 2011; Sakai et al., 2014). It extends from the Galactic disk with the scale hight of a few kpc.

The CXB is believed to come from numerous faint extragalactic sources such as active galactic nuclei. Actually, the deep observations with Chandra and XMM-Newton resolved 80 % of the CXB into point sources (Mushotzky et al., 2000; Moretti et al., 2003). Kushino et al. (2002) and Smith et al. (2007) proposed emission models of the CXB by a power-law function with its photon index of 1.4 or modified power-law functions.

In some locations, the High temperature component with strong emission of Fe-L complex and Ne-K lines appear in the XDB spectra Sekiya et al. (2014a). It is considered to be from the hot and optically-thin plasma with the temperature of $kT \sim 1$ keV. However, its origin, distance, extension and density are still open questions.

As a whole, the XDB spectra are simple, easy to model and have low time variability above 1 keV energy range. In high Galactic latitudes ($> 20°$) or around the Galactic anti-center blank sky fields, observational direction variation of the XDB is also negligible above 1 keV. The XDB is frequently observed with X-ray observatories as blank sky field or background observations, and their data are in open archives. We are able to use the deep (having long exposure time) XDB data by stacking archival data sets of blank sky regions in order to collect an adequate amount of photon emission from dark matter in the Milky Way.

3.6   Instrument selection

In order to search for weak X-ray line emission against diffuse plasma emission, the most sensitive way is the imaging spectroscopic observation with the CCDs onboard X-ray astronomy satellites at present. We selected the most sensitive instrument for the dark matter line search from the X-ray CCD instruments of existing satellites, Chandra, XMM-Newton and Suzaku. In Table 3.1, we summarized the notable characters of the five X-ray CCD instruments, the ASIS-I and -S of Chandra, the EPIC-MOS and -PN of XMM-Newton, and the XIS of Suzaku.

We here discussed their advantages and disadvantages for the dark matter search. These instruments have relatively wide energy ranges of the 0.2 – 15 keV and moderate energy resolution of $\sim$ 100 eV. In order to detect the weak line search in a diffuse target, the "grasp" (the product of effective area and FoV) is one of the important parameters. In Figure 3.8, we compared the five instruments by the grasp. The XMM-Newton PN has the largest grasp of all. If we select the target with the weak background plasma emission, the contamination by "Non-X-ray Background" (NXB; described in Section 4.5) is not ignorable. In Figure 3.9, we compared the five instruments by the NXB intensities. The Suzaku XIS has the lowest NXB of all. The NXB intensity of the Suzaku XIS is lower than that of the XDB below 2 keV. Furthermore, the time variability of the NXB intensity is also low as contrasted with that of the other instruments. In the case of the XMM-Newton and Chandra instruments, NXB widely fluctuates by their orbital locations. As shown in Figure 3.10, the Suzaku XIS is the most sensitive for the low background target such as the XDB because of moderate grasp and the lowest and most-stable NXB.

Additionally, we are able to use the hundreds of blank sky data in the Suzaku XIS archive whose total exposure time is over 10 Msec. We possibly detect the low intensity line of $\sim$ 0.01 photons cm^{-1} s^{-1} sr^{-1} in the 1 – 7 keV range by the 10 Msec observation of the XDB with the Suzaku XIS as shown in Figures 3.10 and 3.11.

Table 3.1   Characters of the five X-ray CCD instruments of the three satellites.

Satellite	Chandra	XMM-Newton	Suzaku
CCD instrument	ACIS	MOS+PN	XIS
Field of view*	8.3×8.3×(4FI+6BI)	∼700×(2MOS+1PN)	17.8×17.8×(3FI+1BI)
Angular resolution†	0.5	5(MOS), 6(PN)	110(FI), 140(BI)
Energy range‡	0.3 – 12	0.15 – 15	0.2 − 12
Energy resolution§	50 – 200	50 – 200	50 – 200
Effective area∥	200(4FI), 400(6BI)	800(2MOS), 1200(PN)	660(3FI), 320(BI)
NXB rate♯	10 – 1000(unstable)	5 – 100(unstable)	1 – 10(stable)

Notes.

∗ In unit of arcmin^2.

† Half power diameter in unit of arcmin.

‡ In unit of keV.

§ FWHM in unit of eV.

∥ At 1 keV in unit of cm^2.

♯ In unit of $\text{cm}^{-2}\ \text{s}^{-1}\ \text{sr}^{-2}\ \text{keV}^{-1}$.
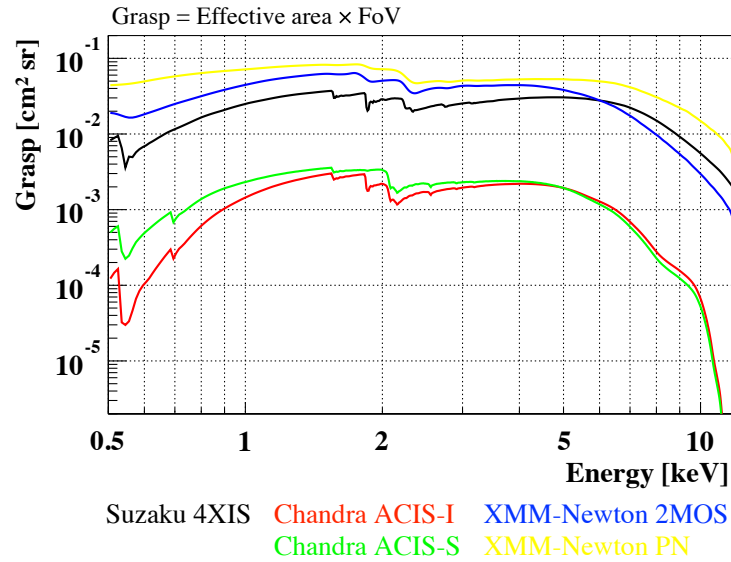
Figure 3.8   Grasp of the five CCD instruments.
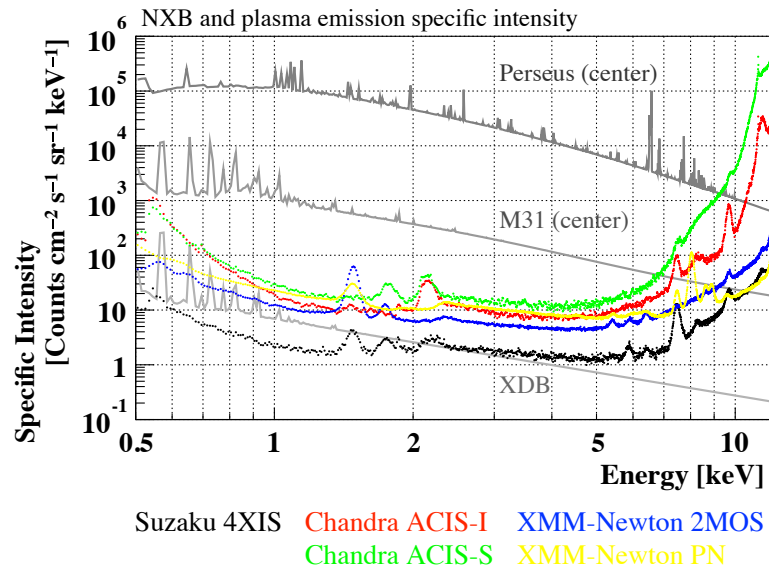
Figure 3.9 NXB intensities of the five CCD instruments. For comparison, plasma emission intensities of the XDB, the M31 and the Perseus are indicated. The lowest cases of NXB for the XMM-Newton and Chandra instruments are shown.
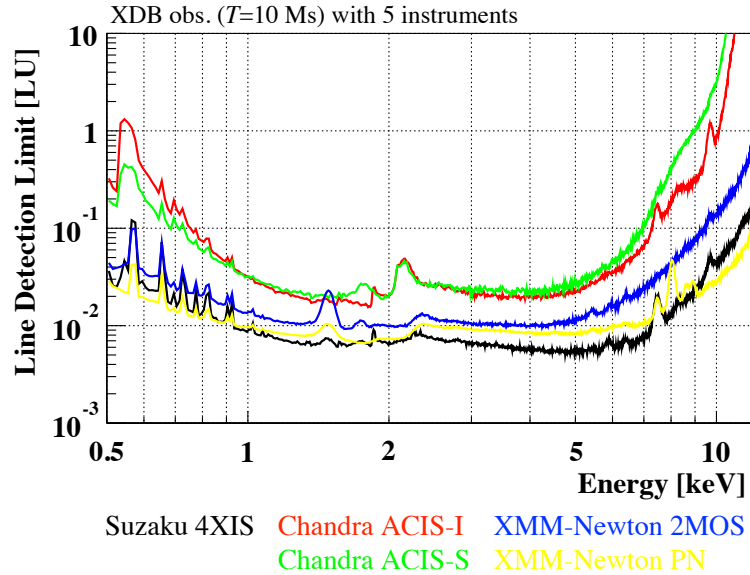
Figure 3.10 3σ line detection limits estimated from Eq.3.9 with the five CCD instrument observations of the XDB for 10 Msec of exposure time. The lowest cases for the XMM-Newton and Chandra instruments are shown.
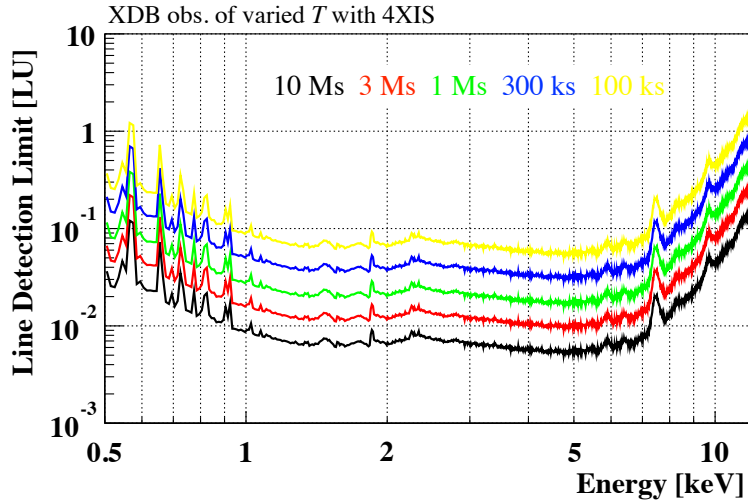
Figure 3.11 3σ line detection limits with the Suzaku XIS observations of the XDB for various exposure time.

3.7   Strategy for the most sensitive dark matter search

We found that the XDB and the Suzaku XIS are the best observational target and instrument, respectively, for the dark matter line search in the keV energy range at present time, due to the following reasons:

1. In considering expected intensities of both dark matter line emission and background X-ray plasma emission including NXB, the XDB is the best target for the dark matter line search in the keV range under the same observational conditions (effective area, FoV, energy resolution and exposure time).

2. There are little atomic lines as obstacles for the dark matter line search above ~ 1 keV in the XDB.

3. Through the instrumental advantages (especially grasp, NXB intensity and stability), the Suzaku XIS is the most sensitive for the weak line search with the XDB observations.

4. In the Suzaku XIS archive, there are hundreds of data sets of blank sky fields for the deep XDB analysis.

As the most sensitive way, we decided to search for dark matter associated with the Milky Way by using the multiple Suzaku XIS observational data of the XDB in this thesis.

4 Suzaku XIS for dark matter search
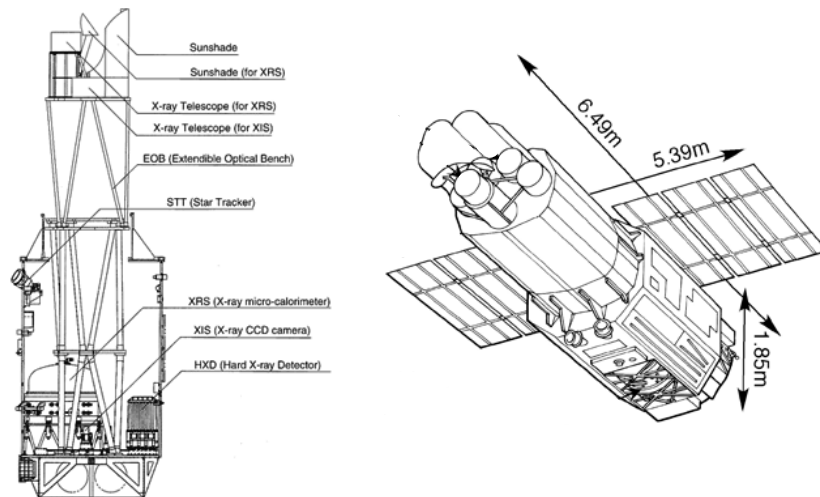
Figure 4.1　Side view (left) and outer view (right) of the Suzaku satellite[*4.1].

4.1　Overview of Suzaku satellite

The fifth Japanese X-ray astronomy satellite, Suzaku (Mitsuda et al., 2007), was launched on Jury 10, 2005 (Figure 4.1). It is placed in an approximate circular orbit with an altitude of the 550 – 600 km, an inclination angle of 31° and an orbital period of 96 minutes. Suzaku has the 0.3 – 600 keV broad energy band-pass and high sensitivity in the whole band. It is realized by two instruments. One is the set of four X-ray Imaging Spectrometers (XISs; Koyama et al., 2007b) covering the 0.3 – 10 keV energy range and placed at focal planes of X-ray Telescopes (XRTs; Serlemitsos et al., 2007). The other is Hard X-ray Detector (HXD; Takahashi et al., 2007) covering the 10 – 600 keV range (not used in this thesis). Hereafter we focused on the modules of XRT and XIS as the best observational system for the dark matter line search in the below 10 keV range.

4.2　XRT-XIS modules

Suzaku has four XISs and four XRTs dedicating each XIS. The XRTs are the X-ray collectors which consist of closely nested thin-foil reflectors (Figure 4.2 right). Especially,

---

[*4.1] `http://www.isas.jaxa.jp/e/enterp/missions/suzaku`

[*4.2] `http://www.astro.isas.ac.jp/suzaku/doc/suzaku_td`

Figure 4.2   Photographs of the XRT (left) and the XIS (right) from the Suzaku Technical Description[*4.2].

Table 4.1   Overview of the XRT-XIS modules.

XRT	Focal length	4.75 m
	Field of view	17′ @ 1.5 keV
		13′ @ 8 keV
	Plate scale	0.724 arcmin/mm
	Effective area	440 cm^2 @ 1.5 keV
		250 cm^2 @ 8 keV
	Angular resolution	2′ (HPD)
XIS	Field of view	17.8′ × 17.8′
	Energy range	0.2 – 12 keV
	Pixel grid	1024 × 1024
	Pixel size	24 μm × 24 μm
	Energy resolution	∼ 130 eV @ 6 keV
	Effective area	340 cm^2 (FI), 390 cm^2 (BI) @ 1.5 keV
	(incl XRT)	150 cm^2 (FI), 100 cm^2 (BI) @ 8 keV
	Time resolution	8 s (Normal mode)

the four XRT-I are used for the XISs. The XISs are the X-ray sensitive imaging CCD cameras (Figure 4.2 left). The three of XISs are front-illuminated (FI; energy range 0.4 – 12 keV) and one is back-illuminated (BI; energy range 0.2 – 12 keV). The overview of the XRTs and XISs are summarized in Table 4.1 and detail descriptions are in Serlemitsos et al. (2007) and Koyama et al. (2007b). In this thesis, we searched for X-ray line emission from dark matter associated with the Milky Way by using these modules. It is important for the dark matter line search in this thesis to understand conditions and performances of these modules involved in the spectral analysis and their uncertainties. Here, we collected up the instrumental factors which were important for this study.

4.3   Degradation of the XIS

The conditions of observational modules in X-ray satellites change from moment to moment. The Suzaku XISs are no exception. The performances of the XISs change both continuously and discontinuously. For example, the XIS energy resolution varies by the observational date as shown in Figures 4.3 and 4.4). The energy gain and the energy resolution have gradually degraded by increasing charge transfer inefficiency due to charge traps made by cosmic rays (charged particles). The low-energy efficiency also ages because of accumulating contamination on the optical blocking filters (OBFs)*4.3 as circumstantially described in Section 4.4. Additionally, the XIS performances can drastically shift after noticeable condition changes. Some major events in the XISs and their causes were summarized in Table 4.2. Especially, the energy gain and the energy resolution leap at the points of micro-meteorite hits and the setting conversions of the spaced-raw charge injection (SCI)*4.4 as shown in Figure 4.4. We must take into account these effects to make the best use of this instrument. These effects have been already reflected to the instrumental response function by calibration (detailed in Section 4.4).
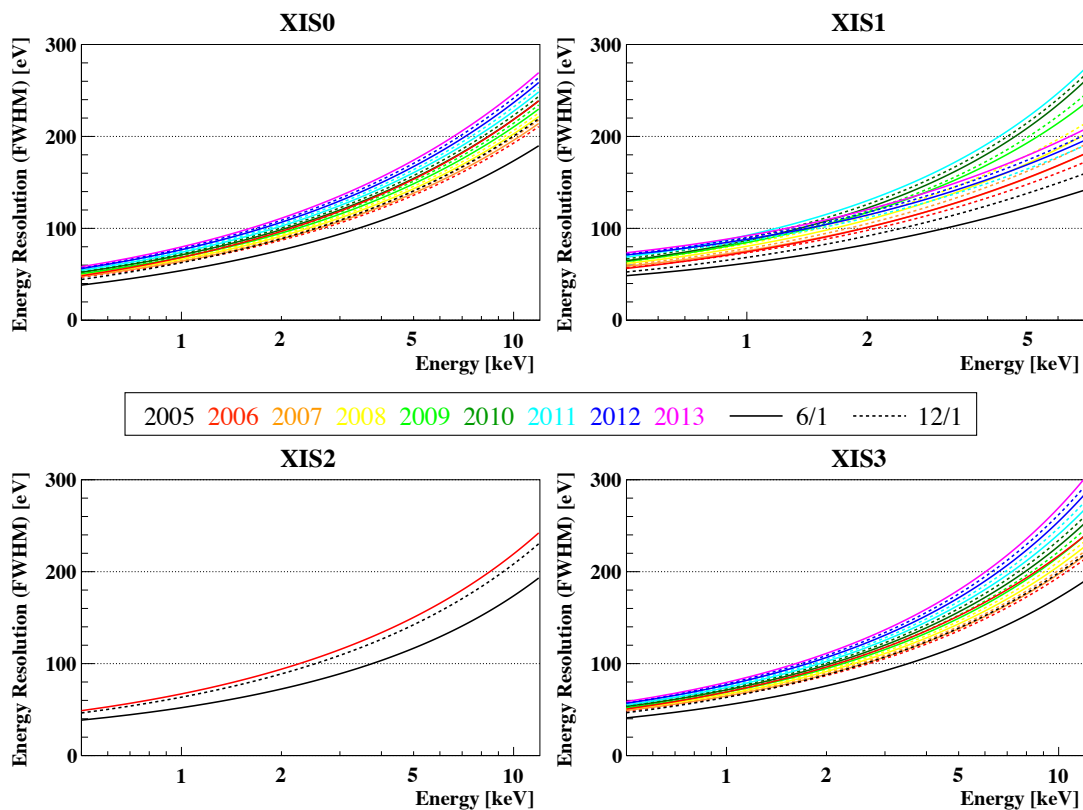
Figure 4.3   Energy dependence of energy resolution of the XISs.

---

*4.3 The filters located in front of the XISs and made of aluminum coated polyimide in order to attenuate optical and UV photons contaminating the X-ray signal.

*4.4 The function to mitigate the charge transfer inefficiency by artificial injection of electrons.
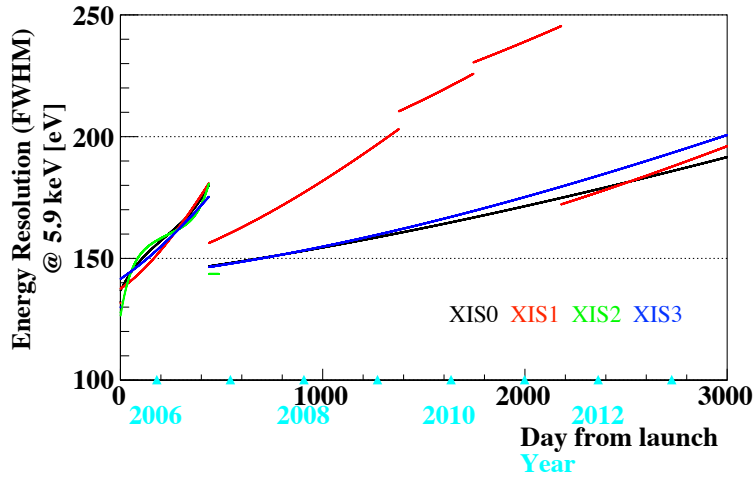
Figure 4.4   Time variability of energy resolution (FWHM) for a 5.9 keV X-ray signal of the XISs. The two large leaps on September 21, 2006 (day 438) and June 1, 2011 (day 2180) were due to the SCI setting changes. The operation of XIS2 (green line) ended on November 9, 2006 (day 487) by a micro-meteorite hitting.

Table 4.2   Operation history of the XISs involving in the spectral analysis.

Date	Instrument	Description
2005/08/11	All	First light.
2006/10/–	All	SCI operation started.
2006/11/09	XIS2	A micro-meteorite hit.
		The entire imaging area became dysfunctional.
2009/06/23	XIS0	A micro-meteorite hit.
		1/8 of the imaging area became dysfunctional.
2009/12/18	XIS1	A micro-meteorite hit.
		No major impact in scientific capability.
2010/04/01	All	SCI off operation support terminated.
2011/06/01	XIS1	Injection charge increased to 6 keV.

4.4   Instrumental response function

The XRT-XIS modules are frequently calibrated in tune with their conditions. With the calibration data, we can reproduce the instrumental response function at the time of each observation. The energy gain, the energy resolution and the contamination on the OBFs are particularly time-variable. The uncertainty of the response function depends on their determination accuracy (shown in Table 4.3).

The response function for the XRT-XIS modules: the energy redistribution matrix files (RMFs) and ancillary response files (ARFs) are generated with the calibration data and the Monte-Carlo ray-tracing simulation (Ishisaki et al., 2007). The RMF includes the quantum

Table 4.3 Error budgets of instrument calibrations of the XRT-XIS modules involved in the spectral analysis.

Calibration item	Oct 2008	Requirement	Goal
On-axis effective area*	$\sim 2\ \%$	5 %	5 %
Energy scale	max{0.2 %, 5 eV}	0.1 %	0.1 %
Energy resolution at 5.9 keV	5 % (FWHM)†	1 %	1 %
Contamination thickness‡	$10^{18}\ \mathrm{cm}^{-2}$	N/A	N/A

∗ Valid in the $1-8$ keV range. Calibration uncertainty may become larger outside this energy range, especially below 0.3 keV (BI) and above 10 keV.
† When the Ftool `xisrmfgen` detailed in Appendix D is used. Note that an error of 5 % in the energy resolution could produce an artificial line width of as large as ~ 25 eV in 1σ at the iron band.
‡ Uncertainty represented as the carbon-equivalent column density. Valid only at the center of the FoV.

efficiency of the XIS and the energy response such as the energy scale and the energy resolution. The ARF includes the angular response and the effective area which is related with the XRT mirror geometry and reflectivity, transmission efficiency of the thermal shields and the OBFs. Since the contamination of the OBFs grows (Figure 4.5), X-ray transmission through the OBFs decrease (Figure 4.6) and the effective area changes especially in the soft X-ray energy band (Figure 4.7). Moreover, a certain level of deviation exists in effective area reproduction in the $1.5-3.5$ keV (especially 1.8 keV residual is known as "Si edge problem") due to the complicated model of the X-ray absorption fine structure of instrumental elements. Since we aimed at accurate analysis of the XDB in this thesis, these uncertainties needed to be adequately evaluated.
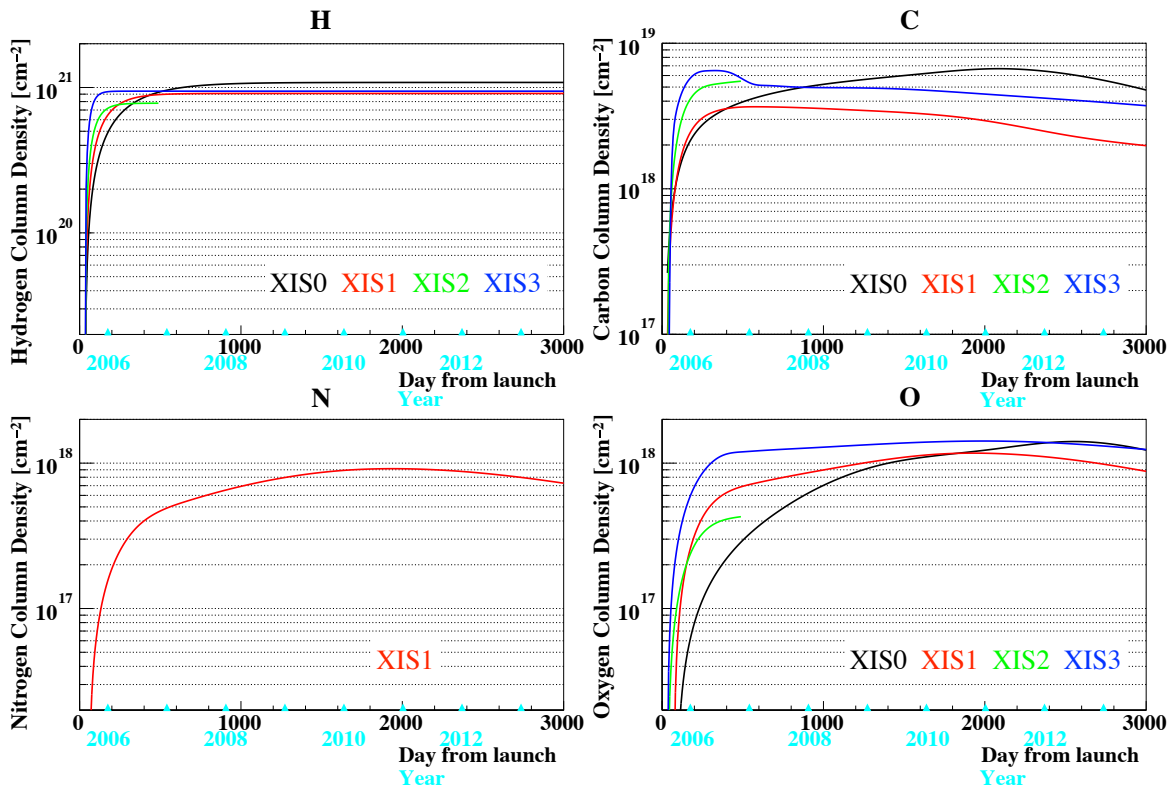
Figure 4.5   Time variability of contamination on the OBFs (column densities).
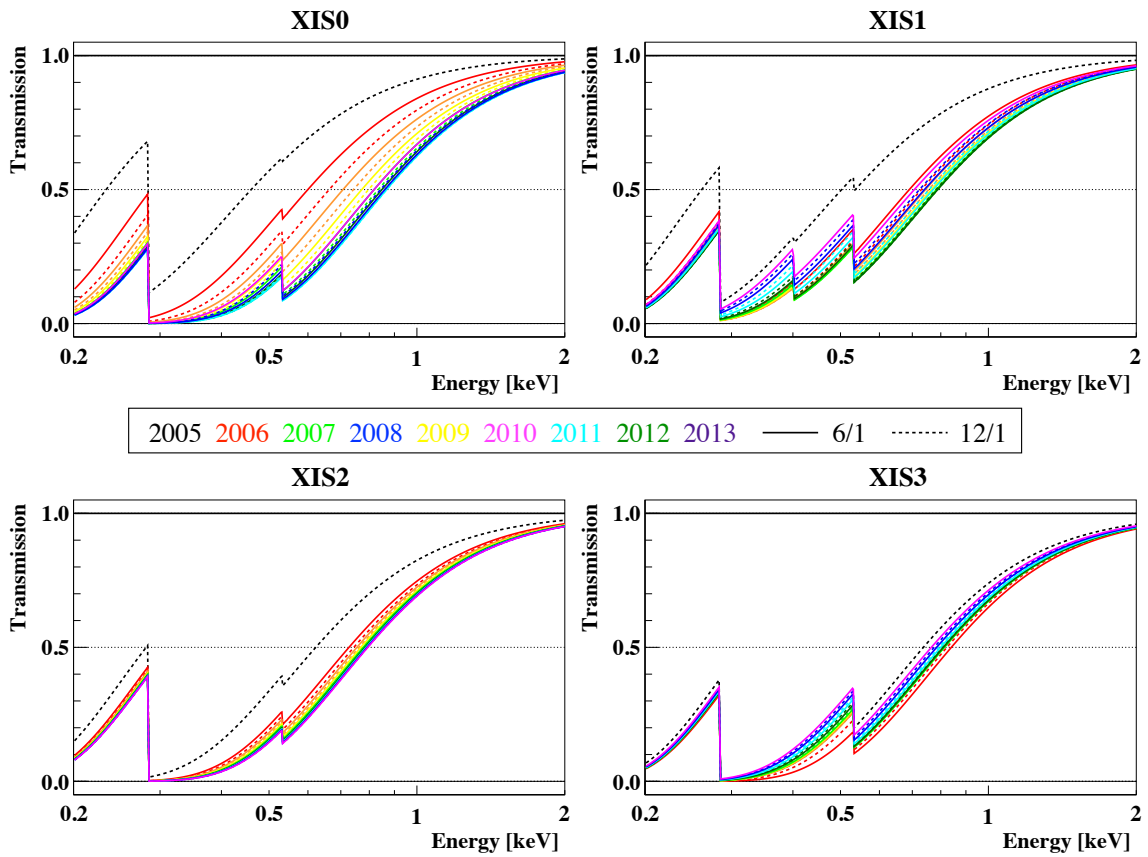
Figure 4.6   X-ray transmission efficiency of the OBFs including contamination.
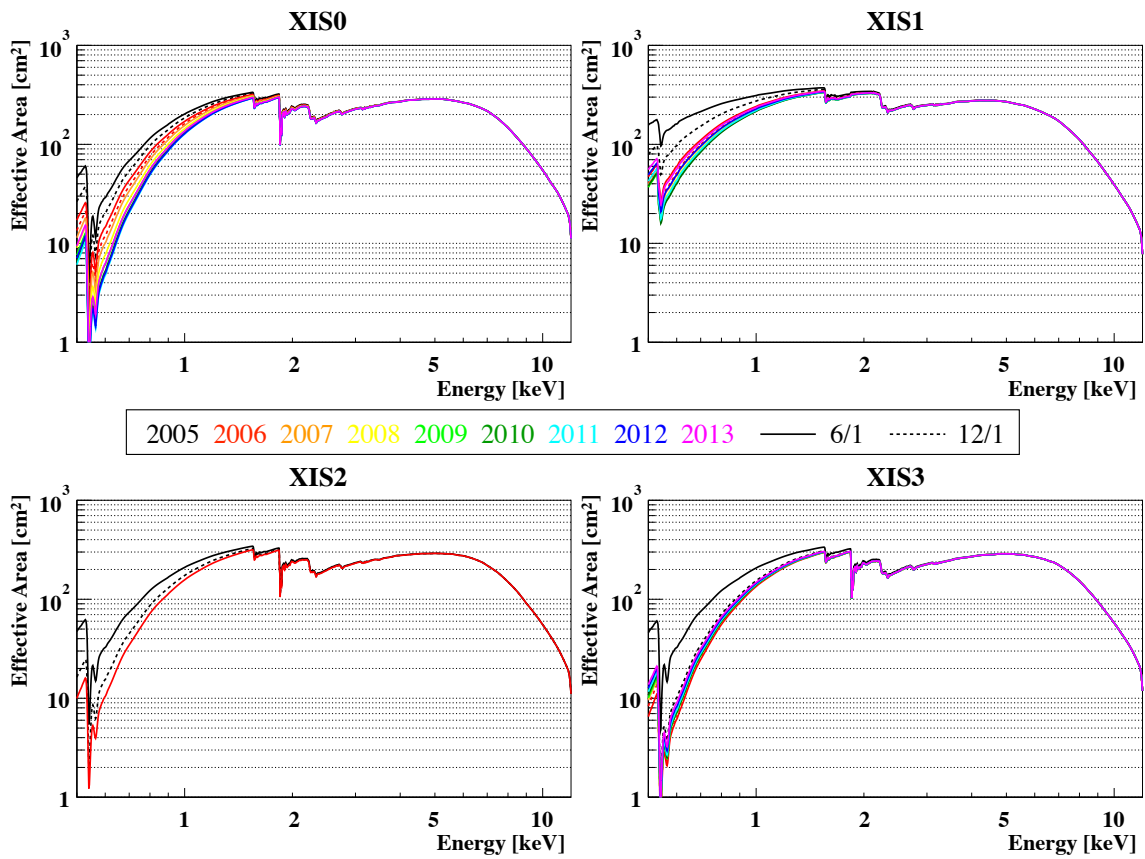
Figure 4.7   Energy dependence of the effective area of the XRT-XIS modules.
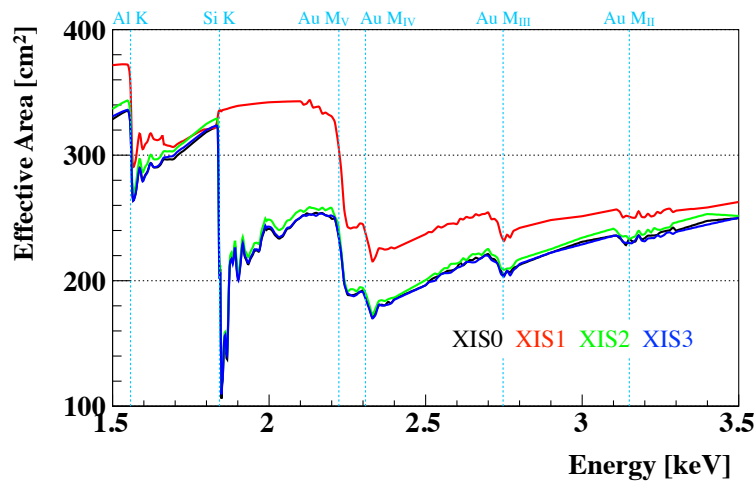
Figure 4.8   Same as Figure 4.7 but close up of the 1.5 – 3.5 keV range in which multiple absorption edges exist. The positions of absorption edges are marked by cyan dashed lines.

4.5   Non-X-ray Background and instrumental line emission

Non-X-ray Background (NXB) consists of signals by charged particles, electrical noises, scattered and fluorescent X-ray emission from instrumental elements. It contaminates observational spectra; especially weak emission such as the XDB. It includes instrumental line emission shown in Table 4.4. Fortunately, owing to a combination of the low-Earth orbit and the instrumental design, the XISs have lower and more stable NXB than those of CCDs onboard XMM-Newton or Chandra which are on the extended elliptical orbits. In this thesis, we maximally used this advantage.

The NXB contributions in given spectra are able to be estimated and subtracted with night-Earth observational data. In order to obtain the NXB data with high reproducibility, it is recommended to stack the night-Earth observational data over long term (typically a few hundred days), and sort it by the geomagnetic cut off rigidity (COR) which is correlated with the momentum of charged particles. In this method, the typical reproducibility of NXB data was reported to a few % for data with the 50 ksec of exposure time in the $1-7$ keV range (Tawa et al., 2008). However, we must evaluate the effect by a few % uncertainty of the NXB contributions on our analysis.

Table 4.4   Instrumental line emission below 7.0 keV (Tawa et al., 2008).

Line	Energy [keV]	Origin
Al-Kα	1.486	OBF, housing, alumina substrate of XIS
Si-Kα	1.740	XIS
Au-Mα	2.123	Housing, XIS substrate, heat-sink
Mn-Kα	5.895	Calibration source
Mn-Kβ	6.490	Calibration source

5 Spectral analysis of the XDB

Suzaku XIS archival data sets (2005–2013)

Step 1. Data selection

187 data sets

Step 2. Data reduction

2-1. Point source removal

2-2. Good time interval selection

Total exposure time: 31.5 Msec

Step 3. Spectral analysis of individual data

(Systematic study of XDB)

Step 4. Data stacking (each XIS, each year)

25 stacked data

Step 5. Spectral analysis of stacked data

Line search   Line search

Figure 5.1   Process flow of data analysis in Chapter 5.

5.1   Data selection (Step 1 in Figure 5.1)

In order to search for X-ray line emission from dark matter associated with the Milky Way, we selected multiple Suzaku XIS observational data of the XDB and analyzed them. In this analysis, Ftools in HEAsoft version 6.15 and XSPEC version 12.8.1 were utilized[*5.1].

Since the XDB is distributed over the whole sky, all X-ray observational data include the XDB emission. In this thesis, we required to collect approximately-pure XDB data. We decided to use Suzaku XIS archival data from 2005 to 2013 satisfied the requirements as shown below:

1. Observational aims are blank sky fields or (maskable) faint compact sources.
2. Galactic latitudes $|b| > 20°$ to avoid the X-ray emission peculiar to the Galactic disk (Masui et al., 2009).
3. Separate from the Galactic central region occupied by the North Polar Spur.

Eventually, the 187 Suzaku XIS observational data sets were selected as shown in Figure 5.2. Their observational logs (e.g. observational date, exposure time) and their aim points were summarized in Appendix A.
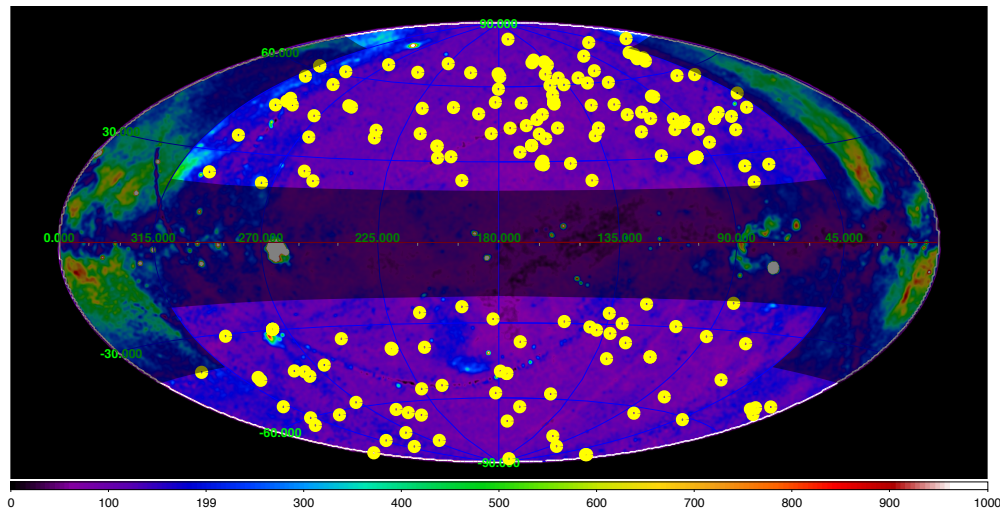
Figure 5.2   187 regions for a keV signature search of dark matter. These are superimposed on the all sky survey map of the ROSAT R45 band (the 0.4 – 1.2 keV energy range) with the Galactic coordinate system centered at the Galactic anti-center. The grey shaded regions were not used for this dark matter line search. The color scale indicates photon count rates in unit of 10^{-6} counts s^{-1} deg^{-2}.

[*5.1] `http://heasarc.gsfc.nasa.gov/lheasoft/`

5.2 Data reduction (Step 2 in Figure 5.1)

In this thesis, we used cleaned event files of the FI-CCDs (XIS0, 2 and 3) and the BI-CCD (XIS1) of Suzaku detailed in Chapter 4. Since many complex unresolvable emission appear in the low energy range (< 0.7 keV) and XDB photons are not adequately available (NXB photons dominate) in the high energy range (> 5.0 keV), we utilized the $0.7 - 7.0$ keV and the $0.5 - 5.0$ keV energy ranges for the FI-CCDs and the BI-CCD, respectively. In all the selected 187 observations, the XISs were set to the normal clocking mode and the 3×3 or 5×5 editing mode. Signals from anomalous (hot and flickering) pixels in the XISs were screened out[*5.2]. Over all the data sets, we conducted imaging analysis in order to reject resolvable X-ray point sources contaminating the XDB spectra in the following way:

1. We extracted XIS images of the $0.5 - 7.0$ keV energy range. The NXB component was subtracted from each image. The vignetting and exposure correction were applied. The resultant 187 images with XIS1 were shown in Appendix A.

2. Point sources in the XIS FoVs of the 187 observations were detected and rejected with the wavelet function of similar size to the point spread function of the XRT-XIS (by using `wavdetect` from the Chandra Interactive Analysis of Observations version 4.6).

3. Point sources whose fluxes were larger than 1.0×10^{-14} erg cm^{-2} s^{-1} in the $0.5 - 7.0$ keV range were removed with circular regions centered at their positions. The radius of the circular regions were $> 1.5'$ determined so that these regions included > 90 % of source photons.

In order to remove X-ray emission contaminating the XDB, we also selected good time interval in the following criteria:

1. The elevation angle from bright/dark Earth limb $> 20°/5°$ to avoid the fluorescent line emission from the Earth's atmosphere.

2. Cancel time intervals during the South Atlantic Anomaly passage due to the harsh radiation environment.

3. The Cut Off Rigidity (COR2) > 8 GV c^{-1} to reduce high-energy-charged-particle background due to the low Earth's magnetic field (Tawa et al., 2008).

4. Time periods when the proton flux in the Solar wind fell below the typical threshold, 4.0×10^8 cm^{-2} s^{-1}, to lower effects of the G-SWCX detailed in Section 3.5 (Fujimoto et al., 2007). The proton flux was observed with monitoring satellites: ACE/SWEPAM[*5.3] and WIND/SWE[*5.4].

[*5.2] With the Ftool `cleansis` detailed in Appendix D

[*5.3] `http://www.srl.caltech.edu/ACE/ASC/level2/lvl2DATA_SWEPAM.html`

[*5.4] `http://web.mit.edu/space/www/wind_data.html`

Figure 5.3 shows a good-time interval selection by the proton flux in the Solar wind in the case of "HIGH LAT. DIFFUSE B" (Obs. ID: 500027020) data. Since ACE and WIND are in the Lagrange point (L1) of the Solar-Earth system (1.5×10^6 km away from the Earth), we have to consider and correct the arrival time (typically $3 - 5$ ksec) of the Solar wind from L1 to the Earth. The same data reduction was conducted in Sekiya et al. (2014b) which revealed the increasing tendency of O I fluorescent line contamination in the Suzaku XIS observations especially after 2011; it was caused by the Solar activity.
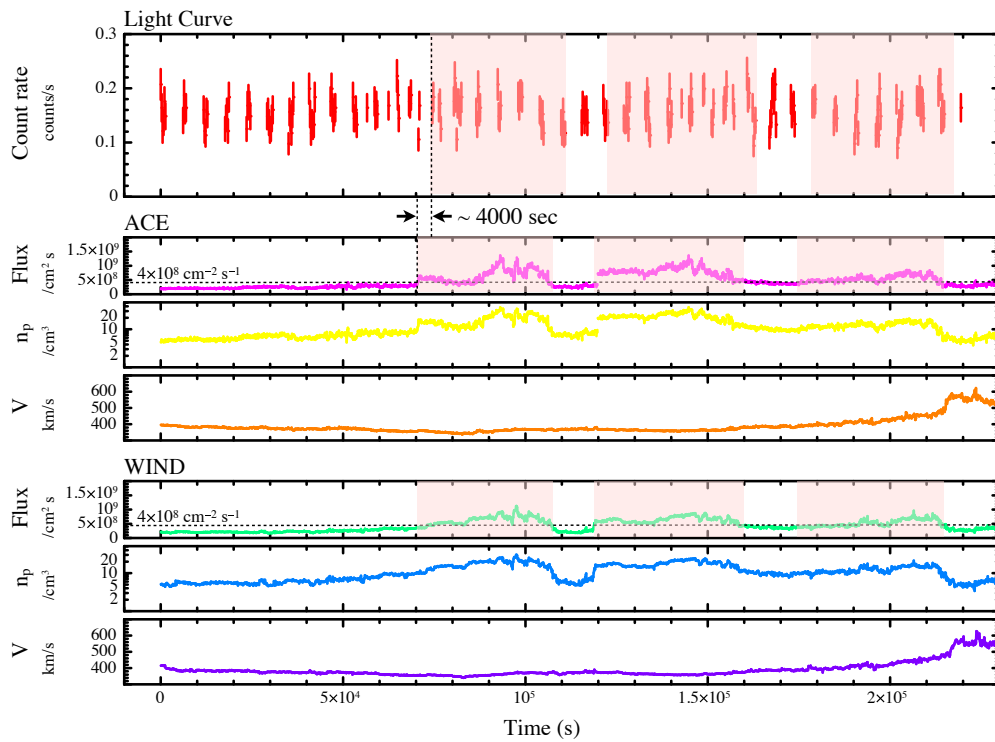
Figure 5.3   Good-time interval selection by the proton flux in the Solar wind in the case of "HIGH LAT. DIFFUSE B" (Obs. ID: 500027020) data. The red shaded time regions with proton flux in the Solar wind $> 4.0 \times 10^8$ cm^{-2} s^{-1} were removed. We considered and corrected the arrival time (~ 4 ksec) of the Solar wind from L1 to the Earth.

After data screening, the total exposure time is 31.5 Msec ~ 1 year. In total, we obtained $\sim 2 \times 10^6$ counts of photons in the $0.5 - 7.0$ keV range. Its spectral breakdown (Figure 5.4) obviously shows continuum structure of the XDB affected by response of the XRT-XIS modules and strong instrumental line emission. The exposure-time-weighted average energy resolution and the product of grasp $\times$ exposure time are shown in Figures 5.5 and 5.6.
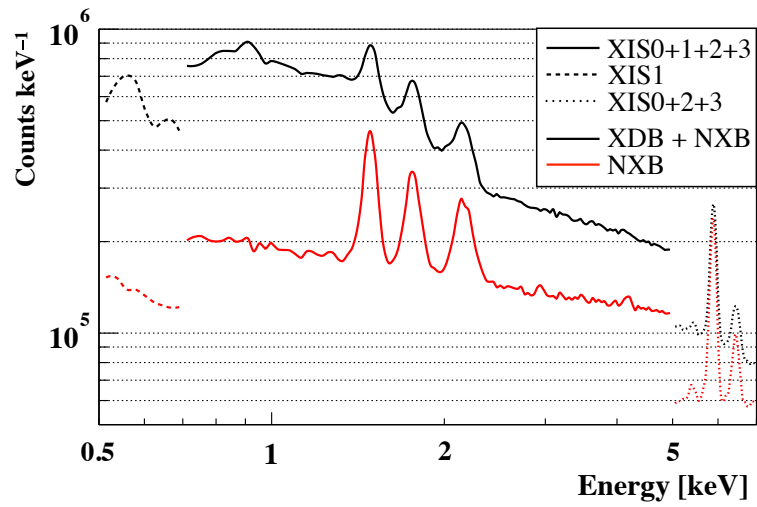
Figure 5.4   Total photon count (/keV) of XDB + NXB (or only NXB) in the 187 observations after data screening. The NXB contributions were estimated by night-Earth observations described in Section 5.3.
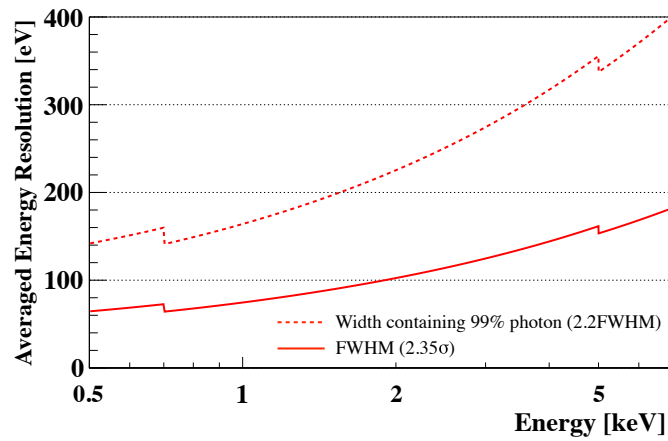
Figure 5.5   Exposure-time-weighted average of energy resolution of all 187 observations.

Figure 5.6   Average grasp (effective area × FoV) × exposure time of all 187 observations.

5.3   Spectral analysis of 187 individual XDB data (Step 3 in Figure 5.1)

We collected the most XDB data observed by the Suzaku XIS ever before. In order to study the XDB systematically and check to fit these data with the typical model, we performed spectral analysis for the 187 individual observations, according to the method shown in Sekiya et al. (2014b).

We first reproduced the instrumental responses at the time of each observation. The energy redistribution matrix files (RMFs) and ancillary response files (ARFs) were generated[*5.5]. Second, NXB including the instrumental line emission was estimated from accumulated night-Earth observations[*5.6]. Then, we performed spectral analysis with the 187 sets of observational energy spectra, RMFs, ARFs and NXB data. The estimated NXB were subtracted from all the spectra. The NXB-subtracted spectra were fitted by spectral models multiplied by the instrumental responses. We fitted the spectra in the energy range of the $0.5 - 7.0$ keV ($0.7 - 7.0$ keV for XIS0, 2 and 3, the $0.5 - 5.0$ keV for XIS1) with the typical XDB emission model: (1) H-SWCX and LHB + (2) MWH + (3) CXB + (4) High temperature component, detailed in Section 3.5. (1): the H-SWCX and LHB blend is explained an unabsorbed optically-thin thermal collisionally-ionized (CIE) plasma emission model with the temperature $kT \sim 0.1$ keV. (2): the MWH is described by an absorbed optically-thin thermal CIE plasma emission model with the temperature $kT \sim 0.2$ keV. (3): the CXB is represented by an absorbed power-law[*5.7] emission model with its photon index $\Gamma \sim 1.4$ (Kushino et al., 2002). (4): the High temperature component is an absorbed optically-thin thermal CIE plasma ($kT = 0.4 - 1.2$ keV) emission model. As the optically-thin thermal CIE emission model, we used APEC[*5.8] (version 2.0.1; Smith et al., 2001; Foster et al., 2012). The element abundances and redshift for three APEC models were set to the Solar-neighbor values (Anders & Grevesse, 1989) and zero, respectively. The temperature of the APEC for the H-SWCX + LHB was fixed to $kT = 0.1$ keV (Yoshitake et al., 2013). In Suzaku XIS observational data, O I fluorescent line from the Earth's exosphere sometimes appears especially after 2011 due to the Solar maximum, despite of the contamination of the fluorescent lines are mostly removed when we apply the elevation angle criteria as described in Section 5.2 (Sekiya et al., 2014b). If the situation calls for it, we added a Gaussian (centroid: 0.525 keV) for O I[*5.9] in the spectral fitting. Finally, the following model for the 187 individual spectral fitting was adopted: ["APEC$_1$"+"Galactic absorption"$\times$("APEC$_2$"+"APEC$_3$"+"CXB")+"O I"] where "Galactic absorption" was for a photoelectric absorption by the interstellar medium

---

*5.5 By the Ftools `xisrmfgen` and `xissimarfgen`, respectively detailed in Appendix D

*5.6 With the Ftool `xisnxbgen` detailed in Appendix D

*5.7 `powerlaw` in XSPEC detailed in Appendix D.

*5.8 `apec` in XSPEC detailed in Appendix D.

*5.9 `gaussian` in XSPEC detailed in Appendix D.

of the Milky Way galaxy which were able to be estimated from accurate observational data of the neutral hydrogen column densities $(N_\mathrm{H})^{*5.10}$ (LAB survey; Kalberla et al., 2005), $\mathrm{APEC_1}$, $\mathrm{APEC_2}$ and $\mathrm{APEC_3}$ correspond to the H-SWCX + LHB, the MWH and the High temperature component, respectively.

The results of 187 sets of spectral fitting were summarized in Figures 5.7 – 5.12 and Table A.3. Figures 5.7, 5.8 (left) and 5.9 (left) show the histograms of the three APEC normalizations for the H-SWCX + LHB, the MWH and the High temperature components: the emission measure integrated over the line of sight: $(1/2\pi) \int n_\mathrm{e} n_\mathrm{H} ds$ in unit of 10^{14} cm^{-5} sr^{-1}, where n_e and n_H are the electron and the hydrogen densities (cm^{-3}), respectively. Figures 5.8 (right) and 5.9 (right) show the distributions of the two APEC temperatures for the MWH and the High temperature components in unit of keV. The MWH temperatures kT were distributed between 0.1 and 0.4 keV. About 70 % of $\mathrm{APEC_3}$ normalizations were consistent with zero and about 30 % (55 out of 187) of all the XDB spectra included the High temperature components ($kT = 0.4 - 1.2$ keV). Figure 5.10 shows the histogram of the photon indices and normalizations (The surface brightness in unit of photons cm^{-2} s^{-1} sr^{-1} keV^{-1} at 1 keV) of the power-law models for the CXB. We checked that all the CXB power-law parameters are consistent with typical values reported in (Kushino et al., 2002). Figure 5.11 indicates the long-term time dependence of O I fluorescent line intensities in the 187 observations. Figure 5.12 is the histogram of the reduced chi-squared in order to check the goodness of fit. As reasonable continuum X-ray emission in the 0.5 – 7.0 keV range of the 187 individual spectra, no other additional component was required.

---

*5.10 `phabs` in XSPEC detailed in Appendix D.
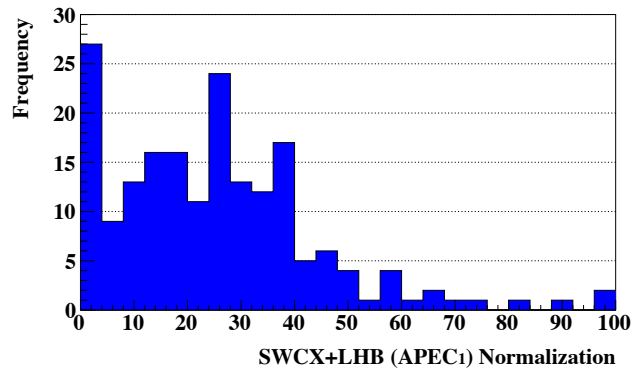
Figure 5.7   Distribution of the APEC normalizations: the emission measure integrated over the line of sight in unit of 10^{14} cm^{-5} sr^{-1} for the SWCX + LHB.
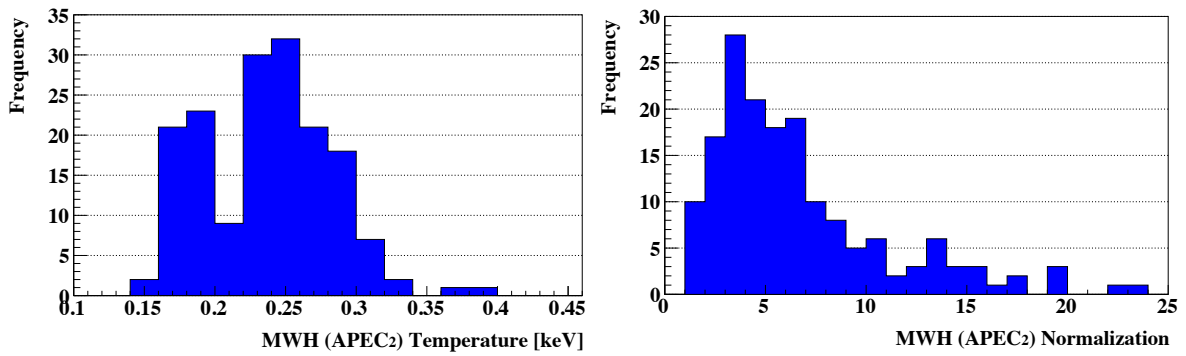
Figure 5.8   Distribution of the APEC parameters for the MWH: the temperature kT in unit of keV (left panel) and the APEC normalization in unit of 10^{14} cm^{-5} sr^{-1} (right panel).
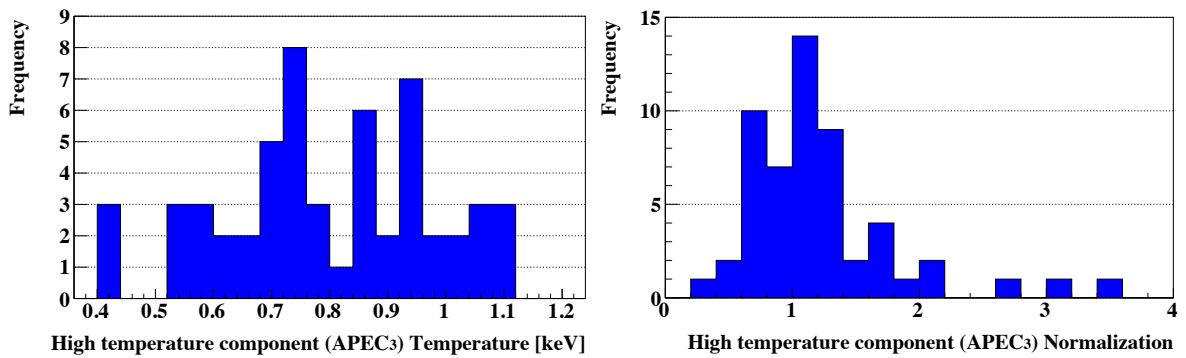
Figure 5.9   Same as Figure 5.8 but for the High temperature component.
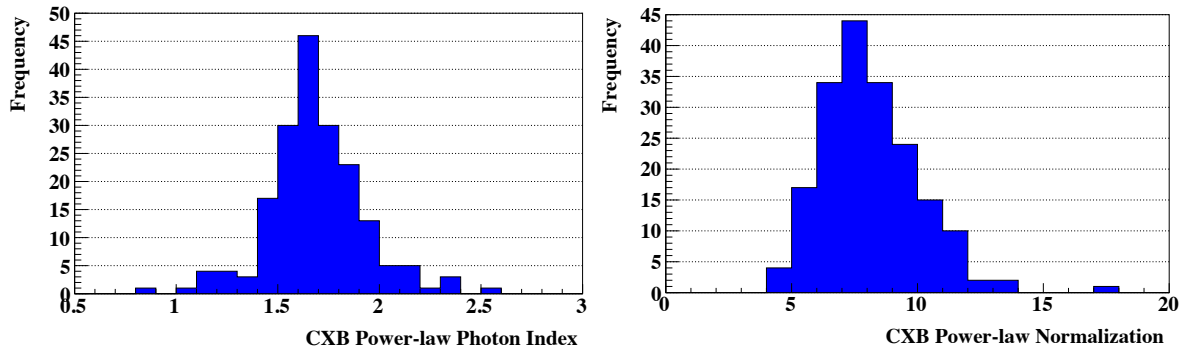
Figure 5.10 Distribution of the CXB power-law parameters: the photon index (left panel) and the surface brightness in unit of photons cm^{-2} s^{-1} sr^{-1} at 1 keV (right panel).
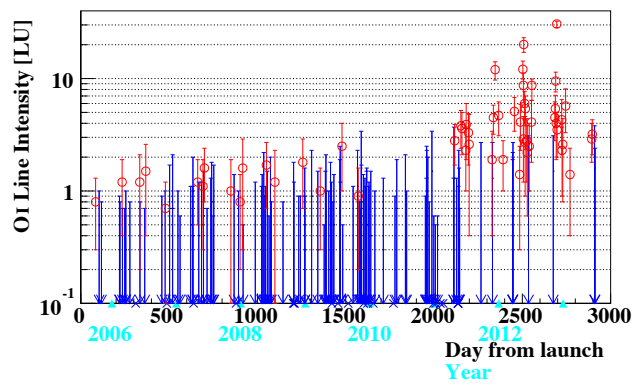
Figure 5.11 Long-term time dependence of O I intensity in the 187 observations. LU (Line Unit) is defined as photons cm^{-2} s^{-1} sr^{-1}.
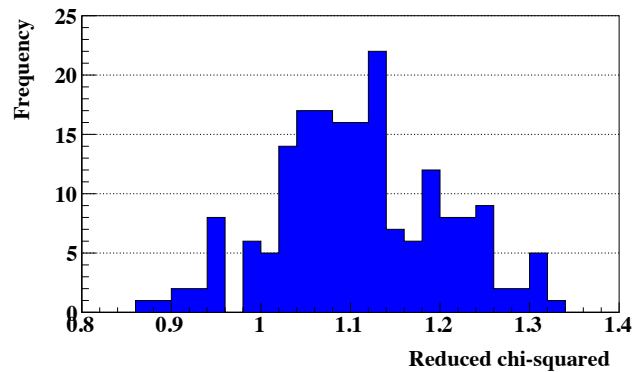
Figure 5.12 Distribution of the reduced chi-squared in order to check the goodness of fit.

5.4   XDB data stacking (Step 4 in Figure 5.1)

In order to analyze the XDB with a little statistical uncertainty, we stacked the XDB spectra[*5.11]. With consideration for instrumental condition change and difference among four kinds of XISs, we divided the entire period (2005 – 2013) into 8 periods to sort instrumental conditions (e.g. SCI setting) as shown in Table 5.1 and stacked the XDB data in each of the short period. The exposure-time-weighted average of the NXB data were also stacked. The total-photon-count-weighted average (in the 0.5 – 7.0 keV range) of RMFs × ARFs (responses) were produced[*5.12]. Then, in total, 8-period 25 stacked data sets (1 period × XIS0, 1, 2, 3 + 7 periods × XIS0, 2, 3) were made.

Table 5.1   Stacked data properties.

Period	Date	Total exposure[*]	Total count[†]	Average $N_{\rm H}$[‡]
2005–2006	2005/10/01 – 2006/09/30	3.2	205071	0.029
	(SCI operation started for all XISs from October, 2006.)			
2006–2007	2006/10/01 – 2007/08/31	4.2	261725	0.035
2007–2008	2007/09/01 – 2008/08/31	3.4	212512	0.029
2008–2009	2008/09/01 – 2009/08/31	4.4	284447	0.030
2009–2010	2009/09/01 – 2010/05/31	4.0	242187	0.030
2010–2011	2010/06/01 – 2011/05/31	4.5	271709	0.029
	(Injection charge increased to 6 keV for XIS1 on June 1, 2011.)			
2011–2012	2011/06/01 – 2012/05/31	2.3	250229	0.027
2012–2013	2012/06/01 – 2013/07/01	3.5	220777	0.034

Notes.

∗ Exposure time (XIS0+1+2+3) in unit of Msec after data screening.

† Total photon count in the 0.5 – 7.0 keV range.

‡ The exposure-time-weighted average of the neutral hydrogen column density in unit of 10^{22} cm^{-2} derived from the LAB Galactic H I Survey.

∗5.11 With the Ftool `mathpha` detailed in Appendix D
∗5.12 By the Ftool `addrmf` detailed in Appendix D

5.5   Spectral analysis of 25 stacked XDB data (Step 5 in Figure 5.1)

We performed the deepest spectral analysis with the 25 stacked XDB spectra, averaged responses and NXB data. Because of low statistical uncertainty, the goodness of fit sensitively change by a little modification of the spectral model. In order to find the best-fit model for the stacked XDB spectra, we tried to fit them with five spectral models as shown below:

Model 1: a two-temperature and an index-fixed-power-law model:
    $APEC_1$ + Galactic absorption $\times$ ($APEC_2$ + CXB(Γ=1.4))

Model 2: a three-temperature and an index-fixed-power-law model:
    $APEC_1$ + Galactic absorption $\times$ ($APEC_2$ + $APEC_3$ + CXB(Γ=1.4))

Model 3: a three-temperature and a double-broken-power-law model:
    $APEC_1$ + Galactic absorption $\times$ ($APEC_2$ + $APEC_3$ + CXB(dbpl))

Model 4: a three-temperature and an index-free-power-law model:
    $APEC_1$ + Galactic absorption $\times$ ($APEC_2$ + $APEC_3$ + CXB(Γ_{free}))

Model 5: a three-temperature (Ne, Mg abundances free) and an index-free-power-law model:
    $APEC_1$ + Galactic absorption $\times$ ($APEC_2$ + $VAPEC_3$ + CXB(Γ_{free}))

where CXB(dbpl) is a double-broken-power-law model: a combination of 2 improvement CXB power-law models with their photon indices of 1.54 or 1.96 below 1.2 keV and 1.4 above the energy (Smith et al., 2007), and VAPEC is a modified APEC model whose abundances of the individual trace elements are movable. We fixed the indices of the CXB power-law at 1.4 for Model 1 and 2 (those of Model 4 and 5 were free). We fixed the normalization of the broken-power-law with the low-energy photon index of 1.54 to 5.7 photons cm^{-2} s^{-1} sr^{-1} keV^{-1} at 1 keV in Model 3. The abundances of Ne and Mg were free in Model 5. The neutral hydrogen column densities N_{H} for the Galactic absorption models were fixed exposure-time-weighted average values (Table 5.1). All models include O I fluorescent line emission model.

The results of spectral fitting with the 25 stacked XDB energy spectra and the five models were summarized in Tables 5.2 – 5.6 and Figures 5.13 – 5.19. Because of large residuals around 1 keV energy range in the results of Model 1, the need for the High temperature component were suggested. In the results of Model 2, the goodness of fit for all spectra improved as compared with Model 1 (Tables 5.2, 5.3 and Figures 5.13, 5.14). The index-free-power-law was better model than the index-fixed-power-law or the double-broken-power-law (Tables 5.3, 5.4, 5.5 and Figures 5.14, 5.15, 5.16). As a whole, definitely, we found that Model 5: the three-temperature model (Ne, Mg abundances free) and the index-free-power-law model was the best-fit model for the 25 stacked XDB spectra whose χ^2/dof (dof) = 1.24

(3693). The best-fit parameter of Model 5 was shown in Table 5.19. The 8 periods (25 sets) of stacked XDB energy spectra and their best-fit models were shown in Figures 5.17, 5.18 and 5.19. We used these spectra and best-fit models to search for dark matter line emission in next Chapter.

Table 5.2 Spectral fitting results with the stacked energy spectra and Model 1.

Period	$Norm_1$*	kT_2†	$Norm_2$*	S_{CXB}‡	O I§	χ^2/dof (dof)
2005–2006	$23.1^{+2.4}_{-2.4}$	$0.25^{+0.01}_{-0.01}$	$4.2^{+0.4}_{-0.4}$	$6.9^{+0.1}_{-0.1}$	$0.4^{+0.2}_{-0.2}$	1.39(595)
2006–2007	$25.7^{+1.8}_{-1.8}$	$0.28^{+0.01}_{-0.01}$	$3.5^{+0.4}_{-0.2}$	$8.0^{+0.1}_{-0.1}$	$0.5^{+0.2}_{-0.2}$	1.76(439)
2007–2008	$24.9^{+2.4}_{-3.8}$	$0.28^{+0.01}_{-0.02}$	$4.4^{+0.6}_{-0.3}$	$7.9^{+0.1}_{-0.1}$	$0.5^{+0.2}_{-0.2}$	1.55(439)
2008–2009	$24.4^{+3.2}_{-3.2}$	$0.26^{+0.01}_{-0.01}$	$4.1^{+0.5}_{-0.5}$	$7.9^{+0.1}_{-0.1}$	$0.4^{+0.2}_{-0.2}$	1.71(439)
2009–2010	$29.7^{+2.9}_{-2.9}$	$0.28^{+0.01}_{-0.01}$	$4.3^{+0.3}_{-0.3}$	$8.1^{+0.1}_{-0.1}$	$0.2^{+0.3}_{-0.2}$	1.69(439)
2010–2011	$47.1^{+3.1}_{-3.1}$	$0.29^{+0.01}_{-0.01}$	$4.8^{+0.3}_{-0.3}$	$7.5^{+0.1}_{-0.1}$	$0.3^{+0.3}_{-0.3}$	1.83(439)
2011–2012	$43.7^{+3.6}_{-3.6}$	$0.28^{+0.01}_{-0.01}$	$5.2^{+0.3}_{-0.3}$	$7.8^{+0.1}_{-0.1}$	$4.2^{+0.3}_{-0.3}$	1.60(439)
2012–2013	$44.5^{+5.3}_{-5.3}$	$0.25^{+0.01}_{-0.01}$	$8.0^{+0.7}_{-0.7}$	$7.7^{+0.1}_{-0.1}$	$5.2^{+0.4}_{-0.4}$	1.07(439)

Notes.

∗ The emission measure of the optically-thin thermal CIE plasma integrated over the line of sight (the APEC model normalization): $(1/2\pi) \int n_e n_H ds$ in unit of 10^{14} cm^{-5} sr^{-1}, where n_e and n_H are the electron and the hydrogen densities (cm^{-3}).

† The temperature of the optically-thin thermal CIE plasma in unit of keV.

‡ The surface brightness of the CXB component (the power-law model normalization) in unit of photons cm^{-2} s^{-1} sr^{-1} keV^{-1} at 1 keV (the photon index is fixed at 1.4).

§ The intensity of neutral oxygen (O I, centroid: 0.525 keV) in unit of LU (photons cm^{-2} s^{-1} sr^{-1}).

Figure 5.13 Exposure-time-weighted average of the 25 stacked XDB energy spectra from 2005 to 2013 and its spectral model [(the instrumental response) × (the XDB model: Model 1)].

Table 5.3   Same as Table 5.2 but for Model 2.

Period	Norm$_1$*	kT_2†	Norm$_2$*	kT_3†	Norm$_3$*	S_{CXB}‡	O I§	χ^2/dof (dof)
2005–2006	$20.8^{+2.6}_{-6.5}$	$0.22^{+0.01}_{-0.03}$	$4.3^{+1.6}_{-0.4}$	$0.84^{+0.09}_{-0.08}$	$0.5^{+0.1}_{-0.1}$	$6.7^{+0.1}_{-0.1}$	$0.4^{+0.2}_{-0.2}$	1.20(593)
2006–2007	$23.1^{+2.4}_{-2.4}$	$0.24^{+0.01}_{-0.01}$	$3.7^{+0.4}_{-0.4}$	$0.95^{+0.06}_{-0.06}$	$0.6^{+0.1}_{-0.1}$	$7.7^{+0.1}_{-0.1}$	$0.6^{+0.2}_{-0.2}$	1.45(437)
2007–2008	$20.8^{+3.3}_{-3.3}$	$0.24^{+0.01}_{-0.01}$	$4.8^{+0.5}_{-0.5}$	$0.90^{+0.06}_{-0.11}$	$0.7^{+0.1}_{-0.1}$	$7.6^{+0.1}_{-0.1}$	$0.5^{+0.2}_{-0.2}$	1.23(437)
2008–2009	$21.7^{+3.3}_{-3.3}$	$0.23^{+0.01}_{-0.01}$	$4.3^{+0.5}_{-0.5}$	$0.91^{+0.06}_{-0.11}$	$0.5^{+0.1}_{-0.1}$	$7.7^{+0.1}_{-0.1}$	$0.4^{+0.2}_{-0.2}$	1.44(437)
2009–2010	$24.7^{+4.2}_{-14.1}$	$0.23^{+0.02}_{-0.04}$	$4.6^{+3.6}_{-0.6}$	$0.79^{+0.16}_{-0.07}$	$0.8^{+0.2}_{-0.2}$	$7.9^{+0.1}_{-0.1}$	$0.2^{+0.3}_{-0.2}$	1.35(437)
2010–2011	$43.7^{+4.4}_{-4.4}$	$0.24^{+0.02}_{-0.02}$	$4.7^{+0.6}_{-0.6}$	$0.75^{+0.06}_{-0.04}$	$0.8^{+0.2}_{-0.2}$	$7.3^{+0.1}_{-0.1}$	$0.3^{+0.3}_{-0.3}$	1.53(437)
2011–2012	$39.8^{+4.7}_{-4.7}$	$0.25^{+0.01}_{-0.01}$	$5.6^{+0.6}_{-0.6}$	$0.96^{+0.07}_{-0.07}$	$0.5^{+0.1}_{-0.1}$	$7.6^{+0.1}_{-0.1}$	$4.2^{+0.3}_{-0.3}$	1.37(437)
2012–2013	$38.9^{+6.7}_{-30.0}$	$0.22^{+0.03}_{-0.05}$	$8.5^{+5.1}_{-0.8}$	$0.60^{+0.40}_{-0.13}$	$0.7^{+0.9}_{-0.5}$	$7.7^{+0.1}_{-0.1}$	$5.2^{+0.4}_{-0.4}$	1.04(437)

Notes.

∗ The emission measure of the optically-thin thermal CIE plasma integrated over the line of sight (the APEC model normalization): $(1/2\pi) \int n_e n_H ds$ in unit of 10^{14} cm^{-5} sr^{-1}, where n_e and n_H are the electron and the hydrogen densities (cm^{-3}).

† The temperature of the optically-thin thermal CIE plasma in unit of keV.

‡ The surface brightness of the CXB component (the power-law model normalization) in unit of photons cm^{-2} s^{-1} sr^{-1} keV^{-1} at 1 keV (the photon index is fixed at 1.4).

§ The intensity of neutral oxygen (O I, centroid: 0.525 keV) in unit of LU (photons cm^{-2} s^{-1} sr^{-1}).

Figure 5.14   Same as Figure 5.13 but for Model 2.

Table 5.4   Same as Table 5.2 but for Model 3.

Period	Norm$_1$*	kT_2†	Norm$_2$*	kT_3†	Norm$_3$*	S_{CXB}‡	O I§	χ^2/dof (dof)
2005–2006	$18.8^{+3.8}_{-8.8}$	$0.21^{+0.02}_{-0.03}$	$4.3^{+2.4}_{-0.7}$	$0.81^{+0.10}_{-0.08}$	$0.4^{+0.1}_{-0.1}$	$1.5^{+0.1}_{-0.1}$	$0.3^{+0.2}_{-0.2}$	1.20(593)
2006–2007	$22.0^{+2.4}_{-2.4}$	$0.23^{+0.01}_{-0.01}$	$3.2^{+0.4}_{-0.4}$	$0.91^{+0.08}_{-0.12}$	$0.4^{+0.1}_{-0.1}$	$2.8^{+0.1}_{-0.1}$	$0.4^{+0.2}_{-0.2}$	1.43(437)
2007–2008	$19.2^{+3.6}_{-10.3}$	$0.22^{+0.02}_{-0.04}$	$4.4^{+2.6}_{-0.5}$	$0.82^{+0.10}_{-0.09}$	$0.5^{+0.2}_{-0.1}$	$2.6^{+0.1}_{-0.1}$	$0.4^{+0.2}_{-0.2}$	1.21(437)
2008–2009	$17.9^{+5.5}_{-10.6}$	$0.21^{+0.03}_{-0.03}$	$4.4^{+2.9}_{-1.1}$	$0.79^{+0.13}_{-0.09}$	$0.4^{+0.1}_{-0.1}$	$2.8^{+0.1}_{-0.1}$	$0.2^{+0.2}_{-0.2}$	1.41(437)
2009–2010	$15.2^{+10.9}_{-15.2}$	$0.19^{+0.04}_{-0.04}$	$6.4^{+3.9}_{-2.7}$	$0.73^{+0.08}_{-0.10}$	$0.8^{+0.2}_{-0.2}$	$3.0^{+0.1}_{-0.1}$	$0.1^{+0.3}_{-0.1}$	1.32(437)
2010–2011	$31.1^{+15.4}_{-31.1}$	$0.19^{+0.07}_{-0.05}$	$6.9^{+11.0}_{-3.0}$	$0.62^{+0.14}_{-0.04}$	$1.1^{+0.2}_{-0.5}$	$2.3^{+0.1}_{-0.1}$	$0.2^{+0.3}_{-0.2}$	1.51(437)
2011–2012	$13.5^{+19.8}_{-13.5}$	$0.17^{+0.08}_{-0.02}$	$11.1^{+7.0}_{-5.2}$	$0.59^{+0.06}_{-0.03}$	$1.1^{+0.1}_{-0.3}$	$2.7^{+0.1}_{-0.1}$	$4.1^{+0.3}_{-0.3}$	1.36(437)
2012–2013	$38.0^{+6.7}_{-14.3}$	$0.22^{+0.02}_{-0.03}$	$8.1^{+3.6}_{-0.8}$	$0.56^{+0.23}_{-0.13}$	$0.5^{+0.5}_{-0.4}$	$2.7^{+0.1}_{-0.1}$	$5.0^{+0.4}_{-0.4}$	1.04(437)

Notes.

∗ The emission measure of the optically-thin thermal CIE plasma integrated over the line of sight (the APEC model normalization): $(1/2\pi) \int n_e n_H ds$ in unit of 10^{14} cm^{-5} sr^{-1}, where n_e and n_H are the electron and the hydrogen densities (cm^{-3}).

† The temperature of the optically-thin thermal CIE plasma in unit of keV.

‡ The surface brightness of the CXB component (the broken-power-law model normalization) in unit of photons cm^{-2} s^{-1} sr^{-1} keV^{-1} at 1 keV (the photon indices are fixed at 1.54 below 1.2 keV and 1.96 above the energy).

§ The intensity of neutral oxygen (O I, centroid: 0.525 keV) in unit of LU (photons cm^{-2} s^{-1} sr^{-1}).
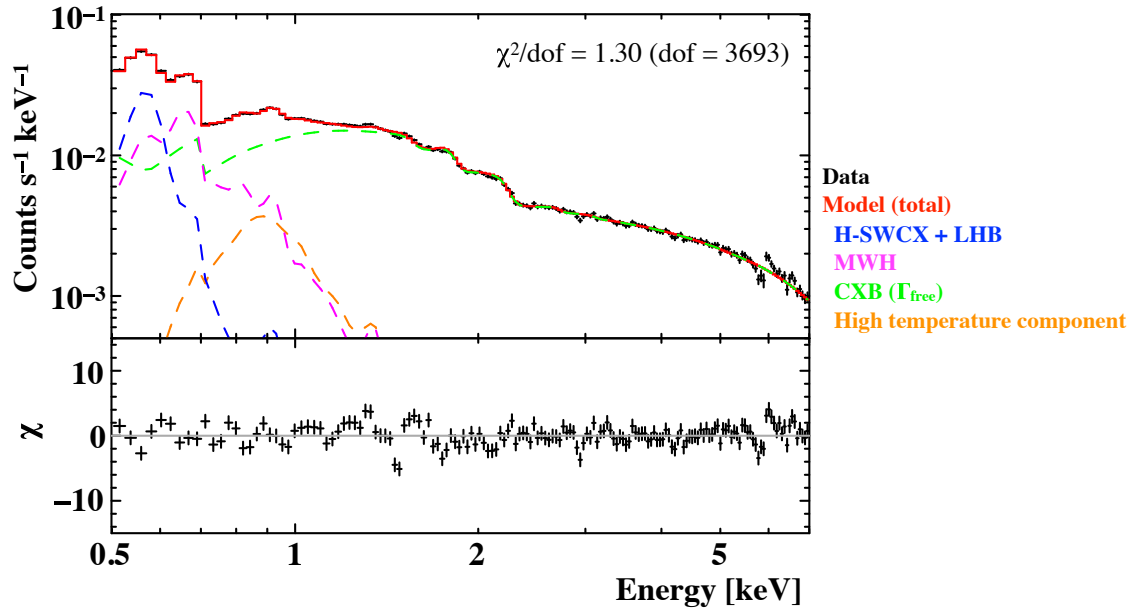
Figure 5.15   Same as Figure 5.13 but for Model 3.

Table 5.5   Same as Table 5.2 but for Model 4.

Period	Norm$_1$*	kT_2†	Norm$_2$*	kT_3†	Norm$_3$*	Γ_{CXB}‖	S_{CXB}‡	O I§	χ^2/dof (dof)
2005–2006	$20.4^{+2.6}_{-7.5}$	$0.22^{+0.01}_{-0.03}$	$4.2^{+1.9}_{-0.4}$	$0.83^{+0.08}_{-0.09}$	$0.4^{+0.1}_{-0.1}$	$1.44^{+0.02}_{-0.02}$	$6.9^{+0.2}_{-0.2}$	$0.4^{+0.2}_{-0.2}$	1.19(592)
2006–2007	$22.7^{+2.4}_{-2.4}$	$0.24^{+0.01}_{-0.01}$	$3.6^{+0.4}_{-0.4}$	$0.92^{+0.07}_{-0.11}$	$0.5^{+0.1}_{-0.1}$	$1.44^{+0.02}_{-0.02}$	$8.0^{+0.2}_{-0.2}$	$0.5^{+0.2}_{-0.2}$	1.43(436)
2007–2008	$20.2^{+3.9}_{-3.6}$	$0.23^{+0.02}_{-0.01}$	$4.8^{+0.5}_{-0.6}$	$0.84^{+0.11}_{-0.07}$	$0.6^{+0.2}_{-0.1}$	$1.42^{+0.02}_{-0.02}$	$7.8^{+0.2}_{-0.2}$	$0.5^{+0.2}_{-0.2}$	1.23(436)
2008–2009	$21.8^{+3.3}_{-3.3}$	$0.23^{+0.01}_{-0.01}$	$4.3^{+0.5}_{-0.5}$	$0.92^{+0.06}_{-0.09}$	$0.6^{+0.1}_{-0.1}$	$1.38^{+0.02}_{-0.02}$	$7.6^{+0.2}_{-0.2}$	$0.4^{+0.2}_{-0.2}$	1.44(436)
2009–2010	$19.3^{+8.5}_{-19.3}$	$0.20^{+0.04}_{-0.04}$	$5.6^{+8.3}_{-1.7}$	$0.73^{+0.11}_{-0.11}$	$0.7^{+0.2}_{-0.2}$	$1.48^{+0.02}_{-0.02}$	$8.4^{+0.2}_{-0.2}$	$0.2^{+0.3}_{-0.3}$	1.27(436)
2010–2011	$42.7^{+4.4}_{-4.4}$	$0.24^{+0.02}_{-0.05}$	$4.7^{+0.6}_{-0.6}$	$0.71^{+0.06}_{-0.09}$	$0.7^{+0.4}_{-0.2}$	$1.48^{+0.02}_{-0.02}$	$7.8^{+0.2}_{-0.2}$	$0.2^{+0.3}_{-0.3}$	1.44(436)
2011–2012	$37.0^{+5.0}_{-5.0}$	$0.23^{+0.02}_{-0.04}$	$5.5^{+0.6}_{-0.6}$	$0.74^{+0.14}_{-0.14}$	$0.4^{+0.4}_{-0.2}$	$1.51^{+0.02}_{-0.02}$	$8.4^{+0.2}_{-0.2}$	$4.2^{+0.3}_{-0.3}$	1.20(436)
2012–2013	$38.7^{+6.8}_{-38.7}$	$0.22^{+0.03}_{-0.06}$	$8.6^{+5.4}_{-0.8}$	$0.60^{+0.44}_{-0.14}$	$0.7^{+1.1}_{-0.5}$	$1.39^{+0.02}_{-0.02}$	$7.6^{+0.2}_{-0.2}$	$5.2^{+0.4}_{-0.4}$	1.04(436)

Notes.

∗ The emission measure of the optically-thin thermal CIE plasma integrated over the line of sight (the APEC model normalization): $(1/2\pi) \int n_e n_H ds$ in unit of 10^{14} cm^{-5} sr^{-1}, where n_e and n_H are the electron and the hydrogen densities (cm^{-3}).

† The temperature of the optically-thin thermal CIE plasma in unit of keV.

‖ The photon index of the power-law model for the CXB component.

‡ The surface brightness of the CXB component (the power-law model normalization) in unit of photons cm^{-2} s^{-1} sr^{-1} keV^{-1} at 1 keV (the photon index is fixed at 1.4).

§ The intensity of neutral oxygen (O I, centroid: 0.525 keV) in unit of LU (photons cm^{-2} s^{-1} sr^{-1}).

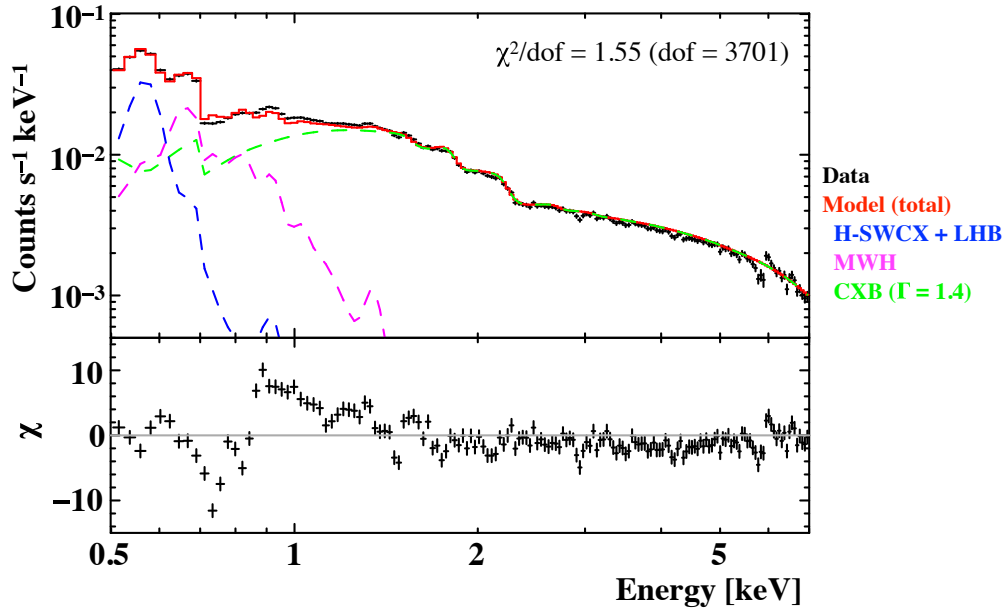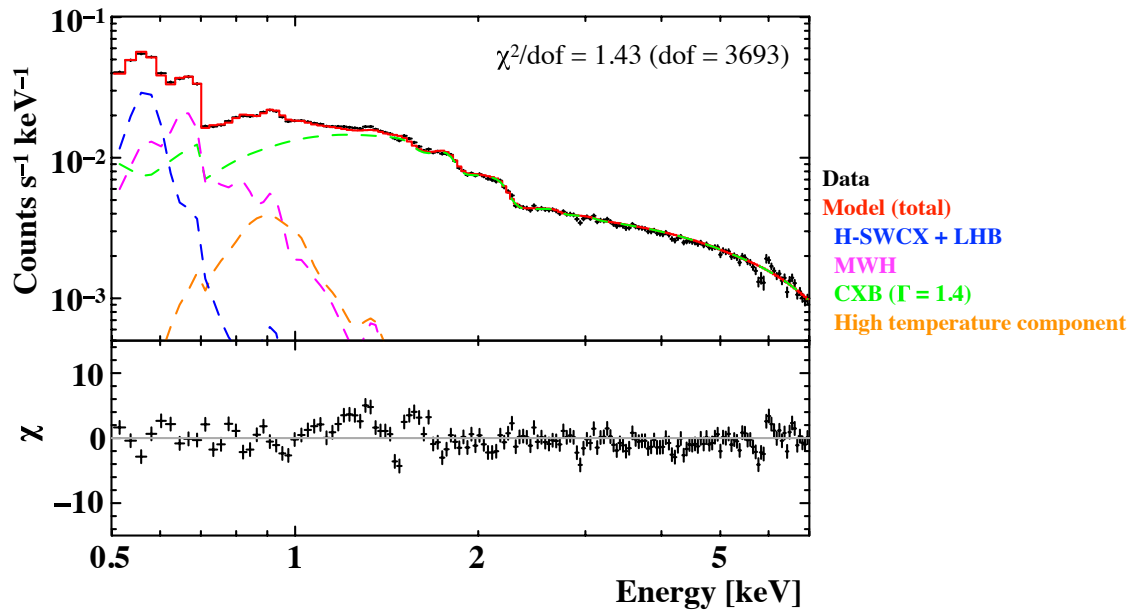Figure 5.16   Same as Figure 5.13 but for Model 4.

Table 5.6 Same as Table 5.2 but for Model 5.

Period	$\mathrm{Norm_1}^*$	$kT_2^\dagger$	$\mathrm{Norm_2}^*$	$kT_3^\dagger$	$\mathrm{Ne}^\sharp$	$\mathrm{Mg}^\sharp$
2005–2006	$20.7^{+2.4}_{-7.3}$	$0.22^{+0.01}_{-0.03}$	$4.2^{+1.8}_{-0.4}$	$0.85^{+0.06}_{-0.10}$	$0.0^{+1.5}_{-0.0}$	$0.0^{+1.9}_{-0.0}$
2006–2007	$22.7^{+2.5}_{-2.9}$	$0.24^{+0.01}_{-0.02}$	$3.7^{+0.4}_{-0.4}$	$0.89^{+0.10}_{-0.14}$	$3.2^{+4.5}_{-3.2}$	$6.5^{+3.3}_{-2.9}$
2007–2008	$19.2^{+3.7}_{-16.0}$	$0.23^{+0.02}_{-0.05}$	$4.9^{+4.2}_{-0.6}$	$0.79^{+0.10}_{-0.16}$	$3.8^{+2.7}_{-2.5}$	$0.1^{+2.3}_{-0.1}$
2008–2009	$20.0^{+3.5}_{-11.9}$	$0.22^{+0.02}_{-0.04}$	$4.5^{+3.2}_{-0.5}$	$0.77^{+0.09}_{-0.11}$	$4.6^{+2.6}_{-2.2}$	$0.0^{+1.2}_{-0.0}$
2009–2010	$14.9^{+11.3}_{-14.9}$	$0.19^{+0.04}_{-0.03}$	$6.8^{+5.9}_{-2.7}$	$0.67^{+0.10}_{-0.08}$	$2.9^{+2.0}_{-1.6}$	$0.5^{+1.5}_{-0.5}$
2010–2011	$42.2^{+4.6}_{-8.4}$	$0.24^{+0.02}_{-0.04}$	$4.7^{+1.7}_{-0.6}$	$0.69^{+0.08}_{-0.07}$	$1.6^{+1.6}_{-1.6}$	$0.0^{+0.0}_{-0.0}$
2011–2012	$34.9^{+5.6}_{-14.6}$	$0.22^{+0.02}_{-0.04}$	$5.8^{+3.6}_{-0.7}$	$0.64^{+0.14}_{-0.07}$	$2.7^{+3.2}_{-1.1}$	$2.8^{+2.7}_{-2.0}$
2012–2013	$36.8^{+6.6}_{-14.0}$	$0.22^{+0.02}_{-0.03}$	$8.9^{+3.8}_{-0.8}$	$0.55^{+0.07}_{-0.11}$	$3.3^{+3.3}_{-1.1}$	$4.0^{+3.8}_{-1.3}$

Period	$\mathrm{Norm_3}^*$	$\Gamma_{\mathrm{CXB}}^{\|}$	$S_{\mathrm{CXB}}^\ddagger$	$\mathrm{O\,I}^\S$	χ^2/dof (dof)
2005–2006	$0.4^{+0.1}_{-0.1}$	$1.44^{+0.02}_{-0.02}$	$7.0^{+0.2}_{-0.2}$	$0.4^{+0.2}_{-0.2}$	1.19(590)
2006–2007	$0.5^{+0.1}_{-0.1}$	$1.42^{+0.02}_{-0.02}$	$7.8^{+0.2}_{-0.2}$	$0.6^{+0.2}_{-0.2}$	1.41(434)
2007–2008	$0.6^{+0.2}_{-0.2}$	$1.42^{+0.02}_{-0.03}$	$7.8^{+0.2}_{-0.2}$	$0.5^{+0.2}_{-0.2}$	1.22(434)
2008–2009	$0.6^{+0.2}_{-0.1}$	$1.39^{+0.02}_{-0.02}$	$7.7^{+0.2}_{-0.2}$	$0.4^{+0.2}_{-0.2}$	1.42(434)
2009–2010	$0.7^{+0.3}_{-0.2}$	$1.48^{+0.02}_{-0.03}$	$8.4^{+0.2}_{-0.2}$	$0.2^{+0.3}_{-0.2}$	1.26(434)
2010–2011	$0.7^{+0.3}_{-0.2}$	$1.48^{+0.02}_{-0.02}$	$7.9^{+0.2}_{-0.2}$	$0.2^{+0.3}_{-0.2}$	1.44(434)
2011–2012	$0.6^{+0.3}_{-0.3}$	$1.50^{+0.02}_{-0.02}$	$8.2^{+0.2}_{-0.2}$	$4.2^{+0.3}_{-0.3}$	1.19(434)
2012–2013	$0.8^{+0.4}_{-0.4}$	$1.35^{+0.02}_{-0.02}$	$7.3^{+0.2}_{-0.2}$	$5.3^{+0.4}_{-0.4}$	0.99(434)

Notes.

$*$ The emission measure of the optically-thin thermal CIE plasma integrated over the line of sight (the APEC model normalization): $(1/2\pi)\int n_e n_H ds$ in unit of 10^{14} cm^{-5} sr^{-1}, where n_e and n_H are the electron and the hydrogen densities (cm^{-3}).

$\dagger$ The temperature of the optically-thin thermal CIE plasma in unit of keV.

$\|$ The photon index of the power-law model for the CXB component.

$\ddagger$ The surface brightness of the CXB component (the power-law model normalization) in unit of photons cm^{-2} s^{-1} sr^{-1} keV^{-1} at 1 keV (the photon index is fixed at 1.4).

$\S$ The intensity of neutral oxygen (O I, centroid: 0.525 keV) in unit of LU (photons cm^{-2} s^{-1} sr^{-1}).

$\sharp$ The abundances of the Ne or Mg in unit of the Solar-neighbor values given in Anders & Grevesse (1989).
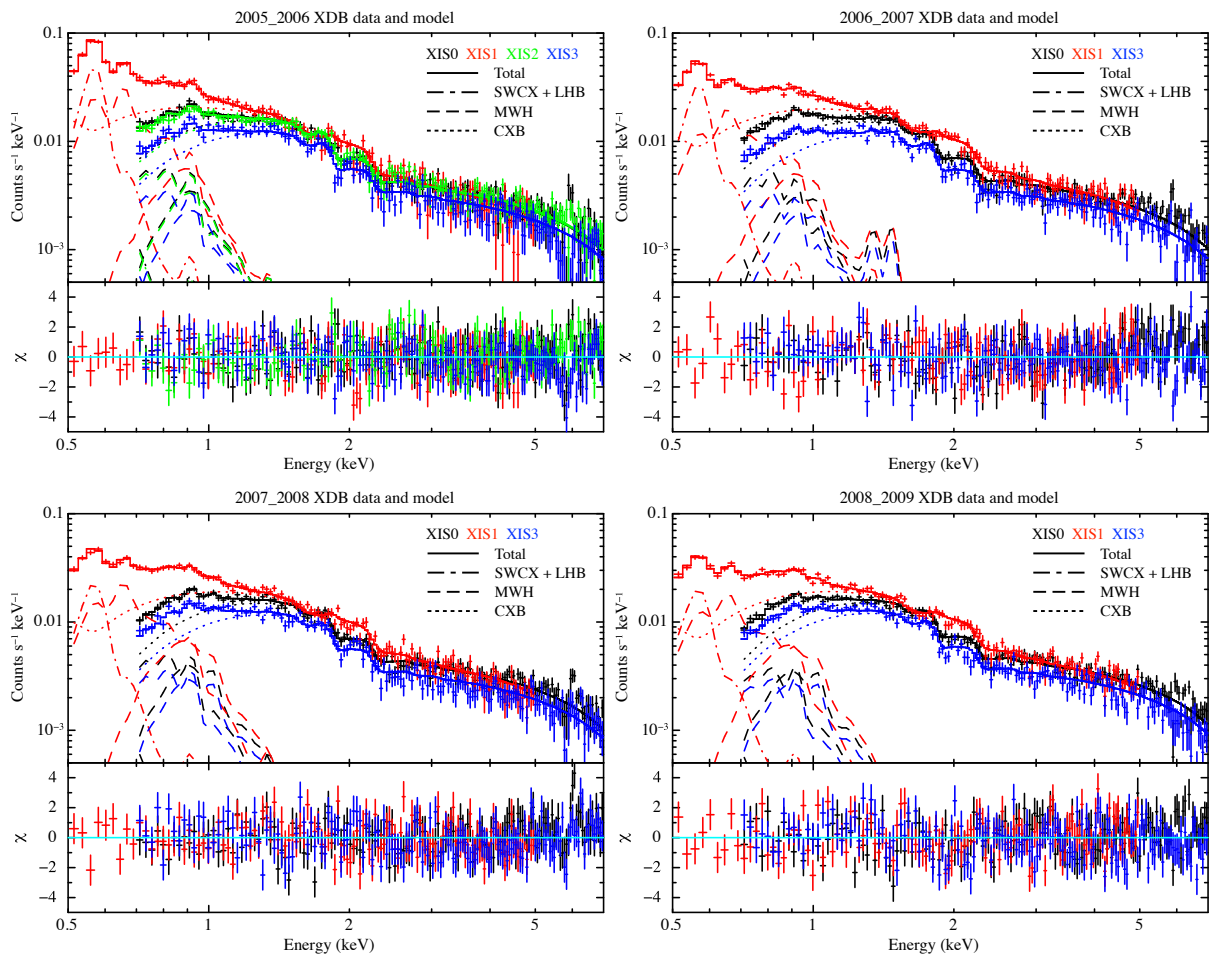
Figure 5.17   Each-period stacked XDB energy spectra from 2005 to 2009 and their best-fit models [(the instrumental responses) $\times$ (the XDB model: Model 5)].
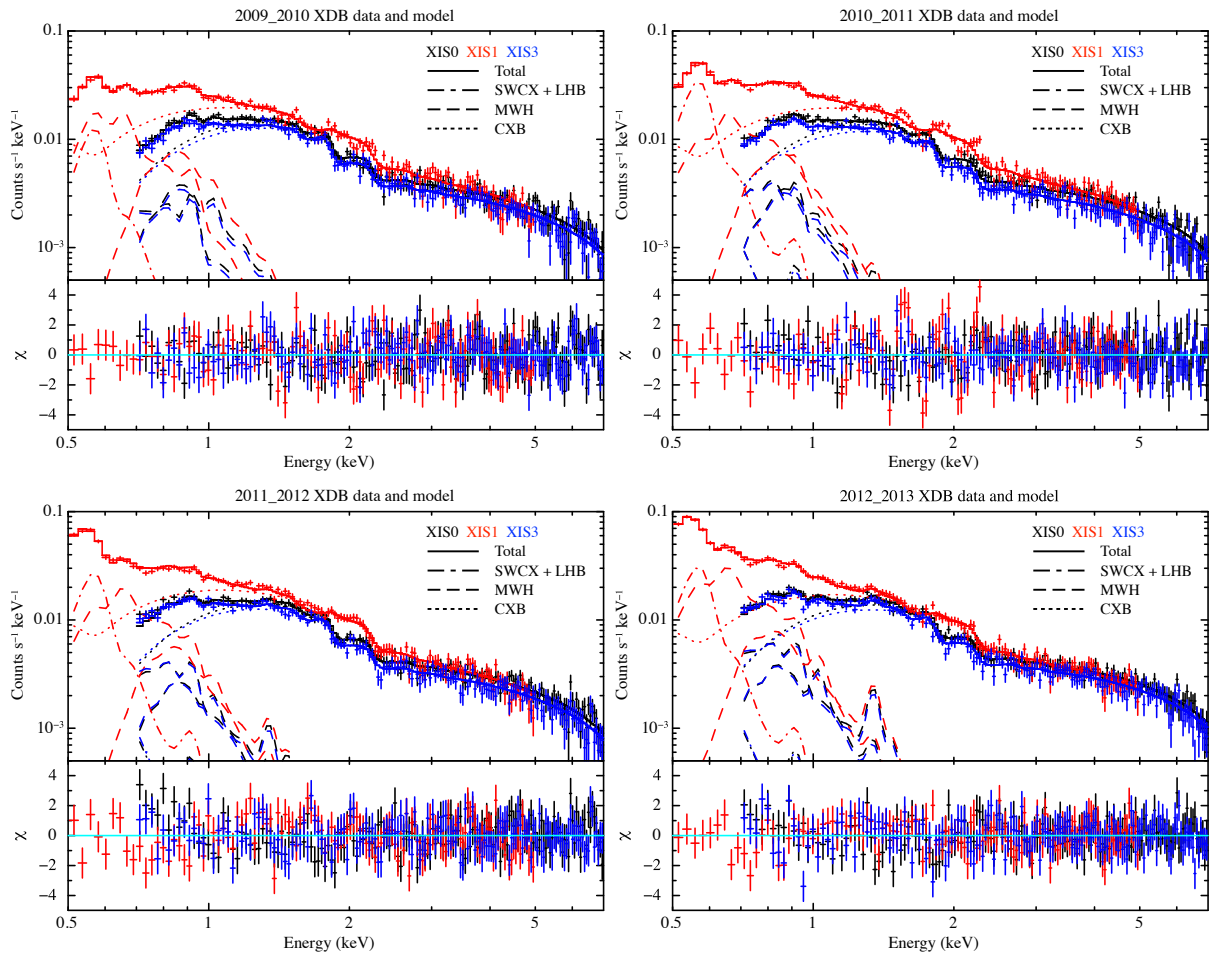
Figure 5.18 Same as Figure 5.17 but from 2009 to 2013.
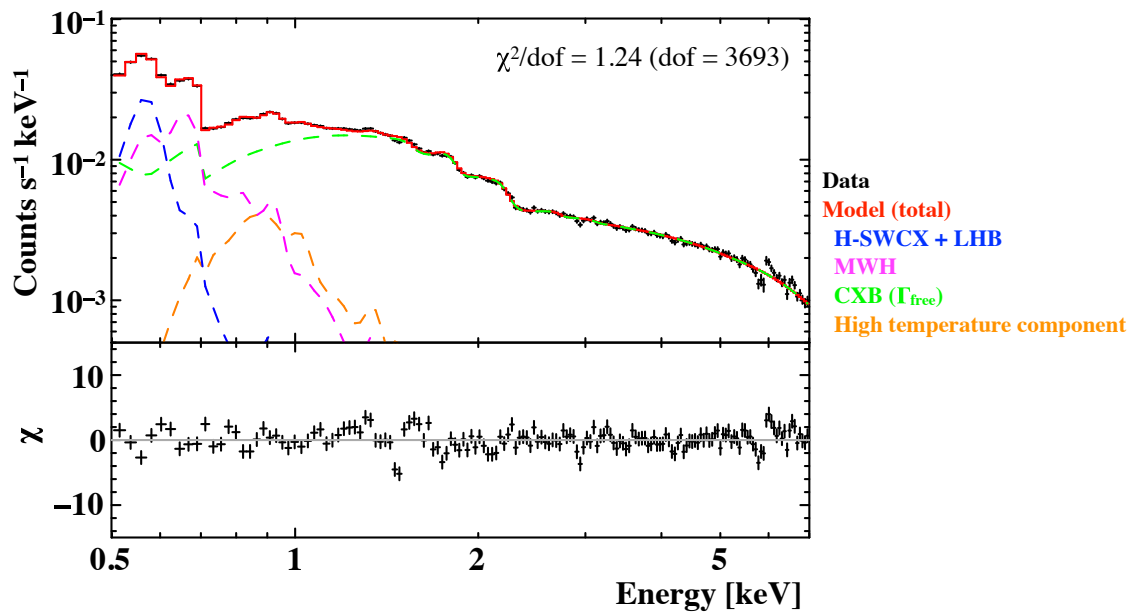
Figure 5.19 Same as Figure 5.13 but for Model 5.

6 Search for a keV signature of dark matter
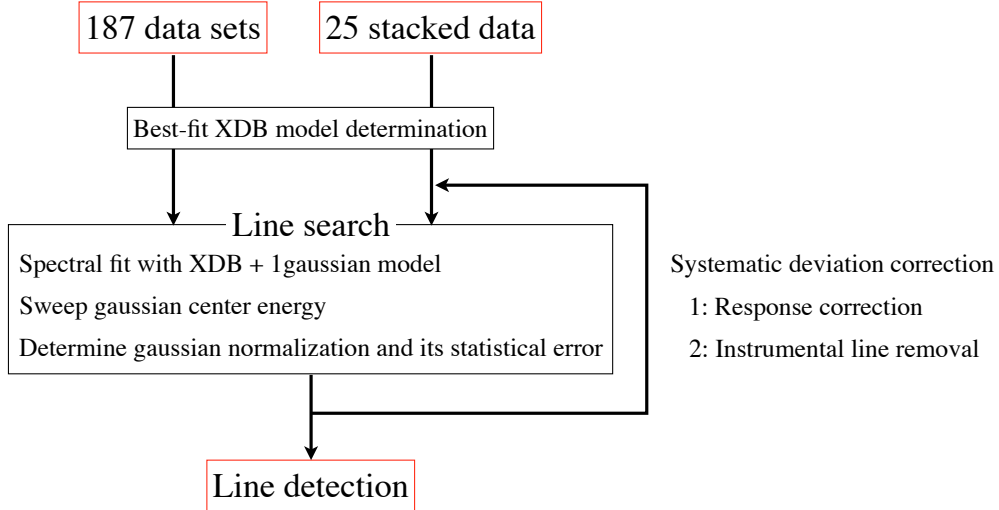
Figure 6.1   Process flow of the dark matter line search in Chapter 6.

6.1   Line search with the 187 individual XDB data

In Chapter 5, we obtained the pure and deep (total 31.5 Msec) XDB spectra, the XRT-XIS responses and the NXB data for them. Using these materials, we searched for X-ray line emission and determined upper limit on line intensities from dark matter associated with the Milky Way.

Firstly, we simultaneously fitted the 187 individual XDB spectra with the model shown in Section 5.3 whose free parameters (the normalizations of the three APEC models and the CXB power-law model) were permitted to vary independently. As the goodness of fit: χ^2/dof (dof) was 1.09 (85316). Then, we added a Gaussian line emission model to the XDB model. The intrinsic line width of the Gaussian was assumed to be 0 eV (WDM velocity dispersion $\leq$ km s^{-1}; Barkana et al., 2001), and its center energy was fixed and swept over the $0.5 - 7.0$ keV energy range with the 261 divisions (the 25 eV step). Since a line profile is broadened by the XIS energy response and this line searching step is smaller than the energy resolution in the $0.5 - 7.0$ keV range (as shown in Chapter 4), the 261 divisions are not all independent. We re-fitted the 187 spectra with [(the instrumental responses) $\times$ (the XDB + one-Gaussian model)] and determined the Gaussian normalizations (line intensities) and

their 1σ statistical error ranges. The line intensities of all the spectra were linked together and allowed to be negative values. The 3σ upper limit on the dark matter line intensities was calculated from sum of the Gaussian normalizations and their 3σ statistical error ranges. If the Gaussian normalization is negative value, the 3σ upper limit was defined as the only 3σ statistical error range: 3σ upper limit = max{Gaussian normalization, 0} + 3σ statistical error range. The line search result with the 187 data sets is shown in Figure 6.2. We found some signatures and dip structures which are suggestive of systematic deviation especially in the 1.5 – 3.5 keV range and around 6 keV.
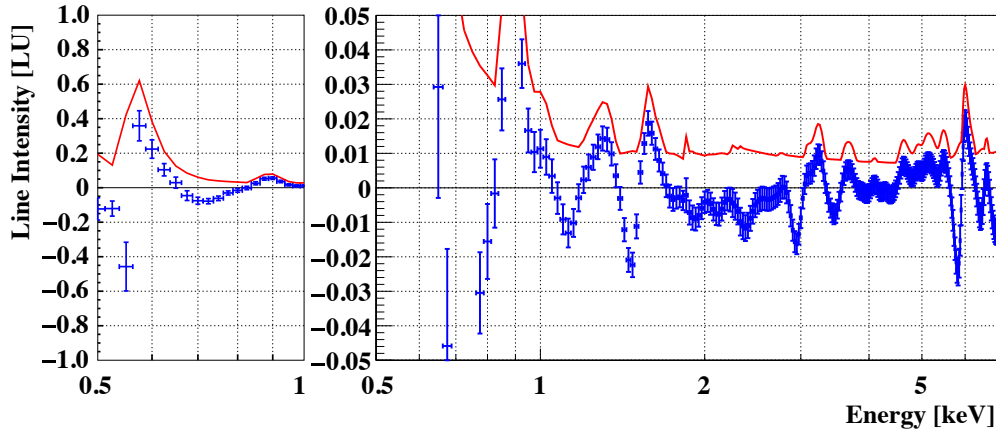
Figure 6.2   Line search result with the 187 individual XDB data sets. The expected dark matter line intensities and their 1σ statistical error ranges are indicated by the blue crosses. The 3σ upper limit on dark matter line intensities (3σ upper limit = max{Gaussian normalization, 0} + 3σ statistical error range) is represented by the red lines. LU (Line Unit) is equal to photons cm^{-2} s^{-1} sr^{-1}.

In order to check dependence on the observational date and direction, we also tried to equally divide the 187 data sets into four groups with observational date (year, season), coordinates (Galactic coordinates, Galactic latitudes, angles from the Galactic center) and performed the line search in each group (Figures 6.3, 6.5, 6.7, 6.9 and 6.11). Figures 6.4, 6.6, 6.8, 6.10 and 6.12 indicate their line intensities and their confidence levels. No appreciable feature appears by divisions with the observation years, the seasons and the quadrants on the Galactic coordinates. Except for a line-like signature at 0.9 keV and dip structures in the 1.5 – 3.5 keV and around 6 keV, most signatures appear and disappear in a irregular pattern. The 0.9 keV signature may have the dependence on the angles from the Galactic center and the Galactic latitudes.
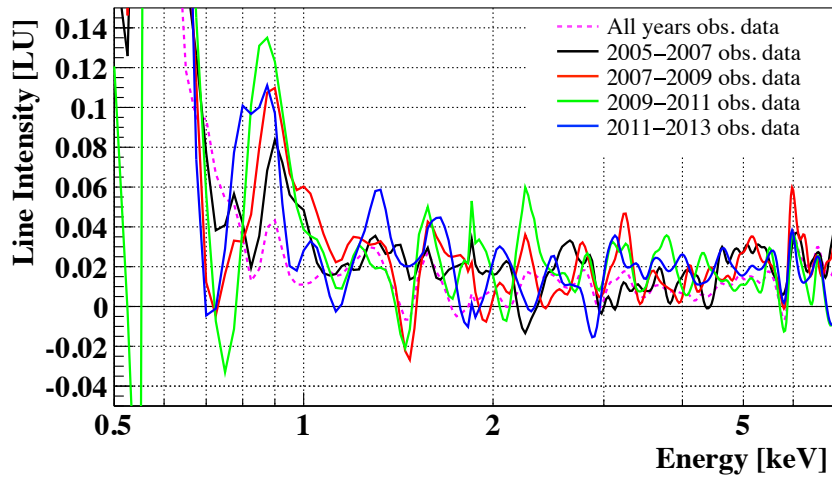
Figure 6.3   Comparison of the line search results with the four data groups divided by observational periods.
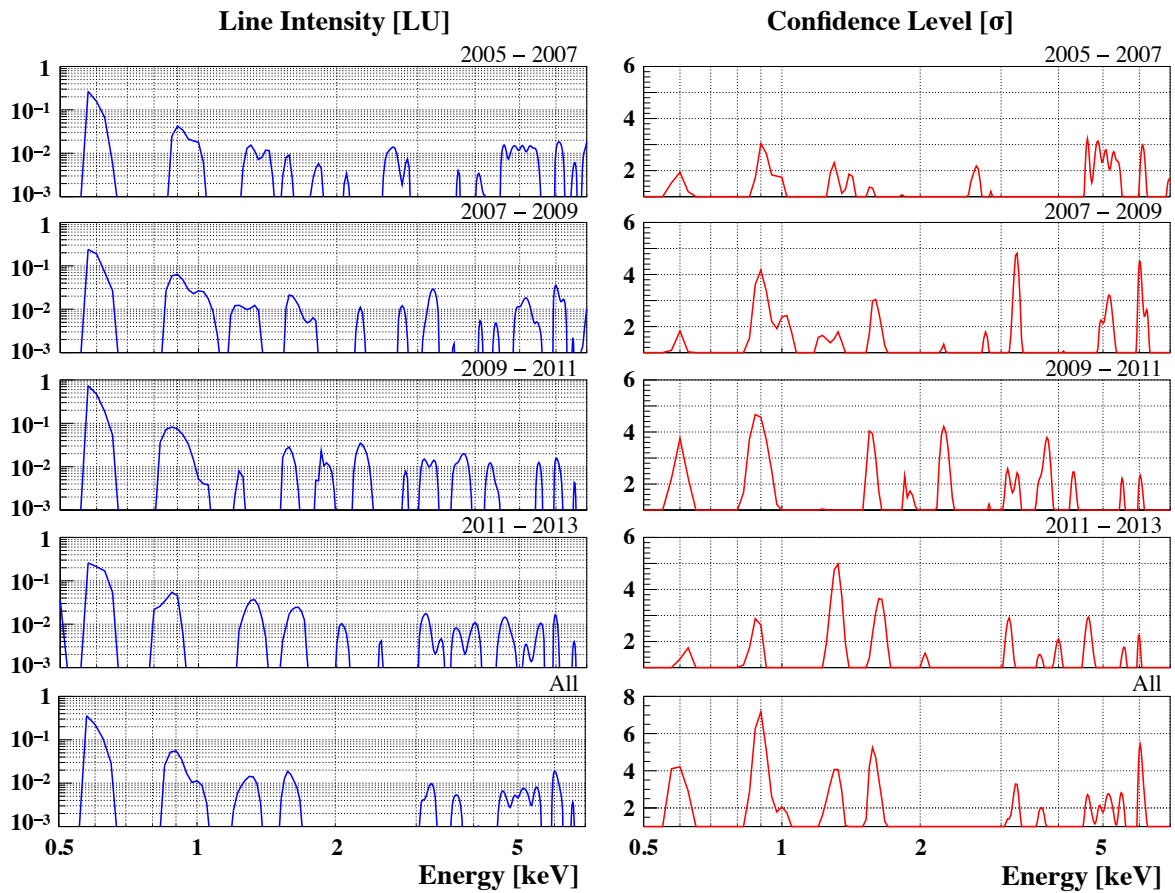
Figure 6.4   Line intensities and their confidence levels of detection as the line search results with the four data groups divided by observational periods.
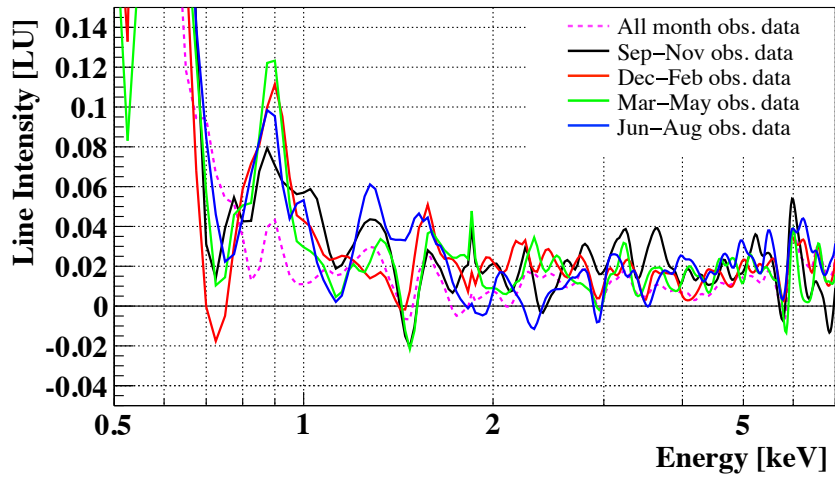
Figure 6.5   Same as Figure 6.3 but sorted by observational seasons.
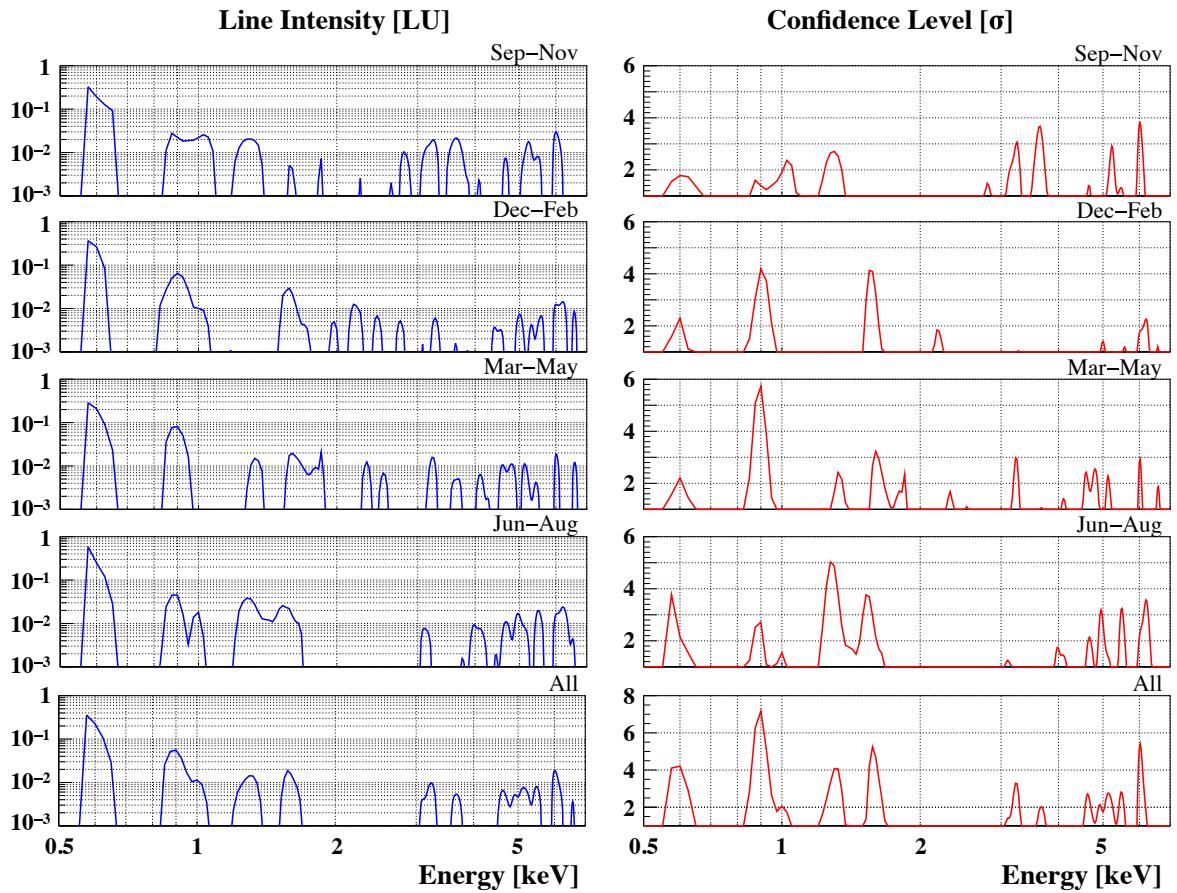
Figure 6.6   Same as Figure 6.4 but for the four data groups divided by observational seasons.
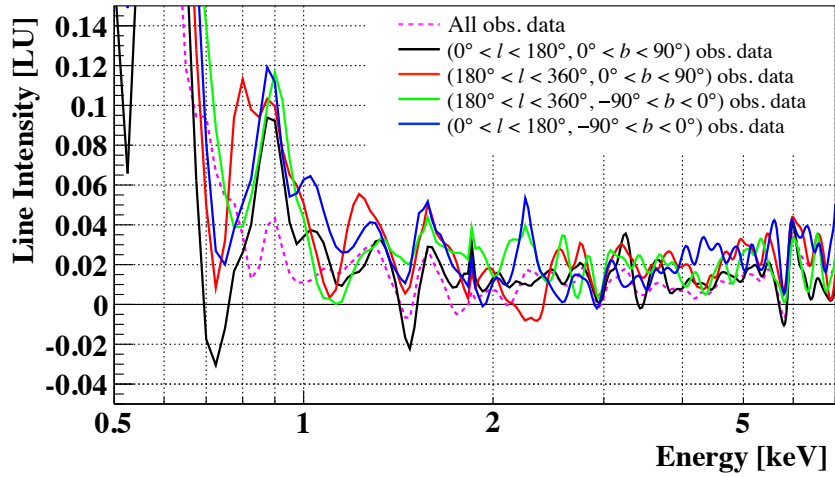
Figure 6.7   Same as Figure 6.3 but for the four different quadrants on Galactic coordinates.
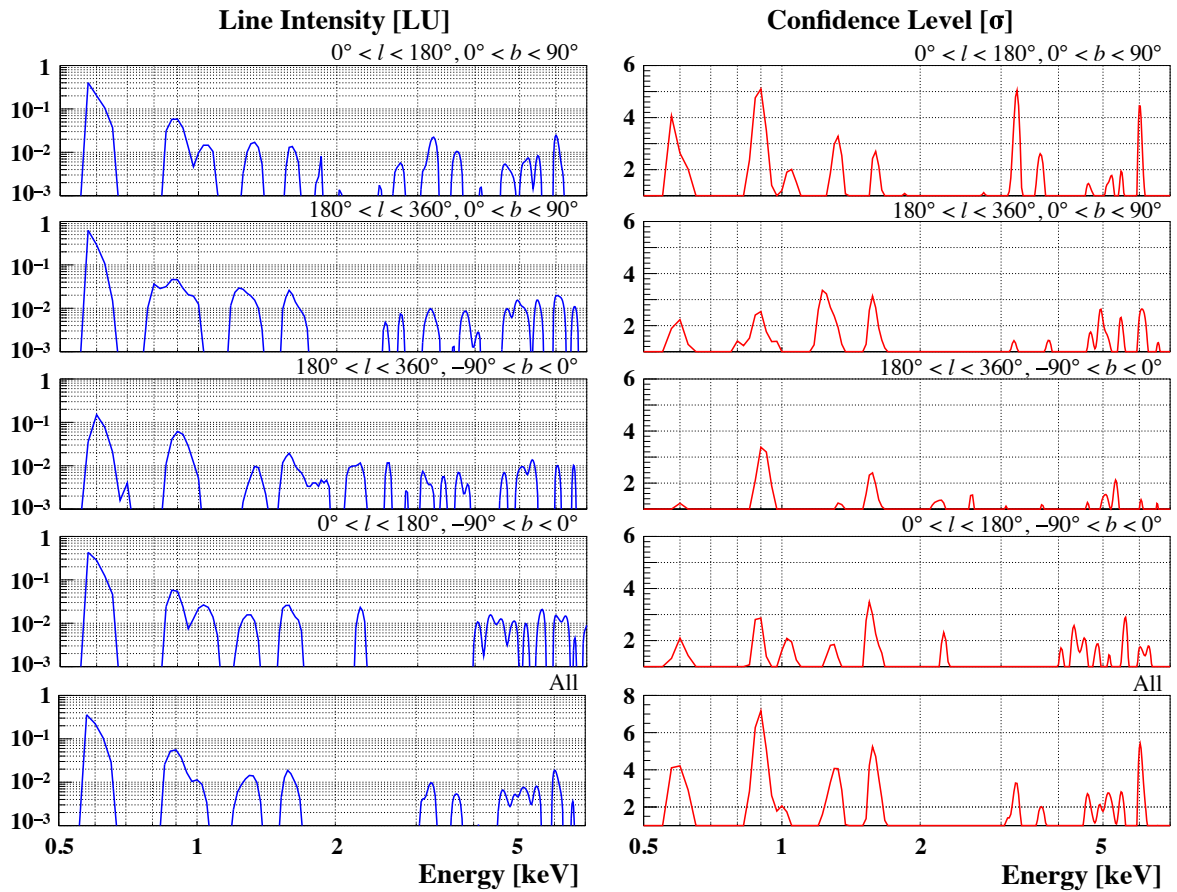
Figure 6.8   Same as Figure 6.4 but for the four data groups divided by observational quadrants on Galactic coordinates.
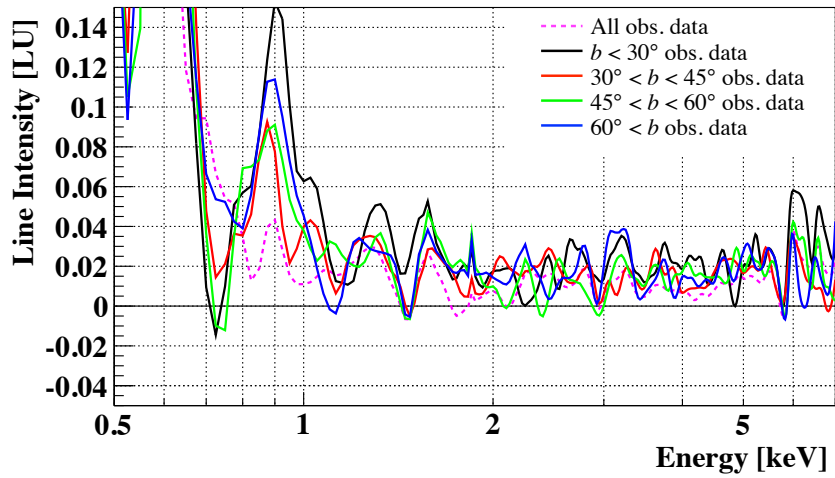
Figure 6.9   Same as Figure 6.3 but sorted by Galactic latitudes.
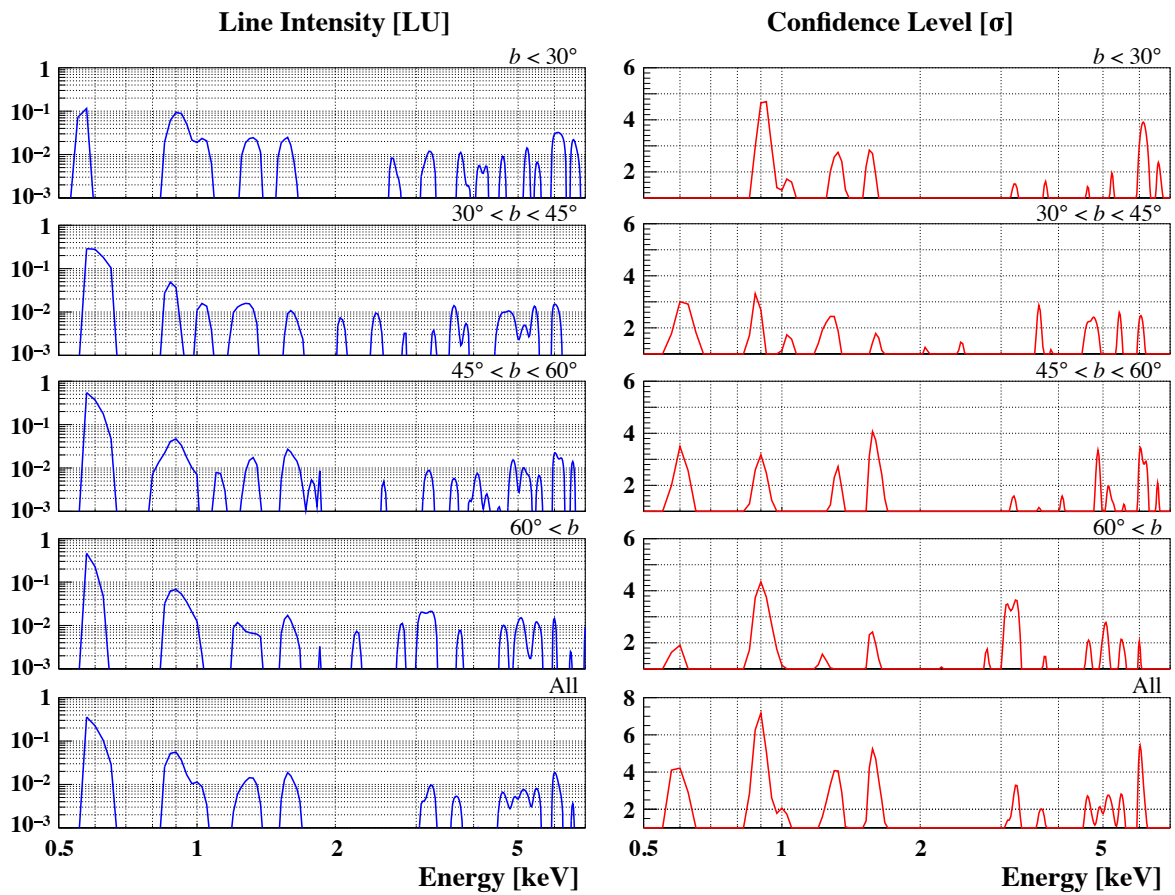
Figure 6.10   Same as Figure 6.4 but for the four data groups divided by Galactic latitudes.
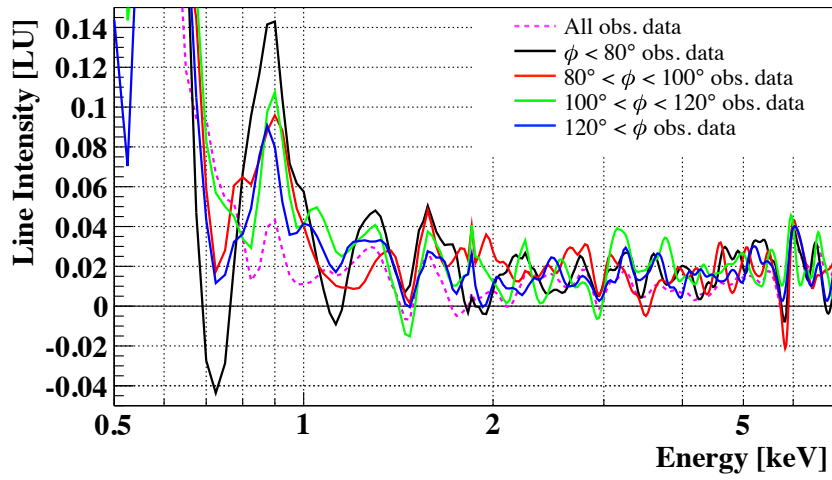
Figure 6.11   Same as Figure 6.3 but sorted by angles from the Galactic center.
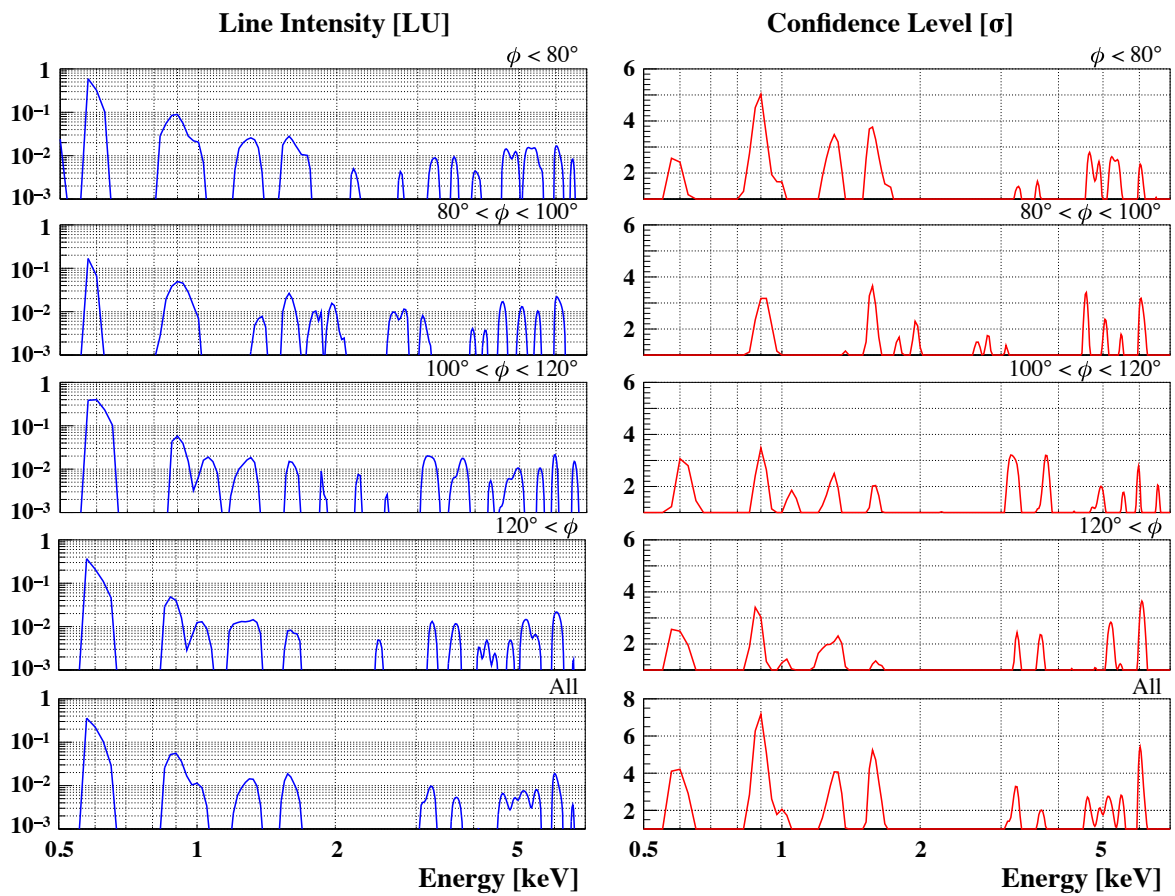
Figure 6.12   Same as Figure 6.4 but for the four data groups divided by angles from the Galactic center.

6.2   Line search with the 25 stacked XDB data

Since a lot of spectra and responses and huge degrees of freedom are treated in above spectral fitting, the line search with the 187 data sets needs for much time-consuming and machine-power-required process. In order to correct systematic deviation and repeat to perform the dark matter line search, we decided to used the 25 stacked XDB data and averaged responses and NXB data. We simultaneously fitted the 25 stacked XDB spectra with the best-fit model (Model 5 in Chapter 5, free parameters: the normalizations of the three APEC models and the power-law model) + a Gaussian line emission model. The line intensities of all the spectra were linked together and allowed to be negative values.

The line search result with the stacked XDB spectra is shown in Figure 6.13. We did not find much differences between the two results; the same signatures found in the line search with the 187 data sets still remained.
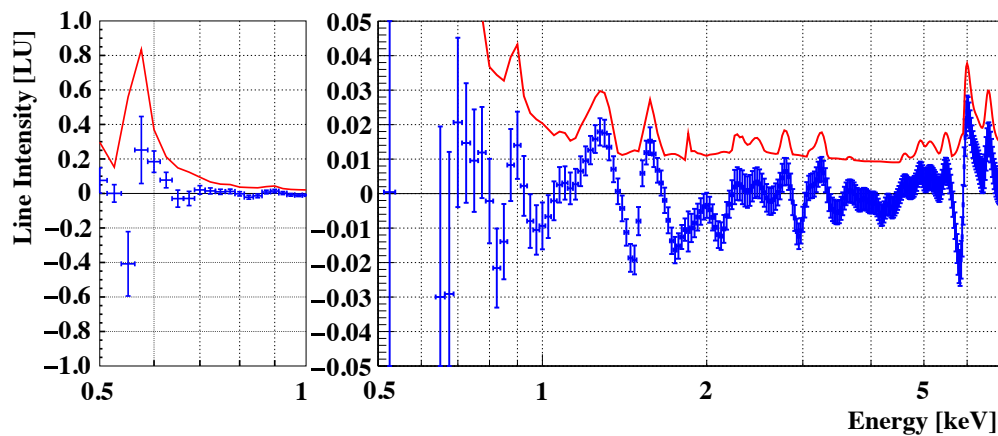
Figure 6.13   Same as Figure 6.2 but with the 25 stacked XDB data sets.

6.3   Response correction with stacked Crab data

In the line search results shown above, systematic deviation could exist in the $1.5 - 3.5$ keV range corresponding to the energy region with multiple absorption edges in the Suzaku XRT-XIS effective area. We suspected mismatching of the XRT-XIS responses reproduced by the Suzaku calibration database and ray-tracing simulation. We evaluated the reproducibility of them.

We used the stacked spectrum of the 34 "Crab Nebula center" (hereafter simply Crab) observational data with the Suzaku XIS for the Suzaku XRT calibration from 2005 to 2013 (total exposure time is ~ 20 ksec). This spectrum had the lowest statistical uncertainty of all Suzaku XIS data (total photon count in the $1.0 - 7.0$ keV range is $\sim 4 \times 10^7$). The Crab is mostly used for instrumental calibration because it has a very high surface brightness and featureless spectra of synchrotron emission (expressed by a power-law function absorbed by the interstellar medium of the Milky Way galaxy; the neutral hydrogen column density $= 0.3 \times 10^{22}$ cm^{-2}, the power-law photon index $= 2.1$ and the surface brightness ~ 10 photons cm^{-2} s^{-1} sr^{-1} at 1 keV). The details of the 34 Crab data were summarized in Appendix B and the result of spectral fitting is shown Figure 6.14. We found the residuals between the stacked Crab spectrum and its model multiplied by the instrumental response up to ~ 10 % especially in the $1.5 - 3.5$ keV range. We corrected this deviation as mismatching of the XRT-XIS responses with the factor shown in Figure 6.14 (right) and re-fitted the stacked XDB spectra with [(the corrected responses) $\times$ (the XDB: Model 5 + one-Gaussian model)]. The line search result with the stacked XDB spectra and the corrected responses by using the stacked Crab spectrum (all 8 years) is shown in Figure 6.15. Some signatures in the 1.5 – 3.5 keV disappeared or weakened.

Moreover, taking into account for time variability of response mismatching, we stacked the Crab spectra every 2 years and conducted spectral analysis to obtain the response correction factors for every 2 years. The spectral fitting results with the stacked Crab spectra (every 2 years) and the response correction factors are shown in Figures 6.16 and 6.17, respectively. The line search result with the stacked XDB spectra and the corrected responses by using the stacked Crab spectra (every 2 years) is shown in Figure 6.18. Along with Figure 6.15, some signatures in the 1.5 – 3.5 keV disappeared or weakened more clearly and were regarded as systematic deviations caused by response mismatching.
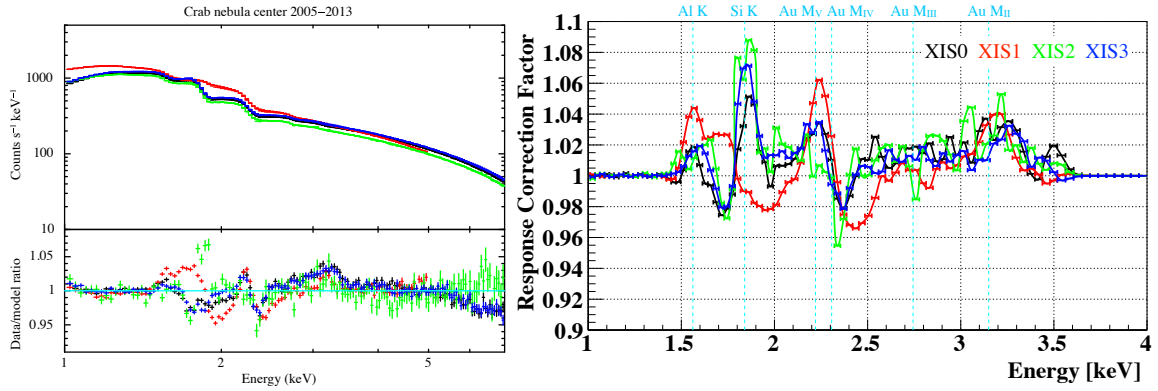
Figure 6.14 Left panel: all-8-year stacked Crab energy spectrum from 2005 to 2013 and its best-fit model (synchrotron emission absorbed by the interstellar medium of the Milky Way galaxy). Right panel: data-to-model ratio of the all-8-year stacked Crab energy spectrum as the response correction factors in the 1.5 – 3.5 keV range.
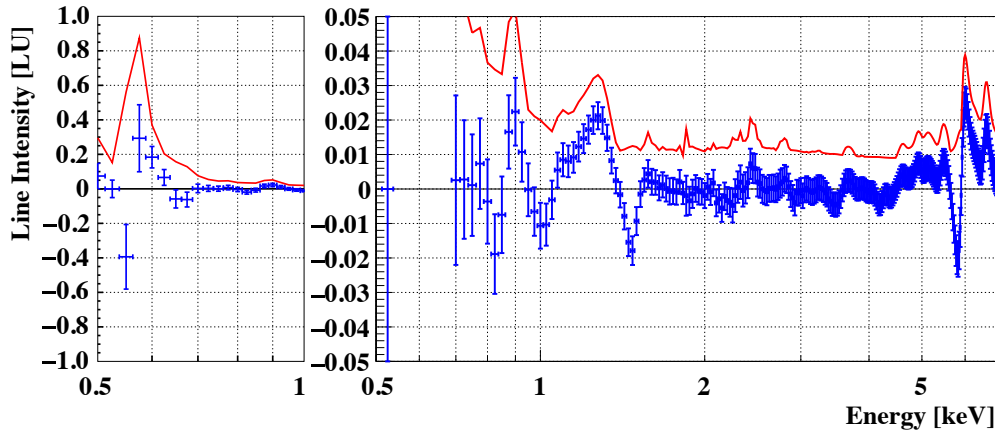
Figure 6.15 Line search result with the stacked XDB spectra and the corrected responses by using the all-8-year stacked Crab spectrum. The expected dark matter line intensities and their 1σ statistical error ranges are indicated by the blue crosses. The 3σ upper limit on dark matter line intensities with the corrected responses is represented by the red lines.
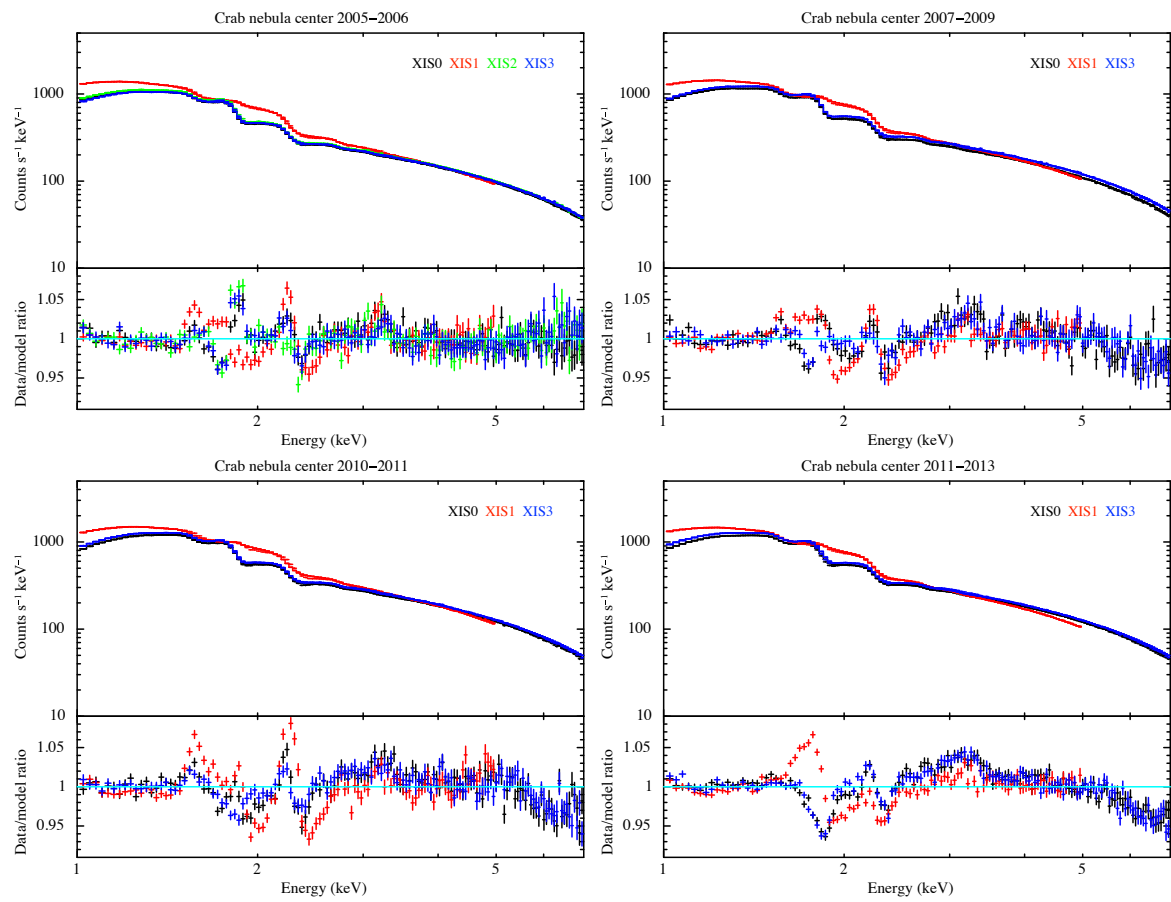
Figure 6.16 Every-2-year stacked Crab energy spectra from 2005 to 2013 and their best-fit models (same as Figure 6.14).
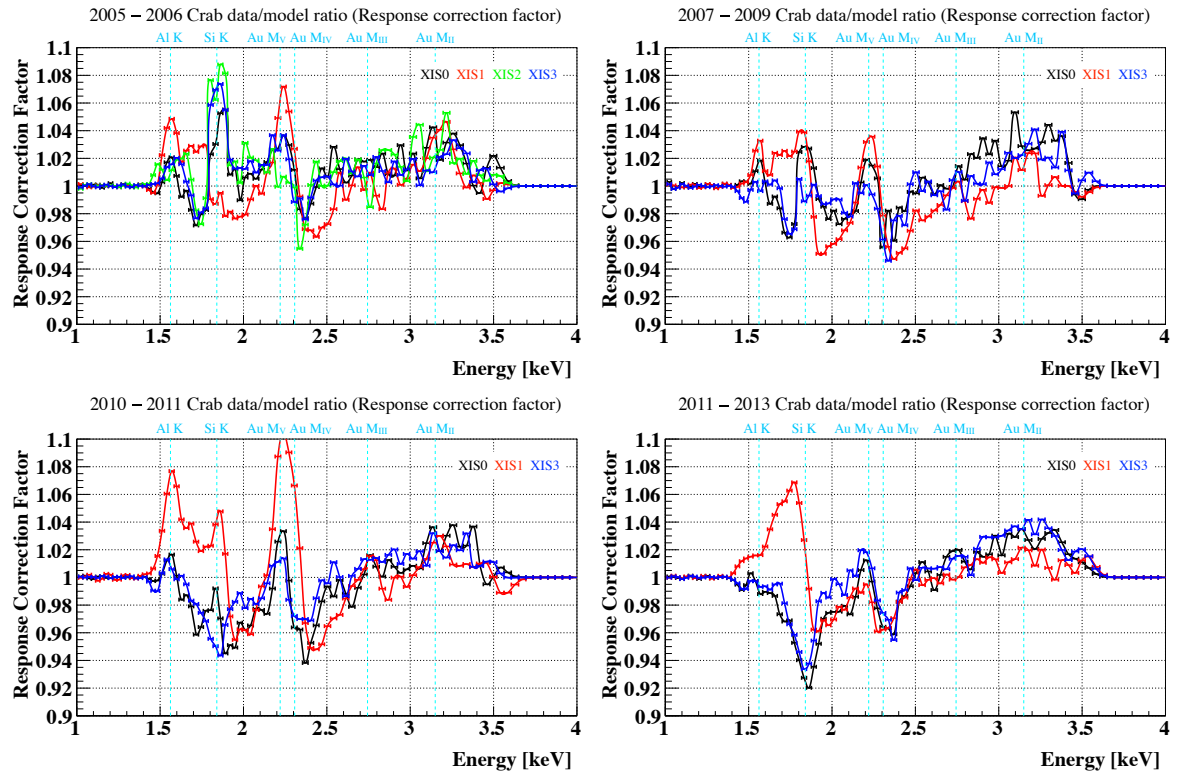
Figure 6.17   Data-to-model ratio of the every-2-year stacked Crab energy spectra as the response correction factors in the 1.5 – 3.5 keV range.
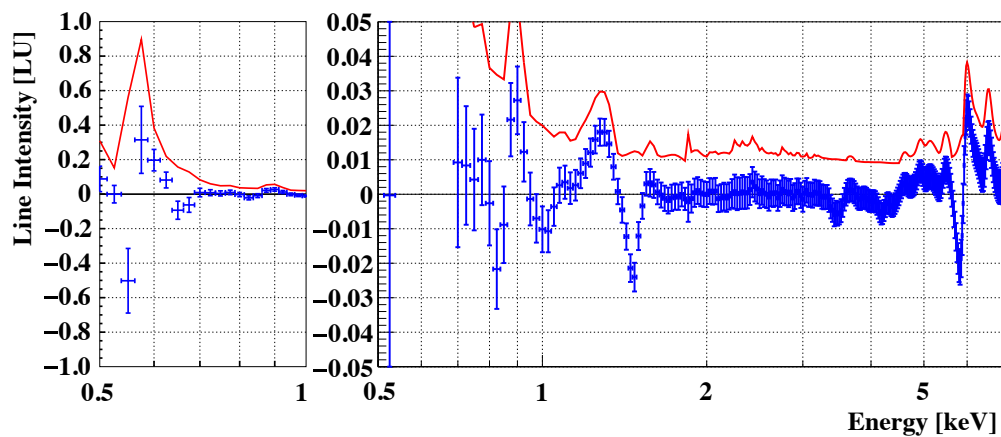
Figure 6.18   Same as Figure 6.15 but for the stacked XDB spectra and the corrected responses by using the every-2-year stacked Crab energy spectra.

6.4   Improvement of instrumental line removal

As can be appreciated from the foregoing, less than 10 % of systematic deviations lead to dummy signatures (mis-detection) in the weak line search with the deep XDB spectra. As the other possibility making systematic deviation, we considered the uncertainty of the NXB and instrumental line subtraction. We used and stacked the NXB data reproduced from the night-Earth observations in order to remove the NXB continuum and instrumental line contributions from the XDB + NXB spectral data. The reproducibility of NXB was reported to be high (detailed in Chapter 4), and the NXB continuum little affected to this line search. However, the instrumental line contributions were not the case. The instrumental line intensities change year by year, especially Mn-K lines from the calibration source as shown in Figure 6.19. In addition, the energy gain and the energy resolution shift by the aging degradation of the XIS. It displaces and distorts line distributions. We actually found the residuals in some spectral fitting results around 6 keV which is near Mn-Kα line energy (centroid: 5.895 keV). We ceased to remove the instrumental line contributions with the night-Earth observational data. As alternated, they were determined and subtracted by spectral fitting with the multiple (five-) Gaussian models. After this subtraction, the line search result with the stacked XDB spectra (and the uncorrected responses) is shown in Figure 6.23. The dip structures around 1.6 keV and 6 keV which correspond to Al- K and Mn-K lines disappeared.

In combining the response correction with the stacked Crab data (every 2 years) and the improved removal of instrumental lines, the results of XDB spectral fitting are shown in Figures 6.20, 6.21 and 6.22. As the goodness of fit, χ^2/dof (dof) was 1.05 (3693), and the null hypothesis probability was 2.5 %. These 25 stacked XDB spectra were consistent with Poisson-distributed functions based on these spectral models [(the corrected responses) $\times$ (the XDB: Model 5 + five-instrumental lines)] as generating functions. The instrumental line contributions were summarized in Appendix C. The line search result with the stacked XDB spectra, the corrected responses by using the stacked Crab spectra (every 2 years) and the improved removal of instrumental lines is shown in Figure 6.24.

For comparison, we changed intensities of instrumental lines to a few % lower or higher values in the range of 90 % statistical error derived from spectral fitting with the Gaussian model and conducted the line search in the same way (Figures 6.25 and 6.26). We could understand that the prominent signatures around 1.8 and 6.0 keV corresponding to Si-Kα and Mn-Kα lines appeared and 3σ upper limit on line intensities were affected by instrumental line incomplete removal. Finally, as shown in Figure 6.24, we carefully corrected the systematic deviations and obtained possible dark matter line intensities, their uncertainties (confidence levels of detection) and their 3σ upper limit over the 0.5 – 7.0 keV range.
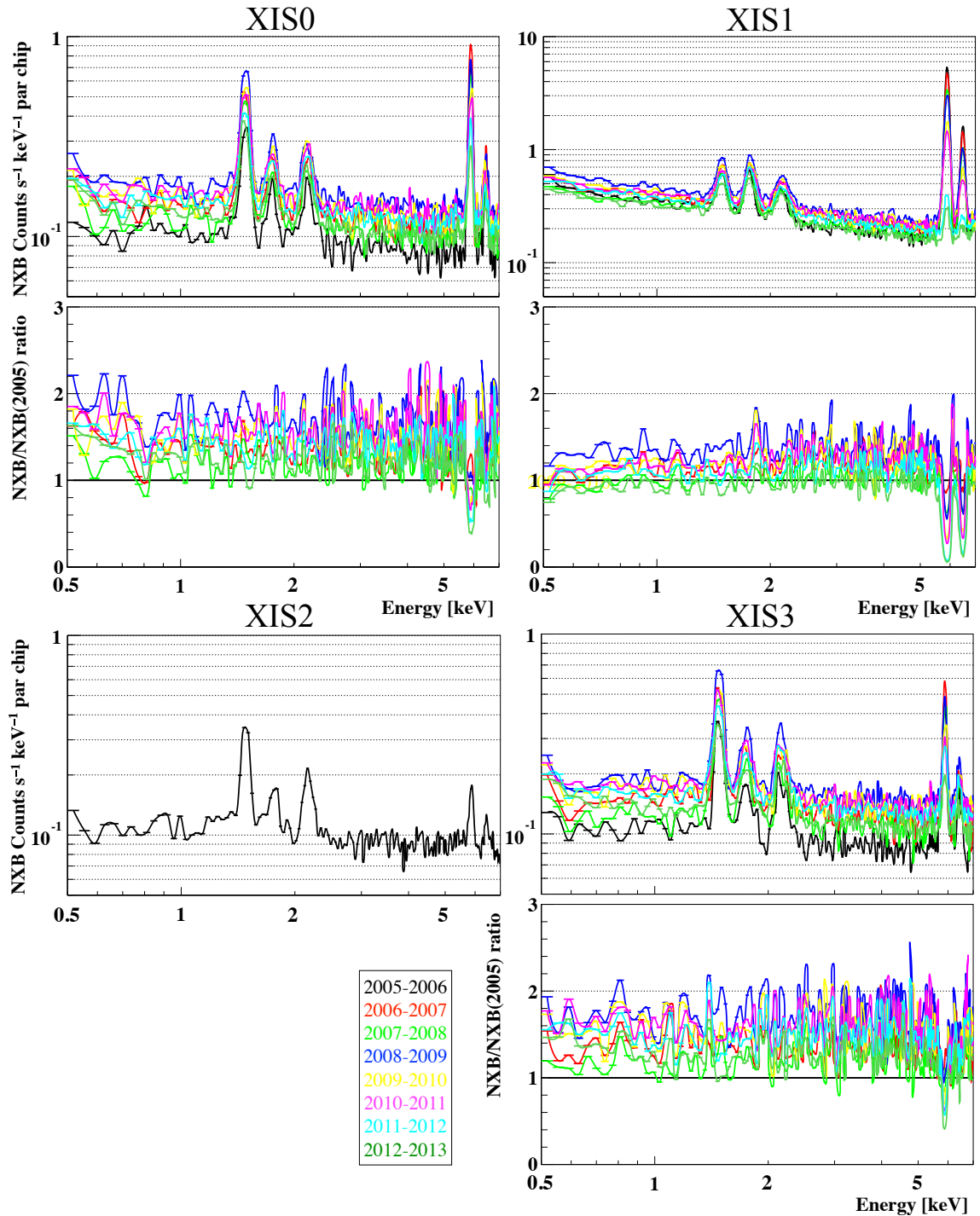
Figure 6.19   Annual change of the stacked NXB data for XIS0 (left top), XIS1 (left bottom) and XIS3 (right top).
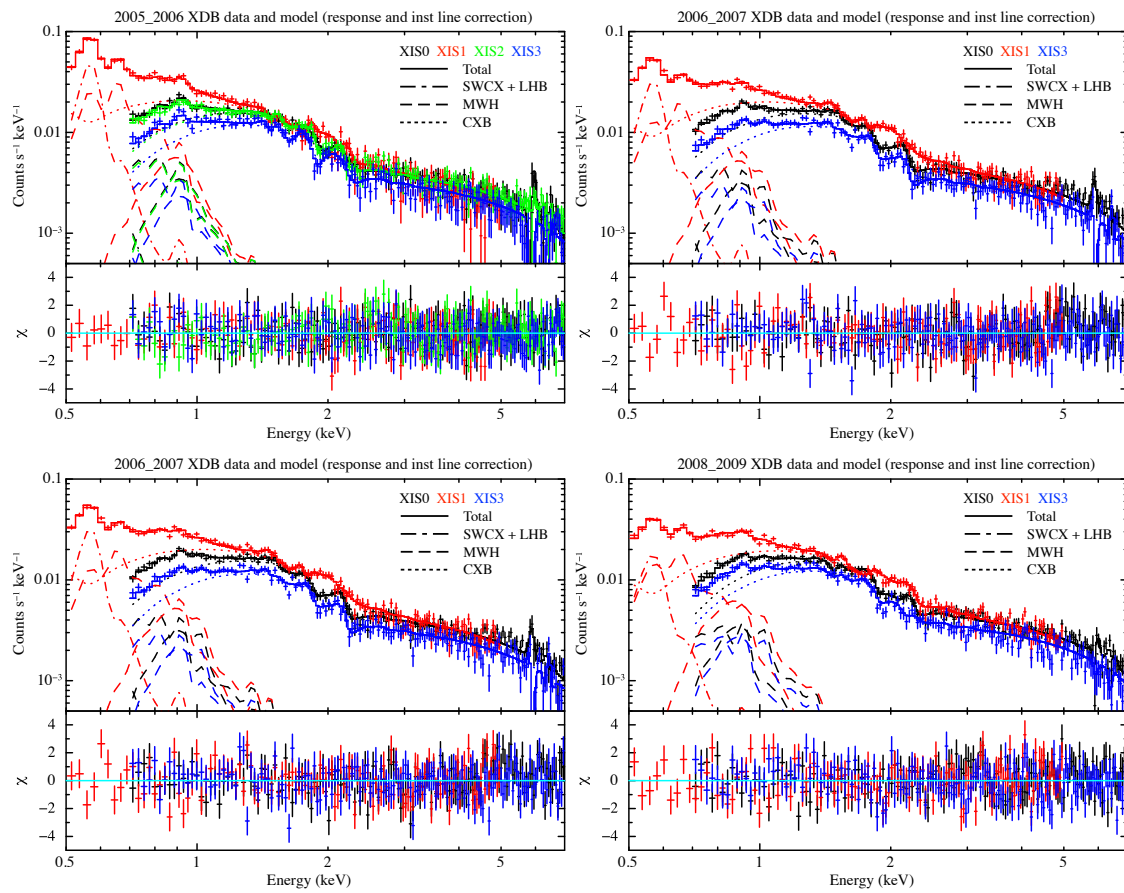
Figure 6.20   Each-period stacked XDB energy spectra from 2005 to 2009 and their best-fit models [(the corrected responses) × (the XDB: Model 5 + five-instrumental lines)]. The corrected responses were derived from the every-2-year stacked Crab energy spectra.
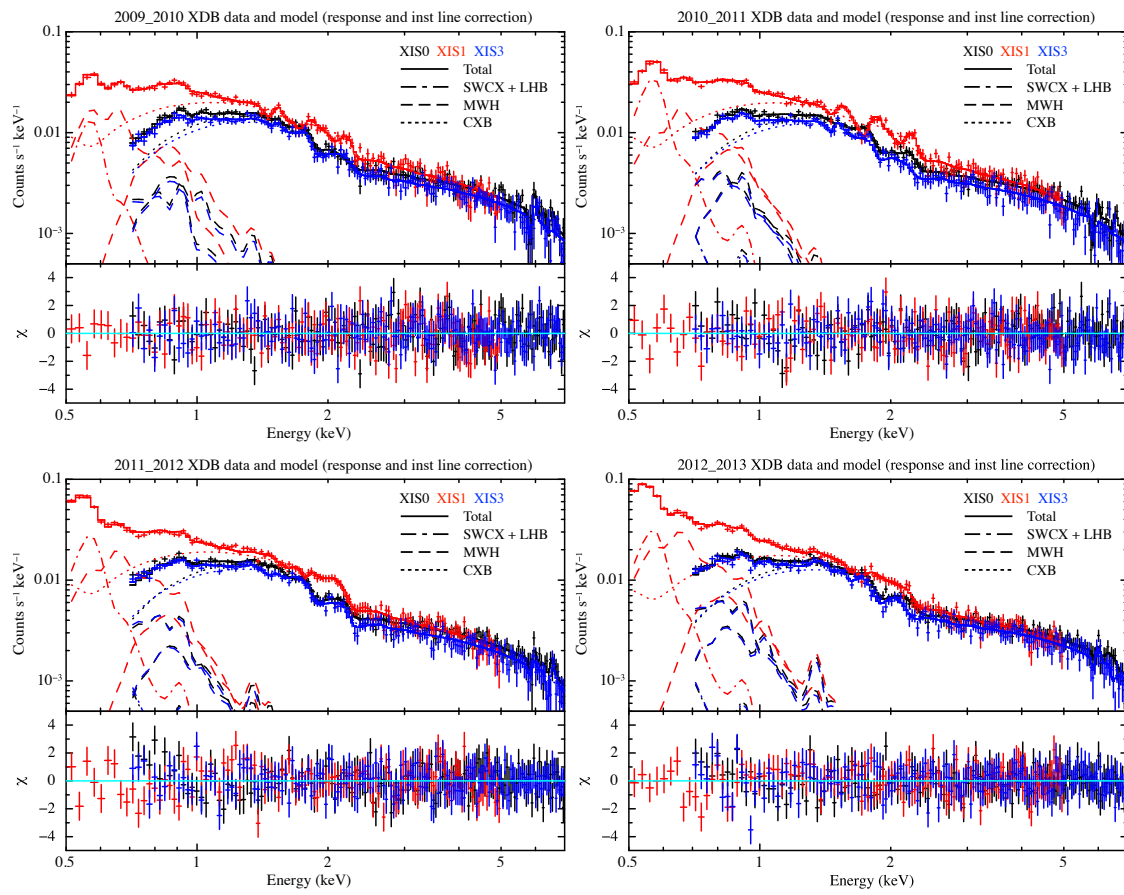
Figure 6.21   Same as Figure 6.20 but from 2009 to 2013.
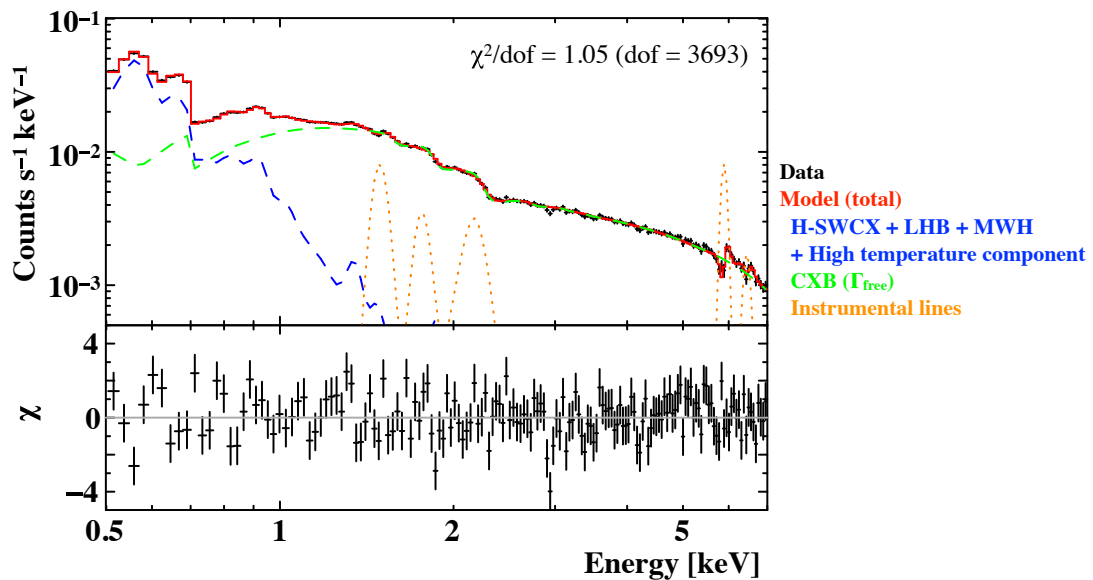
Figure 6.22   Exposure-time-weighted average of the 25 stacked XDB energy spectra from 2005 to 2013 and its spectral model [(the corrected response) × (the XDB: Model 5 + five-instrumental lines)]. The corrected response was derived from the every-2-year stacked Crab energy spectra.
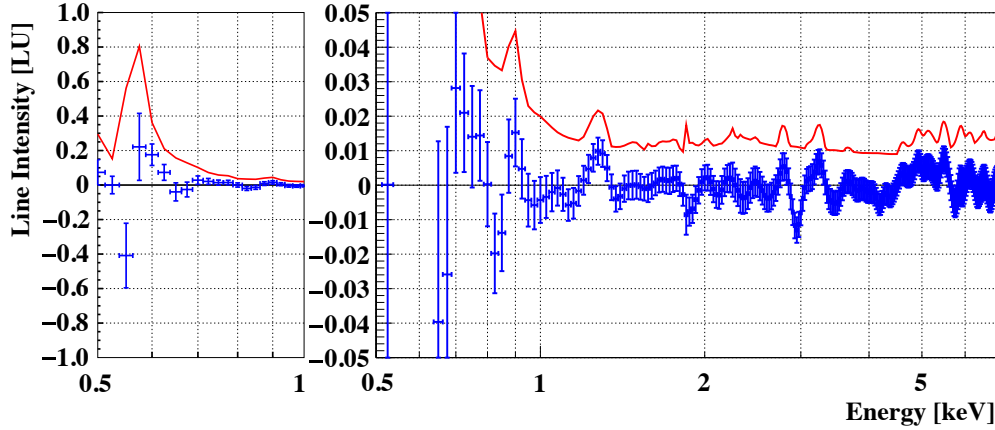
Figure 6.23   Line search result with the 25 stacked XDB energy spectra and their models [(the uncorrected responses) × (the XDB: Model 5 + five-instrumental lines)]. The expected dark matter line intensities and their 1σ statistical error ranges are indicated by the blue crosses. The 3σ upper limit on dark matter line intensities with the uncorrected responses and the improved removal of the instrumental lines is represented by the red lines.
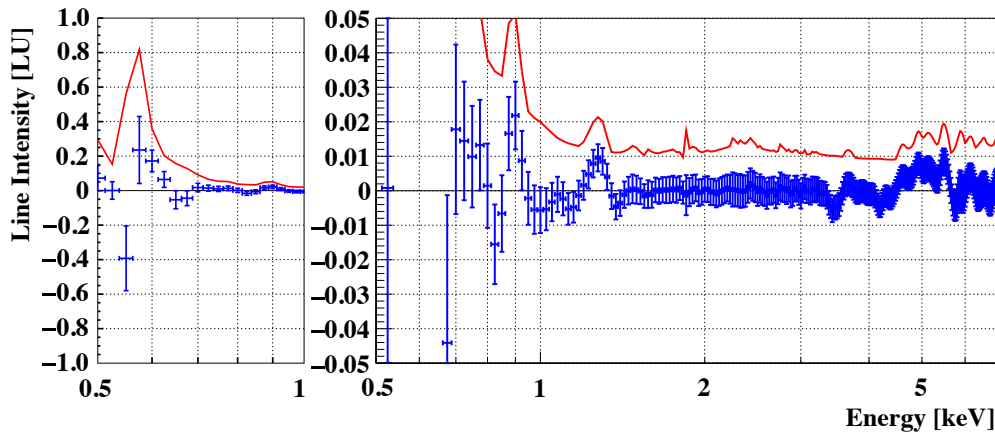
Figure 6.24   Same as Figure 6.23 but with their best-fit models [(the corrected responses) × (the XDB: Model 5 + five-instrumental lines)]. The corrected responses were derived from the every-2-year stacked Crab energy spectra.
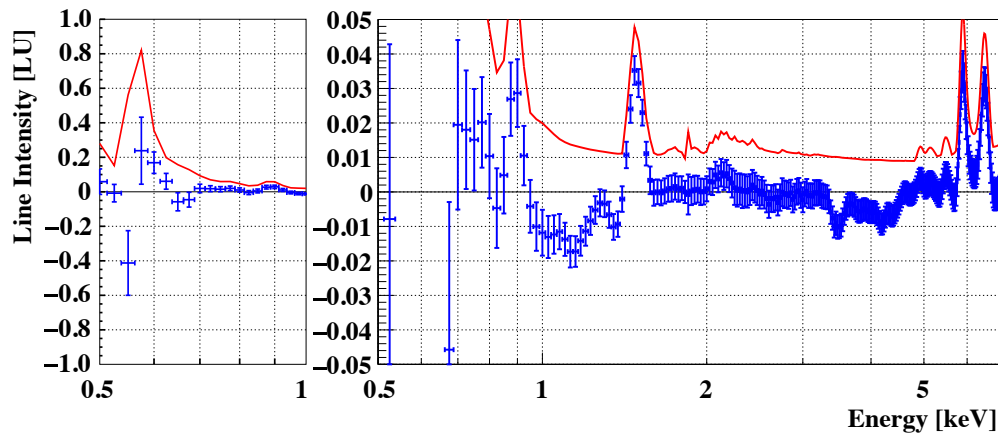
Figure 6.25   Same as Figure 6.24 but for the case of the incomplete removal of instru-
mental lines. Their intensities were underestimated in the 90 % error ranges derived
from the five-Gaussian model spectral fitting.
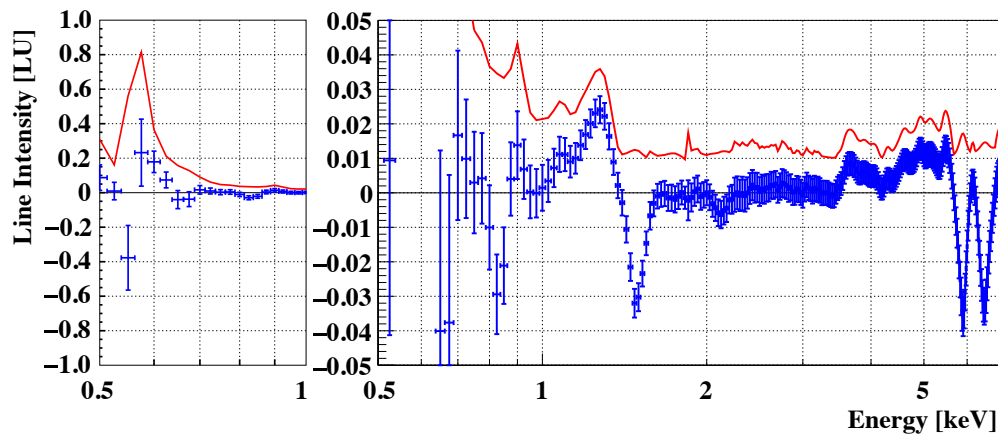
Figure 6.26   Same as Figure 6.24 but for the case of the incomplete removal of instru-
mental lines. Their intensities were overestimated in the 90 % error ranges.

6.5   Line-like signature interpretation by simulation

As shown in Figure 6.24, we found line-like signatures at 0.600, 0.900, 1.275, 4.925 and 5.475 keV. In order to express these signatures by narrow line appearance, we conducted a simulation. We produced mock spectra from the XDB + five-Gaussian (their energy were fixed to 0.600, 0.900, 1.275, 4.925 and 5.475 keV and their width = 0 eV) model and fitted them with the XDB + one-Gaussian model. Here, statistical uncertainty was not considered; we assumed the infinitely-long exposure time in the mock spectra production. The spectral fitting result is shown in Figure 6.27. As shown in Figure 6.27, the signatures at 0.600, 0.900, 1.275, 4.925 and 5.475 keV were well expressed by line emission at such energies.
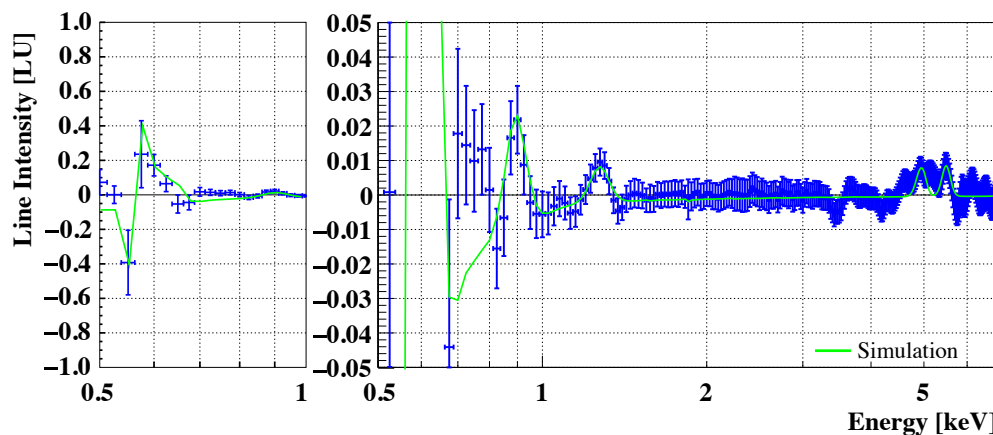
Figure 6.27   Line search result (line intensities and 1σ error ranges; blue crosses) shown in Figure 6.24 and simulation result (determined Gaussian intensities; green line) with a mock spectrum from the XDB + five-Gaussian (their energies were fixed to 0.600, 0.900, 1.275, 4.925 and 5.475 keV) model. This spectrum was fitted with the XDB + one-Gaussian model. The Gaussian center energy was swept over the 0.5 – 7.0 keV range.

6.6   Look elsewhere effect correction

When we searched for line emission whose appearance energy was unknown *a priori*, the risk of mis-detection by statistical fluctuation increases in proportion to the "trial factor": the number of independent energy bins which was roughly the energy range divided by the energy resolution of the detector in the plausible thumb rule. This is known as the "Look elsewhere effect" (LEE; Gross & Vitells, 2010). Above line search results, the significances or the confidence levels of detection were not taken into account the LEE and the false detection probability. These were equivalent to the case of a search for known line emission (the appearance energy is known *a priori*). Although the LEE uncorrected significance was used in most of previous works, we should correct the LEE and degrade the significance based on the trial factor. We derived the actual trial factor as a function of the energy range and the energy resolution or the LEE corrected significance by multiple Monte-Carlo simulations described below. Firstly, we made a mock spectrum with only the XDB model and fitted it with the XDB + one-Gaussian model. The Gaussian center energy was swept over the $0.5 - 7.0$ keV range with the 261 divisions (the 25 eV step). The Gaussian intensities and their 1σ error ranges were determined. We calculated significance (= Gaussian intensity / its 1σ error range ratio) for all the 261 divisions (as shown in Figure 6.28 for example). This process was repeated 4000 times. We checked an upside cumulative distribution of all the 261×4000 significances (Figure 6.29). Since the significances $\geq 4.2\sigma$ appeared 5 times out of 4000 (0.135 %; the one-sided tail of p-value for 3.0σ), the LEE uncorrected 4.2σ corresponded to the LEE corrected 3.0σ in this line search (trial factor of ~ 100; consistent with the ratio of energy range and energy resolution of this line search). Hereafter, we used the LEE uncorrected significance of 4.2σ as the LEE corrected 3σ for determination of line intensity upper limits. We also found that the LEE uncorrected $< 3.2\sigma$ confidence level of detection corresponded to the LEE corrected $< 1.0\sigma$ in this line search.
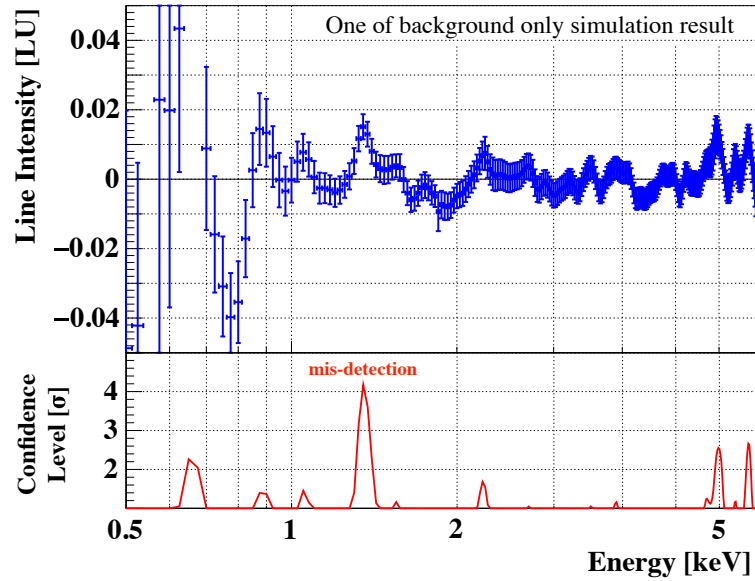
Figure 6.28   One of line search simulation results with a background (XDB) only mock spectrum. The Gaussian intensities with 1σ statistical error ranges are indicated by the blue crosses. The confidence level of detection (significance) was calculated by Gaussian intensity / its 1σ error range (red line). All signatures in this simulation result were caused by statistical fluctuation. In this simulation, $> 4\sigma$ confidence level of false detection (at 1.4 keV) is found.
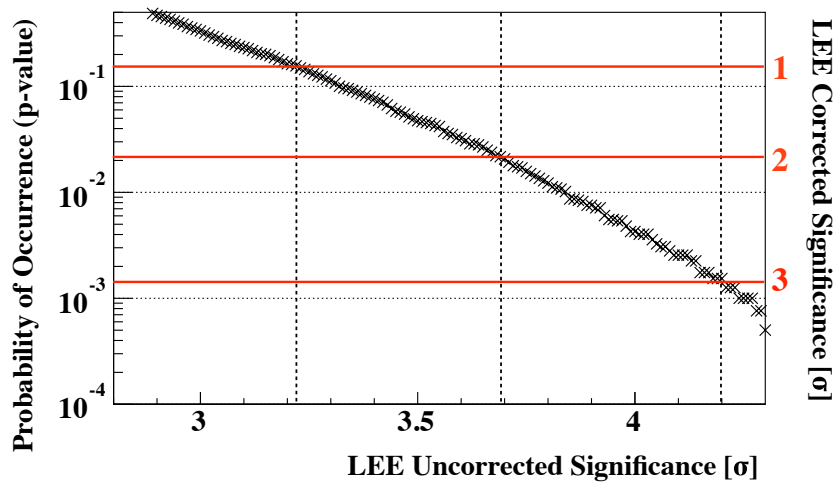
Figure 6.29   Upside cumulative distribution of all the 261×4000 significances in the 4000 simulations. The top 0.135 %, 2.28 % and 15.9 % of all (corresponding to the one-sided tail of p-value for 3.0σ, 2.0σ and 1.0σ) are distributed over 4.2σ, 3.7σ and 3.2σ, respectively.

6.7   Systematic uncertainty

We evaluated the systematic uncertainty in this line search. Three main causes of the systematic uncertainty are possible:

1. XDB model uncertainty.

2. XRT-XIS response function uncertainty.

3. NXB contribution uncertainty.

In this analysis, we carefully modeled the 25 stacked deep XDB spectra (detailed in Section 5.5, 6.3 and 6.4). As shown in Figure 6.22, these spectra were well expressed by [(the corrected responses) × (the XDB: Model 5 + five-instrumental lines)]. Owing to the low statistical uncertainty, these XDB models were firmly determined especially above 1 keV. Below 1 keV energy range (plasma-origin line forest region), we checked that a line search result was nearly-unchanged by change in the element abundance of plasma in the Milky Way (from ×1/2 to ×2). The XDB model uncertainty was considered to be sufficiently-small.

This line search was confirmed to be scarcely affected by a few % deviations of continuum contribution levels of XRT-XIS responses and NXB. However, it was affected by a few % mis-reproduction of the XRT-XIS responses (effective area) in the 1.5 – 3.5 keV with multiple absorption edges and of the instrumental line contributions. We corrected response mismatching with the stacked Crab spectra and removed the instrumental line contributions by spectral fitting. Uncertainties of these correction and removal should be evaluated and add to line intensity upper limits.

Although the biennial time variability of response mismatching (the stacked Crab spectra) was intended to be taken account, we could not distinguish its variability from its short term fluctuation. We assumed that standard deviations of the biennial response correction factors ware systematic uncertainties (Figure 6.30). In consideration of their systematic uncertainties, line intensity upper limits increase by $\sim 2 \times 10^{-3} - \sim 6 \times 10^{-3}$ LU in the 1.5 – 3.5 keV energy range (Figure 6.31).

Uncertainties of instrumental line intensities were derived from 187 night-Earth observations. We checked distributions of their instrumental line intensities and calculated their standard deviations (Figure 6.32 for example). Since Mn-Kα and Mn-Kβ line intensities should follow theoretical curves and decrease with the half-value period (~ 1000 days), we confirmed that they fitted with [initial intensity $\times (1/2)^{(\text{day from launch}/1000)}$] (Figure 6.33 for example). We estimated their systematic uncertainties from the square root of their photon count (standard error for Poisson counting especially in the case of the number of counts > 20). The five instrumental line intensities and their uncertainties were summarized in Table C.2. Influences of their uncertainties on the dark matter line search were shown in Figure 6.34.
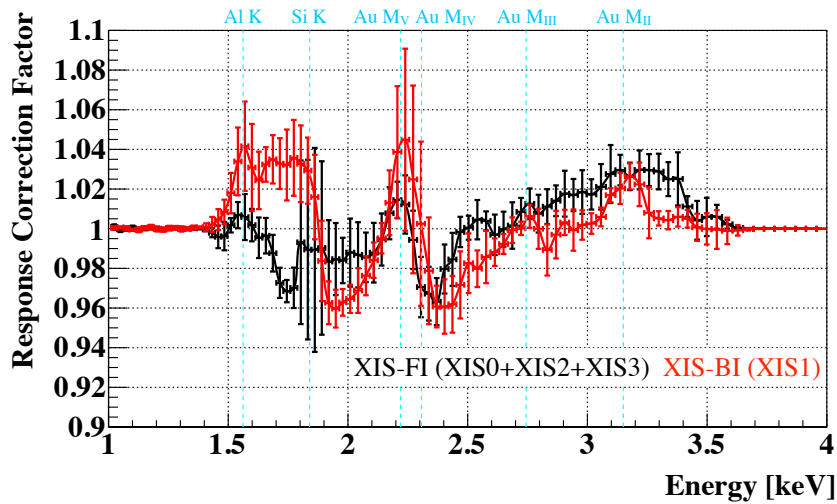
Figure 6.30   Averaged response correction factors of XIS-FI (XIS0+2+3; red crosses) and XIS-BI (XIS1; black crosses). The vertical error bars indicate their uncertainties (standard deviations).
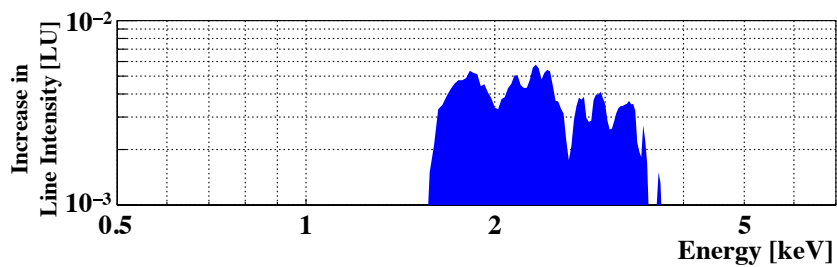
Figure 6.31   Influence of the response correction uncertainties on the dark matter line search as increase in line intensities.
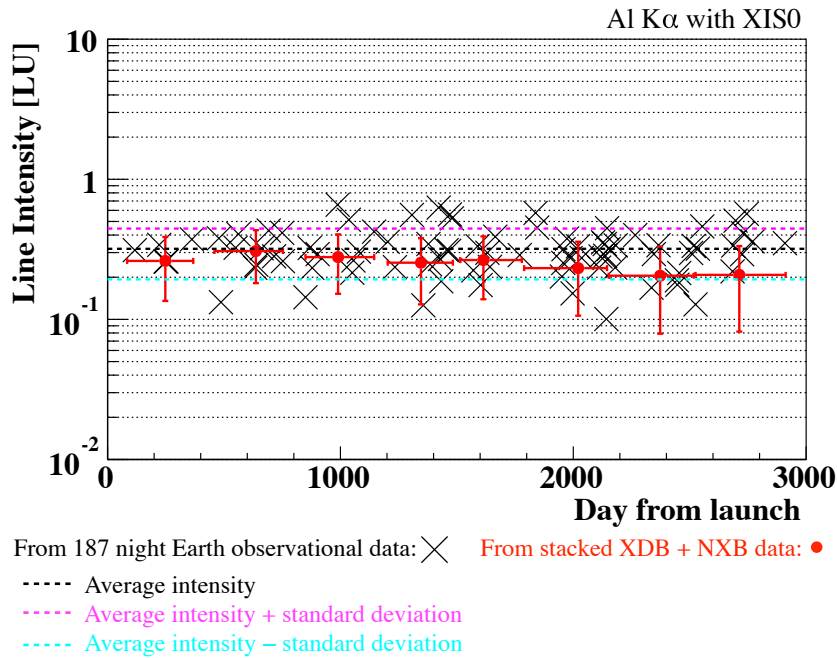
Figure 6.32   Distributions of instrumental line intensities from 187 night-Earth observations (Al-Kα lines with XIS0 for example; black crosses). The average intensity and average $\pm$ its uncertainty (standard deviation) are indicated by the black, magenta and cyan dashed lines, respectively. The instrumental line intensities from the 8-period stacked XDB + NXB data and their uncertainties derived from the night-Earth observations are plotted by the red crosses.
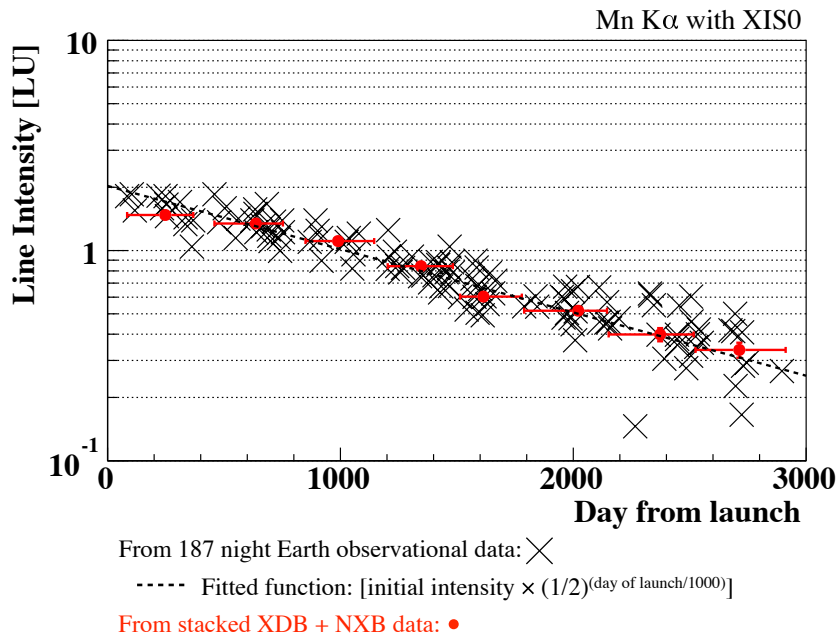
Figure 6.33   Same as Figure 6.32 but for Mn-Kα lines with XIS0. The fitted function: exponential attenuation with the half-value period $\sim$ 1000 days was indicated by the black dashed line. The instrumental line intensities from the 8-period stacked XDB + NXB data and their uncertainties derived from the square root of their photon count are plotted by the red crosses.
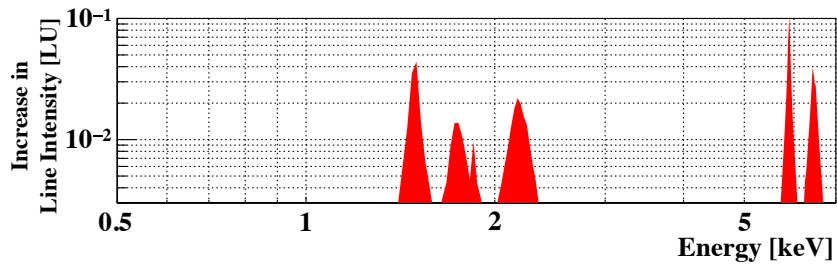
Figure 6.34   Influence of the instrumental line removal uncertainties on the dark matter line search as increase in line intensities.

6.8   Summary of this dark matter search

By analyzing the XDB with the best statistics and searching for a keV signature of dark matter with the careful corrections of systematic deviations (as summarized in Figure 6.35), we found five possible signatures in the $2.2 - 2.8\sigma$ confidence levels ($< 1\sigma$ after the LEE correction) as shown in Figure 6.36 and Table 6.1. Because of low confidence levels ($< 1\sigma$), we do not claim that they originate from dark matter.

We also obtained the upper limit on the dark matter line intensities in the $0.5 - 7.0$ keV range as shown in Figures 6.37 – 6.39. Figure 6.38 (the ratio of the line intensity upper limit and the XDB specific intensity) shows the upper limit on the equivalent width of dark matter line emission. Figure 6.39 (the ratio of the equivalent width upper limit and the energy resolution) indicates that this line search has high sensitivity enough to detect a $1 - 30$ % of bump above the weak XDB as line emission. We compared this result to previous results in next Chapter.

Table 6.1   Top five possible signatures whose LEE uncorrected confidence levels of detection are more than 2σ found in this line search.

Energy	Line intensity	Confidence level	
[keV]	[LU*]	LEE uncorrected	Corrected
0.600	1.7×10^{-1}	2.8σ	$< 1\sigma$
0.900	2.2×10^{-2}	2.2σ	$< 1\sigma$
1.275	9.5×10^{-3}	2.4σ	$< 1\sigma$
4.925	8.0×10^{-3}	2.8σ	$< 1\sigma$
5.475	8.7×10^{-3}	2.4σ	$< 1\sigma$

Notes.

$*$ LU (Line Unit) is photons $cm^{-2} \ s^{-1} \ sr^{-1}$.
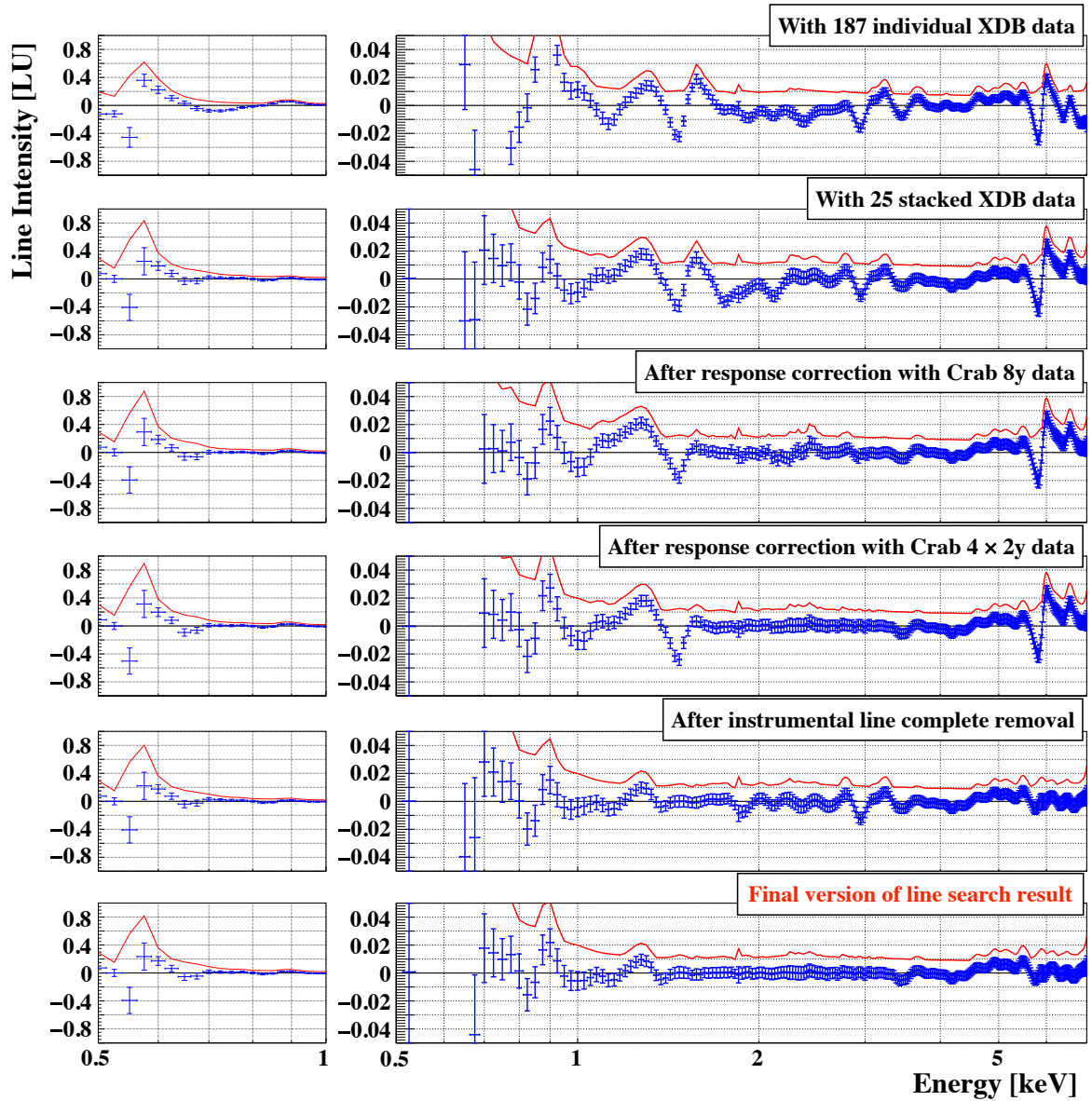
Figure 6.35 Line search results of all improvement steps. The line intensities and their 1σ statistical error ranges are indicated by the blue crosses. The 3σ upper limits on dark matter line intensities are represented by the red lines. The final version of this line search result was derived with the 25 stacked XDB energy spectra and their models [(the corrected responses: from the every-2-year stacked Crab energy spectra) × (the XDB: Model 5 + five-instrumental lines)].
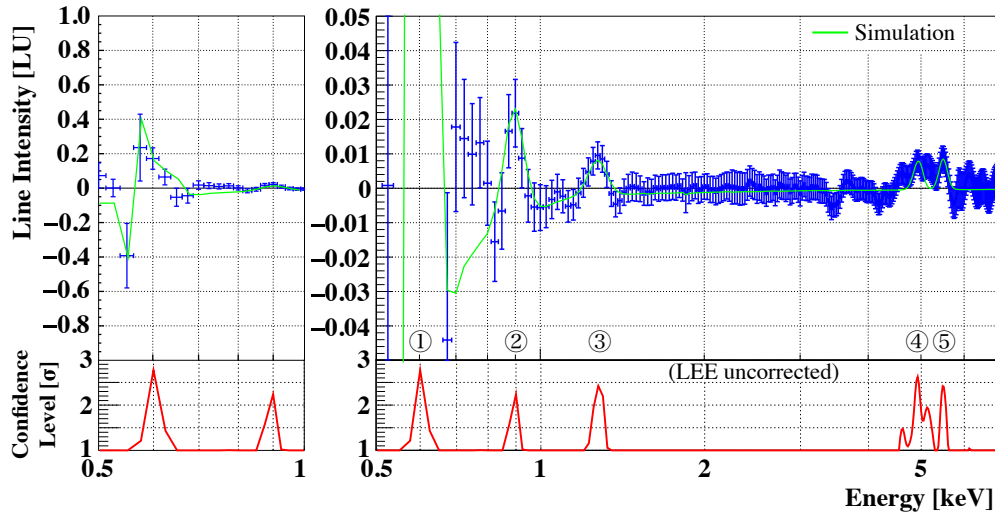
Figure 6.36   Final version of this line search result. Top panel: expected dark matter line intensities and their statistical errors by the XDB observational spectra at the 261 energies in the 0.5 – 7.0 keV range. The expected dark matter line intensities and their 1σ statistical error ranges are indicated by the blue crosses (shown in Figure 6.24). The simulated signatures of the line search without statistical and systematic uncertainties in the case of presence of 0.600, 0.900, 1.275, 4.925 and 5.475 keV lines as shown in Figure 6.27 are represented by the green lines. Bottom panel: five possible signatures and their LEE uncorrected confidence levels (significances) of line detection (red lines).
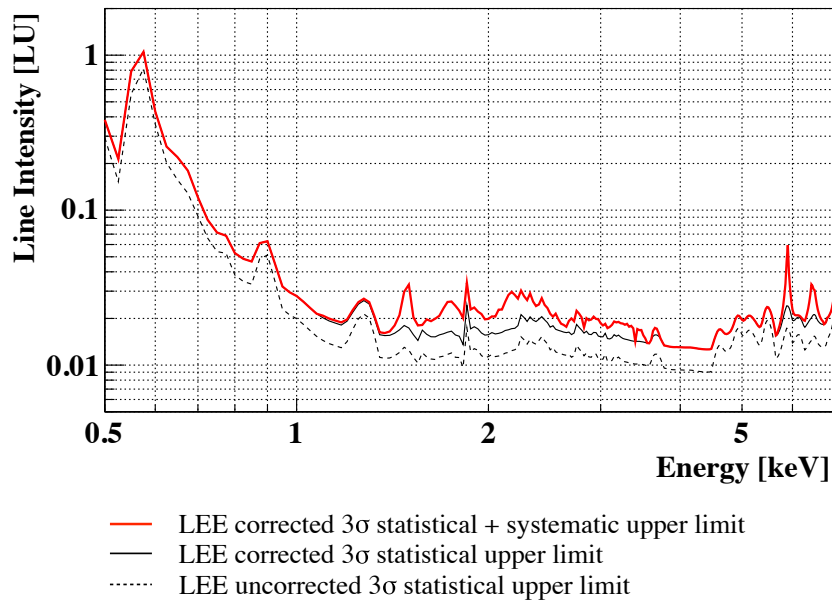
Figure 6.37   Upper limit on dark matter line intensities. The LEE corrected and uncorrected 3σ upper limits are indicated by the black dashed and dotted lines, respectively. The LEE corrected 3σ statistical + systematic upper limit is represented by the red lines.
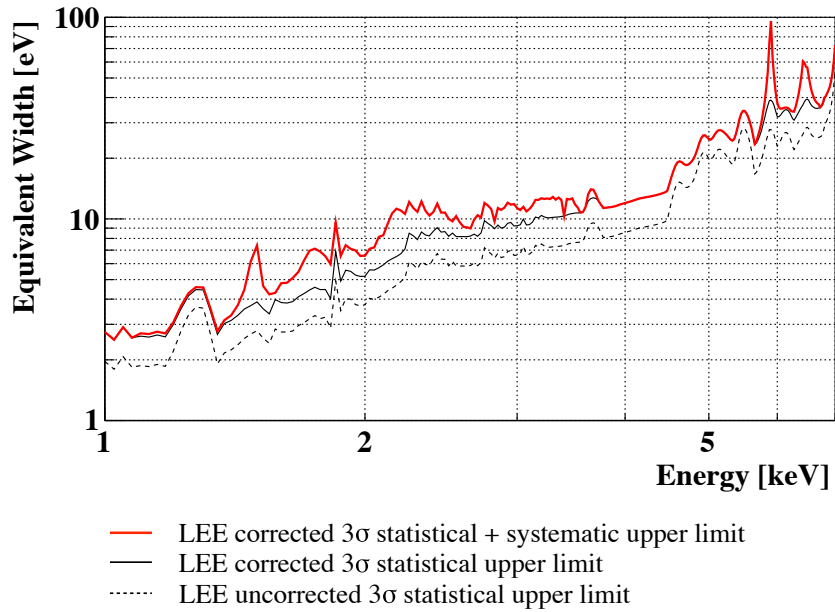
Figure 6.38   Upper limit on the equivalent width of dark matter line emission. The LEE corrected and uncorrected 3σ upper limits are indicated by the black dashed and dotted lines, respectively. The LEE corrected 3σ statistical + systematic upper limit is represented by the red lines.
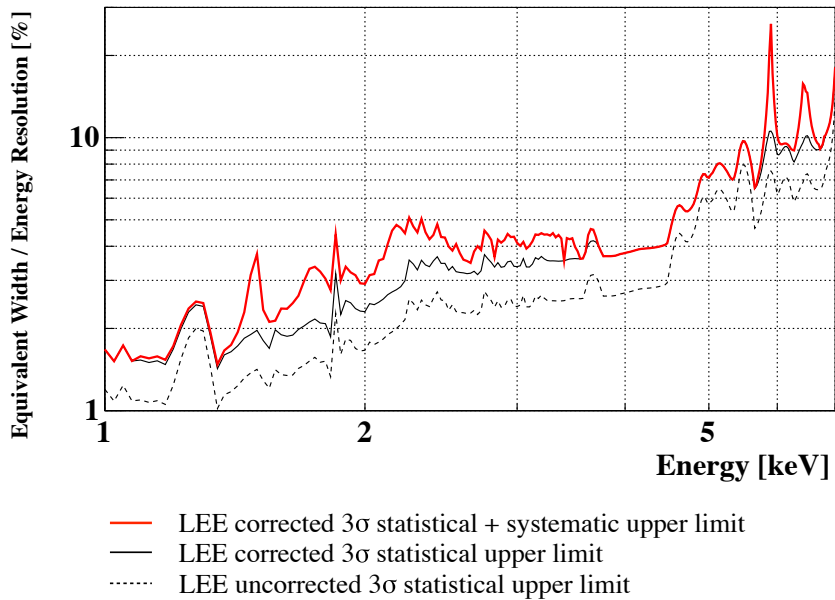
Figure 6.39   Upper limit on the ratio of the equivalent width and the energy resolution (defined as 5.2σ, 2.2 times FWHM, to collect 99 % of photons in the Gaussian line). This ratio indicates the resolution to detect line as percentage of the XDB intensity. The LEE corrected and uncorrected 3σ upper limits are indicated by the black dashed and dotted lines, respectively. The LEE corrected 3σ statistical + systematic upper limit is represented by the red lines.

7 Discussion

7.1 Origin of possible signatures in this dark matter search

In this dark matter line search, we found five possible signatures as shown in Figure 6.36 and Table 6.1. As previously mentioned, we do not claim that they originate from dark matter because of low confidence levels ($< 1\sigma$ of LEE corrected confidence levels), although these are consistent with presence of narrow (width ~ 0 eV) lines. Except for a line-like signature at 0.900 keV, these signatures irregularly appeared and disappeared by the observational date and directions (as shown in Figures 6.3 – 6.12). The 0.600, 1.275, 4.925 and 5.475 keV signatures probably appeared by statistical fluctuation. In this study, we also mentioned increasing tendency of the 0.900 keV line intensity with increasing the mass column density in the Milky Way from the dependence on the angle from the Galactic center and the Galactic latitude as shown in Figures 6.9 and 6.11. This signature is similar to neutral or low-ionized Ne lines (centroids: > 0.849 keV) which are possibly from the exosphere of the Earth or the interstellar medium of the Milky Way.

7.2 3.5 keV line interpretation

The unidentified 3.5 keV line was reported by previous studies described in Chapter 2 (e.g. Bulbul et al., 2014; Boyarsky et al., 2014). According to Bulbul et al. (2014), the average dark matter column density of the clusters of galaxies used in that analysis is 182 $M_\odot$ pc^{-2}. On the other hand, the exposure-time-weighted average of dark matter column density in this work (Figure 7.1) is 51 $M_\odot$ pc^{-3} from the rotation curve as the most pessimistic case (while 63 $M_\odot$ pc^{-3} from the NFW model, described in Chapter 3). When the target moves from the clusters to the Milky Way, the dark matter column density decrease by 72 % (182 $M_\odot$ pc^{-2} to 51 $M_\odot$ pc^{-2}) and the 3.5 keV line intensity as they claimed becomes 1.1×10^{-2} LU which is more or less the same as our upper limit of 1.0×10^{-2} (the LEE corrected value is 1.3×10^{-2}). However we did not detect such line. This result is consistent with the stacked spectral analysis of the Perseus cluster by using Suzaku XIS observational data (Tamura et al., 2014). This was probably caused by systematic uncertainties peculiar to XMM-Newton and Chandra and/or spectral model uncertainties such as absence (or underestimation) of atomic lines reported by Tamura et al. (2014) and Carlson et al. (2015).
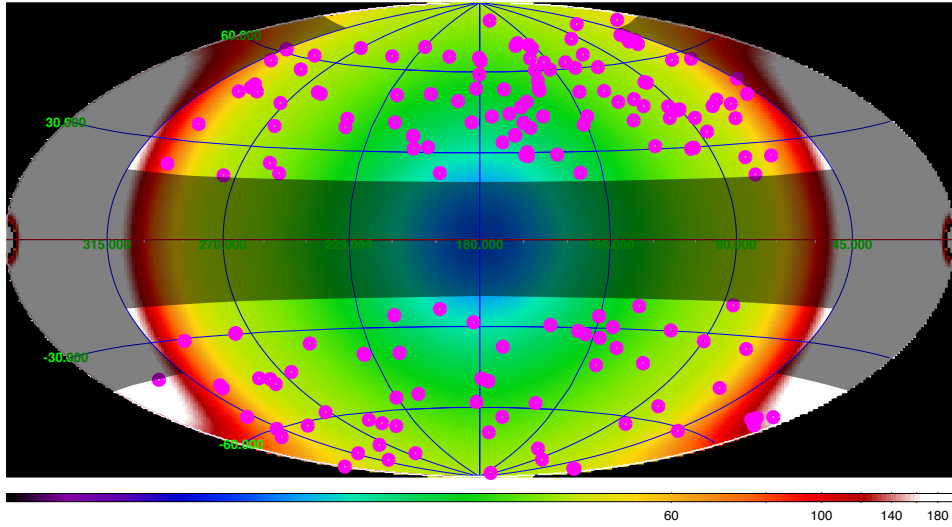
Figure 7.1   Column density map derived from the rotation curve. This map is described
with the Galactic coordinate system centered at the Galactic anti-center. The color scale
indicates dark matter column densities in unit of $M_\odot$ pc^{-2}. The grey shaded regions
were not used for this dark matter line search. The regions we analyzed for this search
are indicated by the pink circles.

7.3   Upper limit on dark matter line intensities

In this thesis, we obtained the upper limit on the intensities of X-ray line emission from dark
matter in the 0.5 – 7.0 keV energy range as shown in Figures 6.37 – 6.39. We compared the
upper limit on dark matter line intensities normalized by their column densities in this work
with that of previous works in Figure 7.2. The dark matter line intensity normalized by its
column density is indifferent value for the target of the dark matter search and corresponds
to the ratio of the dark matter decay rate and its mass. We confirmed that upper limit
obtained by this work is tightest of all the dark matter line search so far.
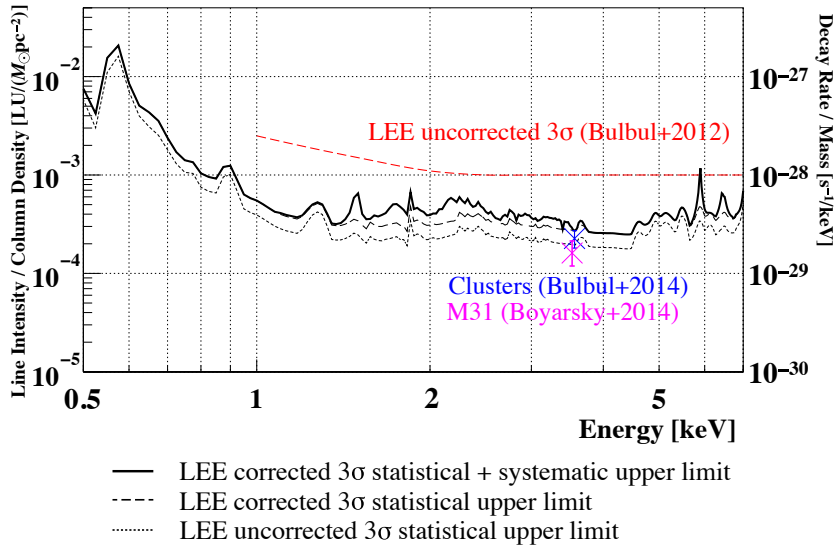
Figure 7.2   Upper limits on the dark matter line intensities normalized by their column densities corresponding to the ratio of dark matter decay rates and their masses. We assumed that the column density for this work was 50.75 $M_\odot$ pc^{-3} from the rotation curve. The LEE corrected and uncorrected 3σ upper limits are indicated by the black dashed and dotted lines. The LEE corrected 3σ statistical + systematic upper limit are represented by the black solid line. The typical 3σ upper limit by previous works (LEE uncorrected; Boyarsky et al., 2012) is indicated by the red line. The possible 3.5 keV line (Bulbul et al., 2014; Boyarsky et al., 2014) are plotted by the blue and magenta crosses.

7.4   Constraints for sterile neutrinos as dark matter candidates

Sterile neutrinos are possible candidates of dark matter described in Chapter 2. Through their mixing with the active neutrinos, the sterile neutrino possibly decay into an active neutrino and a photon whose energy is half of the sterile neutrino mass. If the sterile neutrinos account for a part of (or all) dark matter, we have potential to detect these photons. From Eq.2.1 in Chapter 2 and Eq.3.1 in Chapter 3, the line intensity of their radiative decay ($I = F/\Omega$) is

$$I = 1.3 \times 10^{-5} \left(\frac{m_{\rm s}}{1\ {\rm keV}}\right)^4 \left(\frac{\sin^2 2\theta}{10^{-10}}\right) \left(\frac{f_{\rm s}}{1}\right) \left(\frac{S_{\rm DM}}{10^2 M_\odot {\rm pc}^{-2}}\right)\ {\rm photons\ cm}^{-2}\ {\rm s}^{-1}\ {\rm sr}^{-1}, \quad (7.1)$$

where $f_{\rm s}$ is a fraction of $\nu_{\rm s}$ in dark matter. With Eq.7.1, we obtained the constraints on their masses and mixing angles as shown in Figures 7.3 and 7.4. It is also the tightest constraints of all the sterile neutrino line search.
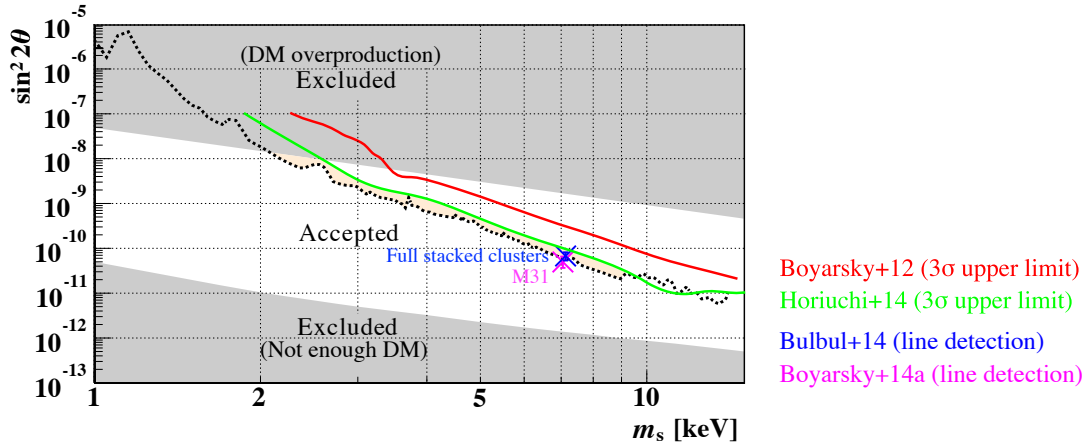
Figure 7.3   Comparison of constraints on (allowed region of) the sterile neutrino masses m_s and mixing angles $\sin^2 2\theta$ by previous works and this work. Their LEE uncorrected 3σ bounds by Boyarsky et al. (2012) (red line), Horiuchi et al. (2014) (yellowish green line) and this work (black dotted line) are indicated. The region above the black dotted line is excluded and the orange shaded region is newly excluded region by this work. The cross marks indicate the parameters (m_s and $\sin^2 2\theta$) derived from the energy and intensities of the lines found by Bulbul et al. (2014) and Boyarsky et al. (2014) if they originate from the sterile neutrinos. The grey shaded regions and the region below 1 keV are ruled out (detailed in Figure 2.2).
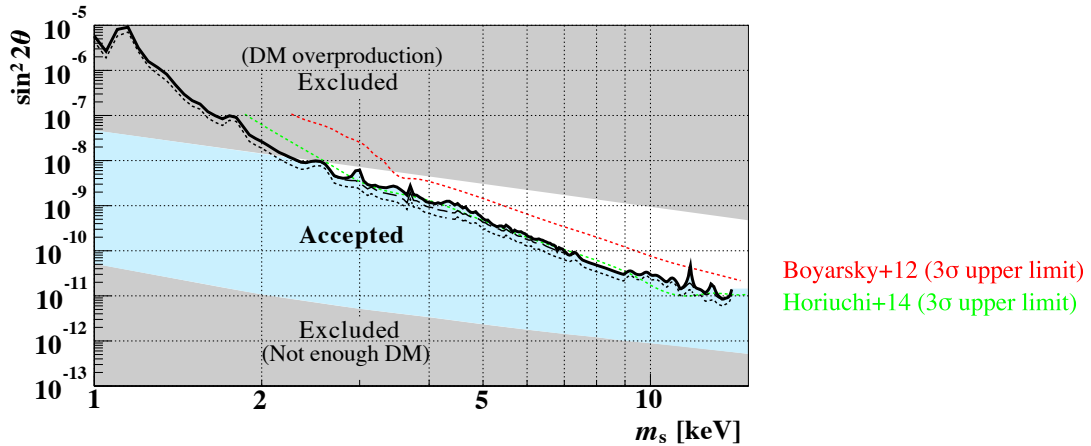
Figure 7.4   Conclusive constraints on the sterile neutrino masses and mixing angles by this work. The LEE corrected 3σ statistical + systematic bound and allowed region are indicated by the black solid line and the cyan shaded region, respectively.

7.5 Future prospects

We conducted the most sensitive search for dark matter line emission by the existing X-ray observatories. In the future, progressive instruments such as X-ray micro-calorimeters with the eV-level energy resolution and large FoV telescopes will be introduced to X-ray observational satellites, and more sensitive dark matter searches will be performed. As near future mission, we focused on the Soft X-ray Spectrometer (SXS) of the ASTRO-H satellite (Takahashi et al., 2010; Mitsuda et al., 2014) and the extended ROentgen Survey with an Imaging Telescope Array (eROSITA) telescope and the PN-CCD camera module of the Spektrum-Roentgen-Gamma (SRG) satellite (Predehl et al., 2014; Meidinger et al., 2014). In Table 7.1, we summarized the notable characters of the ASTRO-H SXS and the SRG eROSITA-PNCCD. The ASTRO-H SXS is an X-ray micro-calorimeter with doped semiconductor thermistors and has the highest energy resolution ever utilized (except for grating instrument only for point sources), although its grasp is lower than that of the existing X-ray observatories. On the other hand, the SRG eROSITA-PNCCD has the largest grasp and all sky survey plan which is suitable for deeper analysis of the XDB, although its energy resolution of the PNCCD is modest. Especially in the ASTRO-H SXS with the high line identification ability by the eV-level energy resolution, it is suitable for the weak line search with "dense" targets such as clusters of galaxies and nearby galaxies although their background plasma emission are strong. In estimating the 3σ line detection limits normalized by their column densities as shown in Figure 7.5, the dark matter line search with ASTRO-H SXS observations of the M31 will be the most sensitive way in these options (instruments: the ASTRO-H SXS or the Suzaku XIS, targets: the XDB, the M31 or the Perseus) under the same FoV and exposure time. The future X-ray observations will give a tighter constraint on dark matter conditions and may reveal the dark matter nature.
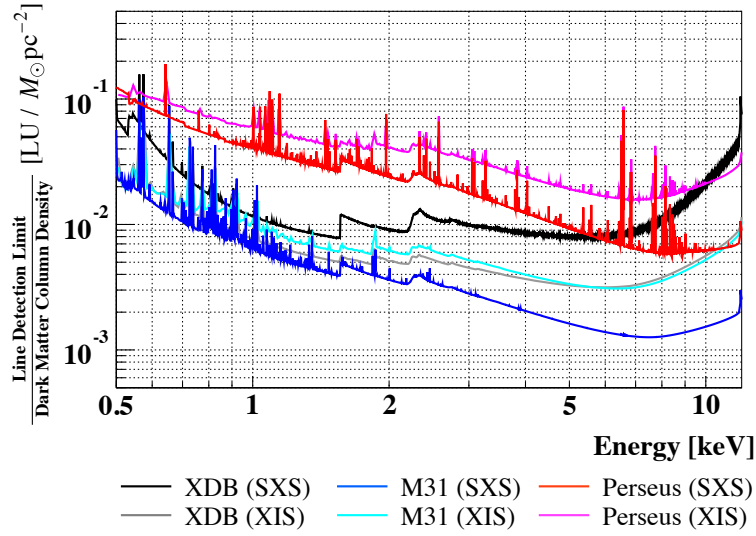
Figure 7.5 3σ line detection limits normalized by their column densities for various targets (the XDB, the M31 and the Perseus) with the Suzaku XIS and the ASTRO-H SXS, $3' \times 3'$ of FoV and 100 ksec of exposure time.

Table 7.1   Characters of the ASTRO-H SXS and the SRG eROSITA-PNCCD (the Suzaku XIS for comparison).

Satellite	Suzaku	ASTRO-H	SRG
CCD instrument	XIS	SXS	eROSITA-PNCCD
Field of view*	17.8×17.8×(3FI+1BI)	3.05×3.05	3000
Angular resolution†	110(FI), 140(BI)	80	15
Energy range‡	0.2 − 12	0.2 − 12	0.2 − 10
Energy resolution§	50 − 200	5	50 − 200
Effective area‖	660(3FI), 320(BI)	230	1400
NXB rate♯	1 − 10(stable)	< 10(stable)	< 10(stable)

Notes.

∗ In unit of arcmin².

† Half power diameter in unit of arcmin.

‡ In unit of keV.

§ FWHM in unit of eV.

‖ At 1 keV in unit of cm².

♯ In unit of cm^{-2} s^{-1} sr^{-2} keV^{-1}.

8 Conclusion

In this thesis, we searched for X-ray line emission from dark matter associated with the Milky Way by using multiple Suzaku XIS observational data of the X-ray Diffuse Background (XDB). This is the most sensitive method for a keV signature search of dark matter which capitalizes on the Suzaku XIS advantages: wide energy range, large effective area and field of view, high energy resolution for diffuse X-ray emission and the lowest and most-stable Non-X-ray Background (NXB). The process flow of our search is described below (detailed in Chapter 5 and 6).

1. We selected 187 Suzaku XIS data sets of blank sky field observations from 2005 to 2013 and performed data reduction with careful removal of contaminant X-ray emission of resolvable point sources, the Earth's atmosphere and NXB contributions.

2. We analyzed the 187 individual spectra in the $0.5 - 7.0$ keV energy range and checked to fit them with the typical XDB emission model: an unabsorbed optically-thin thermal collisionally-ionized (CIE) plasma emission model for the Heliospheric Solar Wind Charge Exchange and the Local Hot Bubble ($kT \sim 0.1$ keV), an absorbed optically-thin thermal CIE plasma emission model for the Milky Way Halo ($kT = 0.1 - 0.4$ keV), and a power-law emission model for unresolved extragalactic point sources (CXB; Cosmic X-ray Background). Additional hot plasma emission ($kT = 0.4 - 1.2$ keV) and O I fluorescent line emission from the Earth's exosphere were partially found. No other component as reasonable continuum X-ray emission in the $0.5 - 7.0$ keV energy range was required.

3. In order to lower the statistical uncertainty, we stacked the XDB spectra. We analyzed the 25 stacked XDB spectra in the $0.5 - 7.0$ keV energy range and determined the best-fit XDB model. This has been the deepest analysis of the XDB. As a result, we decided to use the defined XDB emission model: a three-temperature plasma emission and an index-free-power-law CXB emission model (including O I fluorescent line contribution) as the best-fit XDB model.

4. In order to check the accuracy of the XRT-XIS responses reproduced by the Suzaku calibration database and ray-tracing simulation, we utilized the stacked spectra of the Crab Nebula observational data with the lowest statistical uncertainty of all Suzaku XIS data. We found and corrected response mismatching of up to ~ 10 %, especially in the $1.5 - 3.5$ keV energy range (corresponding to the energy region with multiple absorption edges in the XRT-XIS effective area).

5. We found small residuals between some stacked XDB spectra and their model around

the energies at which the instrumental lines arise. We carefully estimated and completely removed the instrumental line contributions from the stacked XDB spectra by spectral fitting with a five-Gaussian model.

6. The significance (confidence level of detection) was evaluated by considering the "look elsewhere effect" (LEE). In this dark matter line search, the LEE uncorrected significance of 4.2σ was used as the LEE corrected 3σ.

7. We searched for non-baryonic line emission in the stacked XDB spectra by spectral fitting with [(the corrected response by using the stacked Crab spectra) $\times$ (the best-fit XDB + five-instrumental lines + one-Gaussian model)]. The Gaussian center energy was fixed and swept over the $0.5 - 7.0$ keV energy range. We determined the line intensities and their statistical and systematic uncertainties.

By analyzing the XDB with the best statistics and searching for a keV signature of dark matter with careful corrections of systematic deviations, we obtained the following results.

1. We found five line-like signatures as shown in Table 6.1 in Chapter 6. Because of low confidence levels ($< 1\sigma$ after the LEE correction), we do not claim that they originate from dark matter. The 0.900 keV signature is possibly from Ne in the exosphere of the Earth or the interstellar medium of the Milky Way.

2. We did not detect the possible dark matter line at 3.5 keV reported by previous studies (e.g. Bulbul et al., 2014). This result is consistent with the stacked spectral analysis of the Perseus cluster by using Suzaku XIS observational data (Tamura et al., 2014).

3. We obtained the tightest upper limit on the intensities of X-ray line emission from dark matter in the $0.5 - 7.0$ keV energy range as shown in Figure 7.2 in Chapter 7.

4. Assuming sterile neutrinos as dark matter, we tightened the constraints on their masses and mixing angles as shown in Figure 7.3 in Chapter 7.

A Details of Suzaku XIS observations of the XDB

In this thesis, we selected and analyzed the 187 Suzaku XIS observational data of the XDB from 2005 to 2013. Their observational logs (e.g. observational date, exposure time) and their aim points were summarized in Tables A.1 and A.2.

We extracted their X-ray images with XIS1 of the XDB in the 0.5 – 5.0 keV range as shown in Figures A.1 – A.11.

The spectral fitting results of the 187 individual XDB data sets were summarized in Table A.3.

Table A.1: Suzaku XIS observational logs of the XDB.

ID	Field Name	Obs. ID	Date(Day from launch)[*]	Exposure[†]	SCI(XIS0,1,2,3)[‡]
1	A2218_offset	100030020	2005/10/02(84)	158.4	(off,off,off,off)
2	MKN_3	100040010	2005/10/22(104)	180.4	(off,off,off,off)
3	SWIFT_J0746.3+2548	700011010	2005/11/04(117)	321.3	(off,off,off,off)
4	HIGH_LAT._DIFFUSE_A	500027010	2006/02/14(219)	100	(off,off,off,off)
5	HIGH_LAT._DIFFUSE_B	500027020	2006/02/17(222)	110.8	(off,off,off,off)
6	SKY_50.0_–62.4	501001010	2006/03/01(234)	238.4	(off,off,off,off)
7	SKY_53.3_–63.4	501002010	2006/03/03(236)	246.8	(off,off,off,off)
8	NGC_2403	800021010	2006/03/16(249)	219.2	(off,off,off,off)
9	DRACO_HVC_REGION_A	501004010	2006/03/20(253)	205.2	(off,off,off,off)
10	DRACO_HVC_REGION_B	501005010	2006/03/22(255)	211.2	(off,off,off,off)
11	IRAS08572+3915	701053010	2006/04/14(278)	214.4	(off,off,off,off)
12	LOCKMAN_HOLE	101002010	2006/05/17(311)	140	(off,off,off,off)
13	KAZ_102	701012010	2006/06/09(334)	121.1	(off,off,off,off)
14	M106	701095010	2006/06/10(335)	332	(off,off,off,off)
15	MRK_273	701050010	2006/07/07(362)	245.2	(off,off,off,off)
16	NGC4418	701001010	2006/07/13(368)	170	(off,off,off,off)
17	APM_08279+5255	701057010	2006/10/12(459)	105.3	(on,2,–,on)
18	UGC5101	701002020	2006/10/31(478)	87	(on,2,–,on)
19	APM_08279+5255	701057020	2006/11/01(479)	233.4	(on,2,–,on)
20	DRACO_ENHANCEMENT	501101010	2006/11/09(487)	86.4	(off,off,–,off)
21	IRASF11223–1244	701008010	2006/11/25(503)	108.6	(on,6,–,on)
22	3EGJ1234_1318_2	801032010	2006/12/12(520)	63.6	(on,2,–,on)
23	MRK_1	701047010	2007/01/11(550)	274.8	(on,2,–,on)
24	SWIFT_J0255.2–0011	701013010	2007/01/23(562)	226.5	(on,2,–,on)
25	APM_08279+5255	701057030	2007/03/24(622)	248.1	(on,2,–,on)
26	URSA_MINOR	802052010	2007/04/05(634)	157.8	(on,2,–,on)
27	DRACO	802051010	2007/04/06(635)	138.3	(on,2,–,on)

Continued from previous page.

ID	Field Name	Obs. ID	Date(Day from launch)[*]	Exposure[†]	SCI(XIS0,1,2,3)[‡]
28	OJ_287_QUIESCENT	702009010	2007/04/10(639)	203.4	(on,2,–,on)
29	LOCKMANHOLE	102018010	2007/05/03(662)	247.8	(on,2,–,on)
30	LOW_LATITUDE_86–21	502047010	2007/05/09(668)	171	(on,2,–,on)
31	3C_445	702056010	2007/05/25(684)	284.7	(on,2,–,on)
32	NGC_4395	702001010	2007/06/02(692)	232.8	(on,2,–,on)
33	ARC2	502071010	2007/06/05(695)	250.8	(on,2,–,on)
34	47_TUCANAE	502048010	2007/06/10(700)	293.4	(on,2,–,on)
35	BOOTES_GROUP_30	802056010	2007/06/25(715)	96	(on,2,–,on)
36	NGC_1052	702058010	2007/07/16(736)	208.2	(on,2,–,on)
37	NGC_1142	702079010	2007/07/21(741)	94.2	(on,2,–,on)
38	ERIDANUS_HOLE	502076010	2007/07/30(750)	264.3	(on,2,–,on)
39	ESO_506–G027	702080010	2007/08/02(753)	84.6	(on,2,–,on)
40	OJ_287_FLARE	702008010	2007/11/07(850)	147	(on,2,–,on)
41	NGC_1553	802050010	2007/11/25(868)	205.5	(on,2,–,on)
42	BOOTES_GROUP_1	802054010	2007/12/06(879)	102	(on,2,–,on)
43	NGC_4507	702048010	2007/12/20(893)	230.4	(on,2,–,on)
44	MS_1512.4+3647	802034010	2007/12/29(902)	463.8	(on,2,–,on)
45	1RXS_J180340.0+40121	402009010	2008/01/13(917)	101.1	(on,2,–,on)
46	ARC1	502070010	2008/01/15(919)	261.3	(on,2,–,on)
47	BZ_UMA	402046010	2008/03/24(988)	79.1	(on,2,–,on)
48	VICINITY_OF_PKS_2155–1	503082010	2008/04/29(1024)	143.7	(on,2,–,on)
49	VICINITY_OF_PKS_2155–2	503083010	2008/05/02(1027)	148.8	(on,2,–,on)
50	NGC_7130	703012010	2008/05/11(1036)	82.5	(on,2,–,on)
51	LOCKMANHOLE	103009010	2008/05/18(1043)	127.5	(on,2,–,on)
52	SWIFT_J0134.1–3625	703016010	2008/05/20(1045)	108.6	(on,2,–,on)
53	NGC_3079	803039020	2008/05/26(1051)	187.2	(on,2,–,on)
54	SWIFT_J1200.8+0650	703009010	2008/05/31(1056)	198	(on,2,–,on)
55	NGC_5347	703011010	2008/06/10(1066)	98.1	(on,2,–,on)
56	SWIFT_J0959.5–2258	703013010	2008/06/18(1074)	111	(on,2,–,on)
57	BOOTES_GROUP_37	803044010	2008/06/23(1079)	111.3	(on,2,–,on)
58	NGC_788	703032010	2008/07/13(1099)	113.4	(on,2,–,on)
59	MCG–02–14–009	703060010	2008/08/28(1145)	353.7	(on,2,–,on)
60	SWIFT_J0911.2+4533	703008010	2008/10/25(1203)	141	(on,2,–,on)
61	Q0827+243	703003010	2008/10/27(1205)	101.4	(on,2,–,on)
62	AM_HERCULES	403007010	2008/10/29(1207)	248.7	(on,2,–,on)
63	AM_HERCULES_BGD	403008010	2008/11/01(1210)	108	(on,2,–,on)
64	NGC3556	803013010	2008/11/25(1234)	214.5	(on,2,–,on)
65	NGC_1313	703010010	2008/12/05(1244)	161.7	(on,2,–,on)
66	IGR_J12391–1612	703007010	2008/12/18(1257)	229.8	(on,2,–,on)
67	NGC_253_OFFSET	803004010	2008/12/29(1268)	137.4	(on,2,–,on)
68	ARC_BACKGROUND	503104010	2008/12/30(1269)	318.8	(on,2,–,on)
69	BOOTES_GROUP_32	803045010	2009/02/06(1307)	88.8	(on,2,–,on)
70	RCS0442–2815	803060010	2009/03/13(1342)	112.8	(on,2,–,on)
71	J081618.99+482328.4	703042010	2009/03/27(1356)	231.9	(on,2,–,on)
72	IC_2497	704053010	2009/04/18(1378)	160.8	(on,2,–,on)

Continued from previous page.

ID	Field Name	Obs. ID	Date(Day from launch)*	Exposure†	SCI(XIS0,1,2,3)‡
73	NGC_4686	704015010	2009/04/25(1385)	92.1	(on,2,–,on)
74	SWIFT_J0904.3+5538	704027010	2009/04/28(1388)	84.9	(on,2,–,on)
75	NGC_454	704009010	2009/04/29(1389)	265.2	(on,2,–,on)
76	MKN_279	704031010	2009/05/14(1404)	385.2	(on,2,–,on)
77	SDSS_J0943+5417	704052010	2009/05/24(1414)	84	(on,2,–,on)
78	NGC4102	704057010	2009/05/30(1420)	260.4	(on,2,–,on)
79	FERMI_0291	804019010	2009/06/01(1422)	102.9	(on,2,–,on)
80	UGC_12741	704014010	2009/06/07(1428)	108.3	(on,2,–,on)
81	LOCKMAN_HOLE	104002010	2009/06/12(1433)	182.4	(on,2,–,on)
82	NGC_669	804049010	2009/07/05(1456)	95.1	(on,2,–,on)
83	EUVE_J0317–85.5	404019010	2009/07/16(1467)	126.9	(on,2,–,on)
84	2MASX_J02485937+2630	704013010	2009/07/18(1469)	94.7	(on,2,–,on)
85	HD6903	404034010	2009/07/19(1470)	70.8	(on,2,–,on)
86	FERMI_0265	804017020	2009/07/28(1479)	114.3	(on,2,–,on)
87	NGC1194	704046010	2009/08/01(1483)	127.5	(on,2,–,on)
88	IRAS_04507+0358	704058010	2009/09/01(1514)	199.8	(on,2,–,on)
89	NGC_4125	804047010	2009/09/29(1542)	203.1	(on,2,–,on)
90	NGC_3718	704048010	2009/10/24(1567)	144.3	(on,2,–,on)
91	NGC3516	704062010	2009/10/28(1571)	485.4	(on,2,–,on)
92	NGC_4138	704047010	2009/11/02(1576)	134.4	(on,2,–,on)
93	HD72779	404035010	2009/11/06(1580)	164.7	(on,2,–,on)
94	MRK_421_OFFSET	504086010	2009/11/09(1583)	169.2	(on,2,–,on)
95	MRK_421_OFFSET	504087010	2009/11/11(1585)	223.5	(on,2,–,on)
96	SEP_#1	504069010	2009/11/14(1588)	72.9	(on,2,–,on)
97	NEP_#1	504070010	2009/11/15(1589)	141.9	(on,2,–,on)
98	IGR_J22517+2218	704060010	2009/11/26(1600)	105.3	(on,2,–,on)
99	A1246_OFF	804029010	2009/11/28(1602)	168.9	(on,2,–,on)
100	SEP_#2	504071010	2009/12/05(1609)	96	(on,2,–,on)
101	NEP_#2	504072010	2009/12/07(1611)	127.2	(on,2,–,on)
102	SEP_#3	504073010	2009/12/14(1618)	86.1	(on,2,–,on)
103	NEP_#3	504074010	2009/12/15(1619)	102	(on,2,–,on)
104	VICINITY_OF_NGC_4051	504062010	2009/12/19(1623)	208.9	(on,2,–,on)
105	SEP_#4	504075010	2009/12/27(1631)	105.3	(on,2,–,on)
106	NEP_#4	504076010	2009/12/28(1632)	127.5	(on,2,–,on)
107	RCS1620+3046	804081010	2010/01/07(1642)	99	(on,2,–,on)
108	MRK_573	704002010	2010/01/21(1656)	165	(on,2,–,on)
109	PKS_0326–288	704039010	2010/01/30(1665)	123.9	(on,2,–,on)
110	DA_240_EAST_LOBE	704020010	2010/03/19(1713)	183.9	(on,2,–,on)
111	LEDA_84274	705023010	2010/05/15(1770)	97.2	(on,2,–,on)
112	NGC_3147	705054010	2010/05/24(1779)	241.2	(on,2,–,on)
113	MCG–03–58–007	705052010	2010/06/03(1789)	227.7	(on,2,–,on)
114	ABELL_115_OFFSET	805078010	2010/07/22(1838)	166.8	(on,2,–,on)
115	FILAMENT_OF_GALAXIES	805029010	2010/07/29(1845)	179.7	(on,2,–,on)
116	1150+497	705003010	2010/11/12(1951)	228.3	(on,2,–,on)
117	NGC2841	805028010	2010/11/18(1957)	194.4	(on,2,–,on)

Continued from previous page.

ID	Field Name	Obs. ID	Date(Day from launch)*	Exposure†	SCI(XIS0,1,2,3)‡
118	L168_B53	505058010	2010/11/19(1958)	128.1	(on,2,–,on)
119	RCS2343–3517	805088010	2010/11/23(1959)	94.2	(on,2,–,on)
120	RCS2318–0024	805089010	2010/11/26(1965)	117.6	(on,2,–,on)
121	IRAS_12072–0444	705045010	2010/12/04(1973)	118.5	(on,2,–,on)
122	ESP_39607	705048010	2010/12/19(1988)	78.9	(on,2,–,on)
123	IRAS_00397–1312	705046010	2010/12/28(1997)	101.7	(on,2,–,on)
124	NGC_720_OFFSET	805069010	2010/12/30(1999)	333.3	(on,2,–,on)
125	L139_B–32	505044010	2011/01/08(2008)	202.2	(on,2,–,on)
126	IRAS_01250+2832	705024010	2011/01/10(2010)	144.9	(on,2,–,on)
127	NGC_1332	805095010	2011/01/20(2020)	206.4	(on,2,–,on)
128	EG_AND	405034010	2011/02/05(2036)	216.3	(on,2,–,on)
129	A478_OFFSET_D	805004010	2011/02/20(2051)	116.1	(on,2,–,on)
130	FILAMENT_JUNCTION_3	806005010	2011/04/21(2111)	120.6	(on,2,–,on)
131	SPT–CL_J2337–5942	806073010	2011/04/23(2113)	79.5	(on,2,–,on)
132	MRK_231	706037010	2011/04/27(2117)	349.2	(on,2,–,on)
133	RCS211853–6334.5	806079010	2011/05/08(2128)	140.1	(on,2,–,on)
134	H2356_VICINITY_A	506028010	2011/05/15(2135)	98.1	(on,2,–,on)
135	H2356_VICINITY_B	506029010	2011/05/17(2137)	100.5	(on,2,–,on)
136	FILAMENT_JUNCTION_2	806004010	2011/05/18(2138)	170.1	(on,2,–,on)
137	NGC5866	806053010	2011/05/20(2140)	238.2	(on,2,–,on)
138	SPT–CL_J2341–5119	806072010	2011/05/22(2142)	215.4	(on,2,–,on)
139	FILAMENT_JUNCTION_1	806003010	2011/05/25(2145)	120.6	(on,2,–,on)
140	G236+38_ON	506055010	2011/06/01(2152)	180	(on,6,–,on)
141	G236+38_OFF	506056010	2011/06/07(2158)	144.3	(on,6,–,on)
142	1FGL_J2339.7–0531	406007010	2011/06/29(2180)	189.9	(on,6,–,on)
143	RX_J1633+4718	706027010	2011/07/01(2182)	98.4	(on,6,–,on)
144	MRK_478	706041010	2011/07/14(2195)	198.3	(on,6,–,on)
145	RX_J1633+4718	706027020	2011/07/18(2199)	88.5	(on,6,–,on)
146	RCS044406–2820.4	806080010	2011/09/23(2266)	102.9	(on,6,–,on)
147	NGC3628	806018010	2011/11/25(2329)	196.5	(on,6,–,on)
148	PG_1322+659	706018010	2011/11/27(2331)	181.5	(on,6,–,on)
149	LOCK–365	806077010	2011/12/02(2336)	303.3	(on,6,–,on)
150	ES1–230	806076010	2011/12/12(2346)	116.7	(on,6,–,on)
151	EN2–109	806075010	2012/01/01(2366)	198.3	(on,6,–,on)
152	3C_59_VICINITY_2	506025010	2012/01/26(2391)	444.6	(on,6,–,on)
153	UGC03957_NORTH	806091010	2012/03/20(2445)	109.8	(on,6,–,on)
154	UGC03957_SOUTH	806092010	2012/03/21(2446)	124.2	(on,6,–,on)
155	UGC03957_EAST	806094010	2012/03/22(2447)	88.5	(on,6,–,on)
156	RCS051838–4324.9	806083010	2012/03/30(2455)	121.8	(on,6,–,on)
157	2FGL_J0923.5+1508	707007010	2012/04/29(2485)	234.3	(on,6,–,on)
158	IRAS_00182–7112	707036010	2012/05/03(2489)	133.2	(on,6,–,on)
159	SWIFT_J164449.3+1573	707018010	2012/05/17(2503)	147.6	(on,6,–,on)
160	EUVE_J1439+75.0	407039010	2012/05/20(2506)	74.7	(on,6,–,on)
161	ESO_565–G019	707013010	2012/05/20(2506)	118.8	(on,6,–,on)
162	2FGL_J1502.1+5548	707008010	2012/05/22(2508)	101.7	(on,6,–,on)

Table continued on next page.

Continued from previous page.

ID	Field Name	Obs. ID	Date(Day from launch)*	Exposure†	SCI(XIS0,1,2,3)‡
163	RXJ1159+5531	807064010	2012/05/27(2513)	203.7	(on,6,–,on)
164	2FGL_J0022.2–1853	707009010	2012/05/30(2516)	95.1	(on,6,–,on)
165	NGC_7796	807047010	2012/05/31(2517)	253.2	(on,6,–,on)
166	FILAMENT_JUNCTION_A	807038010	2012/06/08(2525)	151.2	(on,6,–,on)
167	NGC_3431	707012010	2012/06/11(2528)	149.1	(on,6,–,on)
168	ANTLIA_EB	807071010	2012/06/18(2535)	102.9	(on,6,–,on)
169	NGC_4941	707001010	2012/06/22(2539)	205.5	(on,6,–,on)
170	IRAS_12127–1412	707037010	2012/07/05(2552)	121.2	(on,6,–,on)
171	PG_1658_+440	407040010	2012/07/07(2554)	100.8	(on,6,–,on)
172	A2256BKG	807025010	2012/11/05(2675)	103.2	(on,6,–,on)
173	RE_J1034+396	707039010	2012/11/14(2684)	204.3	(on,6,–,on)
174	SEGUE_1	807046010	2012/11/17(2687)	153.3	(on,6,–,on)
175	IC_5157	807048010	2012/11/19(2689)	177.3	(on,6,–,on)
176	RCS110619–0423.6	807075010	2012/11/22(2692)	105.9	(on,6,–,on)
177	DDO_120	807044010	2012/11/25(2695)	191.4	(on,6,–,on)
178	MRK_520	407014010	2012/11/27(2697)	193.8	(on,6,–,on)
179	PG_1404+226	707026010	2012/12/23(2723)	184.2	(on,6,–,on)
180	RCS110104–0351.3	807076010	2012/12/25(2725)	181.8	(on,6,–,on)
181	RXJ0134–4258	707014010	2012/12/29(2729)	139.8	(on,6,–,on)
182	A2061_1	807029010	2013/01/14(2745)	92.4	(on,6,–,on)
183	MBM16	507076020	2013/02/08(2770)	152.1	(on,6,–,on)
184	MKN_335	708016010	2013/06/11(2893)	296.1	(on,6,–,on)
185	MKN_335	708016020	2013/06/14(2896)	311.4	(on,6,–,on)
186	ABELL_1689_(OFFSET)	808089010	2013/06/27(2909)	95.4	(on,6,–,on)
187	ABELL_1689_(OFFSET)	808089020	2013/06/30(2912)	133.5	(on,6,–,on)

Notes.

$*$ Observational start date (UT).

$\dagger$ Exposure time (XIS0+1+2+3) in unit of ksec after the data screening.

$\ddagger$ off: SCI off operation, on: SCI on operation for XIS-FI (2 keV equivalent),

2: SCI on operation for XIS1 (2 keV equivalent), 6: SCI on operation for XIS1 (6 keV equivalent).

Table A.2: 187 Suzaku XIS observational aim points of the XDB.

ID	Equatorial (R.A., Dec.)	Galactic (Lat., Lon.)	Ecliptic (Az., Alt.)	ϕ^*	$n_H^\dagger$
1	(244.477, 65.447)	(97.721, 40.119)	(174.334, 79.635)	95.897	0.023
2	(93.884, 71.048)	(143.284, 22.716)	(91.871, 47.634)	137.682	0.097
3	(116.614, 25.879)	(194.520, 22.918)	(113.852, 4.617)	153.081	0.044
4	(246.175, 43.485)	(68.417, 44.392)	(228.836, 63.559)	74.761	0.009
5	(38.747, −52.277)	(272.403, −58.273)	(4.398, −61.406)	88.737	0.030
6	(50.051, −62.433)	(278.676, −47.082)	(354.787, −72.639)	84.104	0.022
7	(53.240, −63.455)	(278.622, −45.308)	(354.161, −74.404)	83.948	0.046
8	(114.201, 65.592)	(150.581, 29.180)	(103.455, 43.279)	139.509	0.044
9	(243.960, 60.059)	(91.207, 42.381)	(196.942, 76.759)	90.891	0.018
10	(243.960, 59.174)	(90.077, 42.684)	(199.767, 76.170)	90.057	0.015
11	(135.066, 39.009)	(183.474, 40.965)	(126.116, 21.051)	138.914	0.021
12	(162.937, 57.256)	(149.703, 53.201)	(137.119, 45.118)	121.145	0.006
13	(270.666, 67.637)	(97.623, 29.552)	(76.771, 88.893)	96.627	0.046
14	(184.712, 47.238)	(138.434, 68.898)	(138.434, 68.898)	105.627	0.016
15	(206.132, 55.819)	(108.096, 59.754)	(168.562, 59.029)	99.001	0.009
16	(186.707, −0.938)	(290.032, 61.316)	(290.032, 61.316)	80.537	0.020
17	(127.927, 52.764)	(165.744, 36.242)	(116.238, 32.724)	141.416	0.041
18	(144.019, 61.418)	(152.382, 42.894)	(122.522, 43.937)	130.476	0.030
19	(127.923, 52.764)	(165.744, 36.240)	(116.235, 32.723)	141.418	0.041
20	(239.313, 61.287)	(93.987, 43.987)	(187.020, 75.698)	92.867	0.010
21	(171.224, −12.966)	(272.545, 44.739)	(177.197, −15.367)	88.192	0.042
22	(188.017, −13.087)	(295.657, 49.511)	(295.657, 49.511)	73.672	0.035
23	(19.060, 33.029)	(128.907, −29.555)	(30.566, 23.028)	123.116	0.053
24	(43.816, −0.240)	(175.954, −49.917)	(175.954, −49.917)	129.963	0.058
25	(127.920, 52.747)	(165.765, 36.238)	(116.238, 32.707)	141.426	0.041
26	(227.252, 67.231)	(104.987, 44.804)	(158.021, 73.543)	100.572	0.019
27	(260.027, 57.929)	(86.385, 34.734)	(86.385, 34.734)	87.030	0.023
28	(133.689, 20.048)	(206.877, 35.788)	(130.506, 2.540)	136.350	0.025
29	(162.926, 57.258)	(149.707, 53.195)	(137.110, 45.116)	121.151	0.006
30	(332.317, 30.217)	(86.004, −20.790)	(347.608, 38.421)	86.265	0.061
31	(335.953, −2.100)	(61.867, −46.709)	(61.867, −46.709)	71.136	0.045
32	(186.411, 33.488)	(162.541, 81.552)	(162.541, 81.552)	98.056	0.019
33	(39.937, −39.101)	(247.811, −64.495)	(247.811, −64.495)	99.359	0.016
34	(6.211, −71.996)	(305.832, −44.982)	(305.832, −44.982)	65.539	0.053
35	(219.443, 33.511)	(55.012, 66.256)	(55.012, 66.256)	76.651	0.010
36	(40.231, −8.213)	(181.912, −57.928)	(181.912, −57.928)	122.052	0.028
37	(43.783, −0.130)	(175.796, −49.864)	(41.285, −16.099)	130.007	0.058
38	(67.140, −17.075)	(213.437, −39.092)	(213.437, −39.092)	130.367	0.023
39	(189.694, −27.358)	(299.482, 35.429)	(299.482, 35.429)	66.358	0.054
40	(133.712, 20.170)	(206.744, 35.848)	(130.493, 2.663)	136.374	0.025
41	(64.025, −55.779)	(265.634, −43.701)	(265.634, −43.701)	93.155	0.010
42	(218.714, 35.724)	(60.713, 66.412)	(60.713, 66.412)	78.711	0.011
43	(188.899, −39.912)	(299.636, 22.858)	(299.636, 22.858)	62.893	0.070
44	(228.606, 36.620)	(59.439, 58.401)	(59.439, 58.401)	74.549	0.015

Continued from previous page.

ID	Equatorial (R.A., Dec.)	Galactic (Lat., Lon.)	Ecliptic (Az., Alt.)	ϕ^*	$n_{\mathrm{H}}{}^\dagger$
45	(270.932, 40.210)	(66.858, 25.776)	(271.603, 63.644)	69.274	0.031
46	(40.861, −42.007)	(253.287, −62.755)	(253.287, −62.755)	97.565	0.019
47	(133.424, 57.801)	(159.017, 38.830)	(117.904, 38.494)	136.665	0.041
48	(329.237, −30.528)	(17.169, −51.867)	(320.679, −16.905)	53.844	0.015
49	(330.186, −29.965)	(18.229, −52.620)	(321.689, −16.674)	54.786	0.016
50	(327.065, −34.896)	(10.029, −50.338)	(317.234, −20.335)	51.060	0.019
51	(162.937, 57.255)	(149.705, 53.202)	(137.120, 45.117)	121.144	0.006
52	(23.435, −36.466)	(261.714, −77.057)	(4.419, −42.262)	91.850	0.020
53	(150.497, 55.612)	(157.901, 48.392)	(130.115, 40.278)	127.970	0.009
54	(180.219, 6.749)	(270.135, 66.346)	(270.135, 66.346)	89.946	0.012
55	(208.272, 33.440)	(62.069, 75.292)	(191.043, 41.515)	83.170	0.015
56	(149.843, −22.872)	(259.028, 24.982)	(161.273, −32.732)	99.934	0.039
57	(216.370, 32.937)	(54.593, 68.885)	(54.593, 68.885)	77.953	0.010
58	(30.262, −6.759)	(165.150, −63.769)	(165.150, −63.769)	115.292	0.021
59	(79.066, −10.511)	(211.752, −25.863)	(77.082, −33.461)	139.922	0.093
60	(137.906, 45.531)	(174.709, 43.112)	(126.029, 27.901)	136.628	0.012
61	(127.716, 24.187)	(200.017, 31.876)	(200.017, 31.876)	142.929	0.029
62	(274.126, 49.808)	(77.811, 25.819)	(77.811, 25.819)	79.044	0.038
63	(282.096, 47.979)	(77.403, 20.285)	(294.697, 70.383)	78.196	0.052
64	(167.883, 55.684)	(148.299, 56.246)	(148.299, 56.246)	118.212	0.008
65	(49.557, −66.536)	(283.403, −44.621)	(283.403, −44.621)	80.504	0.041
66	(189.807, −16.129)	(298.659, 46.641)	(298.659, 46.641)	70.775	0.030
67	(12.093, −25.048)	(104.447, −87.808)	(0.370, −27.641)	90.547	0.015
68	(39.206, −35.728)	(240.487, −66.023)	(20.765, −47.721)	101.548	0.036
69	(217.481, 33.298)	(55.134, 67.907)	(55.134, 67.907)	77.584	0.009
70	(70.560, −28.250)	(228.441, −39.401)	(62.938, −49.879)	120.839	0.026
71	(124.077, 48.384)	(171.018, 33.698)	(114.888, 27.847)	145.263	0.048
72	(145.222, 34.680)	(190.268, 48.816)	(135.807, 19.600)	130.386	0.011
73	(191.551, 54.512)	(124.583, 62.599)	(159.097, 52.494)	105.142	0.014
74	(136.117, 55.575)	(161.505, 40.696)	(120.649, 36.936)	135.974	0.022
75	(18.511, −55.385)	(296.211, −61.447)	(343.272, −55.773)	77.813	0.022
76	(208.225, 69.302)	(115.057, 46.875)	(115.057, 46.875)	106.829	0.015
77	(145.825, 54.275)	(161.230, 46.416)	(127.752, 37.907)	130.750	0.014
78	(181.532, 52.653)	(138.207, 63.110)	(153.576, 47.378)	109.706	0.017
79	(203.296, 51.017)	(107.389, 64.833)	(107.389, 64.833)	97.302	0.009
80	(355.445, 30.641)	(105.656, −29.883)	(9.274, 29.656)	103.531	0.057
81	(162.938, 57.255)	(149.704, 53.202)	(137.120, 45.117)	121.144	0.006
82	(26.811, 35.568)	(135.528, −25.935)	(38.039, 22.813)	129.921	0.045
83	(48.986, −85.500)	(299.847, −30.729)	(278.555, −69.752)	64.671	0.078
84	(42.225, 26.571)	(153.134, −29.324)	(47.760, 9.864)	141.056	0.102
85	(17.451, 19.662)	(128.848, −42.999)	(23.624, 11.325)	117.307	0.037
86	(187.799, −14.167)	(295.529, 48.413)	(295.529, 48.413)	73.378	0.034
87	(45.952, −1.104)	(179.179, −48.962)	(43.151, −17.670)	131.033	0.060
88	(73.364, 4.123)	(194.584, −23.846)	(72.495, −18.311)	152.272	0.067
89	(182.057, 65.178)	(130.168, 51.339)	(140.389, 57.005)	113.763	0.017

Continued from previous page.

ID	Equatorial (R.A., Dec.)	Galactic (Lat., Lon.)	Ecliptic (Az., Alt.)	ϕ^*	$n_\mathrm{H}^\dagger$
90	(173.234, 53.112)	(146.876, 60.214)	(146.876, 60.214)	114.584	0.011
91	(166.866, 72.621)	(133.140, 42.385)	(133.140, 42.385)	120.336	0.035
92	(182.443, 43.735)	(147.092, 71.387)	(147.092, 71.387)	105.543	0.013
93	(128.831, 19.593)	(205.510, 31.338)	(126.213, 0.902)	140.430	0.026
94	(166.803, 37.734)	(180.505, 65.696)	(152.018, 29.319)	114.303	0.016
95	(165.384, 38.630)	(179.319, 64.356)	(150.413, 29.628)	115.642	0.017
96	(89.966, −66.577)	(276.403, −29.825)	(276.403, −29.825)	84.448	0.047
97	(270.049, 66.560)	(96.383, 29.792)	(96.383, 29.792)	95.536	0.039
98	(342.977, 22.287)	(89.690, −32.758)	(353.700, 27.110)	89.739	0.049
99	(171.128, 21.419)	(224.301, 69.416)	(163.241, 16.137)	104.573	0.017
100	(89.966, −66.571)	(276.396, −29.825)	(276.396, −29.825)	84.454	0.047
101	(270.052, 66.566)	(96.389, 29.791)	(96.389, 29.791)	95.542	0.039
102	(89.958, −66.568)	(276.393, −29.828)	(276.393, −29.828)	84.457	0.047
103	(270.048, 66.570)	(96.394, 29.792)	(96.394, 29.792)	95.546	0.039
104	(180.469, 44.115)	(150.131, 70.303)	(159.285, 39.866)	106.994	0.011
105	(89.980, −66.568)	(276.393, −29.819)	(276.393, −29.819)	84.457	0.047
106	(270.045, 66.579)	(96.405, 29.794)	(96.405, 29.794)	95.555	0.039
107	(245.042, 30.791)	(50.543, 44.604)	(50.543, 44.604)	63.098	0.022
108	(26.016, 2.290)	(148.320, −57.964)	(24.962, −7.913)	116.835	0.025
109	(52.155, −28.697)	(224.905, −55.397)	(39.556, −45.732)	113.717	0.010
110	(117.357, 55.877)	(161.847, 30.163)	(108.149, 34.148)	145.242	0.049
111	(220.585, 66.095)	(106.760, 47.400)	(158.410, 70.673)	101.255	0.013
112	(154.243, 73.387)	(136.298, 39.477)	(117.476, 56.075)	123.919	0.029
113	(342.380, −19.215)	(42.201, −60.967)	(336.401, −10.851)	68.929	0.021
114	(13.778, 26.185)	(123.960, −36.679)	(23.092, 18.654)	116.615	0.050
115	(238.880, 27.131)	(43.896, 49.284)	(228.375, 46.175)	61.962	0.035
116	(178.362, 49.532)	(145.519, 64.976)	(145.519, 64.976)	110.407	0.021
117	(140.401, 51.023)	(166.897, 44.075)	(125.596, 33.625)	134.405	0.013
118	(153.738, 48.076)	(167.645, 53.187)	(136.570, 34.405)	125.826	0.009
119	(355.993, −35.293)	(359.217, −73.459)	(340.888, −30.490)	73.461	0.011
120	(349.630, −0.417)	(79.219, −55.199)	(79.219, −55.199)	83.871	0.036
121	(182.439, −5.012)	(283.973, 56.318)	(184.232, −3.628)	82.304	0.031
122	(11.592, −40.097)	(307.242, −76.989)	(307.242, −76.989)	82.169	0.034
123	(10.571, −12.950)	(113.890, −75.661)	(4.470, −16.065)	95.756	0.017
124	(28.267, −13.498)	(172.552, −70.175)	(21.053, −23.412)	109.651	0.016
125	(28.093, 28.684)	(138.759, −32.308)	(138.759, −32.308)	129.459	0.056
126	(21.982, 28.787)	(132.513, −33.405)	(132.513, −33.405)	124.342	0.064
127	(51.573, −21.333)	(212.180, −54.365)	(42.193, −38.612)	119.546	0.022
128	(11.168, 40.673)	(121.547, −22.181)	(27.903, 32.652)	118.978	0.093
129	(63.101, 10.375)	(182.335, −28.540)	(182.335, −28.540)	151.373	0.129
130	(151.416, 39.740)	(181.905, 53.563)	(138.765, 26.117)	126.413	0.012
131	(354.347, −59.706)	(319.158, −55.028)	(322.224, −50.573)	64.303	0.015
132	(193.921, 56.860)	(121.763, 60.258)	(121.763, 60.258)	105.138	0.009
133	(319.716, −63.573)	(330.737, −40.234)	(330.737, −40.234)	48.242	0.028
134	(359.897, −30.209)	(14.719, −78.225)	(346.871, −27.453)	78.616	0.015

Table continued on next page.

Continued from previous page.

ID	Equatorial (R.A., Dec.)	Galactic (Lat., Lon.)	Ecliptic (Az., Alt.)	ϕ^*	$n_{\mathrm{H}}^{\dagger}$
135	(359.987, −29.949)	(15.897, −78.352)	(347.080, −27.255)	78.804	0.015
136	(149.254, 26.150)	(204.131, 51.210)	(142.296, 12.815)	124.871	0.028
137	(226.598, 55.755)	(92.037, 52.505)	(186.827, 67.082)	91.240	0.014
138	(355.301, −51.333)	(326.935, −62.397)	(330.136, −44.107)	67.151	0.012
139	(204.175, 43.831)	(97.208, 70.967)	(179.615, 48.842)	92.345	0.015
140	(146.535, 0.506)	(235.933, 38.214)	(235.933, 38.214)	116.111	0.061
141	(149.412, 1.472)	(237.071, 41.120)	(237.071, 41.120)	114.175	0.019
142	(354.908, −5.547)	(81.348, −62.470)	(353.127, −3.069)	86.013	0.029
143	(248.330, 47.307)	(73.537, 42.626)	(228.778, 67.669)	77.965	0.017
144	(220.496, 35.371)	(59.091, 65.077)	(59.091, 65.077)	77.499	0.011
145	(248.334, 47.299)	(73.526, 42.624)	(73.526, 42.624)	77.956	0.017
146	(71.022, −28.343)	(228.678, −39.026)	(63.528, −50.053)	120.861	0.025
147	(170.070, 13.599)	(240.833, 64.785)	(165.517, 8.572)	101.983	0.020
148	(200.979, 65.707)	(117.624, 51.086)	(117.624, 51.086)	106.933	0.017
149	(161.910, 57.711)	(149.750, 52.486)	(136.112, 45.204)	121.738	0.006
150	(9.191, −44.181)	(311.806, −72.694)	(311.806, −72.694)	78.562	0.035
151	(248.677, 40.380)	(64.118, 42.556)	(64.118, 42.556)	71.243	0.010
152	(31.435, 28.923)	(141.954, −31.189)	(39.297, 15.198)	132.352	0.054
153	(114.914, 55.810)	(161.766, 28.792)	(106.549, 33.793)	146.343	0.044
154	(115.526, 55.024)	(162.704, 29.045)	(107.149, 33.094)	146.585	0.042
155	(115.974, 55.497)	(162.198, 29.351)	(107.330, 33.609)	146.088	0.043
156	(79.659, −43.417)	(248.715, −34.616)	(71.164, −66.181)	107.383	0.025
157	(140.989, 15.081)	(215.968, 40.483)	(138.613, −0.175)	127.994	0.030
158	(5.146, −70.928)	(306.551, −45.983)	(312.996, −61.495)	65.555	0.033
159	(251.162, 57.587)	(86.723, 39.464)	(86.723, 39.464)	87.470	0.017
160	(219.946, 75.082)	(114.113, 40.136)	(130.300, 72.233)	108.200	0.030
161	(143.680, −21.935)	(253.873, 21.675)	(154.563, −34.144)	104.959	0.041
162	(225.583, 55.858)	(92.731, 52.904)	(92.731, 52.904)	91.647	0.013
163	(179.964, 55.412)	(137.706, 60.212)	(137.706, 60.212)	111.561	0.010
164	(5.543, −18.896)	(82.152, −79.370)	(82.152, −79.370)	88.557	0.020
165	(359.741, −55.456)	(317.904, −60.121)	(317.904, −60.121)	68.306	0.013
166	(165.659, 29.245)	(201.460, 65.985)	(155.088, 21.240)	112.257	0.018
167	(162.811, −17.015)	(266.038, 37.101)	(171.112, −22.388)	93.159	0.042
168	(160.085, −35.330)	(274.842, 20.292)	(274.842, 20.292)	85.459	0.063
169	(196.053, −5.560)	(308.801, 57.167)	(308.801, 57.167)	70.138	0.022
170	(183.831, −14.497)	(289.945, 47.462)	(289.945, 47.462)	76.667	0.038
171	(254.935, 44.009)	(69.112, 38.066)	(69.112, 38.066)	73.697	0.013
172	(259.059, 79.132)	(111.318, 31.032)	(111.318, 31.032)	108.150	0.044
173	(158.663, 39.649)	(180.263, 59.064)	(180.263, 59.064)	120.935	0.013
174	(151.766, 16.086)	(220.471, 50.427)	(220.471, 50.427)	118.988	0.033
175	(330.866, −34.934)	(10.022, −53.455)	(10.022, −53.455)	54.100	0.013
176	(166.577, −4.392)	(260.073, 49.528)	(260.073, 49.528)	96.425	0.048
177	(185.317, 45.820)	(138.735, 70.372)	(138.735, 70.372)	104.625	0.011
178	(330.177, 10.545)	(69.390, −34.038)	(69.390, −34.038)	73.040	0.043
179	(211.594, 22.404)	(21.505, 72.365)	(21.505, 72.365)	73.629	0.021

Continued from previous page.

ID	Equatorial (R.A., Dec.)	Galactic (Lat., Lon.)	Ecliptic (Az., Alt.)	ϕ^*	$n_H{}^\dagger$
180	(165.266, −3.854)	(257.987, 49.141)	(257.987, 49.141)	97.826	0.033
181	(23.569, −42.967)	(276.928, −71.932)	(276.928, −71.932)	87.856	0.017
182	(229.994, 30.530)	(47.895, 57.435)	(47.895, 57.435)	68.845	0.017
183	(49.769, 11.580)	(170.606, −37.272)	(170.606, −37.272)	141.730	0.169
184	(1.577, 20.209)	(108.759, −41.418)	(108.759, −41.418)	103.955	0.036
185	(1.576, 20.209)	(108.759, −41.417)	(108.759, −41.417)	103.955	0.036
186	(198.182, −1.269)	(314.010, 61.144)	(314.010, 61.144)	70.409	0.019
187	(198.182, −1.269)	(314.011, 61.144)	(314.011, 61.144)	70.409	0.019

Notes.

∗ See Eq.(3.12).

† The neutral hydrogen column density in unit of 10^{22} cm^{-2} derived from the LAB Galactic H I Survey.

Table A.3: Spectral fitting results with the 187 individual XDB spectra.

ID	Norm$_1$*	kT_2†	Norm$_2$*	kT_3†	Norm$_3$*	Γ_{CXB}‖	S_{CXB}‡	O I§	χ^2/dof (dof)
1	$6.6^{+9.9}_{-6.6}$	$0.17^{+0.01}_{-0.03}$	$6.3^{+4.2}_{-2.5}$	$0.92^{+0.15}_{-0.14}$	$0.6^{+0.3}_{-0.3}$	$1.5^{+0.1}_{-0.1}$	$6.5^{+0.7}_{-0.7}$	$0.8^{+0.5}_{-0.5}$	1.18(592)
2	$16.3^{+4.5}_{-4.5}$	$0.29^{+0.05}_{-0.04}$	$3.5^{+1.2}_{-0.9}$	–	0(fix)	$1.4^{+0.1}_{-0.1}$	$5.7^{+0.6}_{-0.6}$	$0.5^{+0.5}_{-0.5}$	1.20(594)
3	$16.3^{+5.4}_{-5.7}$	$0.25^{+0.03}_{-0.02}$	$4.1^{+1.2}_{-1.0}$	–	0(fix)	$1.5^{+0.0}_{-0.0}$	$9.3^{+0.5}_{-0.5}$	$0.4^{+0.4}_{-0.4}$	0.96(594)
4	$0.1^{+16.9}_{-0.1}$	$0.17^{+0.03}_{-0.02}$	$6.5^{+2.0}_{-3.9}$	–	0(fix)	$1.8^{+0.1}_{-0.1}$	$7.0^{+0.7}_{-0.4}$	$0.1^{+0.8}_{-0.1}$	1.16(594)
5	$0.0^{+9.9}_{-0.0}$	$0.17^{+0.05}_{-0.03}$	$3.9^{+1.8}_{-2.8}$	–	0(fix)	$1.9^{+0.1}_{-0.1}$	$5.4^{+0.7}_{-0.7}$	$0.1^{+0.7}_{-0.1}$	1.21(594)
6	$5.7^{+33.6}_{-5.7}$	$0.17^{+0.05}_{-0.02}$	$14.5^{+5.4}_{-8.3}$	$0.69^{+0.18}_{-0.06}$	$0.8^{+0.3}_{-0.5}$	$1.7^{+0.1}_{-0.1}$	$6.4^{+0.6}_{-0.5}$	$1.2^{+0.7}_{-0.8}$	1.12(592)
7	$22.2^{+8.1}_{-20.9}$	$0.23^{+0.03}_{-0.05}$	$6.2^{+6.3}_{-1.7}$	$0.85^{+0.11}_{-0.19}$	$0.6^{+0.5}_{-0.3}$	$1.5^{+0.1}_{-0.1}$	$6.2^{+0.5}_{-0.5}$	$0.1^{+0.6}_{-0.1}$	1.05(592)
8	$21.6^{+7.8}_{-15.8}$	$0.22^{+0.05}_{-0.04}$	$3.9^{+4.7}_{-1.7}$	–	0(fix)	$1.7^{+0.1}_{-0.1}$	$7.8^{+0.7}_{-0.6}$	$0.0^{+0.7}_{-0.0}$	1.12(594)
9	$26.8^{+7.8}_{-17.0}$	$0.23^{+0.06}_{-0.05}$	$2.7^{+3.9}_{-1.3}$	–	0(fix)	$1.6^{+0.1}_{-0.1}$	$9.4^{+0.6}_{-0.6}$	$0.0^{+0.6}_{-0.0}$	1.11(594)
10	$27.9^{+9.3}_{-27.9}$	$0.22^{+0.05}_{-0.09}$	$3.4^{+5.3}_{-1.4}$	–	0(fix)	$1.6^{+0.1}_{-0.1}$	$9.2^{+0.6}_{-0.6}$	$0.3^{+0.7}_{-0.3}$	1.07(594)
11	$26.8^{+7.4}_{-12.9}$	$0.25^{+0.07}_{-0.06}$	$2.3^{+2.8}_{-1.1}$	–	0(fix)	$1.5^{+0.1}_{-0.1}$	$9.4^{+0.6}_{-0.6}$	$0.1^{+0.7}_{-0.1}$	0.96(594)
12	$13.6^{+5.1}_{-5.1}$	–	0(fix)	$0.55^{+0.29}_{-0.29}$	$0.3^{+0.2}_{-0.2}$	$1.6^{+0.1}_{-0.1}$	$5.6^{+0.6}_{-0.6}$	0(fix)	1.15(595)
13	$0.6^{+15.4}_{-0.6}$	$0.19^{+0.11}_{-0.04}$	$4.4^{+2.0}_{-3.5}$	–	0(fix)	$1.8^{+0.1}_{-0.1}$	$7.6^{+0.9}_{-0.9}$	$1.2^{+0.9}_{-1.0}$	1.21(594)
14	$18.9^{+9.0}_{-18.9}$	$0.25^{+0.07}_{-0.07}$	$3.7^{+3.0}_{-1.6}$	$0.76^{+0.28}_{-0.20}$	$1.2^{+0.7}_{-0.6}$	$1.4^{+0.1}_{-0.1}$	$6.1^{+0.7}_{-0.7}$	$0.0^{+0.8}_{-0.0}$	1.25(592)
15	$10.1^{+16.2}_{-10.1}$	$0.19^{+0.05}_{-0.02}$	$6.2^{+3.5}_{-3.3}$	$0.96^{+0.12}_{-0.16}$	$1.0^{+0.3}_{-0.3}$	$1.5^{+0.1}_{-0.1}$	$5.8^{+0.6}_{-0.6}$	$0.0^{+0.7}_{-0.0}$	0.96(592)
16	$41.4^{+23.4}_{-30.1}$	$0.20^{+0.02}_{-0.02}$	$14.0^{+7.2}_{-4.7}$	–	0(fix)	$1.6^{+0.1}_{-0.1}$	$7.5^{+0.6}_{-0.6}$	$1.5^{+1.1}_{-1.1}$	1.15(594)
17	$0.0^{+9.3}_{-0.0}$	$0.16^{+0.14}_{-0.06}$	$5.4^{+4.0}_{-5.0}$	$1.08^{+0.21}_{-0.27}$	$0.6^{+0.5}_{-0.3}$	$1.8^{+0.2}_{-0.2}$	$6.9^{+0.9}_{-1.0}$	$0.5^{+0.4}_{-0.5}$	1.24(436)
18	$5.6^{+16.7}_{-5.6}$	$0.19^{+0.09}_{-0.04}$	$5.3^{+3.1}_{-3.8}$	–	0(fix)	$1.7^{+0.1}_{-0.1}$	$8.7^{+0.9}_{-0.9}$	$0.1^{+0.9}_{-0.1}$	1.23(437)
19	$2.4^{+13.0}_{-2.4}$	$0.19^{+0.05}_{-0.02}$	$5.6^{+1.8}_{-3.2}$	–	0(fix)	$1.5^{+0.1}_{-0.1}$	$8.4^{+0.5}_{-0.5}$	$0.7^{+0.5}_{-0.6}$	1.00(437)
20	$0.0^{+51.0}_{-0.0}$	$0.14^{+0.55}_{-0.04}$	$15.5^{+27.3}_{-15.1}$	$0.90^{+0.15}_{-0.20}$	$0.9^{+0.5}_{-0.5}$	$1.6^{+0.2}_{-0.1}$	$6.7^{+1.0}_{-0.2}$	0(fix)	1.02(437)
21	$30.9^{+9.2}_{-11.3}$	$0.29^{+0.13}_{-0.07}$	$2.3^{+1.9}_{-1.1}$	–	0(fix)	$1.6^{+0.1}_{-0.1}$	$7.2^{+1.0}_{-0.8}$	$0.7^{+1.0}_{-0.7}$	1.06(437)
22	$27.4^{+18.8}_{-27.4}$	$0.23^{+0.05}_{-0.05}$	$6.8^{+7.9}_{-3.1}$	–	0(fix)	$1.6^{+0.1}_{-0.1}$	$7.8^{+1.1}_{-1.0}$	$0.7^{+1.4}_{-0.7}$	1.31(438)
23	$14.5^{+8.9}_{-14.5}$	$0.22^{+0.03}_{-0.04}$	$7.4^{+5.2}_{-1.8}$	$0.94^{+0.14}_{-0.16}$	$1.0^{+0.4}_{-0.4}$	$1.7^{+0.1}_{-0.1}$	$10.4^{+0.8}_{-0.8}$	$0.4^{+0.6}_{-0.4}$	1.08(436)
24	$11.8^{+4.7}_{-8.1}$	$0.28^{+0.06}_{-0.06}$	$2.4^{+1.7}_{-0.9}$	–	0(fix)	$1.4^{+0.1}_{-0.1}$	$4.9^{+0.6}_{-0.6}$	$0.0^{+0.6}_{-0.0}$	1.02(438)
25	$15.2^{+8.4}_{-13.6}$	$0.24^{+0.06}_{-0.05}$	$3.4^{+3.6}_{-1.4}$	–	0(fix)	$1.5^{+0.1}_{-0.1}$	$9.5^{+0.6}_{-0.6}$	$0.5^{+0.6}_{-0.5}$	1.23(438)
26	$25.2^{+31.4}_{-19.0}$	–	0(fix)	$0.75^{+0.17}_{-0.18}$	$0.6^{+0.3}_{-0.3}$	$1.5^{+0.1}_{-0.1}$	$7.0^{+0.7}_{-0.7}$	$0.4^{+0.7}_{-0.4}$	0.91(438)
27	$27.0^{+9.3}_{-12.8}$	$0.27^{+0.06}_{-0.10}$	$3.0^{+2.0}_{-1.2}$	$0.95^{+0.25}_{-0.22}$	$1.0^{+0.5}_{-0.5}$	$1.7^{+0.1}_{-0.1}$	$6.9^{+1.0}_{-0.9}$	$1.0^{+1.0}_{-1.0}$	1.06(436)
28	$0.0^{+19.1}_{-0.0}$	$0.17^{+0.05}_{-0.02}$	$7.2^{+1.9}_{-5.0}$	–	0(fix)	$1.6^{+0.1}_{-0.1}$	$9.1^{+0.5}_{-0.5}$	0(fix)	1.12(439)
29	$26.9^{+6.6}_{-8.0}$	$0.28^{+0.07}_{-0.05}$	$1.7^{+1.0}_{-0.6}$	–	0(fix)	$1.5^{+0.1}_{-0.1}$	$7.4^{+0.5}_{-0.5}$	$1.2^{+0.7}_{-0.7}$	1.05(438)
30	$32.4^{+9.1}_{-11.0}$	$0.26^{+0.04}_{-0.04}$	$5.1^{+2.2}_{-1.5}$	–	0(fix)	$1.8^{+0.1}_{-0.1}$	$10.3^{+0.8}_{-0.8}$	$0.4^{+0.8}_{-0.4}$	1.13(438)
31	$23.9^{+16.3}_{-23.9}$	$0.19^{+0.03}_{-0.03}$	$10.0^{+6.7}_{-4.1}$	$0.94^{+0.11}_{-0.18}$	$1.3^{+0.4}_{-0.4}$	$1.1^{+0.1}_{-0.1}$	$8.6^{+0.6}_{-0.6}$	$0.5^{+0.7}_{-0.5}$	1.07(427)
32	$32.2^{+9.6}_{-18.0}$	$0.24^{+0.08}_{-0.06}$	$2.3^{+4.6}_{-1.2}$	–	0(fix)	$1.4^{+0.1}_{-0.1}$	$10.8^{+0.6}_{-0.6}$	$1.1^{+0.8}_{-0.8}$	1.11(438)
33	$18.0^{+6.8}_{-7.1}$	–	0(fix)	$0.43^{+0.21}_{-0.19}$	$0.5^{+0.6}_{-0.3}$	$1.8^{+0.1}_{-0.1}$	$6.0^{+0.6}_{-0.6}$	$0.6^{+0.9}_{-0.6}$	1.04(438)
34	$23.5^{+14.1}_{-23.5}$	$0.20^{+0.08}_{-0.06}$	$6.1^{+13.6}_{-3.1}$	$0.74^{+0.33}_{-0.18}$	$0.9^{+0.5}_{-0.6}$	$1.8^{+0.1}_{-0.1}$	$11.1^{+0.8}_{-0.8}$	$1.6^{+0.8}_{-0.8}$	1.19(436)
35	$26.5^{+11.8}_{-24.3}$	$0.24^{+0.05}_{-0.05}$	$4.2^{+4.6}_{-1.8}$	–	0(fix)	$1.9^{+0.1}_{-0.1}$	$7.9^{+0.8}_{-0.8}$	$0.0^{+0.7}_{-0.0}$	1.13(438)
36	$15.6^{+5.7}_{-13.3}$	$0.27^{+0.04}_{-0.07}$	$3.7^{+1.7}_{-1.1}$	$0.86^{+0.12}_{-0.13}$	$1.1^{+0.6}_{-0.4}$	$1.2^{+0.1}_{-0.1}$	$8.2^{+0.7}_{-0.7}$	$0.6^{+0.7}_{-0.6}$	1.14(436)
37	$12.5^{+9.9}_{-12.5}$	$0.25^{+0.17}_{-0.08}$	$2.3^{+4.4}_{-1.5}$	–	0(fix)	$1.4^{+0.1}_{-0.1}$	$6.0^{+0.8}_{-0.8}$	$0.8^{+1.0}_{-0.8}$	1.09(438)
38	$25.8^{+5.3}_{-8.7}$	$0.27^{+0.05}_{-0.05}$	$1.9^{+1.3}_{-0.7}$	–	0(fix)	$1.7^{+0.1}_{-0.1}$	$7.0^{+0.6}_{-0.5}$	$0.0^{+0.6}_{-0.0}$	1.10(438)
39	$45.1^{+17.4}_{-32.6}$	$0.23^{+0.06}_{-0.05}$	$6.1^{+9.7}_{-3.2}$	–	0(fix)	$2.3^{+0.2}_{-0.2}$	$7.3^{+1.2}_{-1.1}$	$0.3^{+1.4}_{-0.3}$	1.24(438)
40	$10.4^{+9.5}_{-10.4}$	$0.24^{+0.11}_{-0.04}$	$2.0^{+3.3}_{-1.2}$	–	0(fix)	$1.5^{+0.1}_{-0.1}$	$10.0^{+0.7}_{-0.7}$	$1.0^{+0.9}_{-0.9}$	1.07(438)
41	$25.1^{+15.7}_{-15.9}$	$0.24^{+0.04}_{-0.05}$	$8.8^{+2.1}_{-2.1}$	$0.75^{+0.14}_{-0.13}$	$1.4^{+0.7}_{-0.6}$	$1.6^{+0.1}_{-0.1}$	$8.7^{+0.7}_{-0.7}$	$0.5^{+0.9}_{-0.5}$	0.96(436)
42	$17.5^{+7.6}_{-7.7}$	–	0(fix)	$0.72^{+0.65}_{-0.66}$	$0.4^{+0.4}_{-0.4}$	$2.1^{+0.2}_{-0.2}$	$6.0^{+0.9}_{-0.9}$	0(fix)	1.23(439)
43	$23.9^{+11.3}_{-18.2}$	$0.22^{+0.02}_{-0.03}$	$13.9^{+6.3}_{-2.7}$	$1.03^{+0.19}_{-0.08}$	$2.1^{+0.5}_{-0.5}$	$1.2^{+0.1}_{-0.1}$	$5.7^{+0.7}_{-0.6}$	$0.2^{+0.8}_{-0.2}$	1.08(436)

Continued from previous page.

ID	Norm$_1$*	kT_2†	Norm$_2$*	kT_3†	Norm$_3$*	Γ_{CXB}‖	S_{CXB}‡	O I§	χ^2/dof (dof)
44	$12.6^{+7.8}_{-7.9}$	$0.24^{+0.04}_{-0.03}$	$3.2^{+1.2}_{-1.1}$	–	0(fix)	$1.5^{+0.1}_{-0.1}$	$7.4^{+0.4}_{-0.4}$	$0.8^{+0.6}_{-0.6}$	1.03(438)
45	0(fix)	$0.19^{+0.02}_{-0.01}$	$13.2^{+2.9}_{-2.9}$	–	0(fix)	$1.6^{+0.1}_{-0.1}$	$8.0^{+0.9}_{-0.8}$	$1.6^{+1.3}_{-1.3}$	1.12(438)
46	$0.0^{+17.5}_{-0.0}$	$0.18^{+0.05}_{-0.02}$	$6.5^{+1.0}_{-4.1}$	–	0(fix)	$1.6^{+0.1}_{-0.1}$	$8.3^{+0.5}_{-0.5}$	$0.0^{+0.5}_{-0.0}$	1.07(438)
47	$12.8^{+8.2}_{-10.3}$	–	0(fix)	–	0(fix)	$2.1^{+0.1}_{-0.1}$	$11.2^{+1.0}_{-0.9}$	$0.0^{+1.2}_{-0.0}$	1.28(440)
48	$39.0^{+11.3}_{-14.7}$	$0.25^{+0.05}_{-0.04}$	$3.8^{+2.1}_{-1.5}$	–	0(fix)	$1.6^{+0.1}_{-0.1}$	$7.0^{+0.7}_{-0.6}$	$0.0^{+1.1}_{-0.0}$	0.99(438)
49	0(fix)	$0.18^{+0.01}_{-0.02}$	$12.5^{+2.1}_{-2.1}$	$1.07^{+0.34}_{-0.24}$	$0.7^{+0.4}_{-0.4}$	$1.6^{+0.2}_{-0.2}$	$5.6^{+0.9}_{-0.9}$	$0.4^{+1.0}_{-0.4}$	1.06(437)
50	$26.5^{+13.0}_{-13.1}$	$0.30^{+0.08}_{-0.05}$	$4.2^{+1.4}_{-1.4}$	–	0(fix)	$1.7^{+0.2}_{-0.1}$	$7.5^{+1.0}_{-0.9}$	$0.9^{+1.3}_{-0.9}$	1.05(437)
51	$18.6^{+8.7}_{-18.6}$	$0.25^{+0.69}_{-0.12}$	$1.3^{+6.7}_{-1.1}$	–	0(fix)	$1.6^{+0.1}_{-0.1}$	$7.7^{+0.7}_{-0.7}$	$0.0^{+0.9}_{-0.0}$	1.20(438)
52	$26.0^{+6.9}_{-9.8}$	–	0(fix)	$0.80^{+0.16}_{-0.15}$	$1.1^{+0.4}_{-0.4}$	$1.7^{+0.1}_{-0.1}$	$7.6^{+1.0}_{-0.9}$	$0.0^{+1.1}_{-0.0}$	1.25(438)
53	$30.3^{+10.1}_{-13.1}$	$0.28^{+0.03}_{-0.04}$	$4.7^{+1.7}_{-1.0}$	–	0(fix)	$1.6^{+0.1}_{-0.1}$	$7.8^{+0.7}_{-0.6}$	$1.7^{+1.0}_{-1.0}$	1.24(438)
54	$29.7^{+9.2}_{-12.7}$	$0.28^{+0.05}_{-0.06}$	$2.7^{+1.7}_{-0.9}$	$1.05^{+0.23}_{-0.19}$	$0.8^{+0.3}_{-0.3}$	$0.8^{+0.1}_{-0.1}$	$4.8^{+0.5}_{-0.5}$	$0.6^{+0.9}_{-0.6}$	1.05(436)
55	$27.2^{+10.6}_{-14.8}$	$0.26^{+0.15}_{-0.08}$	$2.3^{+4.5}_{-1.4}$	–	0(fix)	$1.9^{+0.1}_{-0.1}$	$8.2^{+1.0}_{-0.9}$	$0.0^{+0.6}_{-0.0}$	1.25(438)
56	$24.7^{+14.6}_{-16.4}$	$0.25^{+0.05}_{-0.04}$	$5.7^{+2.8}_{-2.0}$	–	0(fix)	$1.6^{+0.1}_{-0.1}$	$8.8^{+0.9}_{-0.8}$	$0.8^{+1.2}_{-0.8}$	1.08(438)
57	$5.2^{+22.2}_{-0.0}$	$0.20^{+0.06}_{-0.02}$	$6.3^{+2.7}_{-3.1}$	–	0(fix)	$1.8^{+0.1}_{-0.1}$	$9.5^{+0.8}_{-0.8}$	$0.0^{+0.8}_{-0.0}$	1.26(438)
58	$11.1^{+10.2}_{-11.1}$	$0.37^{+0.37}_{-0.12}$	$1.6^{+1.7}_{-0.9}$	–	0(fix)	$1.6^{+0.1}_{-0.1}$	$7.7^{+0.9}_{-0.8}$	$1.2^{+1.1}_{-1.1}$	1.13(438)
59	$23.4^{+6.9}_{-23.4}$	$0.24^{+0.06}_{-0.13}$	$3.5^{+18.4}_{-1.7}$	$0.86^{+0.14}_{-0.15}$	$0.9^{+0.6}_{-0.4}$	$1.6^{+0.1}_{-0.1}$	$13.3^{+0.8}_{-0.8}$	$0.1^{+0.7}_{-0.1}$	1.00(436)
60	$8.1^{+11.9}_{-8.1}$	$0.23^{+0.06}_{-0.04}$	$4.1^{+2.7}_{-1.9}$	–	0(fix)	$1.4^{+0.1}_{-0.1}$	$7.1^{+0.9}_{-0.6}$	0(fix)	1.02(439)
61	$6.9^{+8.9}_{-6.9}$	–	0(fix)	$0.57^{+0.14}_{-0.33}$	$1.2^{+0.5}_{-0.5}$	$1.8^{+0.1}_{-0.1}$	$9.1^{+1.1}_{-1.1}$	$0.6^{+1.2}_{-0.6}$	1.11(438)
62	$27.5^{+23.1}_{-27.5}$	$0.19^{+0.05}_{-0.03}$	$10.7^{+14.1}_{-5.7}$	$0.94^{+0.13}_{-0.18}$	$1.2^{+0.4}_{-0.4}$	$1.5^{+0.1}_{-0.1}$	$8.2^{+0.7}_{-0.7}$	$0.3^{+0.9}_{-0.3}$	1.02(436)
63	0(fix)	$0.16^{+0.02}_{-0.02}$	$17.4^{+6.0}_{-4.5}$	$0.86^{+0.08}_{-0.08}$	$1.2^{+0.5}_{-0.4}$	$1.5^{+0.1}_{-0.1}$	$6.1^{+0.8}_{-0.8}$	0(fix)	1.21(438)
64	$19.0^{+7.4}_{-18.5}$	$0.26^{+0.14}_{-0.08}$	$1.6^{+3.5}_{-0.9}$	–	0(fix)	$1.6^{+0.1}_{-0.1}$	$6.2^{+0.6}_{-0.6}$	$0.0^{+0.9}_{-0.0}$	1.14(438)
65	$21.3^{+13.1}_{-21.3}$	$0.22^{+0.03}_{-0.04}$	$9.2^{+7.8}_{-2.7}$	–	0(fix)	$1.7^{+0.1}_{-0.1}$	$12.7^{+0.5}_{-0.9}$	$0.0^{+0.9}_{-0.0}$	1.04(438)
66	$28.0^{+15.5}_{-15.5}$	$0.23^{+0.02}_{-0.02}$	$10.8^{+2.4}_{-2.4}$	$0.95^{+0.13}_{-0.19}$	$1.2^{+0.4}_{-0.4}$	$1.0^{+0.1}_{-0.1}$	$5.4^{+0.5}_{-0.5}$	$1.8^{+1.1}_{-1.1}$	1.05(436)
67	$17.5^{+10.5}_{-11.8}$	$0.29^{+0.11}_{-0.07}$	$1.9^{+1.4}_{-0.9}$	–	0(fix)	$1.5^{+0.1}_{-0.1}$	$7.5^{+0.7}_{-0.7}$	$0.5^{+1.1}_{-0.5}$	1.09(438)
68	$0.0^{+14.9}_{-0.0}$	$0.18^{+0.06}_{-0.01}$	$5.5^{+1.5}_{-3.5}$	–	0(fix)	$1.5^{+0.1}_{-0.1}$	$6.9^{+0.4}_{-0.4}$	$0.3^{+0.6}_{-0.3}$	1.16(438)
69	$16.3^{+16.6}_{-16.3}$	$0.25^{+0.08}_{-0.06}$	$3.5^{+3.7}_{-1.8}$	–	0(fix)	$2.0^{+0.2}_{-0.2}$	$4.9^{+0.9}_{-0.8}$	$0.9^{+1.4}_{-0.9}$	1.30(438)
70	$25.4^{+8.9}_{-12.9}$	–	0(fix)	$0.52^{+0.15}_{-0.28}$	$0.8^{+1.7}_{-0.4}$	$1.5^{+0.1}_{-0.1}$	$6.7^{+0.8}_{-0.7}$	$0.3^{+1.2}_{-0.3}$	1.21(438)
71	$0.0^{+9.6}_{-0.0}$	$0.23^{+0.06}_{-0.03}$	$3.6^{+1.0}_{-1.7}$	–	0(fix)	$1.5^{+0.1}_{-0.1}$	$9.1^{+0.5}_{-0.5}$	$1.0^{+0.6}_{-0.7}$	1.19(438)
72	$0.0^{+20.8}_{-0.0}$	$0.18^{+0.07}_{-0.02}$	$6.4^{+2.8}_{-4.5}$	–	0(fix)	$1.7^{+0.1}_{-0.1}$	$8.0^{+0.7}_{-0.7}$	$0.0^{+0.5}_{-0.0}$	1.09(438)
73	$9.6^{+23.5}_{-9.6}$	$0.18^{+0.15}_{-0.04}$	$4.7^{+5.8}_{-4.1}$	–	0(fix)	$1.7^{+0.1}_{-0.1}$	$7.0^{+0.8}_{-0.8}$	$0.3^{+1.2}_{-0.3}$	1.11(438)
74	$26.1^{+12.5}_{-13.2}$	–	0(fix)	–	0(fix)	$1.9^{+0.1}_{-0.1}$	$9.8^{+0.9}_{-0.8}$	$0.6^{+1.5}_{-0.6}$	1.32(439)
75	$26.6^{+9.1}_{-26.6}$	$0.26^{+0.05}_{-0.10}$	$3.8^{+1.7}_{-1.4}$	$0.94^{+0.37}_{-0.37}$	$0.6^{+0.3}_{-0.3}$	$1.3^{+0.1}_{-0.1}$	$7.9^{+0.6}_{-0.5}$	$0.2^{+0.8}_{-0.2}$	1.05(436)
76	$19.1^{+19.5}_{-19.1}$	$0.19^{+0.09}_{-0.04}$	$5.8^{+7.6}_{-3.5}$	$0.73^{+0.17}_{-0.10}$	$1.3^{+0.4}_{-0.6}$	$1.4^{+0.1}_{-0.1}$	$10.1^{+0.6}_{-0.6}$	$0.2^{+0.8}_{-0.2}$	1.06(436)
77	$11.9^{+10.8}_{-11.7}$	–	0(fix)	–	0(fix)	$2.0^{+0.1}_{-0.1}$	$9.1^{+0.8}_{-0.7}$	$0.5^{+1.3}_{-0.5}$	1.22(440)
78	$24.0^{+7.8}_{-10.9}$	$0.31^{+0.14}_{-0.08}$	$1.3^{+1.3}_{-0.7}$	–	0(fix)	$1.6^{+0.1}_{-0.1}$	$9.6^{+0.6}_{-0.6}$	$0.2^{+1.0}_{-0.2}$	1.25(438)
79	$25.0^{+10.0}_{-25.0}$	$0.28^{+0.65}_{-0.14}$	$1.3^{+7.7}_{-1.1}$	–	0(fix)	$1.6^{+0.1}_{-0.1}$	$6.4^{+0.8}_{-0.7}$	0(fix)	1.11(439)
80	$17.9^{+8.8}_{-10.5}$	$0.31^{+0.10}_{-0.05}$	$4.0^{+1.7}_{-1.4}$	–	0(fix)	$1.4^{+0.1}_{-0.1}$	$6.2^{+0.7}_{-0.7}$	$0.0^{+0.8}_{-0.0}$	1.10(438)
81	$4.8^{+21.9}_{-4.8}$	$0.18^{+0.09}_{-0.03}$	$4.8^{+2.6}_{-3.6}$	–	0(fix)	$1.5^{+0.1}_{-0.1}$	$6.9^{+0.5}_{-0.5}$	$0.5^{+0.9}_{-0.5}$	1.10(438)
82	$4.4^{+29.2}_{-4.4}$	$0.17^{+0.08}_{-0.03}$	$10.2^{+7.3}_{-8.1}$	$0.91^{+0.40}_{-0.25}$	$1.0^{+0.6}_{-0.6}$	$1.9^{+0.1}_{-0.1}$	$10.1^{+1.4}_{-1.3}$	0(fix)	1.08(437)
83	$12.1^{+35.4}_{-12.1}$	$0.18^{+0.04}_{-0.01}$	$23.8^{+11.0}_{-13.2}$	–	0(fix)	$1.8^{+0.1}_{-0.1}$	$11.6^{+0.9}_{-0.9}$	$0.5^{+1.4}_{-0.5}$	1.04(438)
84	$18.1^{+15.1}_{-18.1}$	$0.23^{+0.11}_{-0.11}$	$5.0^{+16.1}_{-3.2}$	$1.03^{+0.26}_{-0.21}$	$1.7^{+0.7}_{-0.7}$	$1.1^{+0.1}_{-0.1}$	$5.6^{+1.0}_{-1.0}$	$1.2^{+1.3}_{-1.2}$	1.19(436)
85	$38.9^{+11.5}_{-13.2}$	–	0(fix)	$0.73^{+0.25}_{-0.59}$	$1.0^{+0.7}_{-0.7}$	$2.1^{+0.2}_{-0.2}$	$10.3^{+1.6}_{-1.5}$	$0.0^{+1.2}_{-0.0}$	1.22(438)
86	$24.8^{+19.8}_{-22.3}$	$0.24^{+0.05}_{-0.04}$	$6.2^{+4.4}_{-2.5}$	–	0(fix)	$1.8^{+0.2}_{-0.2}$	$6.0^{+0.8}_{-0.8}$	$2.5^{+1.5}_{-1.5}$	1.30(438)
87	$14.7^{+7.0}_{-14.7}$	$0.28^{+0.11}_{-0.10}$	$1.9^{+4.7}_{-0.8}$	–	0(fix)	$1.4^{+0.1}_{-0.1}$	$7.1^{+0.5}_{-0.6}$	$0.0^{+0.5}_{-0.0}$	1.03(438)
88	$0.0^{+33.1}_{-0.0}$	$0.17^{+0.05}_{-0.02}$	$22.2^{+4.5}_{-13.4}$	$0.76^{+0.15}_{-0.08}$	$1.7^{+0.4}_{-0.6}$	$1.4^{+0.1}_{-0.1}$	$6.9^{+0.7}_{-0.6}$	0(fix)	1.12(437)

Continued from previous page.

ID	Norm$_1$*	kT_2†	Norm$_2$*	kT_3†	Norm$_3$*	Γ_{CXB}‖	S_{CXB}‡	O I§	χ^2/dof (dof)
89	$17.3^{+8.8}_{-11.1}$	$0.31^{+0.03}_{-0.02}$	$7.0^{+1.2}_{-1.2}$	–	0(fix)	$1.7^{+0.1}_{-0.1}$	$9.1^{+0.7}_{-0.7}$	$0.1^{+1.0}_{-0.1}$	1.03(438)
90	$14.0^{+15.0}_{-14.0}$	$0.25^{+0.07}_{-0.06}$	$3.3^{+3.4}_{-1.6}$	–	0(fix)	$1.4^{+0.1}_{-0.1}$	$7.9^{+0.6}_{-0.6}$	$1.1^{+1.2}_{-1.1}$	1.02(438)
91	$7.6^{+18.0}_{-7.6}$	$0.17^{+0.05}_{-0.02}$	$7.5^{+5.7}_{-4.7}$	$0.63^{+0.13}_{-0.09}$	$1.0^{+0.3}_{-0.4}$	$1.3^{+0.0}_{-0.0}$	$11.9^{+0.5}_{-0.5}$	$0.9^{+0.7}_{-0.7}$	1.20(436)
92	$14.6^{+11.7}_{-14.6}$	$0.23^{+0.09}_{-0.06}$	$2.6^{+4.5}_{-1.5}$	–	0(fix)	$1.4^{+0.1}_{-0.1}$	$5.6^{+0.6}_{-0.6}$	$0.0^{+0.8}_{-0.0}$	1.04(438)
93	$15.7^{+8.7}_{-9.5}$	–	0(fix)	–	0(fix)	$2.5^{+0.1}_{-0.1}$	$7.5^{+0.7}_{-0.4}$	$0.0^{+0.8}_{-0.0}$	1.12(439)
94	$36.9^{+8.5}_{-9.1}$	–	0(fix)	–	0(fix)	$1.7^{+0.1}_{-0.1}$	$11.5^{+0.6}_{-0.6}$	$0.0^{+0.7}_{-0.0}$	1.08(440)
95	$38.3^{+8.7}_{-8.7}$	–	0(fix)	$0.59^{+0.08}_{-0.13}$	$1.6^{+0.4}_{-0.4}$	$1.6^{+0.1}_{-0.1}$	$8.7^{+0.8}_{-0.7}$	$0.0^{+0.6}_{-0.0}$	1.13(438)
96	0(fix)	$0.17^{+0.02}_{-0.03}$	$13.6^{+8.4}_{-4.5}$	–	0(fix)	$2.3^{+0.2}_{-0.2}$	$10.6^{+1.1}_{-1.3}$	$1.6^{+1.8}_{-1.6}$	1.30(439)
97	$1.7^{+26.7}_{-1.7}$	$0.18^{+0.06}_{-0.03}$	$9.0^{+3.0}_{-6.7}$	–	0(fix)	$1.6^{+0.1}_{-0.1}$	$6.2^{+0.6}_{-0.6}$	$0.8^{+0.9}_{-0.8}$	0.88(438)
98	0(fix)	$0.21^{+0.03}_{-0.02}$	$10.6^{+3.1}_{-3.0}$	–	0(fix)	$1.9^{+0.1}_{-0.1}$	$11.5^{+1.1}_{-1.0}$	$0.2^{+1.2}_{-0.2}$	0.96(439)
99	$26.2^{+17.9}_{-26.2}$	$0.19^{+0.16}_{-0.07}$	$3.5^{+12.8}_{-3.0}$	–	0(fix)	$1.7^{+0.1}_{-0.1}$	$10.5^{+0.8}_{-0.8}$	0(fix)	1.20(439)
100	$35.6^{+12.5}_{-21.8}$	$0.26^{+0.04}_{-0.04}$	$6.9^{+3.7}_{-1.9}$	–	0(fix)	$1.8^{+0.1}_{-0.1}$	$7.6^{+0.9}_{-0.9}$	$0.0^{+1.3}_{-0.0}$	1.15(438)
101	$14.8^{+12.9}_{-14.8}$	$0.22^{+0.06}_{-0.04}$	$5.2^{+5.7}_{-2.5}$	–	0(fix)	$1.5^{+0.1}_{-0.1}$	$7.1^{+0.7}_{-0.7}$	$0.0^{+1.1}_{-0.0}$	1.12(438)
102	$60.6^{+20.0}_{-60.6}$	$0.23^{+0.08}_{-0.09}$	$5.7^{+24.6}_{-3.2}$	–	0(fix)	$2.3^{+0.2}_{-0.2}$	$8.7^{+1.3}_{-1.3}$	$0.0^{+1.5}_{-0.0}$	1.25(436)
103	$8.1^{+21.4}_{-8.1}$	$0.19^{+0.14}_{-0.04}$	$6.1^{+6.4}_{-5.0}$	–	0(fix)	$1.6^{+0.1}_{-0.1}$	$6.5^{+0.8}_{-0.7}$	$0.5^{+1.1}_{-0.5}$	0.99(438)
104	$25.6^{+8.3}_{-7.5}$	$0.28^{+0.11}_{-0.08}$	$2.1^{+1.9}_{-1.0}$	–	0(fix)	$1.6^{+0.1}_{-0.1}$	$8.9^{+0.6}_{-0.6}$	0(fix)	0.90(439)
105	$21.4^{+39.7}_{-0.0}$	$0.21^{+0.03}_{-0.03}$	$10.7^{+9.0}_{-3.9}$	–	0(fix)	$1.8^{+0.1}_{-0.1}$	$6.4^{+0.8}_{-0.8}$	$0.0^{+1.1}_{-0.0}$	1.13(438)
106	$33.7^{+9.6}_{-17.2}$	$0.27^{+0.10}_{-0.08}$	$2.7^{+3.6}_{-1.3}$	–	0(fix)	$1.6^{+0.1}_{-0.1}$	$7.6^{+0.8}_{-0.8}$	$0.0^{+1.2}_{-0.0}$	1.09(438)
107	$2.5^{+24.8}_{-2.5}$	$0.19^{+0.11}_{-0.04}$	$5.8^{+2.4}_{-4.6}$	–	0(fix)	$1.9^{+0.1}_{-0.1}$	$7.6^{+0.9}_{-0.9}$	$0.4^{+1.1}_{-0.4}$	0.99(438)
108	0(fix)	$0.17^{+0.02}_{-0.03}$	$8.4^{+4.2}_{-1.9}$	$0.85^{+0.07}_{-0.11}$	$1.0^{+0.4}_{-0.4}$	$1.7^{+0.1}_{-0.1}$	$8.0^{+0.8}_{-0.7}$	0(fix)	1.09(438)
109	$19.4^{+8.6}_{-9.5}$	$0.28^{+0.12}_{-0.09}$	$2.0^{+3.2}_{-1.0}$	–	0(fix)	$1.4^{+0.1}_{-0.1}$	$5.9^{+0.7}_{-0.7}$	$0.0^{+1.0}_{-0.0}$	1.11(438)
110	$0.2^{+35.1}_{-0.2}$	$0.16^{+0.07}_{-0.02}$	$16.4^{+3.8}_{-12.4}$	$0.71^{+0.13}_{-0.10}$	$1.0^{+0.4}_{-0.4}$	$1.7^{+0.1}_{-0.1}$	$11.2^{+0.8}_{-0.8}$	$0.3^{+1.0}_{-0.3}$	0.99(436)
111	$15.2^{+9.5}_{-9.6}$	–	0(fix)	$0.86^{+0.12}_{-0.13}$	$1.1^{+0.6}_{-0.5}$	$2.0^{+0.2}_{-0.2}$	$8.4^{+1.2}_{-1.2}$	0(fix)	1.11(439)
112	$39.2^{+10.3}_{-13.6}$	$0.25^{+0.06}_{-0.04}$	$3.9^{+2.1}_{-1.5}$	–	0(fix)	$1.6^{+0.1}_{-0.1}$	$10.6^{+0.6}_{-0.6}$	$0.0^{+0.9}_{-0.0}$	1.08(438)
113	$38.1^{+17.1}_{-18.6}$	$0.26^{+0.03}_{-0.02}$	$9.7^{+2.6}_{-2.2}$	$1.04^{+0.30}_{-0.29}$	$0.7^{+0.4}_{-0.4}$	$1.2^{+0.1}_{-0.1}$	$7.9^{+0.7}_{-0.6}$	$0.7^{+1.2}_{-0.7}$	0.96(436)
114	$17.8^{+12.5}_{-17.8}$	$0.28^{+0.08}_{-0.06}$	$3.7^{+3.3}_{-1.4}$	–	0(fix)	$1.7^{+0.1}_{-0.1}$	$5.9^{+0.6}_{-0.6}$	$0.9^{+1.2}_{-0.9}$	1.12(438)
115	$56.9^{+9.9}_{-15.5}$	$0.28^{+0.03}_{-0.03}$	$6.8^{+2.4}_{-1.2}$	–	0(fix)	$1.6^{+0.1}_{-0.1}$	$9.0^{+0.7}_{-0.7}$	$0.0^{+1.0}_{-0.0}$	1.14(438)
116	$38.2^{+14.2}_{-24.3}$	$0.23^{+0.08}_{-0.06}$	$3.1^{+6.2}_{-1.7}$	–	0(fix)	$1.5^{+0.1}_{-0.1}$	$6.7^{+0.7}_{-0.6}$	$0.0^{+0.9}_{-0.0}$	0.92(438)
117	$35.6^{+12.1}_{-17.6}$	$0.26^{+0.06}_{-0.05}$	$3.5^{+2.3}_{-1.4}$	–	0(fix)	$1.6^{+0.1}_{-0.1}$	$7.6^{+0.6}_{-0.6}$	$0.2^{+1.1}_{-0.2}$	1.06(438)
118	$37.7^{+34.9}_{-37.7}$	$0.17^{+0.08}_{-0.05}$	$7.5^{+17.4}_{-6.0}$	–	0(fix)	$1.7^{+0.1}_{-0.1}$	$7.4^{+0.6}_{-0.6}$	$1.0^{+1.5}_{-1.0}$	1.23(438)
119	$40.2^{+21.7}_{-40.2}$	$0.24^{+0.08}_{-0.06}$	$4.3^{+7.7}_{-2.3}$	–	0(fix)	$1.8^{+0.1}_{-0.1}$	$7.4^{+0.9}_{-0.8}$	$0.6^{+1.7}_{-0.6}$	1.25(438)
120	$30.6^{+14.6}_{-20.6}$	$0.28^{+0.13}_{-0.07}$	$3.2^{+3.1}_{-1.6}$	–	0(fix)	$1.7^{+0.1}_{-0.1}$	$8.8^{+0.9}_{-0.8}$	$0.7^{+1.3}_{-0.7}$	1.23(438)
121	$36.1^{+14.2}_{-17.3}$	$0.25^{+0.06}_{-0.05}$	$5.1^{+3.8}_{-2.1}$	–	0(fix)	$1.6^{+0.1}_{-0.1}$	$6.1^{+0.7}_{-0.7}$	$0.0^{+0.8}_{-0.0}$	1.18(438)
122	$29.0^{+20.4}_{-28.1}$	$0.26^{+0.06}_{-0.06}$	$4.5^{+5.3}_{-1.9}$	–	0(fix)	$1.5^{+0.1}_{-0.1}$	$5.9^{+0.9}_{-0.8}$	$1.5^{+1.9}_{-1.5}$	1.19(438)
123	$31.0^{+11.8}_{-23.4}$	$0.27^{+0.19}_{-0.10}$	$2.2^{+4.8}_{-1.4}$	–	0(fix)	$1.7^{+0.1}_{-0.1}$	$10.2^{+0.9}_{-0.9}$	0(fix)	1.03(439)
124	$19.1^{+6.7}_{-10.9}$	$0.27^{+0.02}_{-0.03}$	$4.7^{+1.6}_{-0.8}$	–	0(fix)	$1.5^{+0.1}_{-0.1}$	$7.7^{+0.4}_{-0.4}$	$0.0^{+0.6}_{-0.0}$	1.05(438)
125	$36.8^{+8.2}_{-10.9}$	$0.26^{+0.05}_{-0.04}$	$3.7^{+2.3}_{-1.2}$	–	0(fix)	$1.6^{+0.1}_{-0.1}$	$6.4^{+0.5}_{-0.5}$	$0.0^{+0.5}_{-0.0}$	1.09(438)
126	$14.5^{+16.4}_{-14.5}$	$0.20^{+0.05}_{-0.03}$	$9.1^{+7.3}_{-4.4}$	–	0(fix)	$1.7^{+0.1}_{-0.1}$	$8.7^{+0.7}_{-0.7}$	0(fix)	1.00(439)
127	$34.6^{+7.0}_{-7.5}$	–	0(fix)	$0.58^{+0.04}_{-0.04}$	$3.0^{+0.3}_{-0.4}$	$1.5^{+0.1}_{-0.1}$	$8.2^{+0.7}_{-0.6}$	$0.0^{+0.6}_{-0.0}$	1.16(438)
128	$47.8^{+9.5}_{-11.6}$	$0.26^{+0.03}_{-0.03}$	$8.2^{+3.2}_{-1.9}$	–	0(fix)	$1.6^{+0.1}_{-0.1}$	$8.7^{+0.7}_{-0.6}$	0(fix)	1.06(439)
129	$0.0^{+14.4}_{-0.0}$	$0.17^{+0.15}_{-0.08}$	$7.0^{+36.4}_{-4.3}$	–	0(fix)	$1.7^{+0.1}_{-0.1}$	$17.9^{+1.1}_{-1.1}$	0(fix)	1.18(439)
130	$58.8^{+9.9}_{-12.9}$	–	0(fix)	$0.74^{+0.09}_{-0.11}$	$1.4^{+0.4}_{-0.4}$	$1.7^{+0.1}_{-0.1}$	$7.2^{+0.9}_{-0.8}$	$0.0^{+1.3}_{-0.0}$	1.11(438)
131	$44.2^{+32.9}_{-44.2}$	$0.24^{+0.06}_{-0.05}$	$8.1^{+9.5}_{-3.7}$	–	0(fix)	$2.0^{+0.2}_{-0.2}$	$10.1^{+1.4}_{-1.3}$	$1.3^{+2.4}_{-1.3}$	1.17(438)
132	$56.5^{+77.1}_{-0.0}$	$0.19^{+0.09}_{-0.05}$	$4.1^{+17.5}_{-2.9}$	–	0(fix)	$1.5^{+0.1}_{-0.1}$	$8.9^{+0.5}_{-0.5}$	$2.8^{+1.1}_{-1.1}$	1.06(438)
133	$67.5^{+22.4}_{-67.5}$	$0.22^{+0.09}_{-0.08}$	$6.6^{+31.2}_{-3.5}$	$0.66^{+0.06}_{-0.06}$	$3.4^{+1.1}_{-1.3}$	$1.8^{+0.2}_{-0.2}$	$5.8^{+1.0}_{-0.9}$	$0.0^{+1.3}_{-0.0}$	1.27(436)

Continued from previous page.

ID	Norm$_1$*	$kT_2{}^\dagger$	Norm$_2$*	$kT_3{}^\dagger$	Norm$_3$*	$\Gamma_{\mathrm{CXB}}{}^\|$	$S_{\mathrm{CXB}}{}^\ddagger$	O I§	χ^2/dof (dof)
134	$10.2^{+32.6}_{-10.2}$	$0.20^{+0.06}_{-0.02}$	$11.3^{+4.7}_{-5.9}$	–	0(fix)	$2.2^{+0.2}_{-0.2}$	$6.8^{+1.0}_{-1.0}$	0(fix)	1.13(439)
135	0(fix)	$0.16^{+0.02}_{-0.02}$	$13.8^{+5.5}_{-3.3}$	$0.68^{+0.15}_{-0.13}$	$0.8^{+0.4}_{-0.5}$	$1.8^{+0.2}_{-0.2}$	$5.1^{+0.9}_{-0.8}$	0(fix)	1.13(438)
136	$23.3^{+24.1}_{-23.3}$	$0.17^{+0.09}_{-0.05}$	$7.3^{+31.7}_{-5.9}$	$0.77^{+0.16}_{-0.11}$	$1.2^{+0.4}_{-0.5}$	$1.8^{+0.1}_{-0.1}$	$9.4^{+0.9}_{-0.8}$	$0.0^{+1.1}_{-0.0}$	1.03(436)
137	$80.8^{+15.5}_{-14.8}$	$0.32^{+0.11}_{-0.04}$	$4.0^{+1.2}_{-1.3}$	–	0(fix)	$1.6^{+0.1}_{-0.1}$	$9.9^{+0.6}_{-0.6}$	$1.0^{+1.3}_{-1.0}$	1.15(438)
138	$47.3^{+65.7}_{-0.0}$	$0.22^{+0.08}_{-0.08}$	$4.6^{+15.8}_{-2.3}$	$0.67^{+0.22}_{-0.13}$	$1.1^{+0.8}_{-0.9}$	$1.7^{+0.1}_{-0.1}$	$8.9^{+0.8}_{-0.8}$	$0.3^{+1.3}_{-0.3}$	1.05(436)
139	$45.4^{+12.1}_{-13.7}$	$0.30^{+0.21}_{-0.07}$	$2.8^{+1.1}_{-1.5}$	–	0(fix)	$1.8^{+0.1}_{-0.1}$	$8.4^{+0.8}_{-0.8}$	$0.0^{+0.7}_{-0.0}$	1.05(438)
140	$26.9^{+16.2}_{-21.6}$	$0.24^{+0.13}_{-0.06}$	$3.3^{+5.7}_{-2.1}$	–	0(fix)	$1.6^{+0.1}_{-0.1}$	$8.2^{+0.8}_{-0.7}$	$3.8^{+1.4}_{-1.4}$	1.18(438)
141	$4.8^{+24.5}_{-4.8}$	$0.20^{+0.05}_{-0.02}$	$8.2^{+3.0}_{-4.0}$	–	0(fix)	$1.7^{+0.1}_{-0.1}$	$7.6^{+0.7}_{-0.7}$	$3.6^{+1.4}_{-1.5}$	1.09(438)
142	$33.0^{+14.5}_{-19.1}$	$0.28^{+0.12}_{-0.06}$	$3.3^{+2.6}_{-1.5}$	–	0(fix)	$1.5^{+0.1}_{-0.1}$	$8.5^{+0.7}_{-0.6}$	$2.3^{+1.4}_{-1.3}$	1.01(438)
143	$28.2^{+24.6}_{-28.2}$	$0.22^{+0.07}_{-0.05}$	$4.8^{+10.3}_{-3.0}$	–	0(fix)	$1.8^{+0.1}_{-0.1}$	$11.6^{+1.0}_{-1.0}$	$3.9^{+2.1}_{-2.0}$	1.06(438)
144	$34.8^{+23.1}_{-24.5}$	$0.24^{+0.04}_{-0.03}$	$7.4^{+3.8}_{-2.7}$	–	0(fix)	$1.9^{+0.1}_{-0.1}$	$12.0^{+0.9}_{-0.8}$	$3.3^{+1.6}_{-1.6}$	1.13(438)
145	0(fix)	$0.15^{+0.03}_{-0.04}$	$15.3^{+24.1}_{-7.9}$	–	0(fix)	$2.0^{+0.1}_{-0.1}$	$11.2^{+1.1}_{-1.0}$	$2.6^{+2.2}_{-2.2}$	1.30(437)
146	$30.7^{+14.8}_{-20.4}$	$0.39^{+0.19}_{-0.15}$	$1.8^{+2.5}_{-0.9}$	–	0(fix)	$1.6^{+0.1}_{-0.1}$	$9.7^{+0.9}_{-0.9}$	$1.0^{+1.7}_{-1.0}$	1.10(438)
147	$39.7^{+21.4}_{-21.7}$	$0.24^{+0.04}_{-0.03}$	$6.7^{+3.5}_{-2.5}$	–	0(fix)	$1.6^{+0.1}_{-0.1}$	$8.6^{+0.7}_{-0.7}$	$1.9^{+1.5}_{-1.5}$	1.03(438)
148	$36.3^{+21.0}_{-36.3}$	$0.23^{+0.06}_{-0.05}$	$5.3^{+8.1}_{-2.5}$	–	0(fix)	$1.6^{+0.1}_{-0.1}$	$7.7^{+0.7}_{-0.7}$	$1.3^{+1.4}_{-1.3}$	1.17(438)
149	$39.5^{+13.8}_{-18.2}$	$0.27^{+0.04}_{-0.04}$	$3.5^{+2.0}_{-1.0}$	–	0(fix)	$1.4^{+0.1}_{-0.1}$	$9.6^{+0.5}_{-0.5}$	$4.5^{+1.3}_{-1.3}$	1.15(438)
150	$10.4^{+26.0}_{-10.4}$	$0.22^{+0.04}_{-0.03}$	$9.6^{+5.1}_{-3.6}$	–	0(fix)	$1.8^{+0.1}_{-0.1}$	$6.7^{+0.8}_{-0.8}$	$12.0^{+2.1}_{-2.3}$	0.96(438)
151	$8.7^{+33.2}_{-8.7}$	$0.17^{+0.03}_{-0.01}$	$13.7^{+6.5}_{-6.8}$	$0.75^{+0.23}_{-0.14}$	$0.6^{+0.3}_{-0.3}$	$1.6^{+0.1}_{-0.1}$	$5.4^{+0.6}_{-0.6}$	$4.7^{+1.5}_{-1.6}$	1.06(436)
152	$42.8^{+12.2}_{-12.3}$	$0.24^{+0.04}_{-0.02}$	$5.5^{+2.0}_{-1.7}$	–	0(fix)	$1.5^{+0.1}_{-0.0}$	$9.1^{+0.5}_{-0.4}$	$1.9^{+0.9}_{-0.9}$	1.22(438)
153	0(fix)	$0.17^{+0.01}_{-0.02}$	$17.9^{+6.5}_{-3.6}$	$1.08^{+0.17}_{-0.10}$	$1.6^{+0.8}_{-0.6}$	$1.8^{+0.1}_{-0.1}$	$9.1^{+1.2}_{-1.1}$	$0.6^{+1.3}_{-0.6}$	1.07(437)
154	$29.3^{+21.6}_{-29.3}$	$0.22^{+0.05}_{-0.05}$	$7.6^{+9.6}_{-3.5}$	$1.08^{+0.23}_{-0.20}$	$1.0^{+0.8}_{-0.5}$	$1.9^{+0.1}_{-0.1}$	$10.3^{+0.7}_{-0.7}$	$0.7^{+1.5}_{-0.7}$	1.11(435)
155	$22.7^{+49.4}_{-22.7}$	$0.17^{+0.09}_{-0.04}$	$12.7^{+17.1}_{-10.1}$	$0.97^{+0.14}_{-0.12}$	$2.1^{+0.7}_{-0.7}$	$1.9^{+0.1}_{-0.1}$	$9.2^{+1.4}_{-1.3}$	$0.8^{+1.9}_{-0.8}$	1.15(435)
156	$37.9^{+17.1}_{-17.5}$	$0.32^{+0.05}_{-0.05}$	$3.9^{+1.5}_{-1.5}$	–	0(fix)	$1.6^{+0.1}_{-0.1}$	$8.9^{+0.8}_{-0.8}$	$5.1^{+1.7}_{-1.7}$	1.10(438)
157	$37.4^{+14.5}_{-16.7}$	$0.25^{+0.06}_{-0.05}$	$3.8^{+3.0}_{-1.6}$	–	0(fix)	$1.4^{+0.1}_{-0.1}$	$9.4^{+0.6}_{-0.6}$	$1.4^{+1.1}_{-1.1}$	0.93(438)
158	$50.0^{+18.4}_{-21.3}$	$0.26^{+0.06}_{-0.05}$	$4.2^{+3.1}_{-1.7}$	–	0(fix)	$1.5^{+0.1}_{-0.1}$	$7.5^{+0.7}_{-0.7}$	$4.1^{+1.8}_{-1.8}$	1.05(438)
159	$96.4^{+16.3}_{-25.0}$	–	0(fix)	$0.54^{+0.13}_{-0.33}$	$0.7^{+2.4}_{-0.3}$	$1.5^{+0.1}_{-0.1}$	$8.1^{+0.7}_{-0.7}$	$12.1^{+2.2}_{-2.2}$	1.06(438)
160	$53.1^{+19.8}_{-19.0}$	–	0(fix)	$0.43^{+0.12}_{-0.13}$	$2.6^{+1.8}_{-0.9}$	$1.7^{+0.2}_{-0.2}$	$4.7^{+1.0}_{-0.9}$	$8.7^{+2.5}_{-2.6}$	1.29(437)
161	$32.6^{+19.5}_{-27.1}$	$0.25^{+0.06}_{-0.06}$	$4.2^{+5.7}_{-2.0}$	–	0(fix)	$1.6^{+0.1}_{-0.1}$	$7.3^{+0.8}_{-0.7}$	$2.9^{+1.7}_{-1.7}$	1.15(438)
162	$51.8^{+32.5}_{-51.8}$	$0.22^{+0.09}_{-0.07}$	$4.7^{+18.0}_{-3.0}$	–	0(fix)	$1.7^{+0.1}_{-0.1}$	$8.7^{+0.9}_{-0.9}$	$20.1^{+3.0}_{-3.0}$	1.06(438)
163	$15.2^{+19.0}_{-15.2}$	$0.24^{+0.09}_{-0.06}$	$3.0^{+4.0}_{-1.2}$	–	0(fix)	$2.1^{+0.2}_{-0.1}$	$6.1^{+0.8}_{-0.7}$	$6.0^{+1.7}_{-1.7}$	1.19(438)
164	$34.0^{+16.1}_{-19.0}$	–	0(fix)	$0.42^{+0.14}_{-0.13}$	$1.9^{+1.6}_{-0.8}$	$1.9^{+0.1}_{-0.1}$	$11.0^{+1.2}_{-1.1}$	$2.7^{+1.9}_{-1.8}$	1.11(438)
165	$65.8^{+16.8}_{-16.8}$	$0.30^{+0.03}_{-0.02}$	$8.5^{+1.3}_{-1.4}$	–	0(fix)	$1.8^{+0.1}_{-0.1}$	$8.9^{+0.7}_{-0.7}$	$5.4^{+1.6}_{-1.6}$	1.13(438)
166	$38.2^{+16.5}_{-16.6}$	$0.30^{+0.06}_{-0.03}$	$5.0^{+1.4}_{-1.3}$	–	0(fix)	$1.6^{+0.1}_{-0.1}$	$6.8^{+0.7}_{-0.6}$	$2.8^{+1.6}_{-1.6}$	1.05(438)
167	$28.9^{+35.5}_{-28.9}$	$0.20^{+0.04}_{-0.02}$	$15.0^{+9.6}_{-7.4}$	–	0(fix)	$1.1^{+0.1}_{-0.1}$	$9.0^{+0.6}_{-0.6}$	$2.2^{+1.6}_{-1.6}$	1.03(438)
168	$91.2^{+30.6}_{-31.5}$	$0.24^{+0.03}_{-0.02}$	$19.5^{+5.6}_{-5.5}$	–	0(fix)	$1.9^{+0.1}_{-0.1}$	$10.6^{+1.1}_{-1.0}$	$1.0^{+2.1}_{-1.0}$	1.03(438)
169	$42.1^{+23.6}_{-42.1}$	$0.23^{+0.04}_{-0.05}$	$11.6^{+11.0}_{-3.0}$	$0.72^{+0.23}_{-0.14}$	$1.1^{+1.2}_{-0.7}$	$1.5^{+0.1}_{-0.1}$	$8.6^{+0.7}_{-0.7}$	$2.5^{+1.5}_{-1.5}$	1.10(436)
170	$98.6^{+31.2}_{-31.2}$	$0.23^{+0.03}_{-0.02}$	$13.1^{+5.2}_{-4.2}$	–	0(fix)	$1.6^{+0.1}_{-0.1}$	$6.0^{+0.7}_{-0.6}$	$4.1^{+2.3}_{-2.3}$	1.14(438)
171	$2.1^{+51.1}_{-2.1}$	$0.17^{+0.05}_{-0.03}$	$14.7^{+5.2}_{-10.0}$	–	0(fix)	$2.1^{+0.2}_{-0.2}$	$6.4^{+0.8}_{-0.8}$	$8.7^{+1.2}_{-2.3}$	1.18(437)
172	$35.0^{+23.0}_{-30.5}$	$0.23^{+0.08}_{-0.05}$	$5.8^{+7.3}_{-3.1}$	–	0(fix)	$1.6^{+0.1}_{-0.1}$	$5.5^{+0.7}_{-0.7}$	$1.5^{+1.6}_{-1.5}$	1.19(438)
173	$46.2^{+17.3}_{-20.4}$	$0.28^{+0.04}_{-0.04}$	$6.0^{+2.3}_{-1.4}$	–	0(fix)	$1.8^{+0.1}_{-0.1}$	$9.6^{+0.8}_{-0.8}$	$4.5^{+1.7}_{-1.7}$	0.95(438)
174	$48.9^{+20.0}_{-48.9}$	$0.22^{+0.43}_{-0.11}$	$2.2^{+24.0}_{-2.0}$	–	0(fix)	$1.7^{+0.1}_{-0.1}$	$7.6^{+0.7}_{-0.7}$	$5.4^{+1.7}_{-1.7}$	0.98(438)
175	$56.9^{+18.2}_{-23.7}$	$0.28^{+0.04}_{-0.04}$	$5.9^{+2.6}_{-1.4}$	–	0(fix)	$1.8^{+0.1}_{-0.1}$	$8.0^{+0.7}_{-0.7}$	$9.5^{+1.9}_{-1.9}$	1.09(438)
176	$11.6^{+46.9}_{-11.6}$	$0.18^{+0.04}_{-0.01}$	$19.4^{+9.0}_{-12.2}$	–	0(fix)	$1.6^{+0.1}_{-0.1}$	$7.2^{+0.8}_{-0.7}$	$4.0^{+1.0}_{-2.1}$	1.13(438)
177	$0.0^{+21.6}_{-0.0}$	$0.22^{+0.03}_{-0.02}$	$8.0^{+1.4}_{-2.4}$	–	0(fix)	$1.4^{+0.1}_{-0.1}$	$8.6^{+0.6}_{-0.6}$	$30.6^{+1.7}_{-2.2}$	1.05(438)
178	$28.2^{+16.1}_{-19.2}$	$0.26^{+0.06}_{-0.04}$	$4.8^{+2.8}_{-1.7}$	–	0(fix)	$1.1^{+0.1}_{-0.1}$	$7.1^{+0.6}_{-0.5}$	$3.5^{+1.5}_{-1.5}$	1.18(438)

Table continued on next page.

Continued from previous page.

ID	Norm$_1$*	$kT_2^\dagger$	Norm$_2$*	$kT_3^\dagger$	Norm$_3$*	$\Gamma_{\mathrm{CXB}}^{\parallel}$	$S_{\mathrm{CXB}}^\ddagger$	O I§	χ^2/dof (dof)
179	$68.4^{+31.7}_{-31.7}$	$0.23^{+0.02}_{-0.01}$	$19.5^{+4.1}_{-4.1}$	–	0(fix)	$1.6^{+0.1}_{-0.1}$	$7.4^{+0.7}_{-0.7}$	$4.3^{+2.2}_{-2.2}$	1.08(438)
180	$29.4^{+23.1}_{-29.4}$	$0.19^{+0.10}_{-0.07}$	$5.4^{+19.2}_{-4.0}$	$0.73^{+0.26}_{-0.14}$	$0.6^{+0.4}_{-0.5}$	$1.6^{+0.1}_{-0.1}$	$6.1^{+0.7}_{-0.6}$	$2.3^{+1.4}_{-1.4}$	0.99(436)
181	$40.1^{+21.5}_{-29.1}$	$0.25^{+0.08}_{-0.06}$	$4.5^{+5.0}_{-2.1}$	–	0(fix)	$1.9^{+0.1}_{-0.1}$	$13.1^{+1.0}_{-0.9}$	$2.6^{+1.8}_{-1.8}$	1.00(438)
182	$36.8^{+28.3}_{-32.1}$	$0.25^{+0.06}_{-0.05}$	$6.7^{+5.0}_{-2.8}$	–	0(fix)	$1.7^{+0.1}_{-0.1}$	$10.2^{+1.0}_{-1.0}$	$5.7^{+2.4}_{-2.4}$	1.09(438)
183	$22.0^{+10.1}_{-10.4}$	$0.27^{+0.28}_{-0.10}$	$2.3^{+7.5}_{-1.6}$	–	0(fix)	$1.4^{+0.1}_{-0.1}$	$5.8^{+0.7}_{-0.6}$	$1.4^{+1.0}_{-1.0}$	1.03(438)
184	$32.8^{+14.8}_{-15.5}$	$0.25^{+0.03}_{-0.02}$	$7.3^{+2.3}_{-1.9}$	–	0(fix)	$1.3^{+0.1}_{-0.1}$	$8.4^{+0.5}_{-0.5}$	$2.9^{+1.1}_{-1.1}$	1.06(438)
185	$10.2^{+29.8}_{-10.2}$	$0.18^{+0.06}_{-0.02}$	$12.1^{+5.5}_{-6.5}$	$0.62^{+0.16}_{-0.09}$	$1.3^{+0.5}_{-0.8}$	$1.2^{+0.1}_{-0.1}$	$6.8^{+0.5}_{-0.5}$	$3.2^{+1.1}_{-1.1}$	0.89(436)
186	$72.2^{+23.9}_{-26.7}$	$0.29^{+0.06}_{-0.04}$	$6.2^{+2.9}_{-1.9}$	–	0(fix)	$1.7^{+0.1}_{-0.1}$	$6.5^{+0.9}_{-0.8}$	$1.6^{+2.2}_{-1.6}$	1.04(438)
187	$50.0^{+22.6}_{-27.2}$	$0.26^{+0.05}_{-0.03}$	$8.5^{+3.6}_{-2.7}$	–	0(fix)	$1.5^{+0.1}_{-0.1}$	$7.5^{+0.7}_{-0.7}$	$0.7^{+1.7}_{-0.7}$	1.16(438)

Notes.

$*$ The emission measure of the optically-thin thermal CIE plasma integrated over the line of sight (the `apec` model normalization): $(1/2\pi) \int n_e n_H ds$ in unit of 10^{14} cm^{-5} sr^{-1}, where n_e and n_H are the electron and the hydrogen densities (cm^{-3}).

$\dagger$ The temperature of the optically-thin thermal CIE plasma in unit of keV.

$\parallel$ The photon index of the `powerlaw` model for the CXB component.

$\ddagger$ The surface brightness of the CXB component (the `powerlaw` model normalization) in unit of photons cm^{-2} s^{-1} sr^{-1} keV^{-1} at 1 keV.

$\S$ The intensity of neutral oxygen (O I, centroid: 0.525 keV) in unit of LU (photons cm^{-2} s^{-1} sr^{-1}).
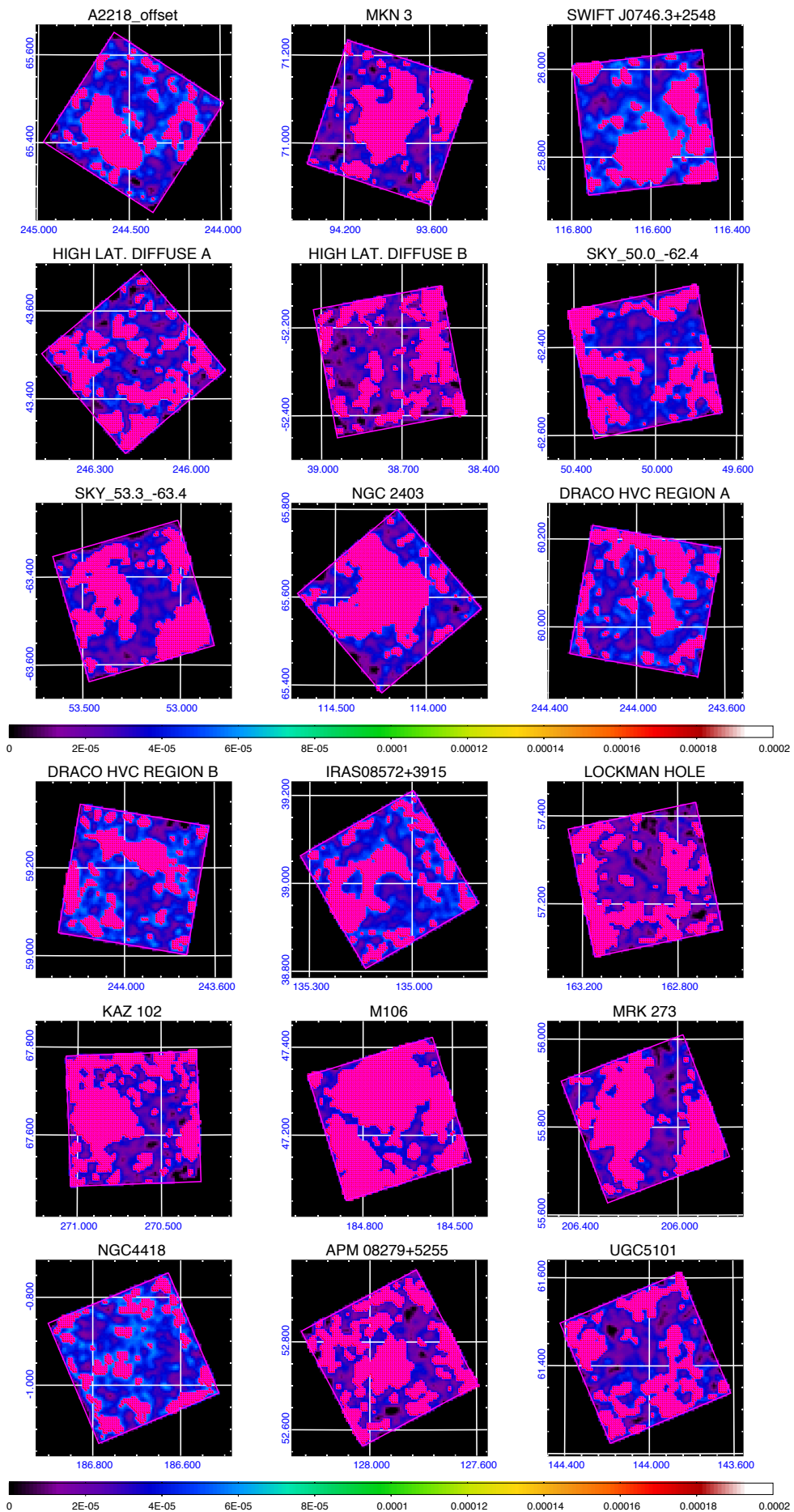
Figure A.1   XIS1 images in the 0.5 – 5.0 keV range of observations ID 1 – 18.
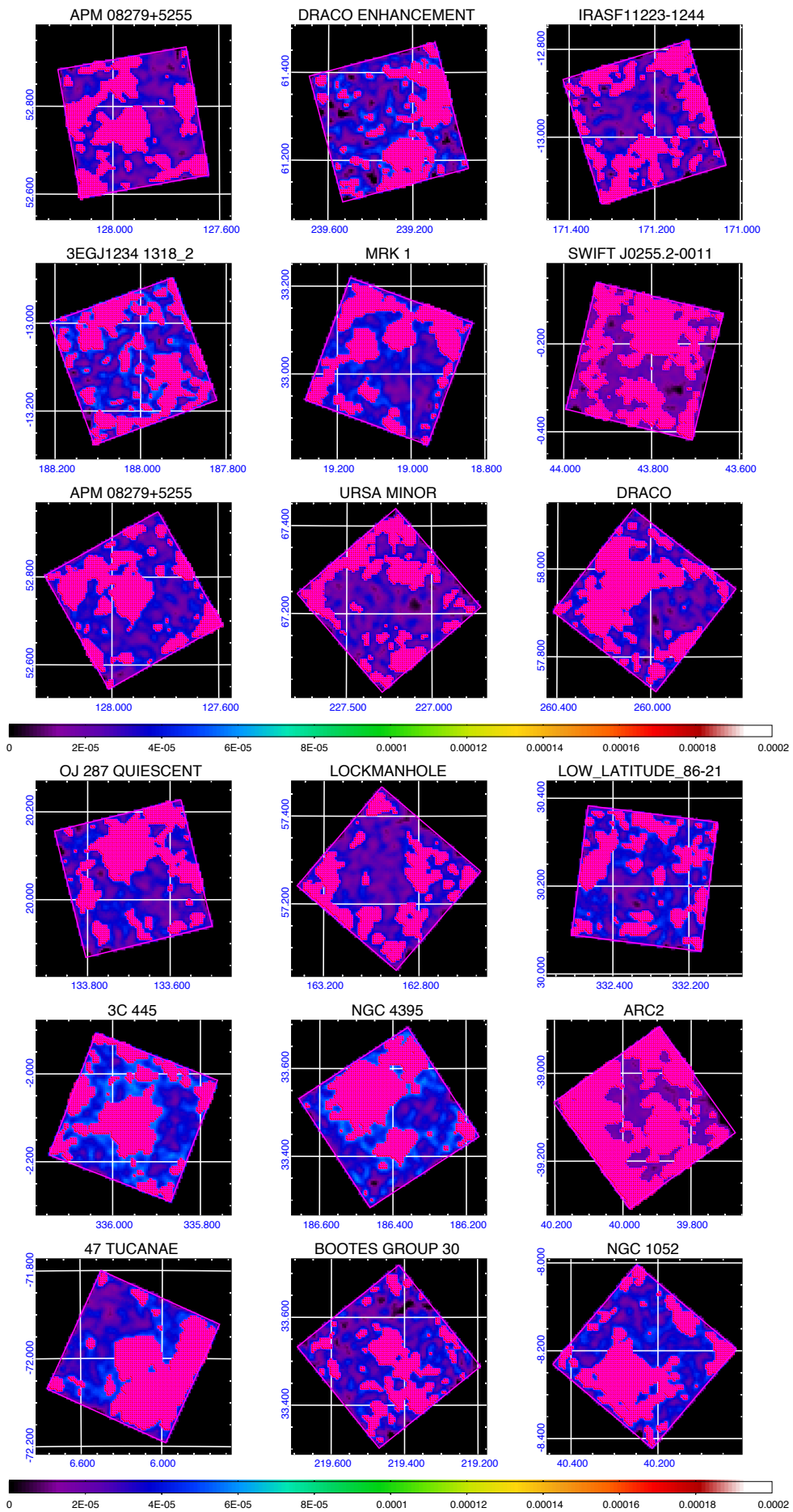
Figure A.2 Same as Figure A.1 but for ID 19 – 36.
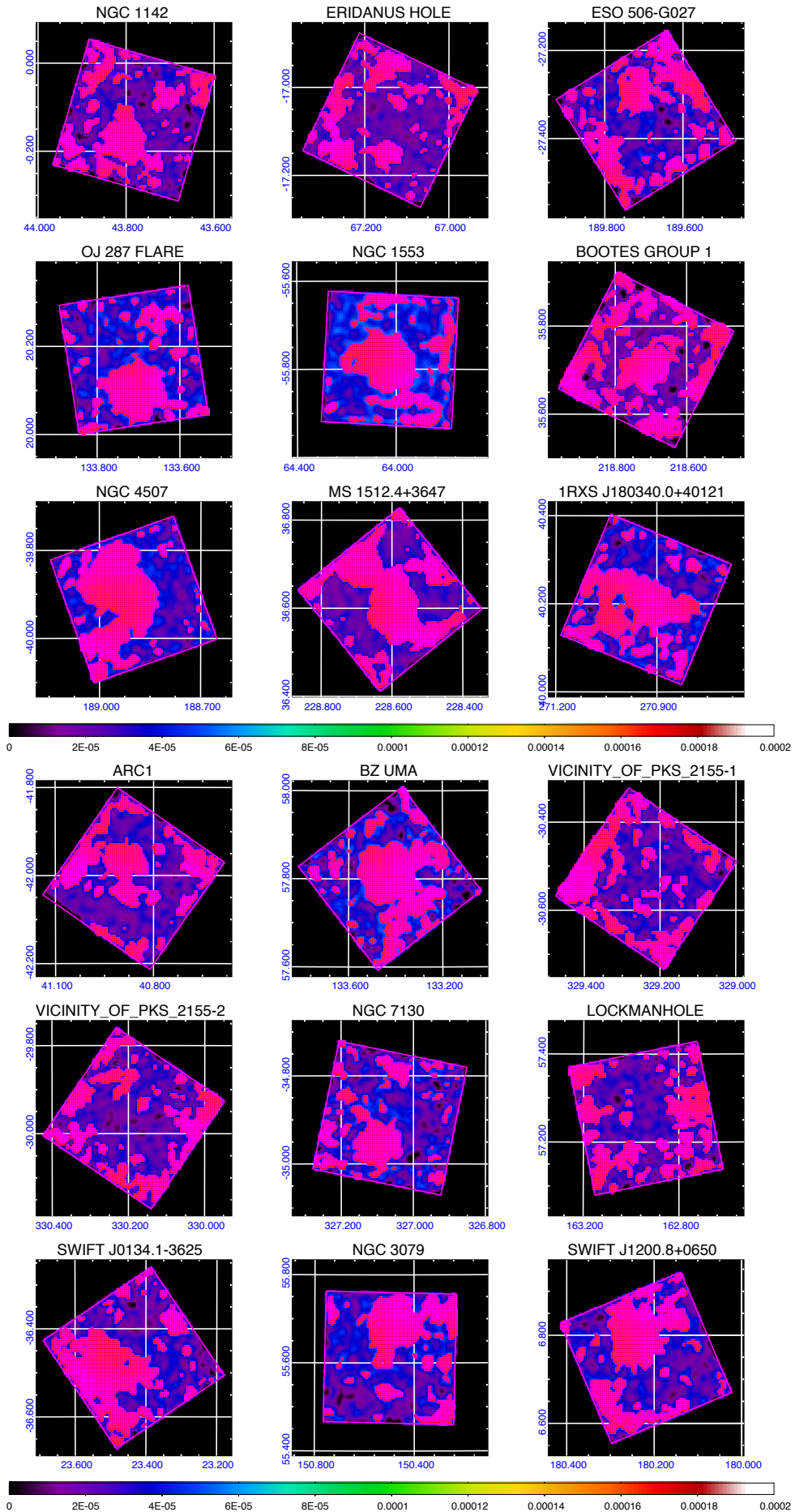
Figure A.3   Same as Figure A.1 but for ID 37 – 54.
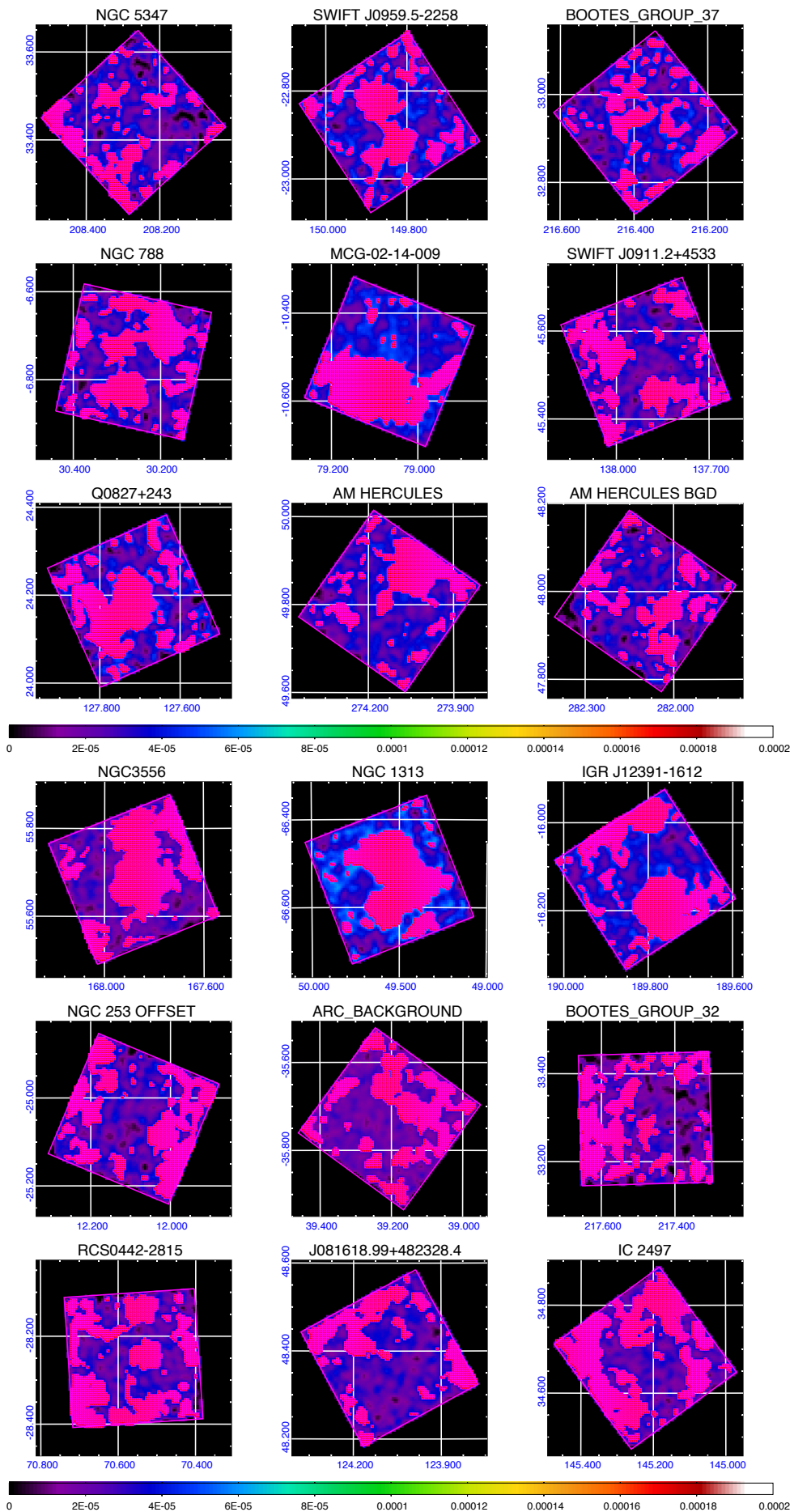
Figure A.4   Same as Figure A.1 but for ID 55 – 72.
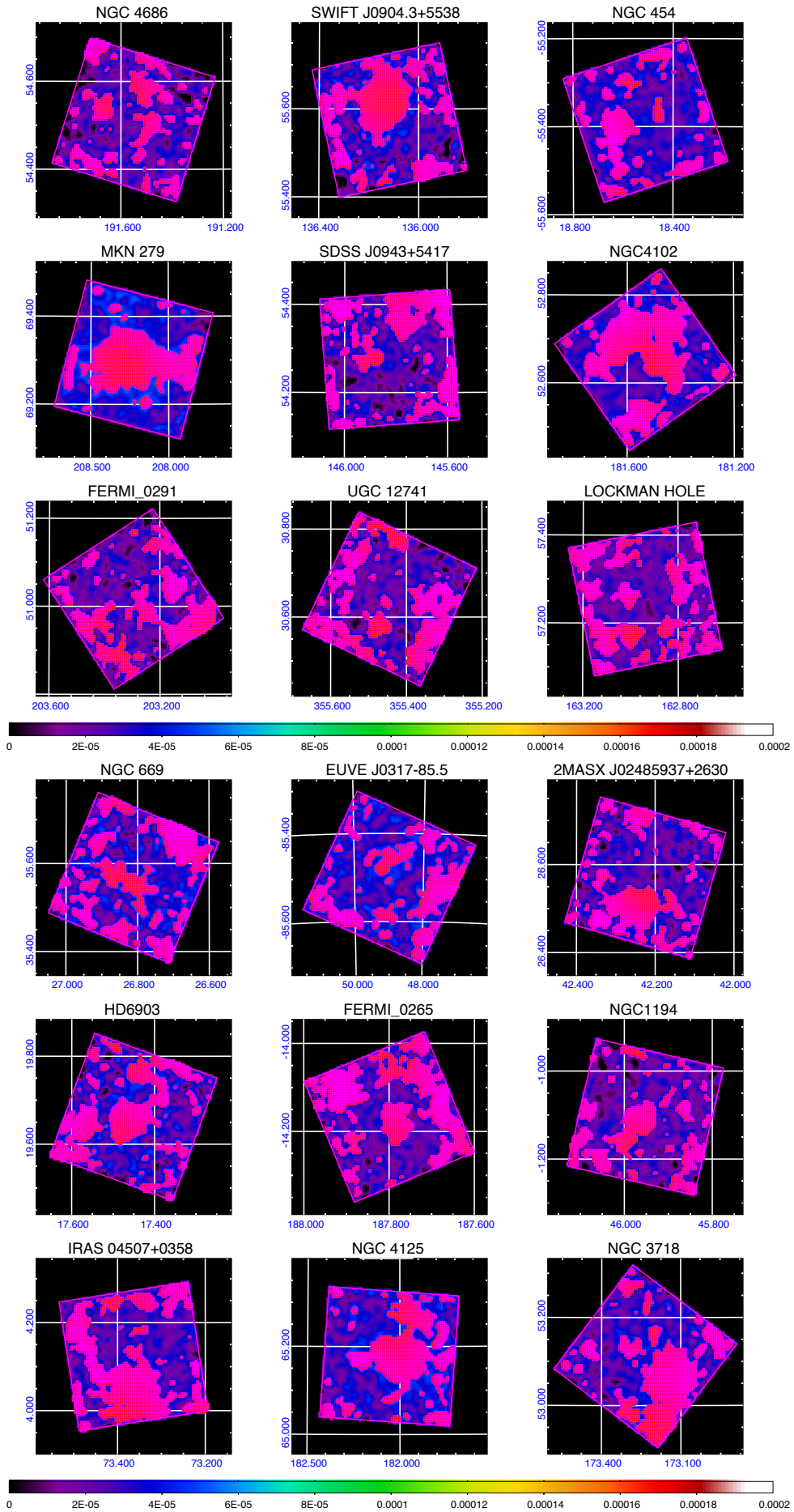
Figure A.5   Same as Figure A.1 but for ID 73 − 90.
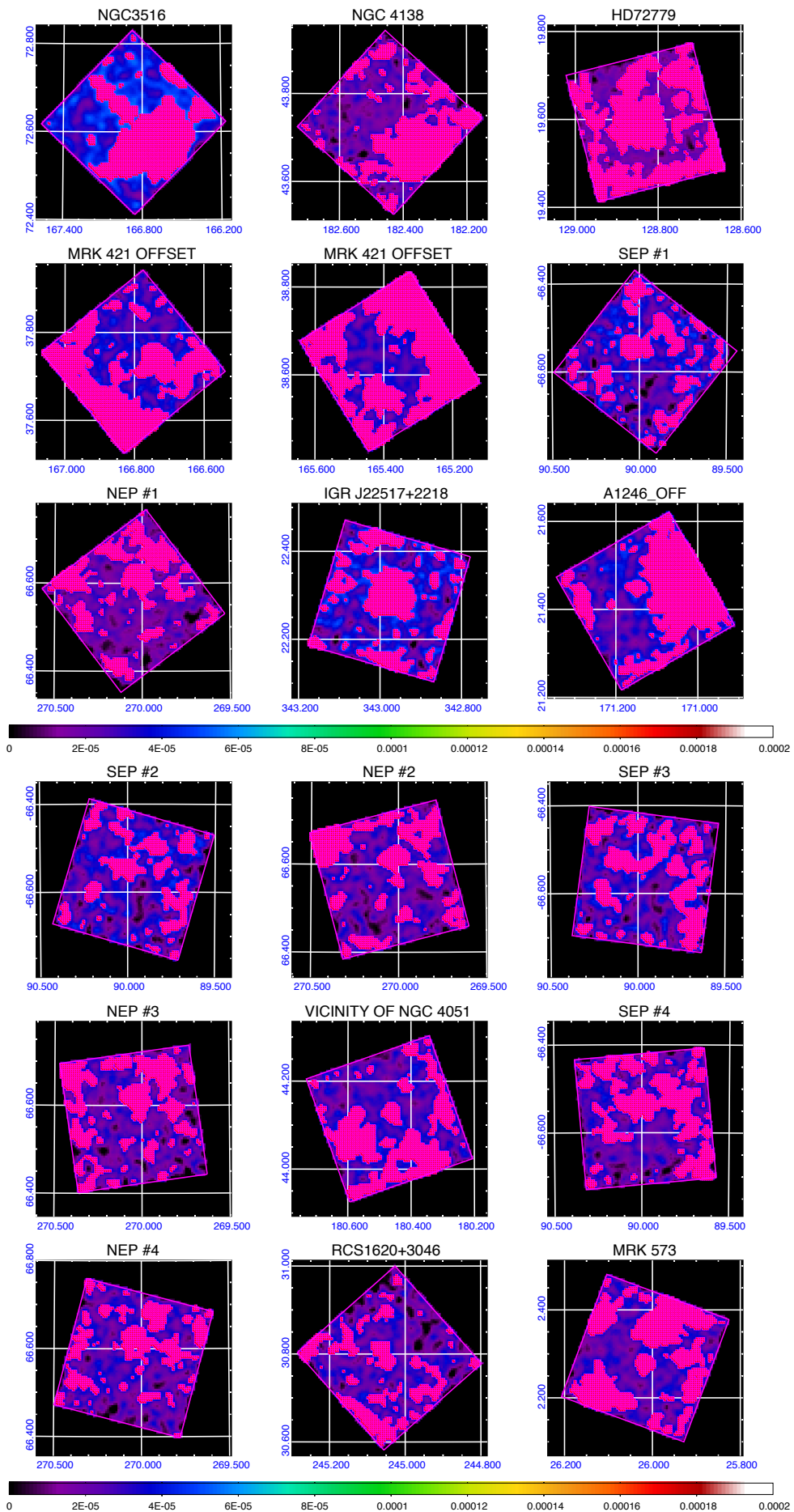
Figure A.6 Same as Figure A.1 but for ID 91 – 108.
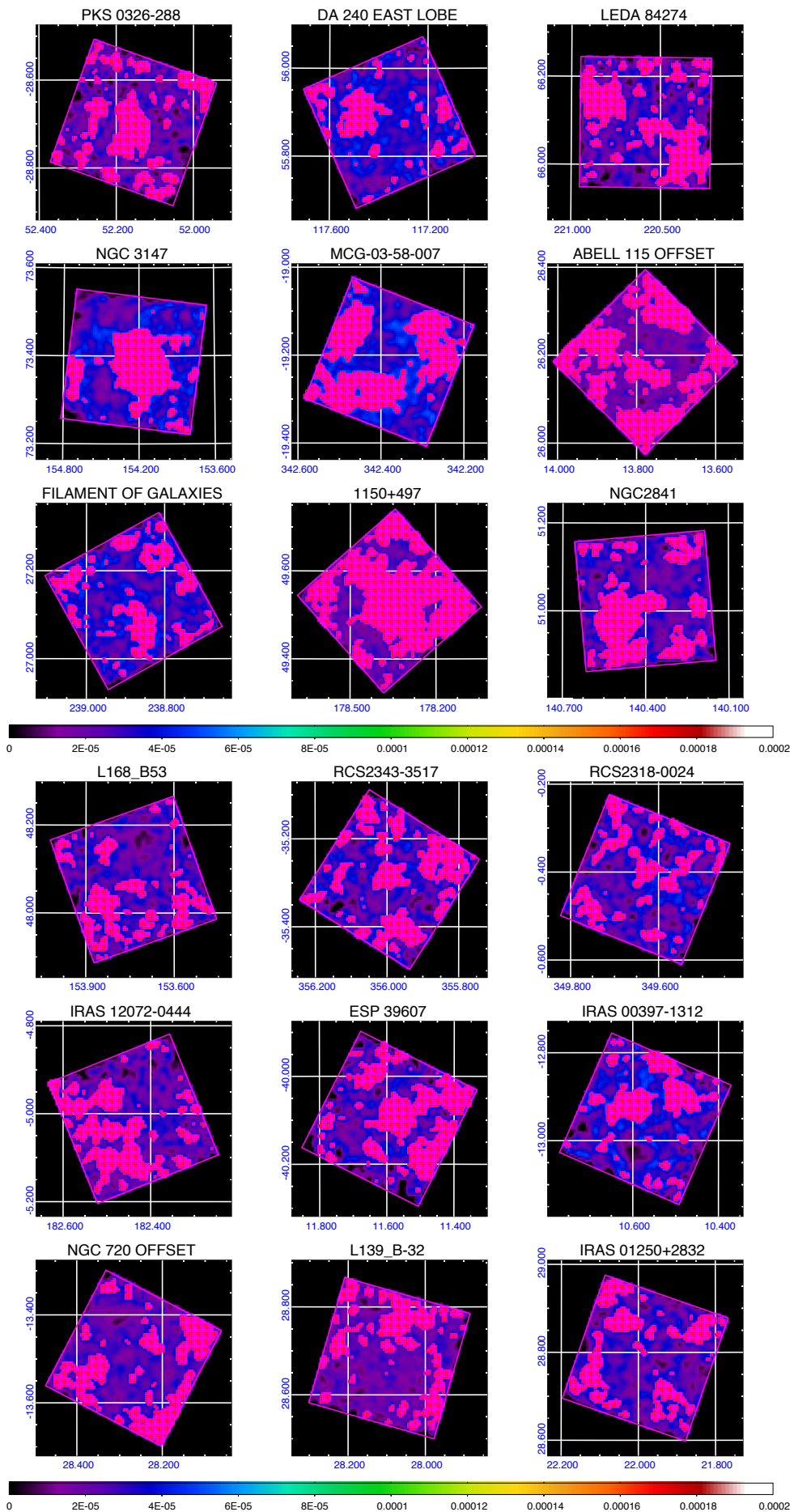
Figure A.7   Same as Figure A.1 but for ID 109 – 126.
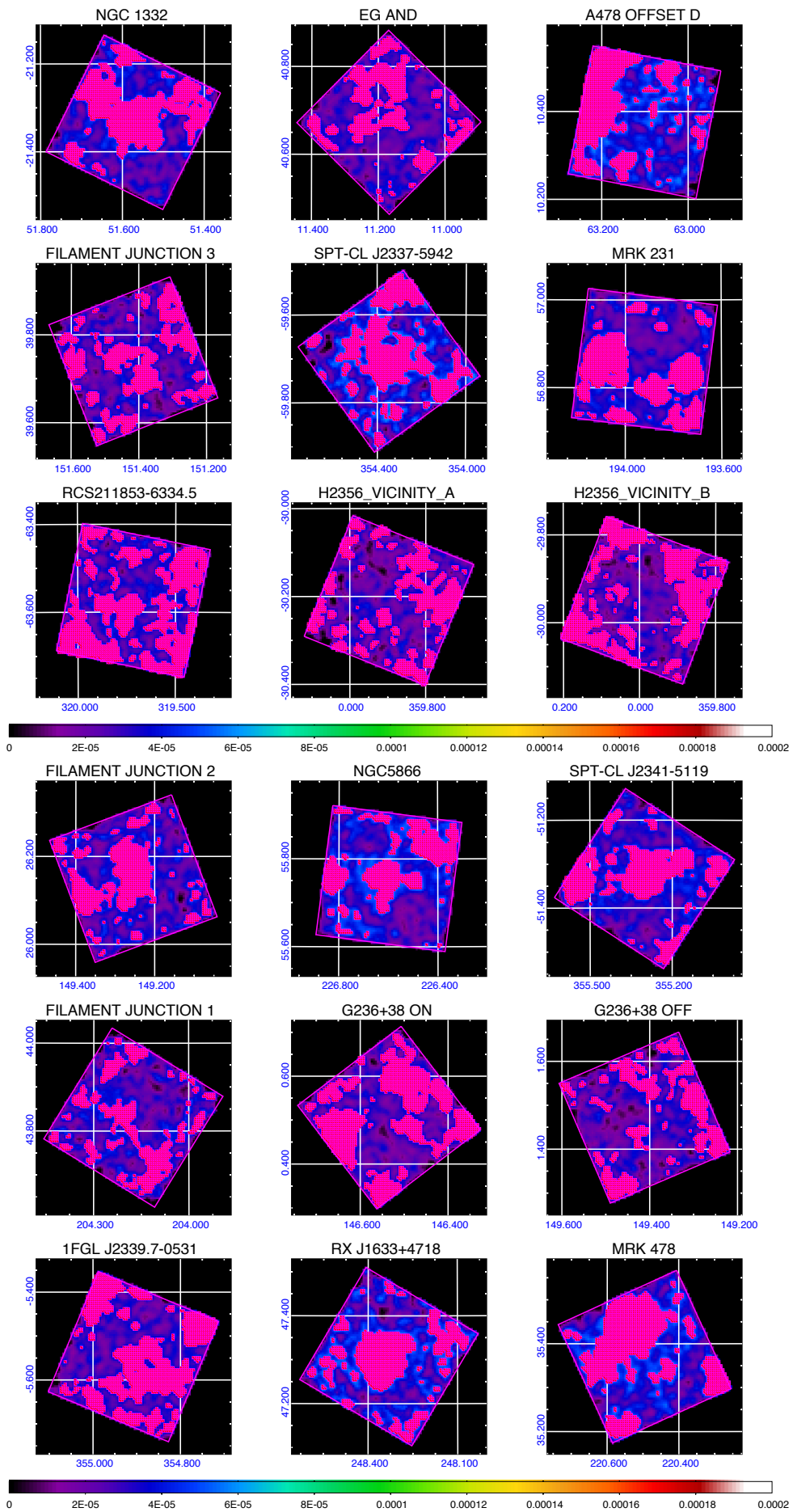
Figure A.8   Same as Figure A.1 but for ID 127 – 144.
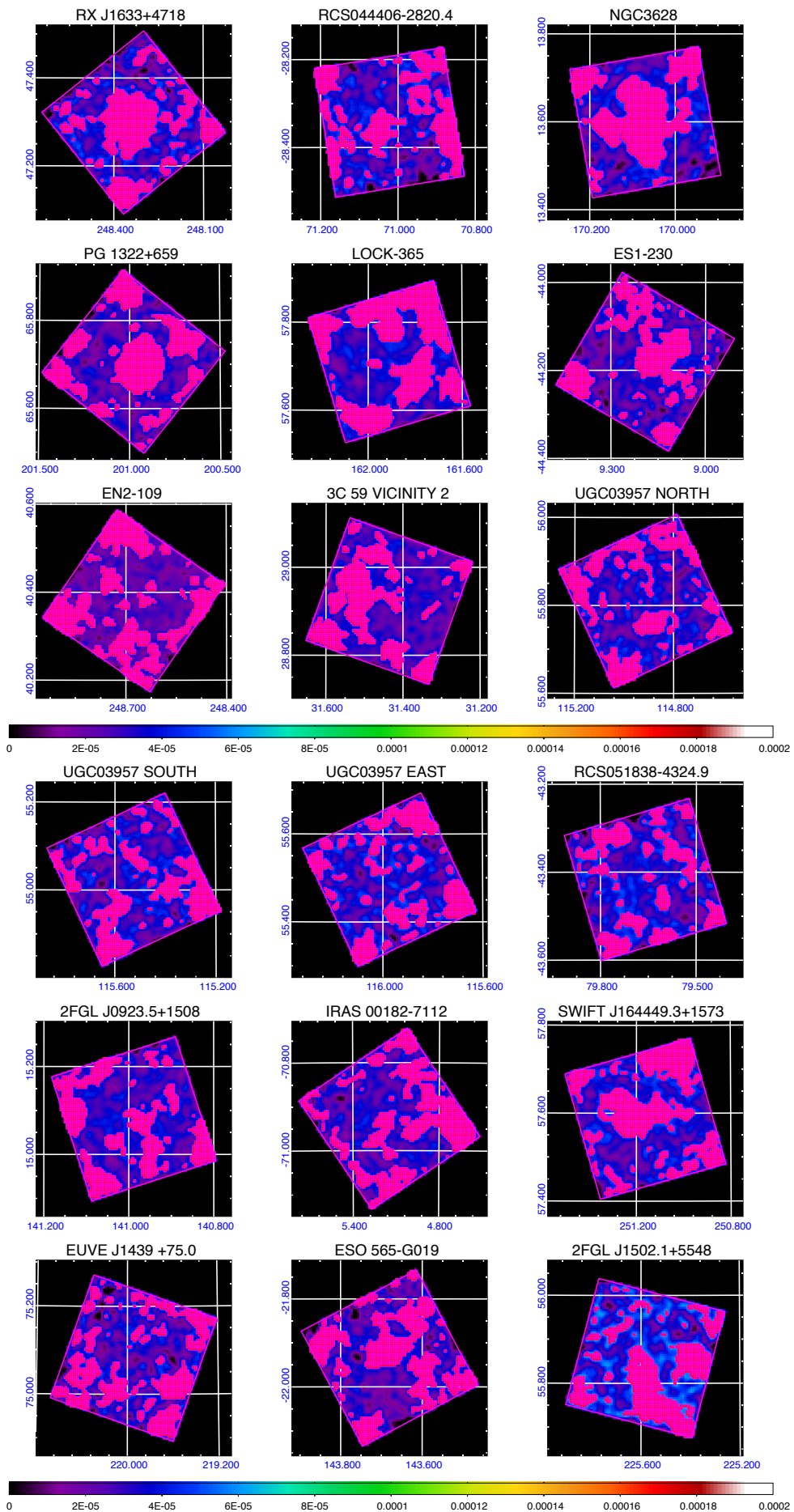
Figure A.9   Same as Figure A.1 but for ID 145 – 162.
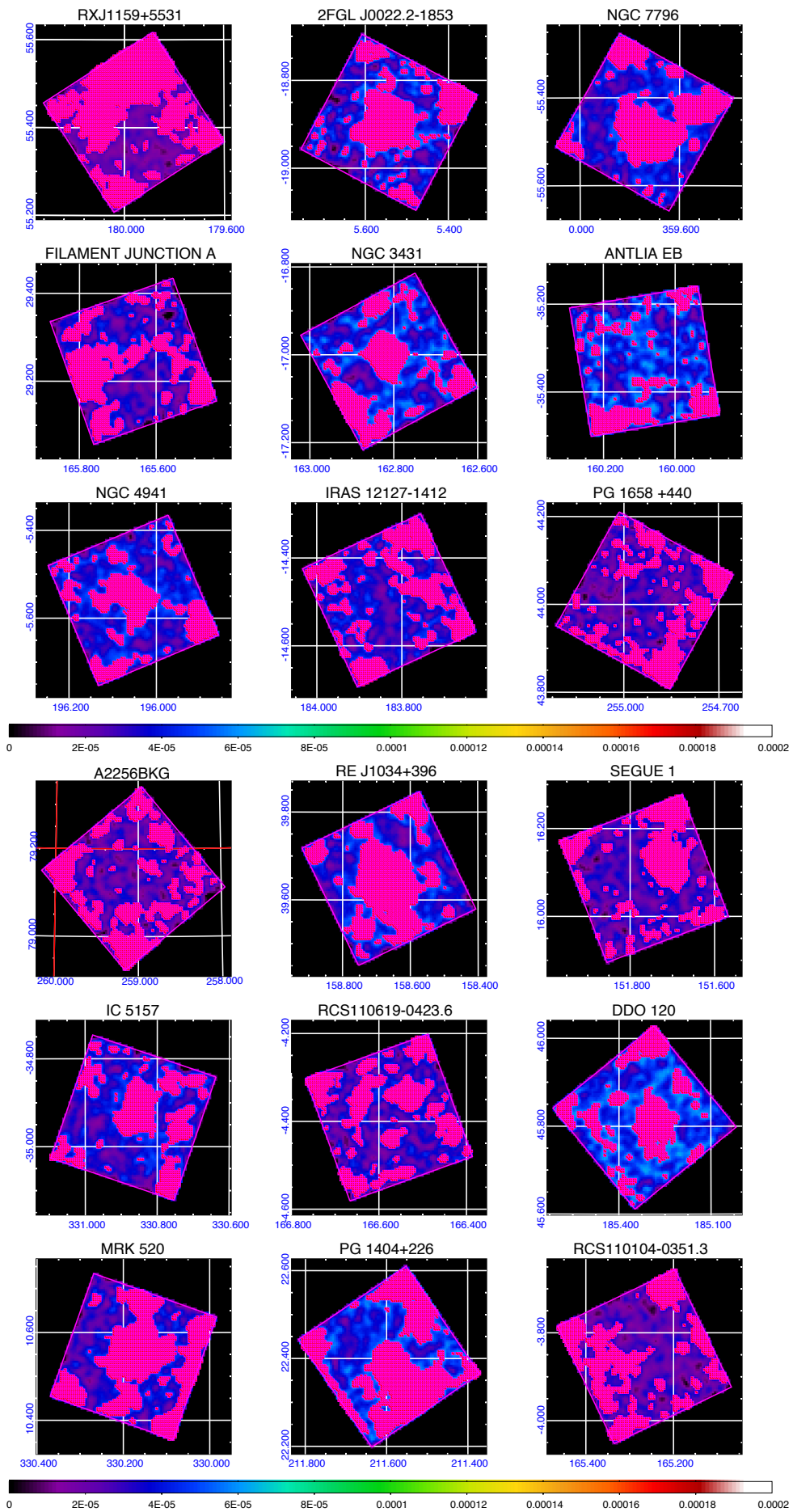
Figure A.10   Same as Figure A.1 but for ID 163 – 180.
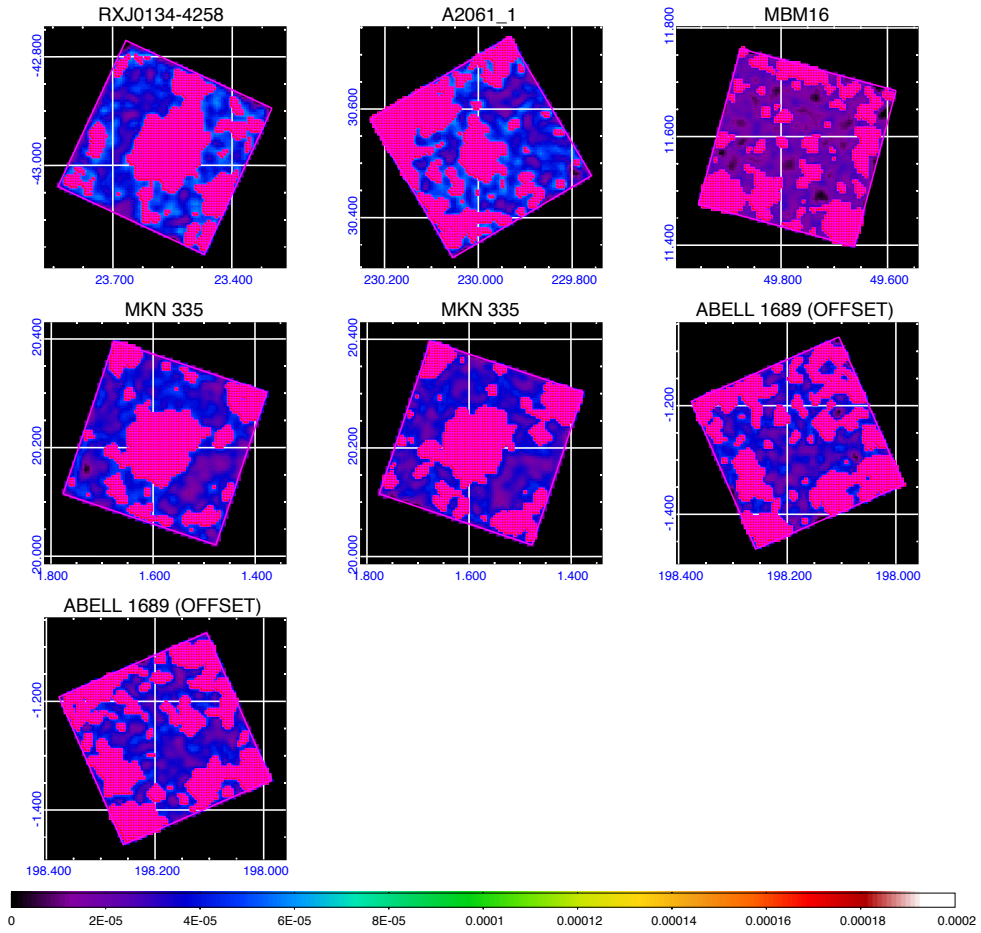
Figure A.11   Same as Figure A.1 but for ID 181 – 187. In Figures A.1 – A.11, the NXB component was subtracted from each image. Vignetting and exposure corrections were applied. Point sources in the XIS FoVs were rejected (magenta shaded regions). Color scale indicates photon count rates (counts par sec).

B Details of Suzaku XIS observations of the Crab

In order to correct XRT-XIS responses mismatching, we used the 34 "Crab Nebula center" observational data with the Suzaku XIS from 2005 to 2013. Their observational logs (e.g. observational date, exposure time) were summarized in Table B.1. Their XIS1 images in the $0.5 - 5.0$ keV range were shown in Figure B.1.

Table B.1   Suzaku XiS observational logs of the Crab.

ID	Obs. ID	Date[*]	Exposure[†]	SCI(XIS0,1,2,3)[‡]
c1	100007010	2005/08/22	86.0	(off,off,off,off)
c2	100010020	2005/08/25	182.8	(off,off,off,off)
c3	100010060	2005/08/25	216.0	(off,off,off,off)
c4	100010070	2005/08/26	204.4	(off,off,off,off)
c5	100015010	2005/08/31	280.8	(off,off,off,off)
c6	100015040	2005/09/01	148.8	(off,off,off,off)
c7	100023010	2005/09/15	600.0	(off,off,off,off)
c8	100023020	2005/09/15	619.2	(off,off,off,off)
c9	101010010	2006/09/05	816.1	(off,off,off,off)
c10	101011020	2006/09/05	100.8	(off,off,off,off)
c11	101011030	2006/09/05	188.8	(off,off,off,off)
c12	101011040	2006/09/06	82.4	(off,off,off,off)
c13	101011050	2006/09/06	72.0	(off,off,off,off)
c14	101011060	2006/09/18	88.8	(off,off,off,off)
c15	101011070	2006/09/18	76.0	(off,off,off,off)
c16	101011100	2006/09/19	77.2	(off,off,off,off)
c17	101011110	2006/09/06	131.6	(off,off,off,off)
c18	101011120	2006/09/06	148.8	(off,off,off,off)
c19	101011130	2006/09/06	162.4	(off,off,off,off)
c20	101011140	2006/09/06	122.2	(off,off,off,off)
c21	101011150	2006/09/06	108.4	(off,off,off,off)
c22	102019010	2007/03/20	920.1	(on,2,–,on)
c23	103007010	2008/08/27	1292.4	(on,2,–,on)
c24	103008010	2008/09/01	1366.2	(on,2,–,on)
c25	104001010	2009/04/02	448.9	(–,2,–,–)
c26	104001070	2010/02/23	1226.4	(on,2,–,on)
c27	105002010	2010/04/05	1028.1	(on,2,–,on)
c28	105029010	2011/03/21	1332.6	(on,2,–,on)
c29	106012010	2011/09/01	1074.3	(on,6,–,on)
c30	106013010	2012/02/28	1077.6	(on,6,–,on)
c31	106014010	2012/03/14	1466.4	(on,6,–,on)
c32	106015010	2012/03/26	1341.0	(on,6,–,on)
c33	107011010	2012/09/26	1121.7	(on,6,–,on)
c34	107012010	2013/02/27	1376.1	(on,6,–,on)

Notes.

[*] Observation start date (UT).

[†] Exposure time (XIS0+1+2+3) in unit of sec after the data screening.

[‡] off: data obtained by SCI off operation, on: SCI on operation for XIS-FI (2 keV equivalent), 2: SCI on operation for XIS1 (2 keV equivalent), 6: SCI on operation for XIS1 (6 keV equivalent).
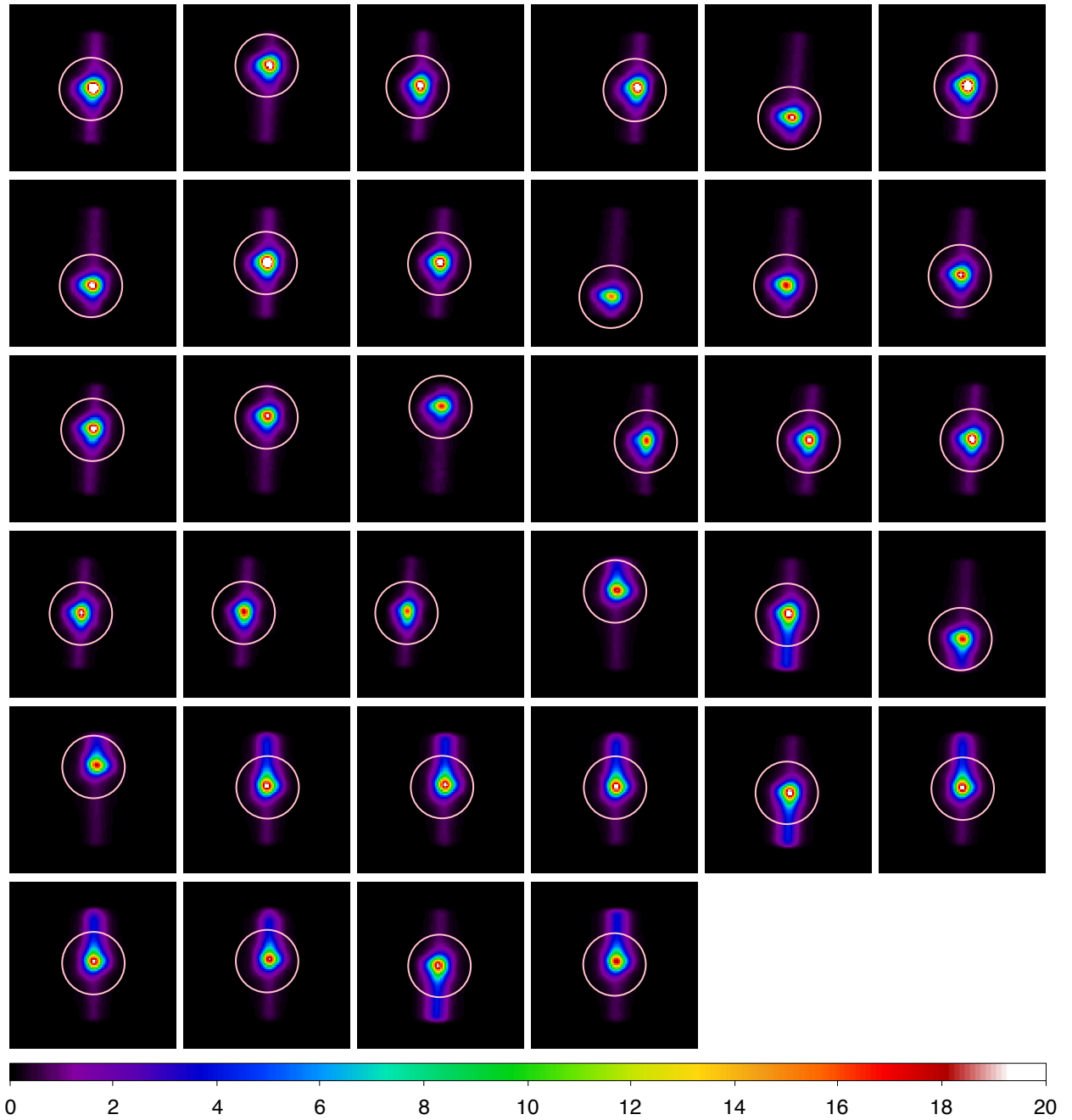
Figure B.1 XIS1 images in the 0.5 – 5.0 keV range of the Crab observations. The regions enclosed by pink circles (their center coordinates are Equatorial (R.A., Dec.) = (83.6, 22.0) or Galactic (Lat., Lon.) = (184.6, −5.8) and their radii are 5 arcmin) were used for the spectral analysis. Color scale indicates photon count rates (counts par sec).

C Details of instrumental line removal

We determined and subtracted the instrumental line contributions from the XDB spectra by spectral fitting. Spectral fitting results (line center energy, width and intensity) for five instrumental lines in the 25 stacked XDB spectra and the night Earth observational spectra with Gaussian models are shown in Table C.1. The instrumental line intensities and their uncertainties (standard deviations for Al-Kα, Si-Kα and Au-Mα, the square root of photon count for Mn-Kα and Mn-Kβ) were summarized in Table C.2.

Table C.1: Spectral fitting results of five instrumental lines with Gaussian models.

| Period	Energy$_{\mathrm{NE}}$[*]	Width$_{\mathrm{NE}}$[†]	Norm$_{\mathrm{NE}}$[‡]	Energy$_{\mathrm{XDB}}$[∥]	Energy dif.[§]	Width$_{\mathrm{XDB}}$[♯]	Norm$_{\mathrm{XDB}}$[**]
			XIS0 Al-Kα line.				
2005–2006	1.487	0.002	0.24	$1.486^{+0.008}_{-0.008}$	0	$0.019^{+0.014}_{-0.019}$	$0.26^{+0.04}_{-0.04}$
2006–2007	1.486	0.000	0.28	$1.485^{+0.005}_{-0.004}$	0	0.011(fix)	$0.31^{+0.04}_{-0.04}$
2007–2008	1.486	0.015	0.35	$1.496^{+0.007}_{-0.006}$	+1	$0.007^{+0.014}_{-0.007}$	$0.28^{+0.05}_{-0.04}$
2008–2009	1.485	0.000	0.33	$1.487^{+0.006}_{-0.006}$	0	$0.009^{+0.015}_{-0.009}$	$0.25^{+0.04}_{-0.04}$
2009–2010	1.487	0.000	0.29	$1.490^{+0.006}_{-0.006}$	0	0(fix)	$0.27^{+0.04}_{-0.04}$
2010–2011	1.485	0.010	0.28	$1.485^{+0.005}_{-0.007}$	0	0(fix)	$0.23^{+0.03}_{-0.03}$
2011–2012	1.482	0.000	0.22	$1.486^{+0.008}_{-0.008}$	0	0(fix)	$0.21^{+0.03}_{-0.03}$
2012–2013	1.479	0.000	0.24	$1.481^{+0.009}_{-0.009}$	0	0(fix)	$0.21^{+0.04}_{-0.04}$
			XIS0 Si-Kα line.				
2005–2006	1.763	0.001	0.00	$1.865^{+0.015}_{-0.021}$	+7	0(fix)	$0.09^{+0.07}_{-0.07}$
2006–2007	1.740	0.028	0.04	–	–	0(fix)	0(fix)
2007–2008	1.790	0.000	0(fix)	–	–	0(fix)	0(fix)
2008–2009	1.740	0.000	0(fix)	–	–	0(fix)	0(fix)
2009–2010	1.772	0.000	0.03	–	–	0(fix)	0(fix)
2010–2011	1.833	0.157	0.08	–	–	0(fix)	0(fix)
2011–2012	1.779	0.146	0.18	–	–	0(fix)	0(fix)
2012–2013	1.791	0.184	0.15	–	–	0(fix)	0(fix)
			XIS0 Au-Mα line.				
2005–2006	2.189	0.025	0.12	$2.173^{+2.210}_{-2.139}$	−1	$0.054^{+0.042}_{-0.031}$	$0.14^{+0.05}_{-0.05}$
2006–2007	2.195	0.058	0.19	$2.151^{+2.169}_{-2.132}$	−3	$0.042^{+0.022}_{-0.023}$	$0.17^{+0.04}_{-0.04}$
2007–2008	2.199	0.072	0.24	$2.215^{+2.240}_{-2.190}$	+1	$0.078^{+0.030}_{-0.027}$	$0.27^{+0.07}_{-0.07}$
2008–2009	2.180	0.081	0.26	$2.204^{+2.222}_{-2.186}$	+2	$0.059^{+0.022}_{-0.022}$	$0.23^{+0.05}_{-0.05}$
2009–2010	2.187	0.072	0.30	$2.193^{+2.224}_{-2.160}$	0	$0.108^{+0.042}_{-0.034}$	$0.30^{+0.08}_{-0.07}$
2010–2011	2.176	0.053	0.21	$2.203^{+2.225}_{-2.183}$	+2	$0.079^{+0.030}_{-0.026}$	$0.30^{+0.07}_{-0.06}$
2011–2012	2.184	0.060	0.20	$2.177^{+2.212}_{-2.086}$	0	$0.099^{+0.116}_{-0.062}$	$0.22^{+0.12}_{-0.08}$
2012–2013	2.185	0.063	0.18	$2.195^{+2.228}_{-2.149}$	+1	$0.097^{+0.068}_{-0.039}$	$0.26^{+0.09}_{-0.07}$
			XIS0 Mn-Kα line.				
2005–2006	5.891	0.010	1.44	$5.902^{+0.004}_{-0.004}$	+1	0(fix)	$1.48^{+0.07}_{-0.07}$
2006–2007	5.888	0.000	1.23	$5.889^{+0.002}_{-0.004}$	0	$0.008^{+0.013}_{-0.008}$	$1.35^{+0.05}_{-0.05}$
2007–2008	5.886	0.000	1.03	$5.900^{+0.003}_{-0.006}$	+1	$0.031^{+0.009}_{-0.011}$	$1.11^{+0.06}_{-0.06}$

Continued from previous page.

Period	Energy$_{\text{NE}}$[*]	Width$_{\text{NE}}$[†]	Norm$_{\text{NE}}$[‡]	Energy$_{\text{XDB}}$[‖]	Energy dif.[§]	Width$_{\text{XDB}}$[♯]	Norm$_{\text{XDB}}$[**]
2008–2009	5.890	0.000	0.82	$5.896^{+0.004}_{-0.005}$	0	$0.025^{+0.010}_{-0.014}$	$0.84^{+0.04}_{-0.04}$
2009–2010	5.890	0.000	0.60	$5.904^{+0.006}_{-0.007}$	+1	$0.013^{+0.020}_{-0.013}$	$0.60^{+0.05}_{-0.04}$
2010–2011	5.888	0.000	0.54	$5.901^{+0.007}_{-0.007}$	+1	0(fix)	$0.52^{+0.04}_{-0.04}$
2011–2012	5.884	0.000	0.39	$5.897^{+0.009}_{-0.009}$	+1	0.019(fix)	$0.40^{+0.04}_{-0.04}$
2012–2013	5.878	0.000	0.32	$5.889^{+0.013}_{-0.013}$	+1	$0.033^{+0.025}_{-0.033}$	$0.34^{+0.04}_{-0.04}$
XIS0 Mn-Kβ line.							
2005–2006	6.472	0.000	0.26	$6.480^{+0.016}_{-0.015}$	+1	$0.032^{+0.028}_{-0.032}$	$0.33^{+0.05}_{-0.05}$
2006–2007	6.466	0.027	0.27	$6.462^{+0.013}_{-0.014}$	0	$0.049^{+0.025}_{-0.032}$	$0.30^{+0.04}_{-0.04}$
2007–2008	6.465	0.062	0.28	$6.463^{+0.023}_{-0.023}$	0	$0.105^{+0.046}_{-0.037}$	$0.36^{+0.07}_{-0.06}$
2008–2009	6.463	0.039	0.21	$6.457^{+0.018}_{-0.017}$	0	$0.064^{+0.029}_{-0.032}$	$0.26^{+0.04}_{-0.04}$
2009–2010	6.435	0.003	0.18	$6.448^{+0.027}_{-0.027}$	+1	$0.072^{+0.042}_{-0.045}$	$0.21^{+0.05}_{-0.05}$
2010–2011	6.453	0.004	0.11	$6.482^{+0.038}_{-0.035}$	+2	$0.068^{+0.046}_{-0.068}$	$0.14^{+0.04}_{-0.04}$
2011–2012	6.430	0.000	0.11	$6.466^{+0.040}_{-0.039}$	+2	$0.084^{+0.055}_{-0.042}$	$0.16^{+0.05}_{-0.04}$
2012–2013	6.428	0.000	0.07	$6.421^{+0.047}_{-0.047}$	0	$0.066^{+0.057}_{-0.066}$	$0.12^{+0.04}_{-0.04}$
XIS1 Al-Kα line.							
2005–2006	1.486	0.000	0.31	$1.488^{+0.009}_{-0.009}$	0	$0.016^{+0.017}_{-0.016}$	$0.23^{+0.04}_{-0.04}$
2006–2007	1.495	0.021	0.34	$1.490^{+0.007}_{-0.006}$	0	$0.025^{+0.010}_{-0.012}$	$0.37^{+0.06}_{-0.06}$
2007–2008	1.491	0.007	0.31	$1.494^{+0.010}_{-0.009}$	0	0.018(fix)	$0.27^{+0.05}_{-0.05}$
2008–2009	1.490	0.000	0.33	$1.501^{+0.007}_{-0.003}$	+1	$0.012^{+0.015}_{-0.012}$	$0.33^{+0.05}_{-0.05}$
2009–2010	1.491	0.017	0.34	$1.507^{+0.007}_{-0.007}$	+1	0(fix)	$0.28^{+0.04}_{-0.04}$
2010–2011	1.491	0.024	0.30	$1.523^{+0.010}_{-0.009}$	+2	$0.021^{+0.024}_{-0.021}$	$0.27^{+0.07}_{-0.05}$
2011–2012	1.495	0.014	0.24	$1.493^{+0.009}_{-0.008}$	0	$0.016^{+0.020}_{-0.016}$	$0.26^{+0.05}_{-0.05}$
2012–2013	1.488	0.018	0.24	$1.488^{+0.010}_{-0.010}$	0	$0.021^{+0.021}_{-0.021}$	$0.25^{+0.06}_{-0.05}$
XIS1 Si-Kα line.							
2005–2006	1.754	0.000	0.40	$1.757^{+0.007}_{-0.007}$	0	$0.021^{+0.011}_{-0.018}$	$0.40^{+0.05}_{-0.05}$
2006–2007	1.762	0.001	0.38	$1.752^{+0.006}_{-0.004}$	−1	0(fix)	$0.39^{+0.04}_{-0.04}$
2007–2008	1.762	0.001	0.41	$1.758^{+0.006}_{-0.006}$	0	0(fix)	$0.40^{+0.05}_{-0.05}$
2008–2009	1.769	0.000	0.41	$1.770^{+0.006}_{-0.006}$	0	0(fix)	$0.36^{+0.04}_{-0.04}$
2009–2010	1.774	0.011	0.41	$1.777^{+0.008}_{-0.005}$	0	0(fix)	$0.36^{+0.04}_{-0.04}$
2010–2011	1.770	0.030	0.41	$1.790^{+0.008}_{-0.008}$	+1	0.008(fix)	$0.32^{+0.04}_{-0.04}$
2011–2012	1.765	0.020	0.38	$1.755^{+0.009}_{-0.009}$	−1	$0.038^{+0.014}_{-0.016}$	$0.39^{+0.05}_{-0.05}$
2012–2013	1.758	0.017	0.32	$1.762^{+0.007}_{-0.010}$	0	0(fix)	$0.28^{+0.04}_{-0.04}$
XIS1 Au-Mα line.							
2005–2006	2.161	0.014	0.11	$2.179^{+0.023}_{-0.021}$	+1	0(fix)	$0.09^{+0.04}_{-0.04}$
2006–2007	2.163	0.083	0.41	$2.159^{+0.021}_{-0.020}$	0	$0.120^{+0.023}_{-0.021}$	$0.47^{+0.07}_{-0.07}$
2007–2008	2.171	0.087	0.46	$2.174^{+0.018}_{-0.017}$	0	$0.081^{+0.023}_{-0.020}$	$0.44^{+0.08}_{-0.07}$
2008–2009	2.192	0.100	0.45	$2.205^{+0.015}_{-0.015}$	+1	$0.093^{+0.017}_{-0.015}$	$0.47^{+0.06}_{-0.06}$
2009–2010	2.180	0.083	0.38	$2.203^{+0.019}_{-0.017}$	+2	$0.072^{+0.028}_{-0.027}$	$0.35^{+0.07}_{-0.07}$
2010–2011	2.190	0.088	0.28	$2.237^{+0.015}_{-0.015}$	+3	$0.052^{+0.026}_{-0.025}$	$0.30^{+0.06}_{-0.05}$
2011–2012	2.177	0.079	0.30	$2.147^{+0.022}_{-0.020}$	−2	$0.095^{+0.028}_{-0.024}$	$0.36^{+0.07}_{-0.06}$
2012–2013	2.170	0.087	0.38	$2.179^{+0.022}_{-0.021}$	+1	$0.103^{+0.030}_{-0.026}$	$0.42^{+0.08}_{-0.07}$
XIS2 Al-Kα line.							
2005–2006	1.480	0.000	0.24	$1.486^{+0.008}_{-0.008}$	0	$0.021^{+0.012}_{-0.021}$	$0.26^{+0.04}_{-0.04}$
XIS2 Si-Kα line.							

Continued from previous page.

Period	Energy$_{\text{NE}}$*	Width$_{\text{NE}}$†	Norm$_{\text{NE}}$‡	Energy$_{\text{XDB}}$‖	Energy dif.§	Width$_{\text{XDB}}$♯	Norm$_{\text{XDB}}$**
2005–2006	1.855	0.109	0.15	$1.853^{+0.059}_{-0.057}$	0	$0.112^{+0.069}_{-0.040}$	$0.18^{+0.07}_{-0.07}$
				XIS2 Au-Mα line.			
2005–2006	2.177	0.000	0.23	$2.164^{+2.175}_{-2.154}$	+1	0(fix)	$0.22^{+0.04}_{-0.04}$
				XIS2 Mn-Kα line.			
2005–2006	5.865	0.011	0.20	$5.869^{+0.021}_{-0.021}$	0	$0.057^{+0.030}_{-0.031}$	$0.25^{+0.04}_{-0.04}$
				XIS2 Mn-Kβ line.			
2005–2006	6.451	0.052	0.12	$6.410^{+0.063}_{-0.062}$	−3	$0.128^{+0.090}_{-0.050}$	$0.18^{+0.05}_{-0.05}$
				XIS3 Al-Kα line.			
2005–2006	1.482	0.008	0.27	$1.490^{+0.008}_{-0.008}$	+1	$0.033^{+0.012}_{-0.012}$	$0.32^{+0.04}_{-0.04}$
2006–2007	1.481	0.000	0.28	$1.477^{+0.005}_{-0.005}$	0	$0.016^{+0.009}_{-0.016}$	$0.31^{+0.04}_{-0.05}$
2007–2008	1.483	0.000	0.32	$1.488^{+0.009}_{-0.007}$	0	$0.019^{+0.022}_{-0.019}$	$0.28^{+0.10}_{-0.06}$
2008–2009	1.484	0.000	0.34	$1.486^{+0.006}_{-0.007}$	0	0.005(fix)	$0.27^{+0.04}_{-0.04}$
2009–2010	1.483	0.000	0.29	$1.488^{+0.007}_{-0.007}$	0	$0.011^{+0.015}_{-0.011}$	$0.24^{+0.05}_{-0.04}$
2010–2011	1.480	0.009	0.25	$1.492^{+0.006}_{-0.006}$	+1	0(fix)	$0.23^{+0.03}_{-0.03}$
2011–2012	1.477	0.027	0.25	$1.484^{+0.012}_{-0.011}$	+1	$0.024^{+0.019}_{-0.024}$	$0.18^{+0.05}_{-0.04}$
2012–2013	1.474	0.012	0.22	$1.477^{+0.013}_{-0.013}$	0	0.044(fix)	$0.28^{+0.05}_{-0.05}$
				XIS3 Si-Kα line.			
2005–2006	1.783	0.175	0.57	$1.732^{+0.021}_{-0.021}$	−3	$0.067^{+0.024}_{-0.017}$	$0.24^{+0.05}_{-0.05}$
2006–2007	1.730	0.006	0.05	$1.741^{+0.052}_{-0.047}$	+1	0.026(fix)	$0.04^{+0.03}_{-0.03}$
2007–2008	1.777	0.209	0.30	$1.708^{+0.093}_{-1.708}$	−5	$0.172^{+0.148}_{-0.100}$	$0.31^{+0.25}_{-0.16}$
2008–2009	1.759	0.001	0.04	1.740	−1	0(fix)	0(fix)
2009–2010	1.713	0.000	0.01	$1.752^{+0.039}_{-0.082}$	+3	0(fix)	$0.03^{+0.03}_{-0.03}$
2010–2011	1.773	0.098	0.11	1.740	−2	0(fix)	0(fix)
2011–2012	1.803	0.070	0.04	1.740	−4	0(fix)	0(fix)
2012–2013	1.804	0.191	0.50	$1.735^{+0.039}_{-0.045}$	−5	0.084(fix)	$0.20^{+0.06}_{-0.08}$
				XIS3 Au-Mα line.			
2005–2006	2.193	0.107	0.38	$2.114^{+0.029}_{-0.030}$	−5	$0.144^{+0.026}_{-0.021}$	$0.53^{+0.07}_{-0.07}$
2006–2007	2.185	0.071	0.23	$2.145^{+0.028}_{-0.021}$	−3	$0.056^{+0.036}_{-0.027}$	$0.18^{+0.06}_{-0.05}$
2007–2008	2.185	0.069	0.20	$2.146^{+0.033}_{-0.032}$	−3	$0.091^{+0.033}_{-0.027}$	$0.30^{+0.09}_{-0.11}$
2008–2009	2.167	0.058	0.27	$2.182^{+0.025}_{-0.025}$	+1	$0.093^{+0.025}_{-0.022}$	$0.27^{+0.06}_{-0.06}$
2009–2010	2.193	0.070	0.26	$2.202^{+0.021}_{-0.021}$	+1	$0.096^{+0.028}_{-0.025}$	$0.37^{+0.07}_{-0.07}$
2010–2011	2.175	0.077	0.24	$2.080^{+0.070}_{-2.080}$	−6	$0.233^{+0.070}_{-0.069}$	$0.36^{+0.10}_{-0.09}$
2011–2012	2.186	0.086	0.29	$2.168^{+0.023}_{-0.024}$	−1	$0.087^{+0.037}_{-0.028}$	$0.27^{+0.07}_{-0.06}$
2012–2013	2.191	0.080	0.25	$2.115^{+0.043}_{-0.060}$	−5	$0.170^{+0.070}_{-0.051}$	$0.44^{+0.14}_{-0.11}$
				XIS3 Mn-Kα line.			
2005–2006	5.886	0.000	0.83	$5.892^{+0.006}_{-0.008}$	0	0(fix)	$0.67^{+0.05}_{-0.05}$
2006–2007	5.890	0.000	0.69	$5.881^{+0.004}_{-0.006}$	−1	$0.014^{+0.015}_{-0.014}$	$0.64^{+0.04}_{-0.04}$
2007–2008	5.891	0.000	0.63	$5.900^{+0.007}_{-0.004}$	+1	0(fix)	$0.60^{+0.04}_{-0.04}$
2008–2009	5.890	0.000	0.43	$5.888^{+0.007}_{-0.008}$	0	0(fix)	$0.41^{+0.03}_{-0.03}$
2009–2010	5.887	0.000	0.36	$5.900^{+0.008}_{-0.012}$	+1	$0.024^{+0.024}_{-0.024}$	$0.36^{+0.04}_{-0.04}$
2010–2011	5.880	0.001	0.23	$5.880^{+0.016}_{-0.013}$	0	$0.027^{+0.029}_{-0.027}$	$0.22^{+0.03}_{-0.03}$
2011–2012	5.891	0.002	0.27	$5.902^{+0.010}_{-0.012}$	+1	0(fix)	$0.28^{+0.03}_{-0.03}$
2012–2013	5.888	0.001	0.21	$5.912^{+0.020}_{-0.019}$	+2	$0.045^{+0.038}_{-0.045}$	$0.23^{+0.04}_{-0.04}$
				XIS3 Mn-Kβ line.			
2005–2006	6.452	0.021	0.19	$6.477^{+0.026}_{-0.029}$	+2	$0.030^{+0.052}_{-0.030}$	$0.17^{+0.04}_{-0.04}$

Continued from previous page.

Period	Energy$_\mathrm{NE}$[*]	Width$_\mathrm{NE}$[†]	Norm$_\mathrm{NE}$[‡]	Energy$_\mathrm{XDB}$[‖]	Energy dif.[§]	Width$_\mathrm{XDB}$[♯]	Norm$_\mathrm{XDB}$[**]
2006–2007	6.445	0.055	0.20	$6.446^{+0.013}_{-0.016}$	0	0(fix)	$0.21^{+0.03}_{-0.03}$
2007–2008	6.448	0.027	0.19	$6.442^{+0.027}_{-0.027}$	0	$0.102^{+0.036}_{-0.032}$	$0.28^{+0.05}_{-0.05}$
2008–2009	6.432	0.000	0.13	$6.448^{+0.030}_{-0.026}$	+1	0(fix)	$0.11^{+0.03}_{-0.03}$
2009–2010	6.440	0.001	0.13	$6.443^{+0.026}_{-0.029}$	0	0(fix)	$0.12^{+0.03}_{-0.03}$
2010–2011	6.434	0.000	0.10	$6.436^{+0.032}_{-0.038}$	0	0(fix)	$0.10^{+0.03}_{-0.03}$
2011–2012	6.414	0.000	0.12	$6.449^{+0.047}_{-0.046}$	+2	$0.093^{+0.055}_{-0.053}$	$0.13^{+0.04}_{-0.04}$
2012–2013	6.446	0.001	0.06	$6.405^{+0.066}_{-0.069}$	−3	0(fix)	$0.05^{+0.03}_{-0.03}$

Notes.

∗ Line center energy obtained by spectral fitting for night Earth observation spectra in unit of keV.

† Line width obtained by spectral fitting for night Earth observation spectra in unit of keV.

‡ Line intensity obtained by spectral fitting for night Earth observation spectra in unit of LU (photons cm^{-2} s^{-1} sr^{-1}).

‖ Line center energy obtained by spectral fitting for the stacked XDB(+NXB) spectra in unit of keV.

§ Line center energy difference (Energy$_\mathrm{XDB}$−Energy$_\mathrm{NE}$)/Energy$_\mathrm{NE}$ [%].

♯ Line width obtained by spectral fitting for the stacked XDB (+ NXB) spectra in unit of keV.

∗∗ Line intensity obtained by spectral fitting for the stacked XDB (+ NXB) spectra in unit of LU.

Table C.2: Instrumental line intensities and their uncertainties.

Period	Instrument	Instrumental line	Intensity[*]	Uncertainty[†]
2005–2006	XIS0	Al Kα	0.26	0.12
		Si Kα	0.09	0.16
		Au Mα	0.14	0.10
		Mn Kα	1.48	0.08
		Mn Kβ	0.33	0.04
	XIS1	Al Kα	0.23	0.13
		Si Kα	0.40	0.11
		Au Mα	0.09	0.10
	XIS2	Al Kα	0.26	0.14
		Si Kα	0.18	0.18
		Au Mα	0.22	0.06
		Mn Kα	0.25	0.03
		Mn Kβ	0.18	0.03
	XIS3	Al Kα	0.32	0.15
		Si Kα	0.24	0.10
		Au Mα	0.53	0.10
		Mn Kα	0.67	0.06
		Mn Kβ	0.17	0.04
2006–2007	XIS0	Al Kα	0.31	0.12
		Si Kα	0	0
		Au Mα	0.17	0.10
		Mn Kα	1.35	0.05
		Mn Kβ	0.30	0.03
	XIS1	Al Kα	0.37	0.13
		Si Kα	0.39	0.11
		Au Mα	0.47	0.10
	XIS3	Al Kα	0.31	0.15
		Si Kα	0.04	0.10
		Au Mα	0.18	0.10
		Mn Kα	0.64	0.04
		Mn Kβ	0.21	0.02
2007–2008	XIS0	Al Kα	0.28	0.12
		Si Kα	0	0
		Au Mα	0.27	0.10
		Mn Kα	1.11	0.05
		Mn Kβ	0.36	0.03
	XIS1	Al Kα	0.27	0.13
		Si Kα	0.40	0.11
		Au Mα	0.44	0.10
	XIS3	Al Kα	0.28	0.15
		Si Kα	0.31	0.10
		Au Mα	0.30	0.10
		Mn Kα	0.60	0.04
		Mn Kβ	0.28	0.02

Continued from previous page.

Period	Instrument	Instrumental line	Intensity*	Uncertainty†
2008–2009	XIS0	Al Kα	0.25	0.12
		Si Kα	0	0
		Au Mα	0.23	0.10
		Mn Kα	0.84	0.04
		Mn Kβ	0.26	0.02
	XIS1	Al Kα	0.33	0.13
		Si Kα	0.36	0.11
		Au Mα	0.47	0.10
	XIS3	Al Kα	0.27	0.15
		Si Kα	0	0
		Au Mα	0.27	0.10
		Mn Kα	0.41	0.03
		Mn Kβ	0.11	0.02
2009–2010	XIS0	Al Kα	0.27	0.12
		Si Kα	0	0
		Au Mα	0.30	0.10
		Mn Kα	0.60	0.04
		Mn Kβ	0.21	0.02
	XIS1	Al Kα	0.28	0.13
		Si Kα	0.36	0.11
		Au Mα	0.35	0.10
	XIS3	Al Kα	0.24	0.15
		Si Kα	0.03	0.10
		Au Mα	0.36	0.10
		Mn Kα	0.36	0.03
		Mn Kβ	0.12	0.02
2010–2011	XIS0	Al Kα	0.23	0.12
		Si Kα	0	0
		Au Mα	0.30	0.10
		Mn Kα	0.52	0.03
		Mn Kβ	0.14	0.02
	XIS1	Al Kα	0.27	0.13
		Si Kα	0.32	0.11
		Au Mα	0.30	0.10
	XIS3	Al Kα	0.23	0.15
		Si Kα	0	0
		Au Mα	0.36	0.10
		Mn Kα	0.22	0.02
		Mn Kβ	0.10	0.02
2011–2012	XIS0	Al Kα	0.21	0.12
		Si Kα	0	0
		Au Mα	0.22	0.10
		Mn Kα	0.40	0.03
		Mn Kβ	0.16	0.01
	XIS1	Al Kα	0.26	0.13

Continued from previous page.

Period	Instrument	Instrumental line	Intensity*	Uncertainty†
		Si Kα	0.39	0.11
		Au Mα	0.36	0.10
	XIS3	Al Kα	0.18	0.15
		Si Kα	0	0
		Au Mα	0.27	0.10
		Mn Kα	0.28	0.02
		Mn Kβ	0.13	0.01
2012–2013	XIS0	Al Kα	0.21	0.12
		Si Kα	0	0
		Au Mα	0.26	0.10
		Mn Kα	0.34	0.03
		Mn Kβ	0.12	0.01
	XIS1	Al Kα	0.25	0.13
		Si Kα	0.28	0.11
		Au Mα	0.42	0.10
	XIS3	Al Kα	0.28	0.15
		Si Kα	0.20	0.10
		Au Mα	0.44	0.10
		Mn Kα	0.23	0.02
		Mn Kβ	0.05	0.01

Notes.

* Instrumental line intensity in unit of LU (photons cm^{-2} s^{-1} sr^{-1}).

† Instrumental line uncertainty in unit of LU.

D Details of analysis tools used in this thesis

D.1 Ftools in HEAsoft

Suzaku XIS spectral data, imaging maps, calibration information files and response files are commonly supplied in the form of Flexible Image Transport System (FITS) format files. Suzaku XIS data reduction and FITS file manipulation were performed by using the Ftools in HEAsoft[*1] in this thesis.

cleansis

The Ftool `cleansis` identifies anomalous (hot and flickering) pixel locations and counts in the XISs.

xisrmfgen

The Ftool `xisrmfgen` creates an XIS energy redistribution matrix files (RMFs) with the XIS calibration data. The RMF includes the quantum efficiency of XIS and an energy response such as an energy scale and resolution. The `xisrmfgen` calculates a line profile of monochromatic X-rays at each energy bins.

xissimarfgen

The Ftool `xissimarfgen` generates an XIS ancillary response files (ARFs) with the XIS calibration data and the Monte-Carlo ray-tracing simulation (Ishisaki et al., 2007). The ARF includes an angular response and an effective area which is related with the XRT mirror geometry and reflectivity, transmission efficiency of the thermal shield and the OBF and the quantum efficiency of XIS. In this thesis, we assumed a uniform sky centered at each observational coordinate with radius of 20 arcmin as an X-ray emitting region for the simulation.

xisnxbgen

The Ftool `xisnxbgen` reproduces the Non-X-ray Background (NXB) including the instrumental lines from an accumulated night Earth observations. In this thesis, we determined to use the night Earth observations around 150 days centered at the day of each observation for the NXB data.

mathpha

The Ftool `mathpha` performs mathematical operations on multiple spectral data.

[*1] `http://heasarc.gsfc.nasa.gov/lheasoft/`

addrmf

The Ftool `addrmf` adds and averages multiple RMFs (or RMFs × ARFs: Responses) with arbitrary weights.

D.2   Models in XSPEC

Suzaku XIS spectral analyses can be carried out using XSPEC. The NXB-subtracted spectra are fitted by spectral models multiplied by the RMFs and ARFs in XSPEC. XSPEC includes about 100 spectral models. Here, we easily explain the spectral models used in this thesis.

powerlaw

`powerlaw` is a simple photon power-law emission model with given photon index and surface brightness.

bknpower

`bknpower` is a broken power-law emission model with given break point, two photon indices and surface brightness.

apec

`apec` reproduces a thermal Bremsstrahlung continuum and line emission from optically-thin thermal collisionally-ionized (CIE) plasma with given temperature, trace element (He, C, N, O, Ne, Mg, Al, Si, S, Ar, Ca, Fe and Ni) abundances and emission measure integrated over the line of sight: $(1/2\pi) \int n_e n_H ds$, where n_e and n_H are the electron and the hydrogen densities. Relative element abundances are set to the Solar-neighbor value (Anders & Grevesse, 1989).

vapec

`vapec` is a modified `apec` model which can change abundances of the individual trace elements.

gaussian

`gaussian` is a simple Gaussian line profile with given line center energy, width and flux.

phabs

`phabs` calculates an effect of photoelectric absorption by the interstellar medium of the Milky Way galaxy which could be estimated from accurate observational data of the neutral hydrogen column densities (N_H) (LAB survey; Kalberla et al., 2005).

Acknowledgment

I would like to express indescribable appreciation for my supervisor associate professor Noriko Y. Yamasaki, Yamasaki-sensei, with all my strength. When I was in the darkness, she gave me words of wisdom and led me to the brightness. Her encouragement always made me happy. Especially, I was heartened by her message: "Your work is one and only. Only you can do it.". This thesis can not be accomplished without her advices and supports. I will never forget her kindness.

I am most grateful to professor Kazuhisa Mitsuda, Mitsuda-sensei. The theme of this thesis, "dark matter search with the XDB", was sparked by a passing conversation with him. His trenchant advices helped me and his strict attitudes for science impressed me. I found that the extend of his understanding of science is vast and now expanding: it is another universe. I truly feel lucky to study with him.

I sincerely thank assistant professor Yoh Takei, Takei-san. He friendly and empathically listens to my problem. My scientific attitudes were imparted by him through instrumental experiments and scientific data analyses. He also taught me the joy and severity of a researcher's life. The memories of the days with him will never fade.

I also acknowledge great debts to my colleagues. Secretary Akiko Yokoyama, Yokoyama-san, your humorous character always make me relaxed. I had a good time thanks to your support and care.

Dr. Tomotake Matsumura, Matsumura-san, I wish I could study more with you. Your creativity, activeness and shapeliness (like Masaharu Fukuyama) attract me. I wanted to meet you earlier. I wish you (and your family with Riho-chan) all the best for a good health and continued success.

Dr. Kazuhiro Sakai, Sakai-san, I was always helped by your tenderness and full of abilities although I did not help you at all. You are a respected colleague and I want to be a resourceful person like you. Simultaneously, I consider that we are coeval friends. I am glad to be awarded Ph.D. with you. I hope we can remain friends. I also thank your wife for her thoughtfulness.

A light-hearted fellow Kenichiro Nagayoshi (I am not sure which is the senior), I have been amazed by your perceptiveness and power of positive thinking. I remember productive discussions with you. You made my laboratory life very memorable by your whim of youth: an alcohol-related bungle, an erratic drive and so on. Thank you.

A brother-like fellow Ryo Yamamoto (I often can not see which is the older brother), your discreetness and enthusiasm for study strike me. We had a lot to talk about wide-ranging topics from personal matters to international issues, played catch and et cetera. I have many important memories of you. Thank you.

My colleagues Ikuyuki Mitsuishi, Hiroshi Yoshitake, Takahiro Kikuchi, Akira Chiba, Tasuku Hayashi, Masatoshi Hoshino, Haruka Muramatsu and Yuki Tsurugasaki, I enjoyed my laboratory life with you.

Mr. Baluta Chris, Chris-san, I appreciate your thinking of me. I wanted to spend more time talking with you.

Finally, I thank my beloved family: my grandparents Toshio and Masako Takagi, Haruji and Sumi Sekiya, my parents Noboru and Yoshie Sekiya, my brother Tomohide Sekiya. I am able to keep going on with the help of your generous supports. I treasure your gifts: curiosity, knowledge, courtesy, love and kindness. Thank you so much.

Norio Sekiya.

References

Abazajian, K., Fuller, G. M., & Patel, M. 2001a, Phys. Rev. D, 64, 023501

Abazajian, K., Fuller, G. M., & Tucker, W. H. 2001b, ApJ, 562, 593

Abe, K., et al. 2014, Physical Review Letters, 113, 121301

Anders, E., & Grevesse, N. 1989, Geochim. Cosmochim. Acta, 53, 197

Asaka, T., & Shaposhnikov, M. 2005, Physics Letters B, 620, 17

Asaka, T., Blanchet, S., & Shaposhnikov, M. 2005, Physics Letters B, 631, 151

Barkana, R., Haiman, Z., & Ostriker, J. P. 2001, ApJ, 558, 482

Biermann, P. L., & Kusenko, A. 2006, Physical Review Letters, 96, 091301

Boyarsky, A., Nevalainen, J., & Ruchayskiy, O. 2007, A&A, 471, 51

Boyarsky, A., & Ruchayskiy, O. 2008, ArXiv e-prints

Boyarsky, A., Ruchayskiy, O., & Iakubovskyi, D. 2009a, JCAP, 3, 5

Boyarsky, A., Lesgourgues, J., Ruchayskiy, O., & Viel, M. 2009b, JCAP, 5, 12

Boyarsky, A., Lesgourgues, J., Ruchayskiy, O., & Viel, M. 2009c, Physical Review Letters, 102, 201304

Boyarsky, A., Neronov, A., Ruchayskiy, O., & Tkachev, I. 2010, Physical Review Letters, 104, 191301

Boyarsky, A., Iakubovskyi, D., & Ruchayskiy, O. 2012, Physics of the Dark Universe, 1, 136

Boyarsky, A., Ruchayskiy, O., Iakubovskyi, D., & Franse, J. 2014, Physical Review Letters, 113, 251301

Bradt, H. 2004, Astronomy Methods: A Physical Approach to Astronomical Observations

Buchmüller, W., Covi, L., Hamaguchi, K., Ibarra, A., & Yanagida, T. T. 2007, Journal of High Energy Physics, 3, 37

Bulbul, E., Markevitch, M., Foster, A., Smith, R. K., Loewenstein, M., & Randall, S. W. 2014, ApJ, 789, 13

Buote, D. A. 2004, in IAU Symposium, Vol. 220, Dark Matter in Galaxies, ed. S. Ryder, D. Pisano, M. Walker, & K. Freeman, 149

Carlson, E., Jeltema, T., & Profumo, S. 2015, JCAP, 2, 9

Chemin, L., Carignan, C., & Foster, T. 2009, ApJ, 705, 1395

Corbelli, E., Lorenzoni, S., Walterbos, R., Braun, R., & Thilker, D. 2010, A&A, 511, A89

Cox, D. P., & Anderson, P. R. 1982, ApJ, 253, 268

Cox, D. P. . 1998, in Lecture Notes in Physics, Berlin Springer Verlag, Vol. 506, IAU Colloq. 166: The Local Bubble and Beyond, ed. D. Breitschwerdt, M. J. Freyberg, & J. Truemper, 121–131

Cravens, T. E. 2000, ApJL, 532, L153

Dar, A. 1995, ApJ, 449, 550

Demidov, S. V., & Gorbunov, D. S. 2014, Phys. Rev. D, 90, 035014

Dodelson, S., & Widrow, L. M. 1994, Physical Review Letters, 72, 17

Einasto, J., & Einasto, M. 2000, in Astronomical Society of the Pacific Conference Series, Vol. 209, IAU Colloq. 174: Small Galaxy Groups, ed. M. J. Valtonen & C. Flynn, 360

Evrard, A. E., Metzler, C. A., & Navarro, J. F. 1996, ApJ, 469, 494

Feng, J. L. 2010, ARA&A, 48, 495

Foster, A. R., Ji, L., Smith, R. K., & Brickhouse, N. S. 2012, ApJ, 756, 128

Fujimoto, R., et al. 2007, PASJ, 59, 133

Fukuda, Y., et al. 1998, Physical Review Letters, 81, 1562

Fuller, G. M., Kusenko, A., Mocioiu, I., & Pascoli, S. 2003, Phys. Rev. D, 68, 103002

Gilmore, G., Wilkinson, M. I., Wyse, R. F. G., Kleyna, J. T., Koch, A., Evans, N. W., & Grebel, E. K. 2007, ApJ, 663, 948

Goerdt, T., Moore, B., Read, J. I., Stadel, J., & Zemp, M. 2006, MNRAS, 368, 1073

Gross, E., & Vitells, O. 2010, European Physical Journal C, 70, 525

Hagihara, T., Yamasaki, N. Y., Mitsuda, K., Takei, Y., Sakai, K., Yao, Y., Wang, Q. D., & Mc-Cammon, D. 2011, PASJ, 63, 889

Hinshaw, G., et al. 2013, ApJS, 208, 19

Holman, R., Lazarides, G., & Shafi, Q. 1983, Phys. Rev. D, 27, 995

Horiuchi, S., Humphrey, P. J., Oñorbe, J., Abazajian, K. N., Kaplinghat, M., & Garrison-Kimmel, S. 2014, Phys. Rev. D, 89, 025017

Iakubovskyi, D. A. 2014, Advances in Astronomy and Space Physics, 4, 9

Ishisaki, Y., et al. 2007, PASJ, 59, 113

Kalberla, P. M. W., Burton, W. B., Hartmann, D., Arnal, E. M., Bajaja, E., Morras, R., & Pöppel, W. G. L. 2005, A&A, 440, 775

Koutroumpa, D., Lallement, R., Kharchenko, V., Dalgarno, A., Pepino, R., Izmodenov, V., & Quémerais, E. 2006, A&A, 460, 289

Koyama, K., et al. 2007a, PASJ, 59, 245

Koyama, K., et al. 2007b, PASJ, 59, 23

Kusenko, A., & Segrè, G. 1997, Physics Letters B, 396, 197

Kusenko, A., Mandal, B. P., & Mukherjee, A. 2008, Phys. Rev. D, 77, 123009

Kusenko, A. . 2004, International Journal of Modern Physics D, 13, 2065

Kusenko, A. . 2006, Physical Review Letters, 97, 241301

Kushino, A., Ishisaki, Y., Morita, U., Yamasaki, N. Y., Ishida, M., Ohashi, T., & Ueda, Y. 2002, PASJ, 54, 327

Laine, M., & Shaposhnikov, M. 2008, JCAP, 6, 31

Lallement, R. 2004, A&A, 418, 143

Lisse, C. M., et al. 1996, Science, 274, 205

Loewenstein, M., & Kusenko, A. 2010, ApJ, 714, 652

Lovell, M. R., Frenk, C. S., Eke, V. R., Jenkins, A., Gao, L., & Theuns, T. 2014, MNRAS, 439, 300

Masui, K., Mitsuda, K., Yamasaki, N. Y., Takei, Y., Kimura, S., Yoshino, T., & McCammon, D. 2009, PASJ, 61, 115

McCammon, D., & Sanders, W. T. 1990, ARA&A, 28, 657

Meidinger, N., et al. 2014, in Society of Photo-Optical Instrumentation Engineers (SPIE) Conference Series, Vol. 9144, Society of Photo-Optical Instrumentation Engineers (SPIE) Conference Series, 1

Mitsuda, K., et al. 2007, PASJ, 59, 1

Mitsuda, K., et al. 2014, in Society of Photo-Optical Instrumentation Engineers (SPIE) Conference Series, Vol. 9144, Society of Photo-Optical Instrumentation Engineers (SPIE) Conference Series, 2

Moretti, A., Campana, S., Lazzati, D., & Tagliaferri, G. 2003, ApJ, 588, 696

Munyaneza, F., & Biermann, P. L. 2005, A&A, 436, 805

Munyaneza, F., & Biermann, P. L. 2006, A&A, 458, L9

Mushotzky, R. F., Cowie, L. L., Barger, A. J., & Arnaud, K. A. 2000, Nature, 404, 459

Navarro, J. F., Frenk, C. S., & White, S. D. M. 1996, ApJ, 462, 563

Nieto, D., & Mirabal, N. 2010, ArXiv e-prints

Pal, P. B., & Wolfenstein, L. 1982, Phys. Rev. D, 25, 766

Petraki, K., & Kusenko, A. 2008, Phys. Rev. D, 77, 065014

Predehl, P., et al. 2014, in Society of Photo-Optical Instrumentation Engineers (SPIE) Conference Series, Vol. 9144, Society of Photo-Optical Instrumentation Engineers (SPIE) Conference Series, 1

Prokhorov, D., & Silk, J. 2010, ApJL, 725, L131

Refregier, A. 2003, ARA&A, 41, 645

Remmen, G. N. 2011, in Bulletin of the American Astronomical Society, Vol. 43, American Astronomical Society Meeting Abstracts #217, #151.04

Saab, T. 2013, in The Dark Secrets of the Terascale (TASI 2011) - Proceedings of the 2011 Theoretical Advanced Study Institute in Elementary Particle Physics. Edited by Matchev Konstantin et al. Published by World Scientific Publishing Co. Pte. Ltd., 2013. ISBN #9789814390163, pp. 711-738, ed. M. Schmaltz & E. Pierpaoli, 711–738

Sakai, K., Yao, Y., Mitsuda, K., Yamasaki, N. Y., Wang, Q. D., Takei, Y., & McCammon, D. 2014, PASJ, 66, 83

Sarazin, C. L. 1986, Reviews of Modern Physics, 58, 1

Sekiya, N., Yamasaki, N. Y., Mitsuda, K., & Takei, Y. 2014a, in Suzaku-MAXI 2014: Expanding the Frontiers of the X-ray Universe, ed. M. Ishida, R. Petre, & K. Mitsuda, 66

Sekiya, N., Yamasaki, N. Y., Mitsuda, K., & Takei, Y. 2014b, PASJ, 66, L3

Serlemitsos, P. J., et al. 2007, PASJ, 59, 9

Shaposhnikov, M., & Tkachev, I. 2006, Physics Letters B, 639, 414

Shaposhnikov, M. . 2008, Journal of High Energy Physics, 8, 8

Shi, X., & Fuller, G. M. 1999, Physical Review Letters, 82, 2832

Smith, R. K., Brickhouse, N. S., Liedahl, D. A., & Raymond, J. C. 2001, ApJL, 556, L91

Smith, R. K., et al. 2007, PASJ, 59, 141

Sofue, Y. 2012, PASJ, 64, 75

Stasielak, J., Biermann, P. L., & Kusenko, A. 2007, Acta Physica Polonica B, 38, 3869

Supper, R., Hasinger, G., Pietsch, W., Truemper, J., Jain, A., Magnier, E. A., Lewin, W. H. G., & van Paradijs, J. 1997, A&A, 317, 328

Takahashi, T., et al. 2007, PASJ, 59, 35

Takahashi, T., et al. 2010, in Society of Photo-Optical Instrumentation Engineers (SPIE) Conference Series, Vol. 7732, Society of Photo-Optical Instrumentation Engineers (SPIE) Conference Series, 0

Tamura, T., Iizuka, R., Maeda, Y., Mitsuda, K., & Yamasaki, N. Y. 2014, ArXiv e-prints

Tamura, T., et al. 2009, ApJL, 705, L62

Tawa, N., et al. 2008, PASJ, 60, 11

Urban, O., Werner, N., Allen, S. W., Simionescu, A., Kaastra, J. S., & Strigari, L. E. 2014, ArXiv e-prints

Widrow, L. M., & Dubinski, J. 2005, ApJ, 631, 838

Wyse, R. F. G., & Gilmore, G. 2008, in IAU Symposium, Vol. 244, IAU Symposium, ed. J. I. Davies & M. J. Disney, 44–52

Yao, Y., Wang, Q. D., Hagihara, T., Mitsuda, K., McCammon, D., & Yamasaki, N. Y. 2009, ApJ, 690, 143

Yoshino, T., et al. 2009, PASJ, 61, 805

Yoshitake, H., Sakai, K., Mitsuda, K., Yamasaki, N. Y., Takei, Y., & Yamamoto, R. 2013, PASJ, 65, 32